AFRL-SN-HS-TR-2005-005

PROCEEDINGS OF THE 2003 ANTENNA APPLICATIONS SYMPOSIUM VOLUME I

Dr. Daniel Schaubert
University of Massachusetts at Amherst
College of Engineering
Amherst MA 01003

FINAL TECHNICAL REPORT   SEPTEMBER 2003

20041214 021

TECHNICAL REPORT

TITLE: 2003 ANTENNA APPLICATIONS SYMPOSIUM

APPROVED FOR PUBLIC RELEASE
DISTRIBUTION UNLIMITED

VOLUME I

NOTICE

USING GOVERNMENT DRAWINGS, SPECIFICATIONS, OR OTHER DATA INCLUDED
IN THIS DOCUMENT FOR ANY OTHER PURPOSE OTHER THAN GOVERNMENT
PROCUREMENT DOEES NOT IN ANY WAY OBLIGATE THE US GOVERNMENT. THE
FACT THAT THE GOVERNMENT FORMULATED OR SUPPLIED THE DRAWINGS,
SPECIFICATIONS, OR OTHER DATA DOES NOT LICENSE THE HOLDER OR ANY
OTHER PERSON OR CORPORATION; OR CONVEY ANY RIGHTS OR PERMISSION TO
MANUFACTURE, USE, OR SELL ANY PATENTED INVENTION THAT MAY RELATE
TO THEM.

THIS TECHNICAL REPORT HAS BEEN REVIEWED AND IS APPROVED FOR
PUBLICATION.

\\SIGNED//

HARVEY E. TOBIN
Antenna Technology Branch
Electromagnetics Technology Division

\\SIGNED\\

LIVIO D. POLES
Chief, Antenna Technology Branch
Electromagnetics Technology Division

\\SIGNED\\

MICHAEL ALEXANDER
Technical Advisor
Electromagnetics Technology Division

REPORT DOCUMENTATION PAGE

Form Approved
OMB No. 0704-0188

The public reporting burden for this collection of information is estimated to average 1 hour per response, including the time for reviewing instructions, searching existing data sources, gathering and maintaining the data needed, and completing and reviewing the collection of information. Send comments regarding this burden estimate or any other aspect of this collection of information, including suggestions for reducing the burden, to Department of Defense, Washington Headquarters Services, Directorate for Information Operations and Reports (0704-0188), 1215 Jefferson Davis Highway, Suite 1204, Arlington, VA 22202-4302. Respondents should be aware that notwithstanding any other provision of law, no person shall be subject to any penalty for failing to comply with a collection of information if it does not display a currently valid OMB control number.
PLEASE DO NOT RETURN YOUR FORM TO THE ABOVE ADDRESS.

1. REPORT DATE *(DD-MM-YYYY)*	2. REPORT TYPE	3. DATES COVERED *(From - To)*
16 January 2004	Final	September 2003

4. TITLE AND SUBTITLE
Proceedings of the 2003 Antenna Applications Symposium Volume I

5a. CONTRACT NUMBER
GSA TASK NUMBER R15701320

5b. GRANT NUMBER

5c. PROGRAM ELEMENT NUMBER

6. AUTHOR(S)
Daniel Schaubert et, al.

5d. PROJECT NUMBER

5e. TASK NUMBER

5f. WORK UNIT NUMBER

7. PERFORMING ORGANIZATION NAME(S) AND ADDRESS(ES)
University of Massachusetts at Amherst
College of Engineering
Amherst, MA 01003

8. PERFORMING ORGANIZATION REPORT NUMBER
Volume I

9. SPONSORING/MONITORING AGENCY NAME(S) AND ADDRESS(ES)
Air Force Research Laboratory
80 Scott Rd
Electromagnetics Technology Division
Sensors Directorate
Hanscom AFB, MA 01731

10. SPONSOR/MONITOR'S ACRONYM(S)

11. SPONSOR/MONITOR'S REPORT NUMBER(S)

12. DISTRIBUTION/AVAILABILITY STATEMENT
Approved for Public Release; Distribution Unlimited

13. SUPPLEMENTARY NOTES
Volume I contains pages 1-230
Volume II contains pages 231-429

14. ABSTRACT
The Proceedings of the 2003 Antenna Applications Symposium is a collection of state-of-the-art papers relating to antenna arrays, millimeter wave antennas, simulation and measurement of antennas, integrated antennas, and antenna bandwidth and radiation improvements.

15. SUBJECT TERMS
Antennas, Arrays, Genetic Antennas, Bandwidth, Impedance Bandwidth, Spaced-Based Arrays

16. SECURITY CLASSIFICATION OF:			17. LIMITATION OF ABSTRACT	18. NUMBER OF PAGES	19a. NAME OF RESPONSIBLE PERSON
a. REPORT	b. ABSTRACT	c. THIS PAGE			
			UL	230	19b. TELEPHONE NUMBER *(Include area code)*

Standard Form 298 (Rev. 8/98)
Prescribed by ANSI Std. Z39.18

2003 ANTENNA APPLICATIONS SYMPOSIUM

17 – 19 September 2003
Monticello, Illinois

Identifiers for Proceedings of Symposia

The USAF Antenna Research and Development Program

Year	Symp. No.	Identifier
1951	First	_____
1952	Second	ADB870006
1953	Third	ADB283180
1954	Fourth	AD63139
1955	Fifth	AD90397
1956	Sixth	AD114702
1957	Seventh	AD138500
1958	Eighth	AD301151
1959	Ninth	AD314721
1960	Tenth	AD244388 (Vol. 1)
		AD319613 (Vol. 2)
1961	Eleventh	AD669109 (Vol. 1)
		AD326549 (Vol. 2)
1962	Twelfth	AD287185 (Vol. 1)
		AD334484 (Vol. 2)
1963	Thirteenth	AD421483
1964	Fourteenth	AD609104
1965	Fifteenth	AD474238L
1966	Sixteenth	AD800524L
1967	Seventeenth	AD822894L
1968	Eighteenth	AD846427L
1969	Nineteenth	AD860812L
1970	Twentieth	AD875973L
1971	Twenty-First	AD888641L
1972	Twenty-Second	AD904360L
1973	Twenty-Third	AD914238L

Antenna Applications Symposium

		TR#	ADA#
1977	First	None	955413
1978	Second	None	955416
1979	Third	_____	077167
1980	Fourth	_____	205907
1981	Fifth	_____	205816
1982	Sixth	_____	129356
1983	Seventh	_____	142003; 142754
1984	Eighth	85-14	153257; 153258
1985	Ninth	85-242	166754; 165535
1986	Tenth	87-10	181537; 181536
1987	Eleventh	88-160	206705; 206704
1988	Twelfth	89-121	213815; 211396
1989	Thirteenth	90-42	226022; 226021
1990	Fourteenth	91-156	237056; 237057
1991	Fifteenth	92-42	253681; 253682
1992	Sixteenth	93-119	268167; 266916
1993	Seventeenth	94-20	277202; 277203
1994	Eighteenth	95-47	293258; 293259
1995	Nineteenth	96-100	309715; 309723
1996	Twentieth	97-189	341737
1997	Twenty First	1998-143	355120
1998	Twenty Second	1999-86	364798
1999	Twenty Third	2000-008 (I) (II)	386476; 386477
2000	Twenty Fourth	2002-001 Vol I & II	
2001	Twenty Fifth	2002-002 Vol I & II	
2002	Twenty Sixth		

Author Index

MULTI-BEAM TRANSMIT RECEIVE MODULE FOR USB AND SGLS BAND SATELLITE LINKS.

Sarjit S Bharj   Princeton Microwave
Paul Oleski   AFRL, Rome
Dr. Boris Tomasic   AFRL, Hanscom
John Turtle   AFRL, Hanscom
S. Liu   Aerospace Corporation
N. Patel   Princeton Microwave
A. Merzhevskiy
Li. Qu
M. Thaduri

ABSTRACT

The development of a low cost Transmit-Receive module (T/R) for the next generation of Phase Array Antennas for the Air Force Satellite Control Network has been achieved. The T/R module consists of dual transmit channels each capable of 30 dBm output power, a 4-Bit phase control and a 4-Bit amplitude control. In addition, beam switching and on board digital control has been implemented. The dual receive channels exhibit a 2 dB Noise Figure associated with a gain of 30 dB per channel. Each channel exhibits four bit phase shift and five-bit amplitude control. In addition to the control functions, built-in test circuits have been incorporated to monitor the health and status of the RF devices. This function utilizes a micro-controller to output digital data for each of the power and low noise amplifiers on command, via A/D converters. The bandwidth of the T/R module has been increased by a factor to encompass both the Unified S-Band (USB) and Satellite Ground Link System (SGLS). The transmit-receive functions are combined at the output via a ceramic resonator diplexer comprised of a bandpass-band stop filter. The control of the T/R module is conducted via a single Field Programmable Gate Array (FPGA) through a GPIB controller. The T/R module has been designed to meet the cost objective for an array with 55000 T/R modules. To this end the paper will detail the performance and innovative methods used to achieve the price performance goals.

INTRODUCTION

The development of a low cost T/R module for the next generation of Phase Array Antennas for the Air Force Satellite Control Network has been achieved. Low cost component design and implementation are critical in developing a practical phase array antenna. Combined RF, digital and monolithic circuits are important but not the only critical issue. This T/R module differs from the previous modules, Ref.1, Ref2, in that this modules has a wider frequency band associated with the transmit section. In addition,

diplexers are utilized between each tansmit and receive section. Both left-hand and right-hand polarization is used in a special polarization matrix.

Affordable antenna arrays operating at microwave frequencies are envisioned to consist of active modules that employ microwave integrated circuits located at each radiating element of the aperture. The antenna system consists of separate receiver and transmit aperture capable of rapid beam motion. The transmitter antenna should be capable of high radiation power levels and the receiver antennas must achieve high G/T ratios. Beam agility and high-radiated power levels in association with the close spacing between the radiators drive the antenna design. The requirement for fast beam switching will require digital control circuits to calculate phase shift settings. A high RF radiated power level developed from closely spaced RF amplifiers generates very large heat densities. This forces the transmit antenna to increase in area to where beam pointing accuracy limits the array size. The great number of elements in the array emphasizes the need to develop a practical method of distributing control signals throughout the array. A Geo-Disic Spherical Phase Array Antenna is considered for Air Force Satellite Communication network. Implicit in the system function array is the need to operate the array in full duplex operation. Additionally the array should be capable of controlling fundamental radiation characteristics such as beam width, beam size, sidelobe levels and radiated power, in order to realize different antenna characteristics required by the various satellites. The array aperture consists of a large number of radiating elements that are spaced approximately half a wavelength at the upper end of the operational frequency band. The frequency response and excitation of each element in the aperture can be independently controlled. The aperture can be fully or partially utilized either to direct energy over a large volume or intentionally directed in a certain direction. Additionally, radar and communications require both transmission and reception of energy where as ESM and ECM systems require only reception of energy. The capability of the array to provide transmit and receive functions simultaneous and to rapidly alter the set of configurations is possible due to active element control circuit. The active control circuits allow the Phase Array Radar to control their radiation characteristics. The aperture can be uniformly illuminated to achieve maximum gain or tapered illuminated to achieve low sidelobes or shaped beam. The combination of the variable attenuator and phase shifter permits the array Illumination to be modified and the antenna beam to be scanned in any direction. The filter specifies the portion of the aperture used by a particular system. The phase shifter, the variable attenuator and the amplifier are components that have been developed in MMIC (Microwave Monolithic Integrated Circuit technology), in the last decade.

The requirement of high degree of isolation between transmit and receive channels focused the effort to investigate the exact performance that can be achieved from the low-cost ceramic diplexing filters. In addition, low cost MMIC based power amplifiers for transmit channel have been used. Other effort was directed towards the design of a low-cost phase shifters. Due to the bandwith of the transmit section a broadband phase shifter using low pass and high pass filter sections was designed. The receive band phase shifter was based on the switched line methodology.

2

Other important factors that were considered in the development of the T/R module were:
- T/R module's interface with beamformer
- Hot condition Operation
- Polarization Diversity
- Dual Transmit and Receive Channels to allow multi beam operation
- Low Cost with Justification
- High Isolation between Transmit and Receive Channels
- Digital Control on Board
- Ruggedness and Reliability
- Built in Test

System Block Diagram

The block diagram for the Transmit/ Receive module is detailed in Figure 1. The transmit section of the T/R module consist of two control circuits at the input, each comprising of a 4-BIT digital phase shifter and a 4-BIT digital attenuator, which are combined in a Wilkinson power combiner. The output of the combiner is amplified in a driver amplifier and fed into a 90-degree hybrid through a single pole double throw switch. The quadrature outputs of the hybrid are amplified via MMIC amplifiers to a power output of in excess of 30 dBm and transmit through diplexer ceramic filters.
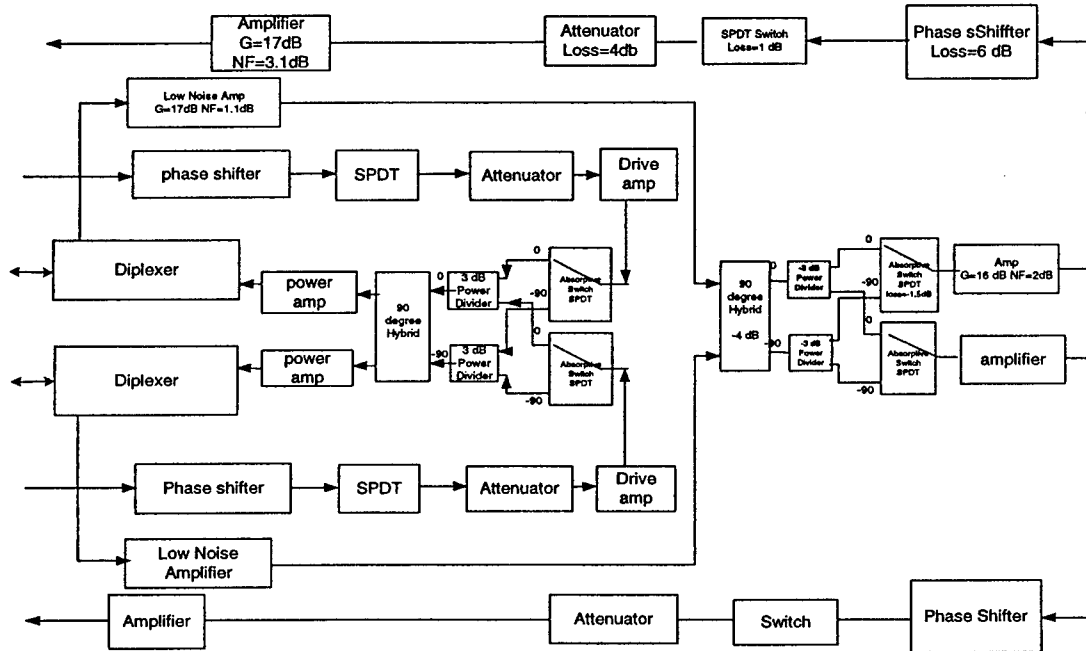
Figure 1: The block diagram of Transmit/Receive module

The specification for the transmit and receive sections of the T/R module are detailed below.

Table I: Specification for Transmit Channel

PARAMETER	SPECIFICATIONS
Frequency	1.75-2.1GHz
Gain	20dB
Power output per channel	30dBm
Phase shift	360°
Control	Electronics
Retrofit	Change in Hot condition
Efficiency	> 40 %
Spurious Levels	<-85
Attenuation	3 to 10 dB

Table II: Specification of Receive Channel

PARAMETER	SPECIFICATIONS
Frequency	2.2-2.3 GHz
Gain	30dB
Noise Figure	1.2dB
Phase shift	360°
Attenuation	30dB min

The main components of the Transmit/Receive module are:
- Ceramic diplexer with high rejection
- Low noise MMIC amplifiers
- High Power MMIC driver and Power MMIC Amplifiers
- Quadrature and in phase hybrids
- 4-Bit Transmit and Receive digital Phase Shifter
- 4-Bit Digital Control Attenuators for Transmit and Receive channel
- Polarization selection
- Xilinx digital controller
- PIC controller for Built-In-Test
- RS-485 and PCI interface

Diplexers

Two diplexers are required to maintain optimum performance. The transmit side of the diplexer filter, inserted after the transmit amplifier, prevents wideband noise from entering the receiver, and degrading performance. The receive section of the diplexer, prevents the coupled transmit signal from degrading the linearity of the receive Low

4

Noise Amplifier (LNA). The diplexer filters are made of high Q ceramic resonators. Two types of diplexers were investigated. The first consisted of a bandpass- bandpass type of response to provide at least 60 dB of rejection at the crossover point between the bands. This filter provided a loss of 1 dB in the transmit pass band and 1.5 dB in the receive path. To maintain a reasonable noise figure an insertion loss of 1 dB was allowed in the receive section. We then investigate d a diplexer with a bandstop bandpass type of diplexer. This filter provided an insertion loss of 1 dB in the receive band consists of six resonators in a coaxial structure. The transmit section loss was 0.5 db with a rejection of 55dB at the crossover frequency. The bandstop filter consisted of three sections of notch filtering using ceramic technology.

Table III: Specification of Transmit Filter

PARAMETER	SPECIFICATIONS
Frequency	1.75-2.1 GHz
Insertion loss	1.0dB Max
Return loss	<-15dB
Rejection at 2.15 GHz	<-50

TABLE IV: Specification of Receive Filter

PARAMETER	SPECIFICATIONS
Frequency	2.2-2.3 GHz
Insertion loss	1.0dB Max
Return loss	<-15dB
Rejection at 2.15 GHz	<-50

The simulated response of the filter is detailed in Figure 2.

DB[S21] --		DB[S11] --		DB[S21] --		DB[S22] --	
1750	2100	2200	2300	1750	2100	2200	2300
-0.323918	-0.45059	-30.4732	-18.9714	-0.323918	-0.45059	-30.4732	-18.9714
-23.0146	-21.6314	-23.185	-31.9105	-21.3316	-19.6886	-0.485238	-0.512915
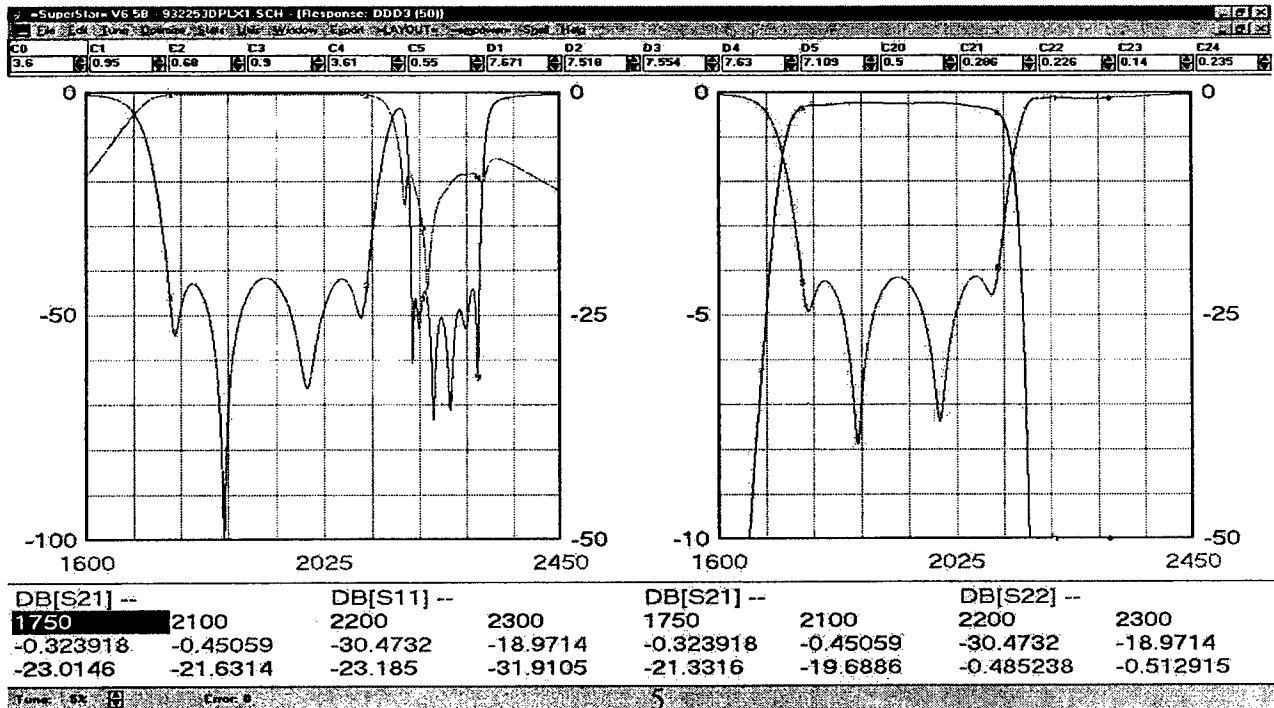
Low Noise MMIC Amplifier

The Low noise amplifier can either be designed or use a MMIC amplifier. For a frequency of 2.2 to 2.3 GHz, a low noise MMIC amplifier developed for the satellite radio market has been used. The device provides a gain of 18 dB with an associated noise figure of 1 dB. It is based on E-D MESFET process and consumes very low current.

5 Bit Transmit and Receive Phase Shifters

A phase shifter design based on the MMIC switch incorporating a single double pole double throw was procured from Marconi. This device essentially replaces two single pole double throw switches. The component count reduced from 10 devices per phase shifter, (Total 40 for T/R module) to 5 devices per phase shifter (20 per T/R module). The design of the Transmit and Receive channel phase shifters was detailed in Ref 1. The insertion loss of the phase shifter was measured at 8 dB with a total change in insertion loss of 0.4 dB in all phase states.

The transmit phase shifters were designed based on low-pass, high-pass filter sections switched between paths. The phase shifter provided 22.5, 45, 90 and 180-degree phase shifts with an error of 10 degree for the 180 degree bit. Total amplitude change for the phase shifter was less than 1 dB for all phase states. The receive phase shifters were based on the switch line approach and exhibited an insertion loss of 6 dB. Again the total amplitude change was less than 1 dB for all phase states. This is shown in figure 3.
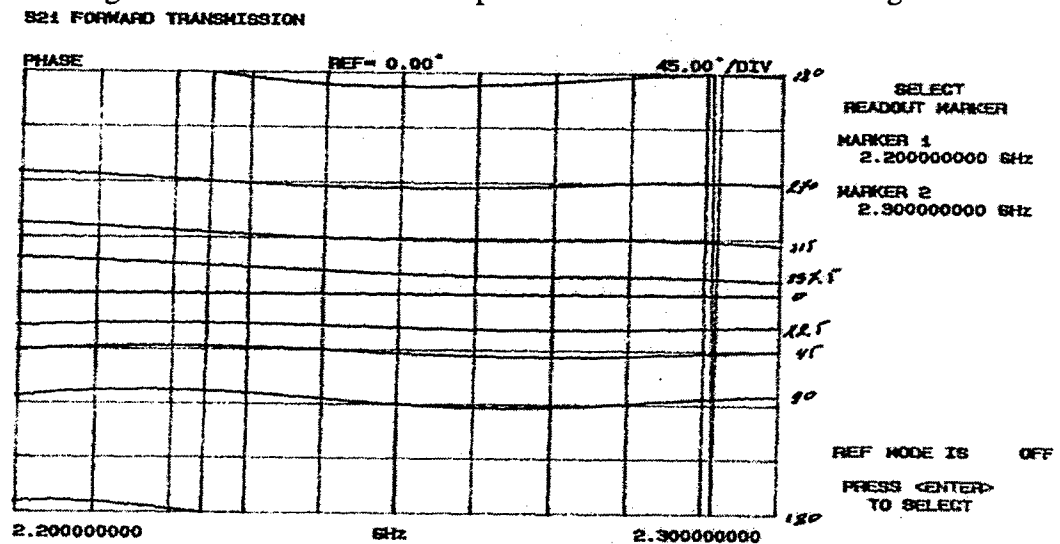
Figure 3 (a) Phase shifter measurements

6
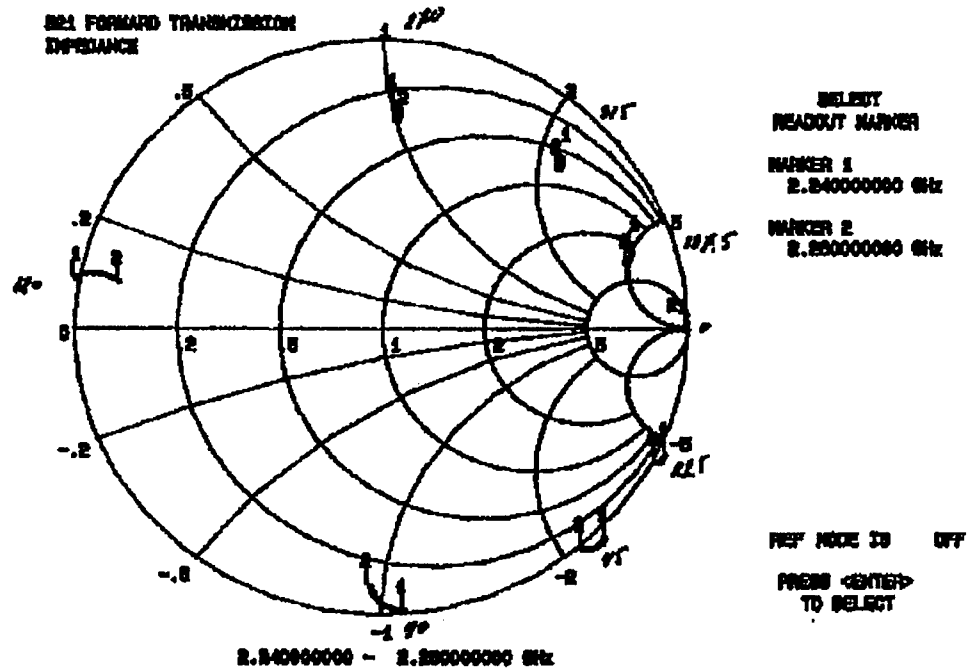
Figure 3: The measured performance of receive channel phase shifter

Polarization Switching

A scheme for polarization switching has been incorporated into the T/R module. The details are shown below in Figure 4. Both LH and RH polarization is achieved in the transmit and receive section of the module. Typical incorporation in the receive section is detailed in Figure 5
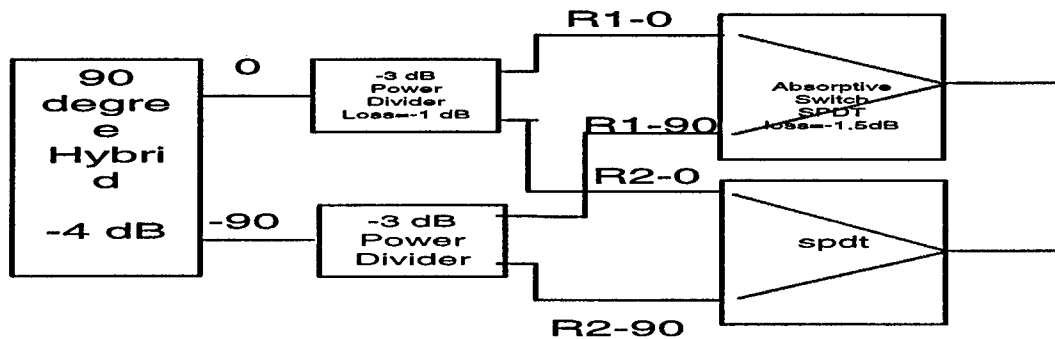
Figure 4: Polarization Switching schematic

7
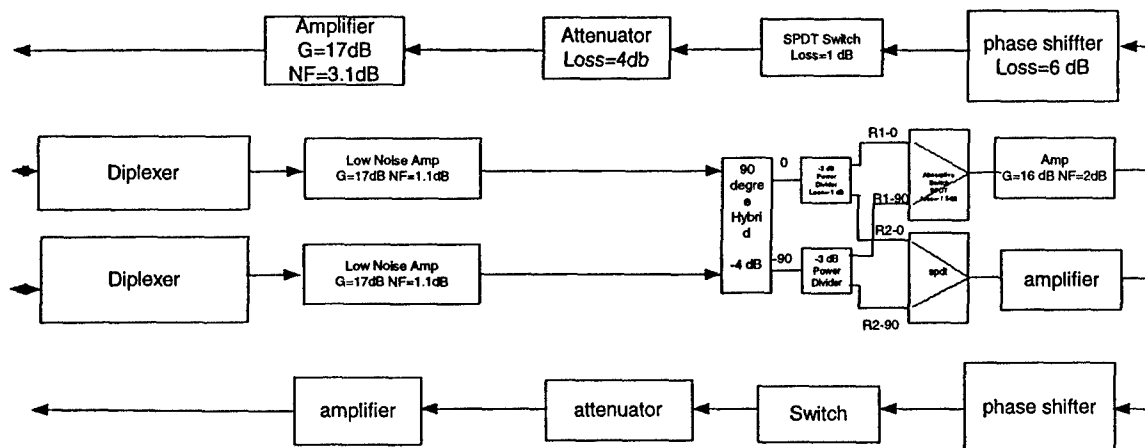
Figure 5: Polarization switching in receives section

Xilinx digital controller

The purpose of the serial to parallel bus arbitrator is to accept serial commands and unit address data and pass these commands to a parallel bus connected to a uniquely addressed unit. The input signals to this circuit are data, clock, latch and enable; the outputs are 16 parallel command lines connected to a single programmable unit. Four addressable units are grouped into a single Transmit/Receive module. In order to avoid hardware redundancy, one unit can be addressed with a base address and the remaining three can be indirectly addressed. In addition, to compensate for data and clock line fan out for a large number of modules, a single module can act as a "Master" module for several modules by buffering the clock, data and latch lines. 32 bits of serial data is clocked into a 32-bit wide shift register. Command data is stored in bits 0 to 15 and the desired unit's address is stored in bits 16 to 31 allowing for 65536 possible units. Once all 32 serial bits are stored in the shift register, a unit with a matching address is determined to exist, and the latch line is subsequently set high for a clock pulse, commands are latched out to the addressed 16 line parallel bus. In each unit, the channel is indirectly addressed 0-3 by subtracting the module's base address from the intended unit's address. The serial to parallel bus arbitrator circuit is now ready to receive the next serial stream of data. Details are shown in Figure 6.

8
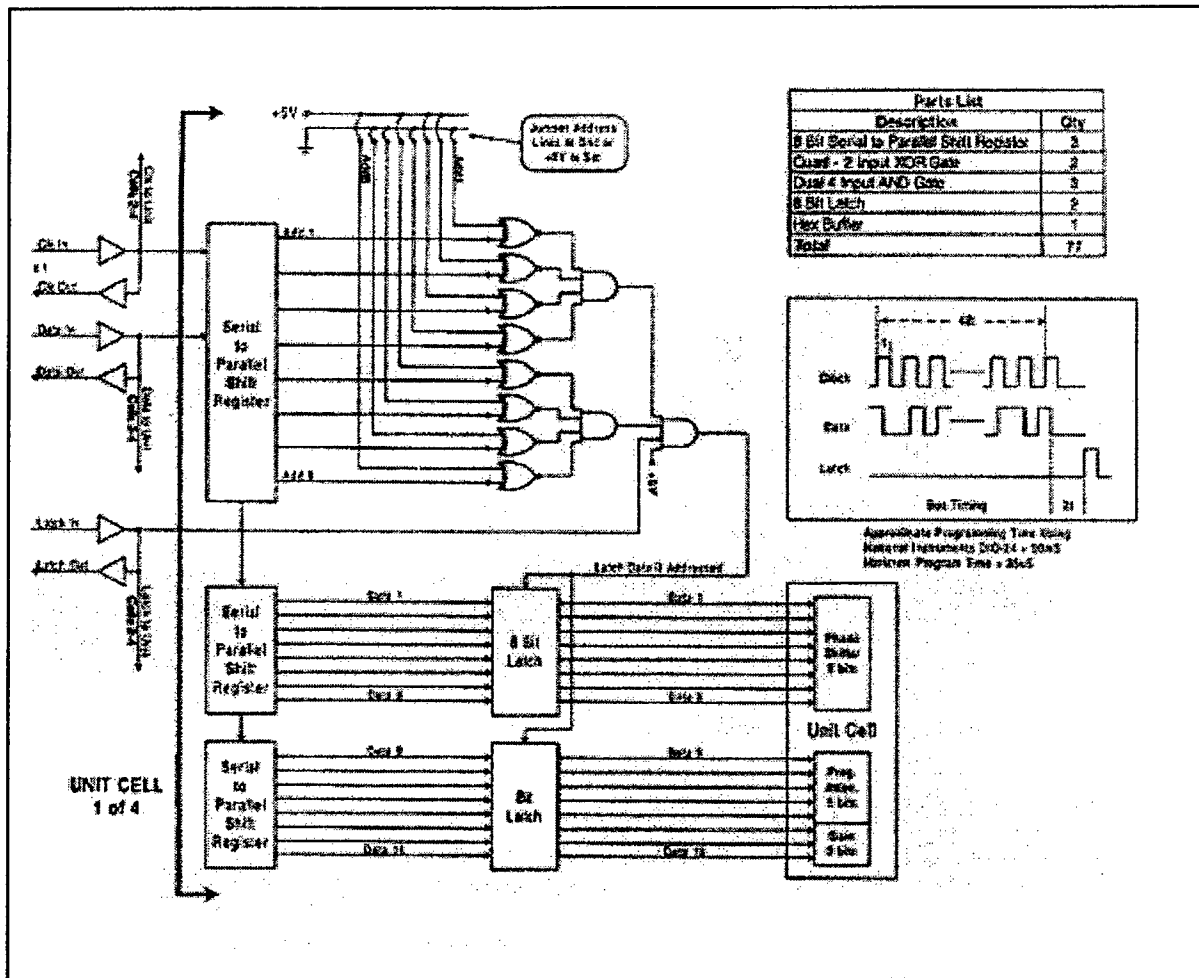
Figure 6: Serial Bus Topology for 200 T/R modules maximum:

T/R Module Layout

The original T/R module layout was conducted in a manner where the Inputs/Outputs (I/O) form the beam former was on the opposite end, to the antenna Output/Input respectively. Later, it was clear that the I/O from the beam former to the antenna output/input needs to be on the same side to allow module exchange in the hot condition. The width of T/R module was restricted to a maximum of 3 inch. The RF board was fabricated using grounded coplanar technology to reduce coupling and grounding effects. The control board was fabricated on Multilayered FR-4 substrate.

The completely assembled Transmitter (TX) section of the T/R module with the associated control circuitry is shown in Figure 7. The Receiver (RX) board is shown in Figure 8.
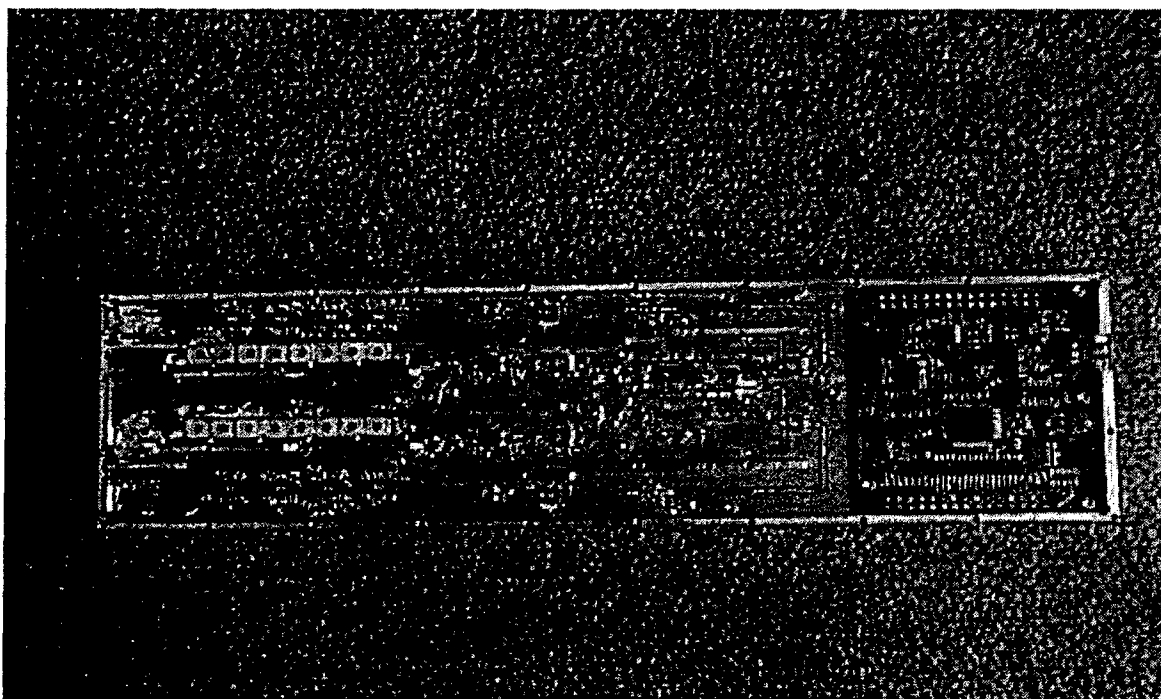
Figure 7: TX Section of the TR Module

10
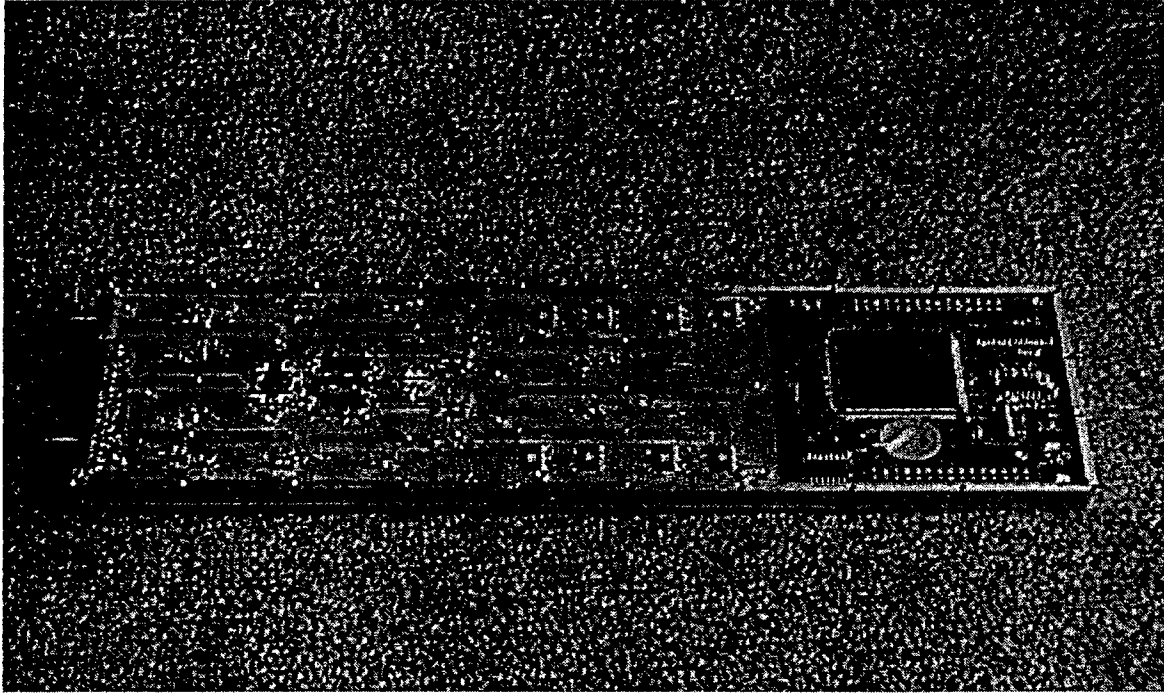
Figure 8: RX section of T/R Module

Design To Cost

The design to cost of the T/R module has been conducted from project initiation. From onset, the cost associated with the components without any compromise in the performance has been the guiding rule. The availability of the active devices for the PCS market has really influenced the cost of amplifiers and phase shifters. Added with novel design and layout, the design to cost goal is near reality.

Measured Data

Measured data for the transmit/ receive module has been taken and detailed below.

S21 FORWARD TRANSMISSION
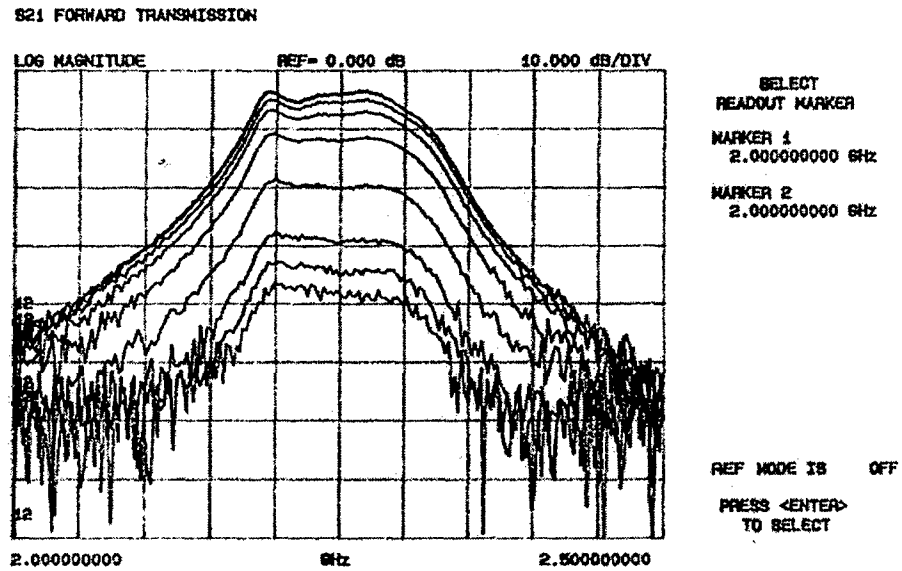
Receive channel
Input 1 to Output 1   In band step Attenuation
0, 1, 2, 4, 8, 16, 24, 28, 31 (dB)
S/N 3507

Figure 9: Receive Channel Amplitude Control

Receive channel
Input 1 to Output 1   4 Bit Phase Shifter
0, 22.5, 45, 90, 180, 270, 315, 337.5
S/N 3507
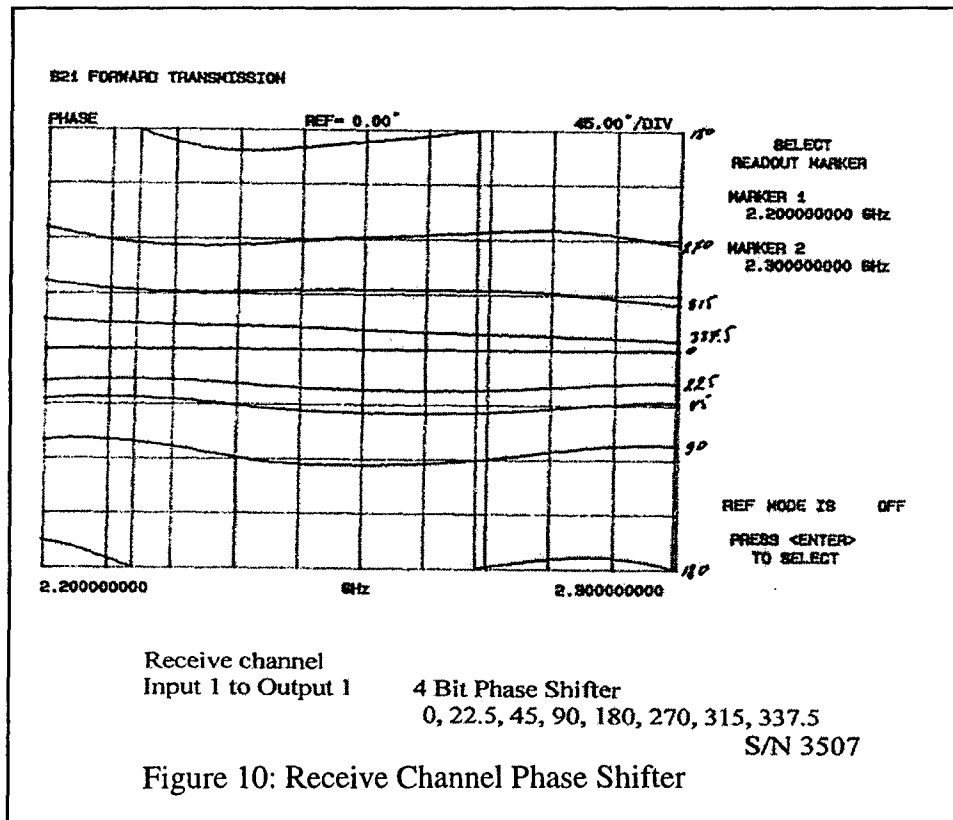
Figure 10: Receive Channel Phase Shifter
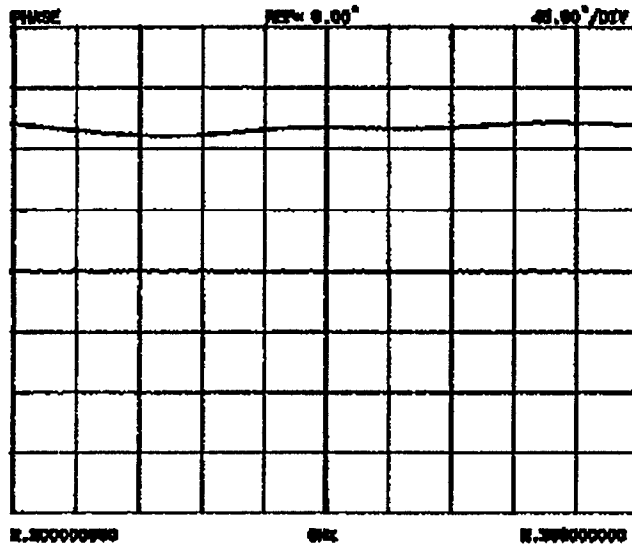
S21 FORWARD TRANSMISSION

Receive channel
Input 1 to Output 1   Switch Polarization
                        0, 90

S/N 3507

Figure 11: Receive Channel Switch Polarization
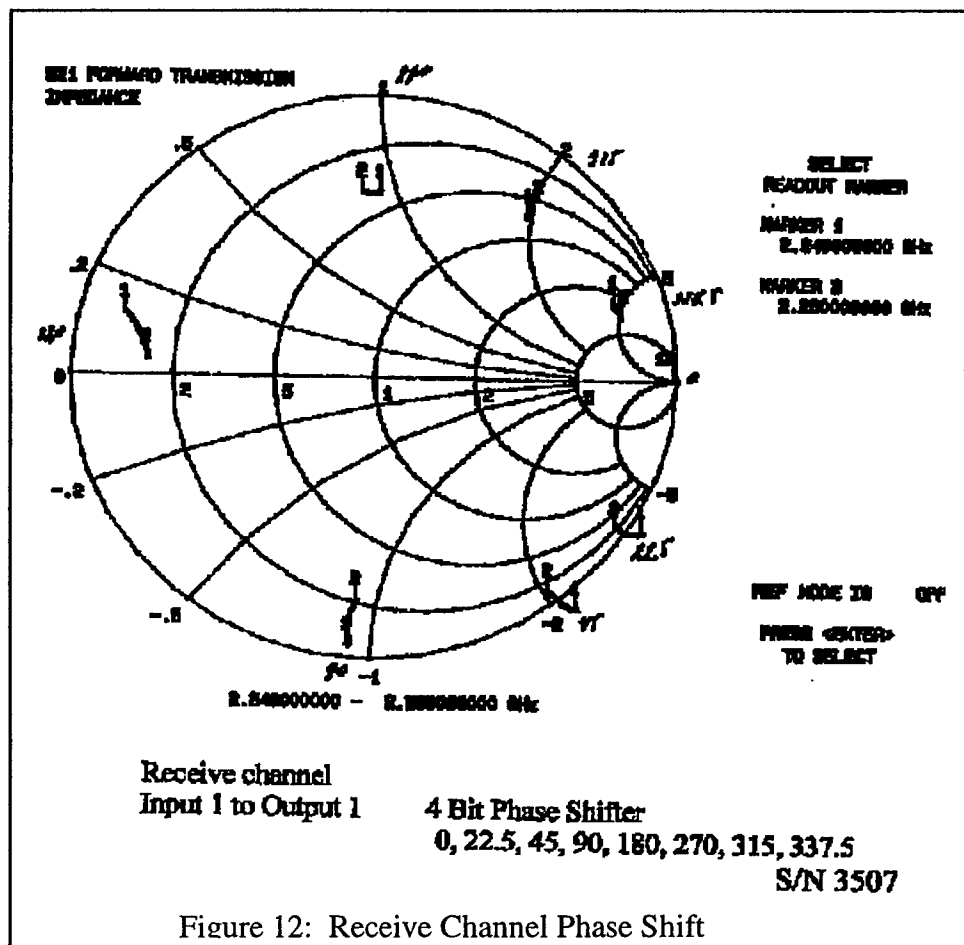
Receive channel
Input 1 to Output 1   4 Bit Phase Shifter
                        0, 22.5, 45, 90, 180, 270, 315, 337.5

S/N 3507

Figure 12: Receive Channel Phase Shift

13

CONCLUSIONS

A T/R module has been developed for the USB-SGLS band operation. T/R modules were fabricated and tested. A design to cost exercise was conducted to ensure a low cost product. In the transmit section a power output of 30 dBm per channel, with a 4-BIT phase shifter and a 4-BIT attenuator, and polarization switching has been achieved. An overall gain of 30 dB was achieved. In the receive channel a noise figure of 2dB was measured with an overall gain of in excess of 20 dB. This channel also included 4-BIT phase shifter and 4-BIT attenuators. In its present form, the T/R module is reproducible. The next phase of development will focus on extending the T/R module for SGLS and USB frequencies.

REFERENCES

Ref [1] 'Affordable Antenna Array For Multiple Satellites Links
2000 Antenna Applications Symposium. P 401
Sarjit S Bharj, A. Merzhevskiy, P. Oleski, B. Tomasic, S. Liu

Ref [2] 'Low cost transmit/Receive module for space ground link subsystem,
2002 Antenna Applications Symposium. P 1
Sarjit S Bharj, A. Merzhevskiy, P. Oleski, B. Tomasic, S. Liu, John Turtle, Narendra Patel

A Novel Approach of a Planar Multi-Band Hybrid Series Feed Network for Use in Antenna Systems Operating at Millimeterwave Frequencies

M. W. Elsallal* and B. L. Hauck
Rockwell Collins, Inc.
400 Collins Road NE
Cedar Rapids, IA 52498
waelsall@ rockwellcollins.com   and   blhauck@ rockwellcollins.com

* Currently a Ph.D. candidate at University of Massachusetts, Amherst

Abstract: Recent advances in the development of multi-band antenna systems have focused on the radiating element. With the advent of antennas such as the notch antennas, radiating elements capable of broadband (DC – 50 GHz) operation have been developed. The problem of how to feed the radiating elements has not been adequately addressed. The corporate feed architecture has been the architecture of choice for feeding these elements. However, for applications where the feed loss is critical, the corporate feed architecture does not present a feasible solution. Other traditional low loss planar feed techniques, such as the series feed and its variations, suffer from narrow operating bands. In this paper, we describe a novel planar hybrid series feed network which exhibits the very low loss properties of the traditional series feed by modifying the resonant structure to operate at multiple distinct bands.

1.   Introduction

With the increased demand for commercial in-flight entertainment and communications systems, coupled with the Military's continued reliance on satellite-based communications for the battlefield of the future, there is a continuing push to advance low cost antenna systems capable of operating at multiple bands. In addition to the low cost requirements, significant space restrictions are being placed on these systems. To meet these demands, it has become necessary to develop wideband antenna systems capable of operating at multiple frequencies in a single aperture. While there have been strides to develop wideband radiating elements, little progress has been made when it comes to the feeding structure. In addition to requiring the antenna aperture to operate at multiple frequencies, there is a continuing call to reduce the overall size of the aperture. In order to reduce the size of the aperture and still be capable of closing the satellite communication link, components such as the feed, which had previously been ignored, must be designed to significantly reduce the losses associated with the feed. This requires moving away from the higher loss corporate feed structure that traditionally has been used as the feeding structure. With the high losses associated with the corporate feed and the narrow bandwidths associated with series feeds, it has become necessary to define a

new hybrid feed architecture which takes advantage of the low loss properties of the series feed while being capable of operating at multiple bands. In this paper, we will present two different planar hybrid architectures that have been designed to operate at dual and tri bands while maintaining low loss characteristics.

2. Definition of Problem

For millimeter wave satellite communications, the common bands are 20 GHz for receive and 30/44 GHz for transmit. Since the goal is to provide all communication functions in a single aperture, the feeding structure must be capable to operate at the multiple transmit and receive bands, compact, low profile and meets the gain requirements at millimeter frequencies. One solution would be to use a separate series feed for each of the frequency bands. However, this significantly adds to the cost and the complexity of the feed. It is desired to have a single feed structure capable of operating at all of the frequency bands of interest, or at the most two separate feed structures (one for the transmit bands and one for the receive bands). In order to meet all of the requirements, it is necessary to define a new class of hybrid feeding structures that combine the bandwidth properties of the corporate feed with the low loss properties of the series feed.

3. Previous approach:

There are many feed topologies and mechanisms are available, not just to couple energy to individual elements, but also to control distribution (for example, tapered illumination, phase shift, ..etc...) of energy in a linear or planar array of elements. A variety of those feed topologies have been surveyed in literatures [1-3]. A list of those electrical and packaging constraints which influence the choice of the feeding architecture are given in Fig.1.

The corporate feed is among the most commonly used architecture, where the feed is divided into two paths and each path divides in a binary order and so on, using the standard impedance split [3], Wilkinson divider [4] or Lange coupler [5]. Sometimes, the divider includes 3 or 5-ways divides [3]. In theory, an instantaneous broad bandwidth could be achieved using this topology. But in practice, the desire to have a low profile and light weight full size phased arrays of hundreds or thousands of radiating elements systems for satellite-on-the-move (SATOM) applications, that require a minimum net gain of 35 dBi, eliminates the feasibility to have this feed on a stack that is co-planar to the array. In other words, the overall depth of the feed structure is going to be a significant problem in an aerodynamics sensitive application. Also, the loss factor arises from line dissipations and reflection from junctions. Another avenue is a multilayer approach but the interconnect loss dramatically increases proportional to the number of layers in the millimeter frequency ranges [6]. Adding low noise amplifier (LNA) might not be attractive because it will add another figure of complexity in the multilayer package and will increase the cost. The series feed has a narrower bandwidth because of its dependency on the resonant frequency [1, 2].

Environmental requirements
- Pressure
- Vibration
- Thermal

Efficiency
Array bandwidth

Sidelobe requirements
- Uniform illumination
- Taper illumination

Array size
- Aperture dimensions
- Profile constraint

System specification
- Polarization diversity
- Number of simultaneous beam

Packaging Testability

Quality

DESIGN

Compliance

Cost

Manufacturability

Mass Production

Demo prototype

Service/Repair

Feed structure
- Coplanar with the antenna
- 3D Multilayer package

Integration of LNA
- Surface mounted
- Embedded

Figure 1: Concurrence of a design to determine of feed structure

A broadband space fed array offers a low-cost alternative whenever multiband feed and beam squint constraints will allow [7,8]. However, the focal/depth ratio of the lens is always a concern. Secondarily, such configuration requires a broadband true time delay phase shifter such as MEMs technology [9] used to enable beam shaping and electronic steering functionalities. MEMs are still in the premature stages and there is an issue of the long term reliability [10], which effects the applicability of this approach.

There are other arrangements of feeds that phased array engineers have used; however, the intent of this section is to exhibit a top level summary of the key attempts and challenges in achieving a broadband feed network.

4.   Planar Multiband Hybrid Series and Corporate Feed Network

a. Feed Structure

With the above background, there was a demand to reveal the fundamental properties of electromagnetic waves and circuit theory, to go beyond the conventional feed topologies and propose a multiband hybrid series feed solution that is illustrated in Fig. 2.

4 Taps Output

Series Feed Topology
- Low loss
- Small Bandwidth

Matching Section

Input

Band Pass Filter
- Distributed or RLC elements
- Operate at freq of interest

Band Pass Filters

Multiband Series Feed
- Low loss
- Large Bandwidth, even in millimeter context!

Matching Section

Input
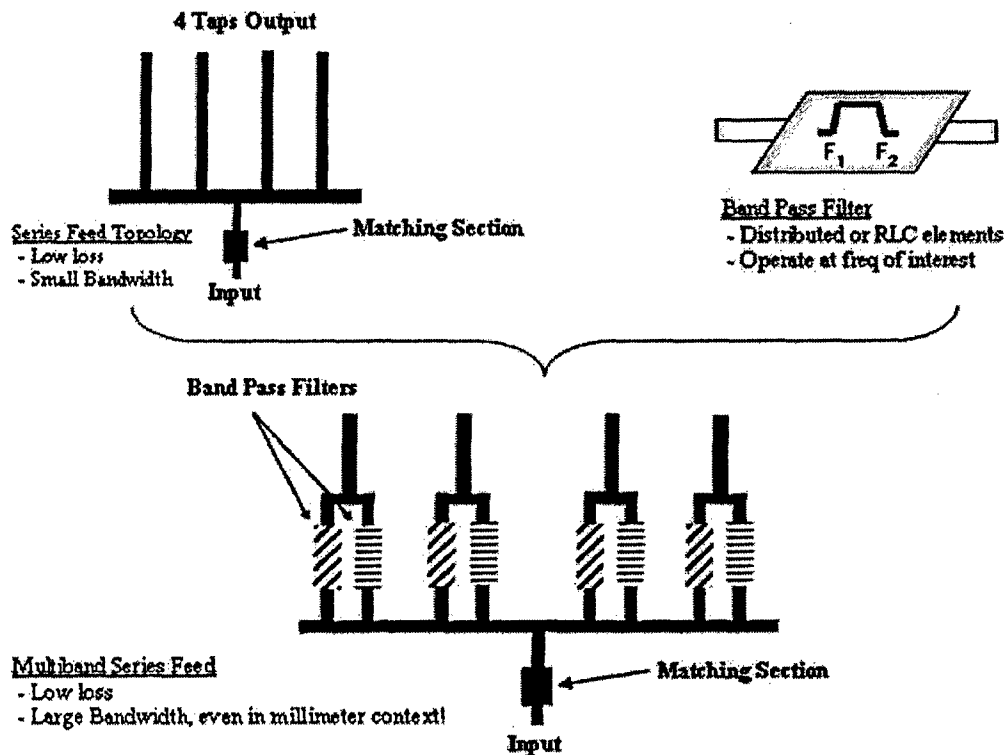
Figure 2: Multiband Hybrid Series Feed Architecture

Similar to the conventional series feed, the multiband hybrid series feed can be fed either from the edge or from the center and is terminated with an open circuit(s). The coupled series line is modified to include multiple sub tap lines for each frequency band. The taps are superimposed by band pass filters that tune the resonance response of that tap line to the desired frequency band. The outputs of the individual frequency sub tap lines are combined after the filtering stage to form a multiband tap line. The spacing between the sub tap lines and the open circuit and their impedances are optimized to provide the desired performance.

For applications requiring more feed tap-lines than a single branch can support, as depicted in Fig. 2, branches can be cascaded together to provide additional tap lines. Figure 3 depicts a solution for a dual band feed in a 16 element array.

18
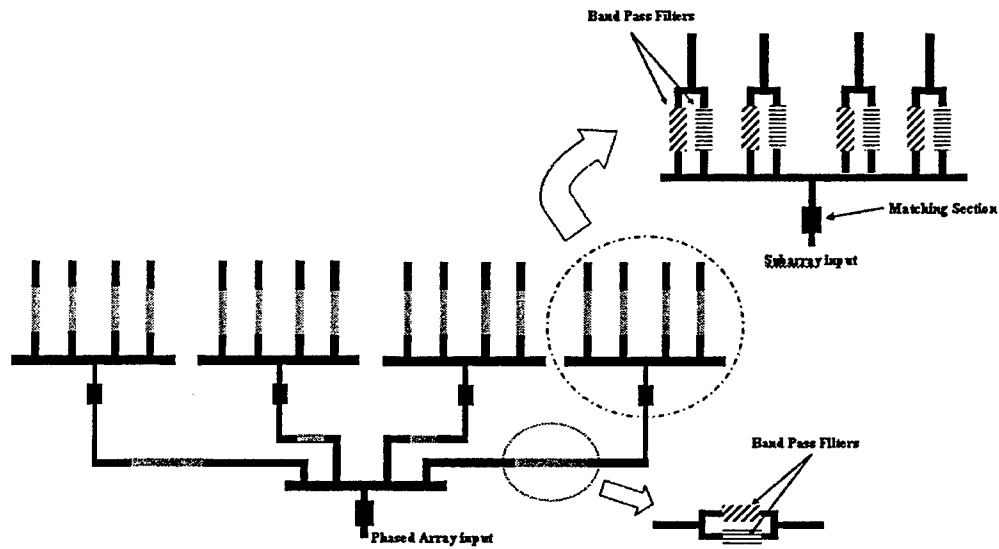
Figure 3: Multi-branch, dual-band hybrid series feed realized from a single branch

The bandpass filters used in the sub tap lines can take any form, including distributed and lumped elements [11, 12]. Selection of the filter architecture is application driven and is determined by factors such as acceptable loss, available space, useable line widths, and/or the periodic nature of the distributed network.

Another feature of this new hybrid-series feed is that it provides substantially uniform and tapered illumination at the output tap-lines. It exhibits an ultra-low loss performance compared with the two distinct types of feed: corporate and series or their combination. The hybrid series feed discussed here can be extended to cover a tri-band operation as shown in Fig. 4.
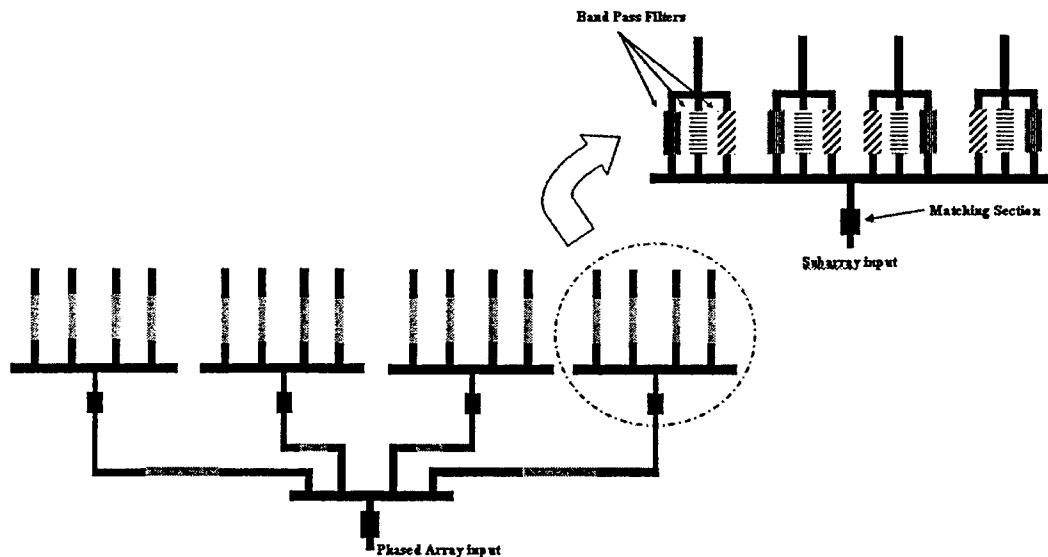
Figure 4: Multi-branch, tri-band hybrid series feed realized from a single branch feed

Additionally, it can be expanded to as many as output taps as desired while preserving the operational bandwidth of the array and the low feed-loss. An example is shown in Fig. 5.
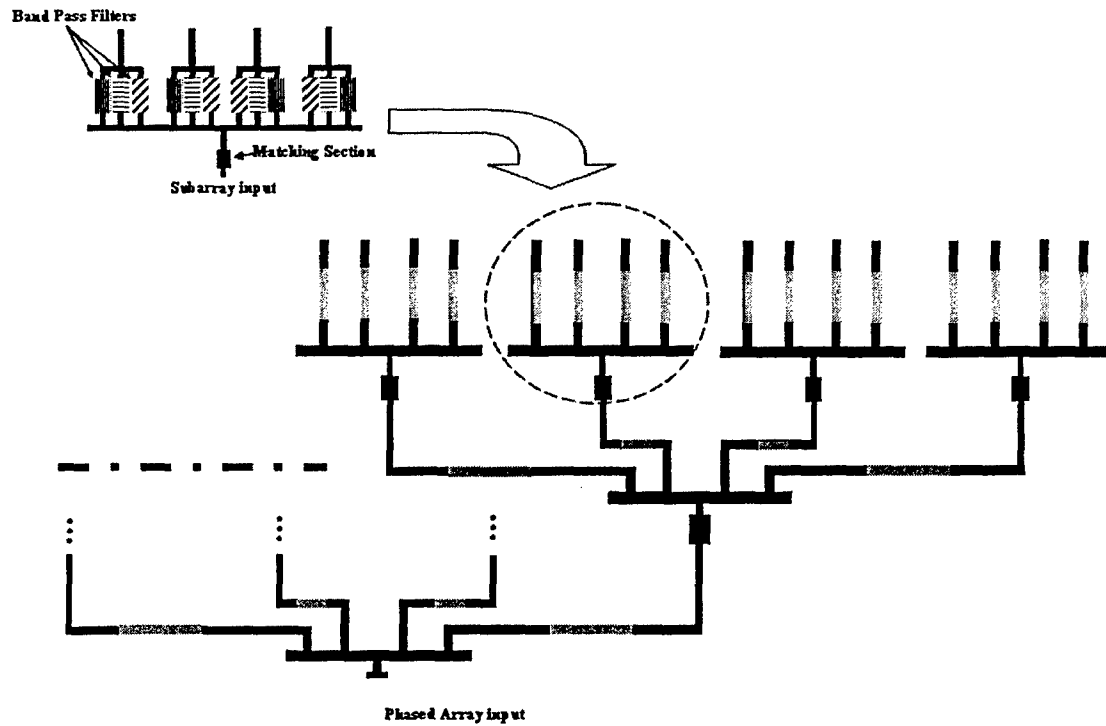
Figure 5: Multi-branch, tri-band hybrid series feed realized from a single branch

A known drawback with the above novel approach is that the more operating bands are desired, the wider the circuit is to be because of the filter components, so a packaging engineer might have a difficulty in assembling all the sub-tap lines behind a single radiating element.

In applications where the circuit width is more critical than the depth, the hybrid series feed may not be applicable due to the required circuit width. A second hybrid series circuit feed topology that allows the width of the circuit to be constrained at the cost of increasing depth is the Hybrid Corporate Feed. The Hybrid Corporate Feed is a modification of the traditional corporate feed that is widely used. The principle of operation for the corporate feed is based on impedance division. A graphical representation of the traditional corporate feed is shown in Fig. 6.
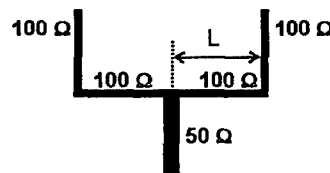
Figure 6: Graphical representation of a traditional corporate feed

In the traditional corporate feed, the distance between the branches (L) can be set as desired. The branch impedance is chosen such that the output ports are matched to the input feed line. In theory, if the dielectric constant of the substrate remains constant over frequency, the power split would be constant over frequency. However, the bends introduce a capacitive loading which causes the power split to vary with frequency (see Fig. 8).

In the alternative hybrid corporate feed architecture, shown in Fig. 7, the distance between the branches of the circuit is fixed to the desired value. The impedance of the branch arm, feed line, and matching sections are optimized to provide the desired response. By choosing the proper combination of the line impedances and lengths, the circuit exhibits a resonance response at the desired frequencies. Through optimization, the circuit can be designed to provide a constant power split over the designed frequency bands, as shown in Fig. 8.
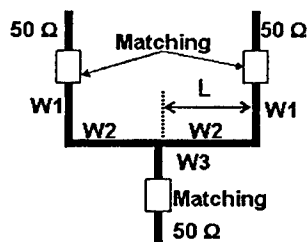
Figure 7: Graphical representation of the proposed hybrid corporate feed
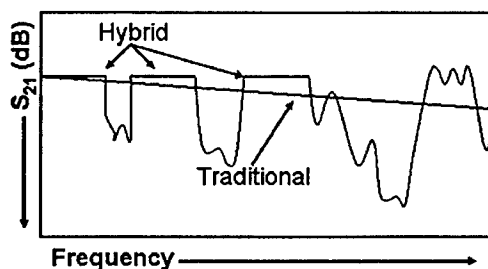
Figure 8: Graphical depiction of hybrid vs. traditional corporate feed performance

b. Simulation Results

The two circuit topologies, the Hybrid Series Feed and Hybrid Corporate Feed, were simulated using Agilent ADS. The circuit board parameters used in the simulations are shown in Table 1. The loss tangent, $\tan\delta$, was set to zero to eliminate the effect of the dielectric loss allowing the simulation to reflect the ideal performance of the circuit design.

Table 1: Simulation Properties

ε_r	3.0
μ_r	1.0
Ground Plane Spacing	20 mils
Conductor Thickness	17 microns
$\tan\delta$	0

Figure 9 shows a graphical representation of a section of the simulated Hybrid Series Feed circuit topology. The Hybrid Series feed model consisted of 1:32 power divider optimized for operation at three simultaneous bands. The resulting $S_{1,x}$ magnitude over the three operating bands should be -15.052 dB for a perfect power split. The results of the simulations are shown in Fig. 10. The $S_{1,x}$ results are within 0.15 dB of the expected value.
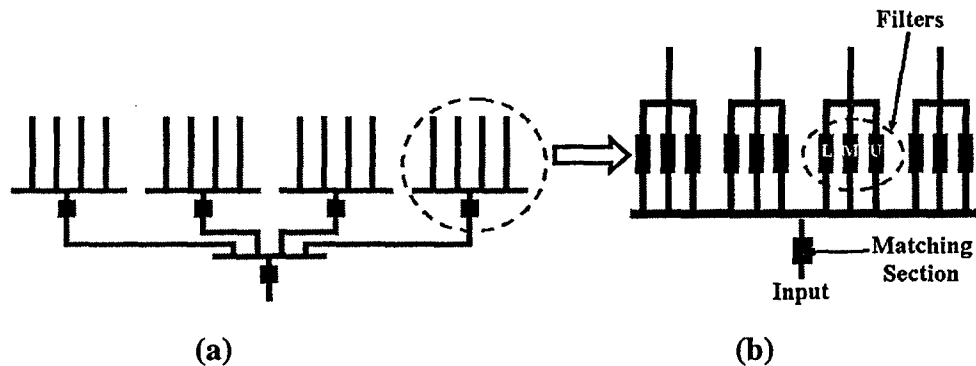
Figure 9: (a) Hybrid Series Feed (b) close up view of one branch
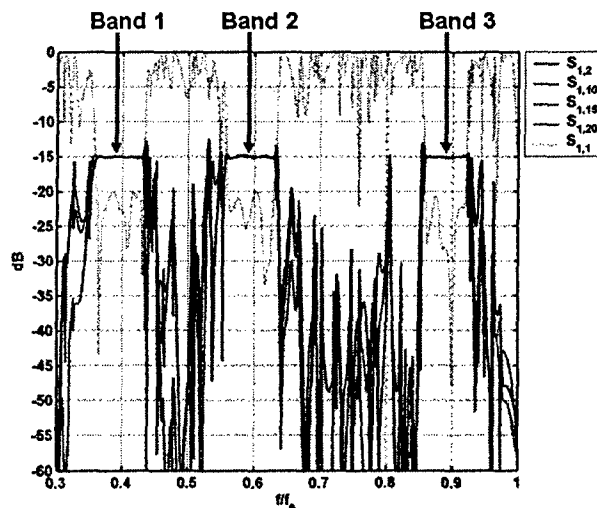
Figure 10: Simulation results showing the normalized frequency response of a 1:32 power divider utilizing the Hybrid Series Feed architecture

The second simulated circuit topology was the Hybrid Corporate feed, a section which is depicted graphically in Fig. 11. The Hybrid Corporate feed modeled consisted of a 1:64 power divider optimized for operation at three simultaneous bands. The resulting $S_{1,x}$ magnitude over the three operating bands should be -18.02 dB for a perfect power split. The simulated results are shown in Fig. 12. The achieved $S_{1,x}$ results are within .15 dB of the expected value.

(a)   (b)
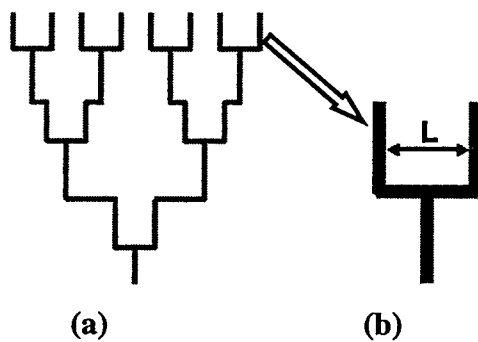
Figure 11:   (a) Hybrid Corporate Series Feed (b) Single branch
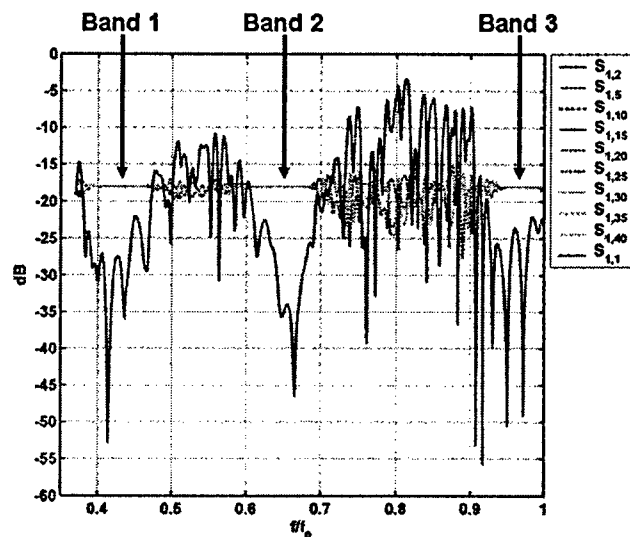
Figure 12: Simulation results showing the normalized frequency response of a 1:40 power divider utilizing the Hybrid Corporate Series Feed architecture

23

5.   Conclusion

This paper describes new approaches for multiband hybrid series and hybrid corporate feeds, that provide additional feed topology and design options for the phased array engineering pool. Results of simulation data have been presented in this paper as evidence that a meaning-full broadband feed can be achieved using a combination of traditional resonance feed tap-lines and RLC circuitry. If the number of desired operating bands is too large to fit in the circuit assembly behind a single radiating element, one can consider the hybrid corporate feed by adding more matching sections where the loss factor has been quantified and shown to be dependent on the mismatch of the junctions and bend. The above results are preliminary and further work is on-going to consolidate the analysis.

6.   References

[1]   W. T. Patton, "Array Feeds," in Handbook from Practical Phased Array Antenna Systems, Eli Brookner, pp 6.1 – 6.19, Norwood, MA, Artech House, 1991.

[2]   R. J. Mailoux, Phased Array Antennas Handbook, pp. 237 – 322. Norwood, MA, Artech House, 1994.

[3]   R. C. Hansen, Phased Array Antennas, pp.164 -214. New York, NY, USA, John Wiley and Sons, Inc. 1998.

[4]   E.J. Wilkinson, "An N-way Hybrid Power Divider," Trans. IEEE, Vol. MTT-8, Jan. 1960, pp 116-118.

[5]   J. Lange, "Intergitiated Stripline Quadrature Hybrid," Trans. IEEE, Vol. MTT-17, Dec. 1969, pp. 1150-1151.

[6]   T. Kushta et. al, "Resonance Stub Effect in a Transition From a Through Via Hole to a Stripline in Multilayer PCBs," IEEE Microwave and Wireless Components Letters, May 2003, pp 169 – 171.

[7]   R. J. Mailloux, "Wideband Subarray Systems: Evolution of A Research Area," IEEE, Vol. APS-2, July 2001, pp 422-425.

[8]   R. J. Mailloux, "Spaced-Fed Subarrays Using Displaced Feed," IEEE, Vol. Electronics Letter-2, Oct. 2002, pp 1241-1243.

[9]   M. Kim, et. al., "A DC-to-40 GHz Four-Bit RF MEMs True Time Delay Network," IEEE, Vol. Microwave and Wireless Components Letters-11, Feb. 2001, pp 56 – 58

[10]   Communications with Jeffery F. DeNatale, Rockwell Scientific Company.

[11]   R. C. Dorf and J. S. Svoboda, Introduction to Electric Circuits, pp. 769 – 816. New York, NY, USA, John Wiley and Sons, Inc. 1999.

[12]   D. M. Pozar, Microwave Engineering, pp. 422 – 496. New York, NY, USA, John Wiley and Sons, Inc. 1998.

Multibeam Spatially-Fed Antenna Arrays with Amplitude-Controlled Beam Steering

Sebastien Rondineau, Stefania Romisch, Darko Popovic, Zoya Popovic
Department of Electrical and Computer Engineering
University of Colorado at Boulder, Boulder CO 80309
zoya@colorado.edu

This paper presents discrete lens antenna array antennas developed for multi-beam communication applications. The lens arrays consist of two back-to-back arrays of antenna element pairs, connected by variable-length transmission lines, which allow the lens to perform a discrete Fourier transform. The array feed is a spatial one, allowing easy and affordable extensions to multiple beams, and straightforward beam reconfigurability. Two prototype arrays at X and K band are discussed. The 10-GHz lens array is designed to have multiple beams up to ±45 degrees off broadside and dual polarization. The array is characterized in a multipath fading channel as an angle-diversity array. The K-band array is a full-duplex array operating around 25 and 27GHz with the two frequencies at two polarizations. The applications for this array are formation-flying satellites, and 5-beam performance will be presented. Continuous steering of half of a beamwidth using amplitude-only control is demonstrated.

1. INTRODUCTION

Multibeam antenna arrays have numerous applications in communications. This paper addresses two such applications: angular diversity applied to a wireless mobile link and links between satellites flying in fixed formation. The goal in both cases is a low-cost array with flexibility to choose among several beams. Additionally, the requirement in the satellite link application is continuous beam steering for fine beam adjustments separately for each beam. These goals are achieved using a printed discrete lens array (DLA) with a spatial feed shared by all the beams [1-3].

A schematic of a DLA is shown in Figure1 and is here discussed in receive mode, although the lens is reciprocal and can also be used in a transmitter. The unit element of the lens array consists of two antennas, interconnected with a delay line [1]. The length of the delay varies across the array such that an incident plane

wave is focused onto a focal point in the near field on the feed side of the array in Figure 1. The transmission lines are of different electrical length for each element: the larger delay at the central element with respect to the external ones mimics an optical lens, thicker in the center and thinner in the periphery. Together with the electrical lengths of the lines, the positions of the array elements on the feed side also determine the focusing properties of the lens. This allows for a design with up to two perfect focal points lying on a focal arc or with a cone of best focus. The two degrees of freedom are the positions of the elements on the feed side and the electrical lengths of the transmission lines connecting the two sides. The main design constraint is the equality of the path length from the feed to each element on the radiating side of the lens. Plane waves incident from different directions are focused onto different points on the focal surface, where receiving antennas and circuitry are placed to sample the image, which is a discrete Fourier transform of the incoming wavefront. Multiple receivers correspond to multiple antenna radiation pattern beams, enabling beam steering and beam forming with no microwave phase shifters.
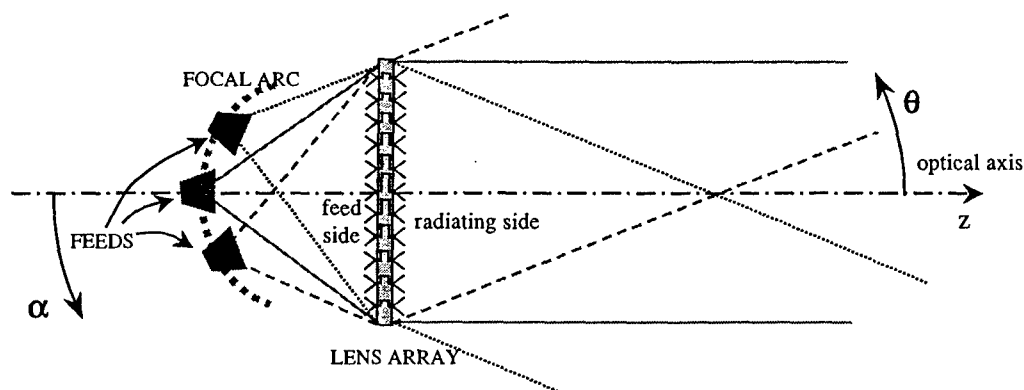
Figure 1. Sketch of a discrete lens array.

The lens array is planar and lightweight, fabricated using standard printed circuit technology. A standard N-element antenna array followed by a feed network is replaced by a discrete lens array in which N array element pairs perform a Fourier transform operation on the incoming wave front, and $M<N$ receivers are placed on a focal surface sampling this image. The lens array can include integrated amplifiers in each element, and different lenses have been demonstrated for spatially-fed transmit-receive arrays at X [2] and Ka bands [3]. In active discrete lenses with distributed amplifiers, in transmission the effective radiated power (ERP) is increased with accompanied increase in reliability and efficiency, while in reception the dynamic range is improved as the low-noise amplifier (LNA) noises add incoherently, while the signal adds coherently. The lens array as the

front end of a system performs spatial separation of the input waves, which enables simplified subsequent processing. The front-end processing benefits when using a discrete lens in an adaptive array, as applied to interference and multipath propagation, were investigated in [4,5].

2. MULTIBEAM DLA FOR ANGLE DIVERSITY WIRELESS COMMUNICATIONS

The benefits of different types of diversity in wireless communications have been known since the first mobile radio systems [7]. Spatial [8,9,10], polarization [9,10,11], angle [8,9], or frequency diversity have been used or proposed to improve signal to noise ratio, bit error rate, channel capacity and power savings in a mobile link. Here we examine the use of more than one type of diversity in the same front-end antenna array – in specific, polarization and angle diversity. Referring to Figure 1, in a multipath environment, the line-of site wave is focused onto one receiver on the focal arc (surface), while the reflected waves are focused onto different receivers, resulting in angle diversity.

27cm

(a)   (b)
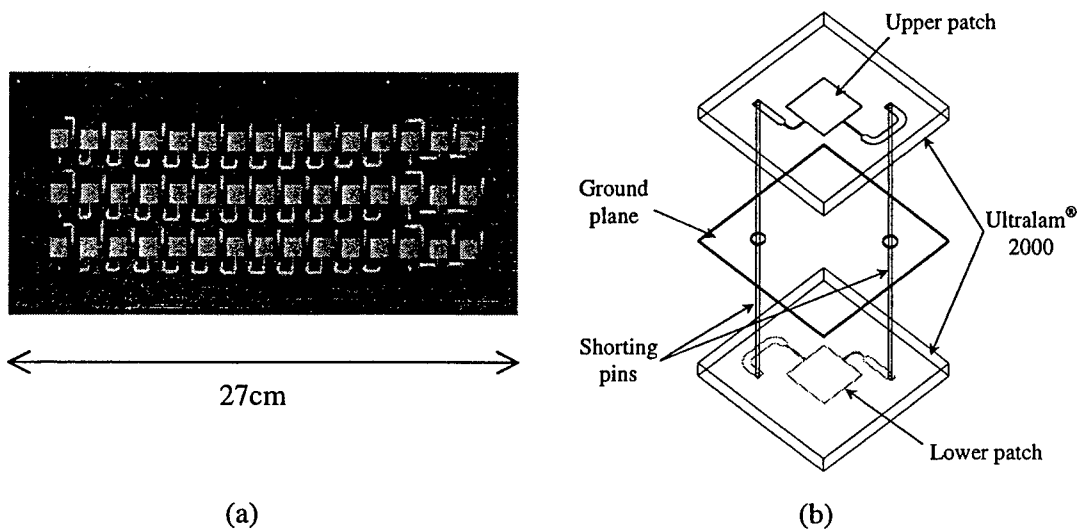
Figure 2. (a) Photograph of the 27-element cyllindrical lens array. (b) Unit cell schematic, stretched in the vertical direction, shows the connections between antenna pair feeds corresponding to the two linear polarizations.

The lens array designed for this study is a cylindrical 45-element array with three 15-element rows, which serve to provide a fan-shaped beam in the vertical direction. The photograph of one side of the lens, Figure 2(a), shows the patch antenna elements with dual-polarization feed lines and the microstrip delay lines connected with via holes to orthogonally polarized patches on the other side of the

two-layer lens array. Orthogonal polarization between the non-feed and feed sides of the lens improves the isolation between the two sides of the lens. A single element of the lens is schematically shown in Figure 2(b). It consists of a pair of dual-polarized patch antennas printed on two microstrip substrates with a common ground plane. The substrates used in this design have a relative permittivity of 2.5 and are 0.508 mm thick. The patches designed to be resonant at 10GHz are 9.1-mm squares, and the feed points are matched to 50-ohm feed lines with quarter wave 112-ohm matching sections. Each feed line is connected with a via to the corresponding orthogonally polarized feed line of the patch on the other side of the ground plane. The vias are metal posts 0.8 mm in diameter.

The 2-port S-parameters of the single element of the array were measured using an HP8510 Network Analyzer with a 3.5 mm coaxial calibration and are compared to simulations obtained using Zeland's IE3D Method of Moments software, as shown in Figure 3(a). From these measurements, it can be seen that the isolation between the two ports of the patch is about 35 dB at resonance, which implies that the two polarization channels are practically independent and can provide polarization diversity. The axial ratio at the two ports is about 30 dB as shown in Figure 3(b), and the two feeds are seen to be in perfect quadrature, i.e. the peak of one polarization coincides with the null of the other.

(a)   (b)
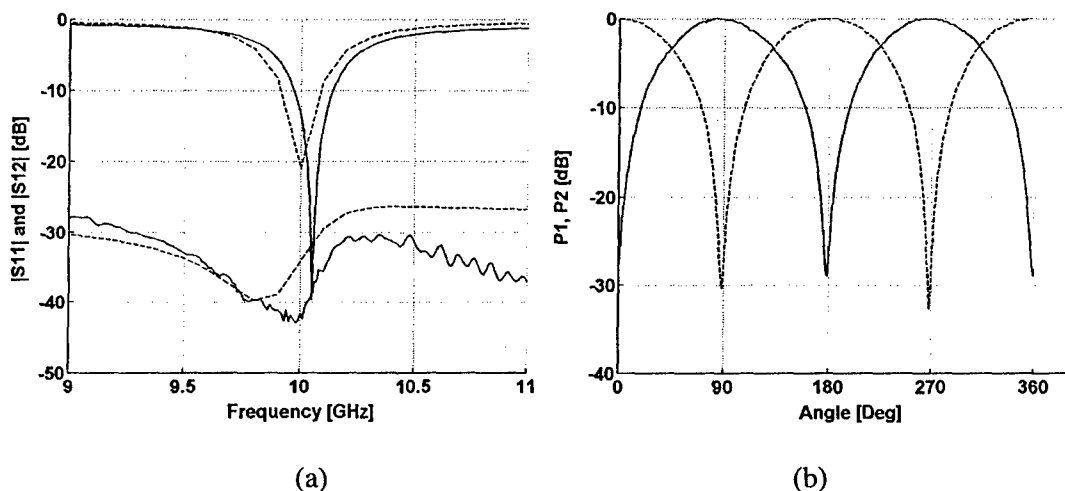
Figure 3. (a) Measured s-parameters of one of the two ports of the dual-polarized antenna element. The other port is identical and is not shown here. (b) Measured axial ratio for the two ports of the dual-linearly polarized patch.

The element spacing in the array from Figure 2(a) is half of a free space wavelength in one plane and 0.85λ in the other plane. The delay lines and the positions of the antenna elements at the feed side with respect to the ones at the

non-feed side are used as the design variables. They are calculated to give two perfect focal points located at the angles $\theta_0=\pm45°$. The design equations are given in [1]. Since perfect focusing exists only for the plane waves incident at +45° and -45°, for any other angle of incidence the path-length errors are present, which in turn degrades the radiation pattern. As described in [1], these errors can be significantly reduced by "refocusing". Therefore, the feeds are not positioned at the focal arc with a constant radius equal to the focal distance, but rather at the optimum focal arc which minimizes the path length errors. The difference in length between the longest and shortest delay line is 0.35λ, the focal distance–to–diameter ratio is $F/D=1.5$, with $F=324$ mm.

(a)

(b)
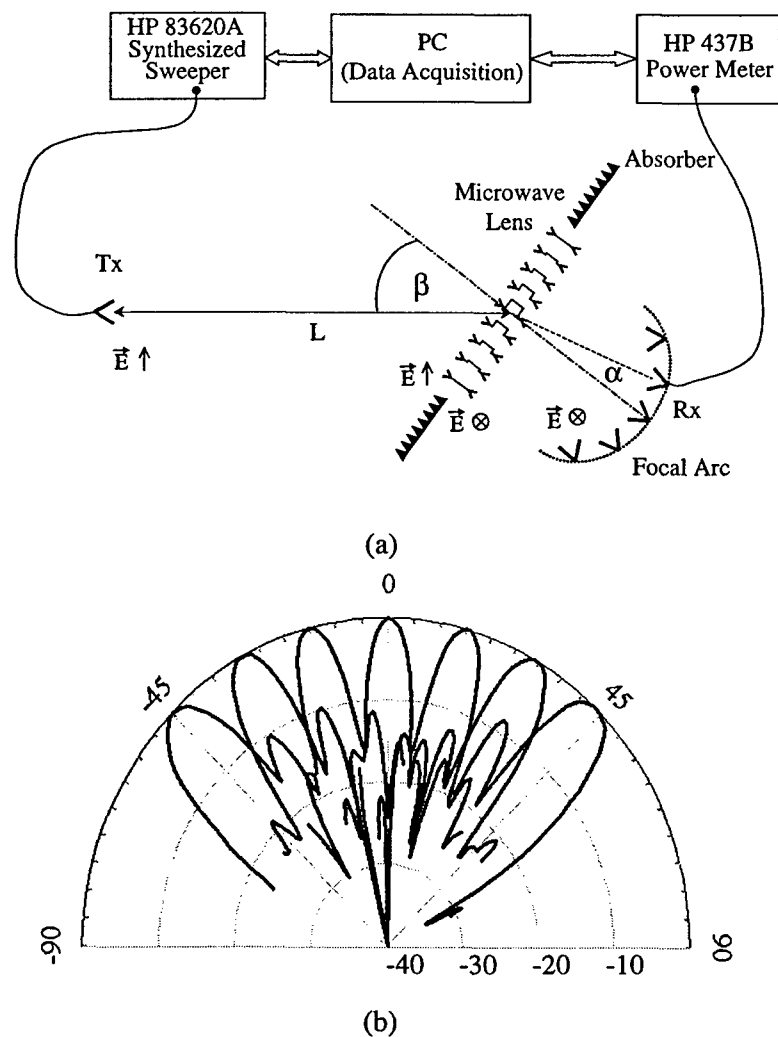
Figure 4. (a) Steup used for measuring the multibeam patterns. (b) Measured multibeam patterns for one of the two identical polarizatins normalized to the peak power.

The lens was characterized in an anechoic chamber using the setup shown in Figure 4(a). A standard gain horn antenna co-polarized with the non-feed side of the lens array and used as a transmitter in the measurements. For measuring radiation patterns corresponding to different beams of the multibeam lens, the lens is rotated and power detected at one receiver at a time. Linearly polarized horn antennas are used as the receiver antennas, but the same patches as the array elements can be alternatively used. The resulting normalized radiation patterns for receivers positioned between –45 and +45 degrees along the focal arc are shown in Figure 4(b). As the scan angle increases, the beam widens and the first sidelobe increases. The maximum received power for each of the patterns varies by about 1.5 dB, the half-power beamwidth varies by 2 degrees and the first sidelobe level varies from –15 dB at 0 degrees to –9 dB at 45 degrees. A example comparison between measured and calculated radiation patterns for a scan angle of 45 degrees is shown in Figure 5(a), and the measured axial ratio as a function of scan angle is shown in Figure 5(b).

(a)   (b)
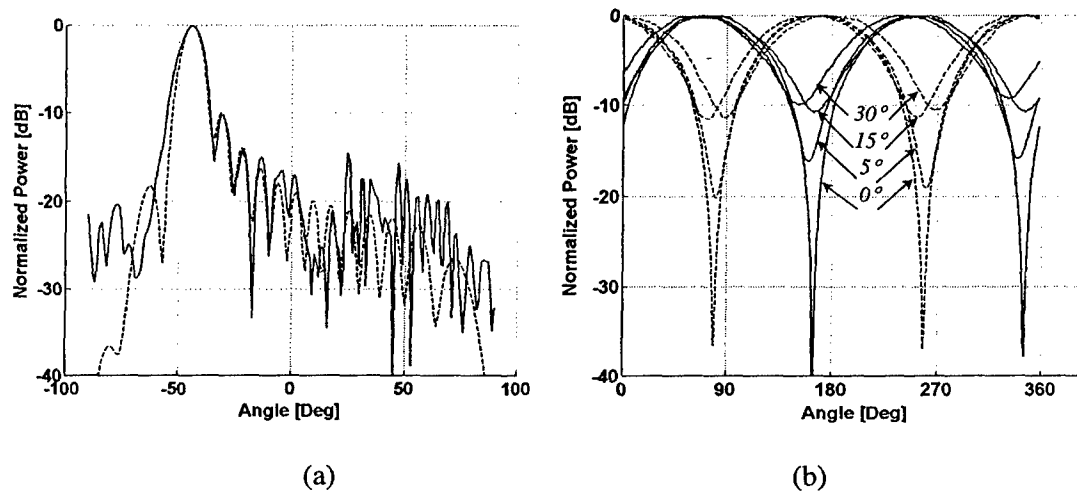
Figure 5. (a) Measured vs. calculated array pattern for a scan angle of –45 degrees (patterns for other scan angles have similar or better agreement). (b) Measured axial ratio for the two feeds of the dual-polarized multibeam array as a function of scan angle.

Since the lens is intended to be the receiving antenna, it is important to minimize the loss in the antennas, feed lines, and spatial feed, as any loss before the LNAs has a detrimental effect on the noise figure. In order to obtain an indication of lens efficiency, "thru" measurements are performed using an HP8510 Network Analyzer. The transmitting and the receiving horn antennas are connected to ports one and two of the network analyzer, respectively. The antennas are copolarized

and the system is calibrated using the "response/thru" calibration and time gating, from 9 to 11 GHz. The lens array is then inserted in front of the receiving horn antenna. It was mentioned before that the lens array has built-in polarization isolation and therefore the receiving horn antenna has to be rotated by 90 degrees. The lens array is mounted in an absorber aperture of the same size as the lens, and the total absorber size is a square 60 cm on the side. The measurements were made for the system that is calibrated in two ways: without the absorber and through the aperture in the absorber. The "thru" loss measured in this way is between 0.7 and 4dB.
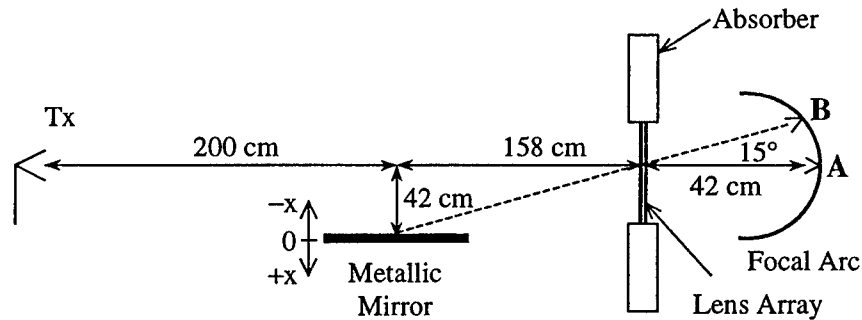
Figure 6. Measurement set up for determining improvement in multipath fading nulls.

(a)   (b)
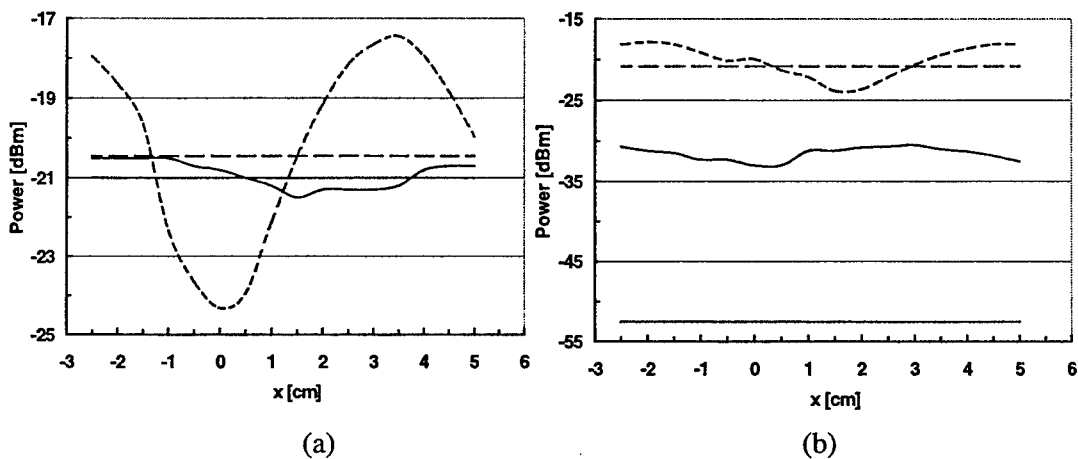
Figure 7. Measured received co-polarized power in the presence of a reflector without lens in link (dashed line) and with the lens added at the front end of the receiver (solid line). The receiver is positioned for a beam at 0 degrees (a) and 15 degrees (b). The straight lines show the reference power levels received with no reflector (no multipath) in the link, for 500mW input power to the transmitting horn antenna in Figure 6.

In order to test improvements in a link in a multipath fading environment when the lens is used at the front end, the lens is placed in a simple controllable multipath environment consisting of a single metal reflector in an anechoic chamber, as shown schematically in Figure 6. The reflector is 15x15 free-space wavelengths large and is translated in the x direction over three free-space wavelengths. The reflector is positioned so that at $x=0$, the reflected wave from the transmitting horn falls into the second null of the lens antenna pattern for a receiver on the optical axis (receiver A in Figure 6). In the first set of measurements, the received power in a line-of-sight link between the transmitting horn antenna and the receiver patch, with no lens array present, was measured without the presence of the mirror, and then as the mirror was translated in the x direction. The power at the input of the transmitting horn is 500 mW. The straight horizontal lines on the plots in Figure 7 are the measured power for the direct link only, without the reflector present. When the reflector is added, there is a standing wave behavior typical of a multipath environment. When the lens array is placed in front of the receiving antenna, the multipath peak-to-null ratio is significantly reduced, partly due to the gain of the array, and partly due to the built-in angle diversity.

When the receiver is positioned at point B on the focal arc corresponding to a beam at 15 degrees, the reference level of the received signal without the mirror is 30 dB below the reference level measured with the feed on optical axis (straight solid lines in Figure 7. This agrees well with the second null at 15 degrees in the radiation pattern in Figure 4(b), which is about 30 dB below the main beam. When the metallic mirror is placed in the experiment, the level of the signal is on average raised by 20 dB compared to the reference power level measured without the mirror (solid lines in Figure 7(b)). Therefore, it is demonstrated experimentally that the reflected multipath signal is spatially separated from the direct signal, and the two are received separately and can subsequently be combined.

3. MULTIBEAM DLA FOR SATELLITE CROSS LINKS

Many antenna systems can benefit from simultaneous multiple beams, one example being satellites flying in fixed formation [16], as well as base-station antennas for wireless communications. This paper addresses the development of a multi-beam lens array antenna for cross-link communications between satellites in tight formation, intended to collect diverse scientific mission data. The application considered requires several simultaneous dual-frequency dual-polarization beams

at different angles. The pointing angle of each beam needs to be fine-tuned continuously by about half of the half-power beamwidth to allow pointing corrections with satellites slightly out of formation. A standard way to perform beam forming and steering is with phased array antennas. A multibeam phased array would require a multi-layer feed structure such as a Butler matrix [3]. The feed network has limited bandwidth and includes lossy phase shifters (typically above 10dB at millimeter wavelengths). The approach in this work is to design a Ka-band DLA such as the one in Figure 1, with the polarization, up- and down-link frequencies, beamwidths and fine tuning requirements needed for a satellite crosslink demonstration prototype.

The DLA operates at 24.7 and 26.7GHz up and downlink frequencies, and is a two-degree of freedom design for a cone of best focus of ± 30 degrees. The antenna elements are rectangular patch antennas fed from the radiating edges for crossed polarization at the two frequencies. The element bandwidth is measured to be 3% for both frequencies. To satisfy the beam requirement of a 10-degree half-power beamwidth, 64 elements are distributed on triangular lattice with 0.6λ and λ periods in the horizontal and vertical directions, as shown in Figure 8. The patch pair is connected with slot couplers in the antenna ground planes to a common buried delay-line sptripline layer, resulting in a 5-layer DLA implementation. The delay line lengths range from 0.11λ to 1.05λ with the longest corresponding to the central array element.
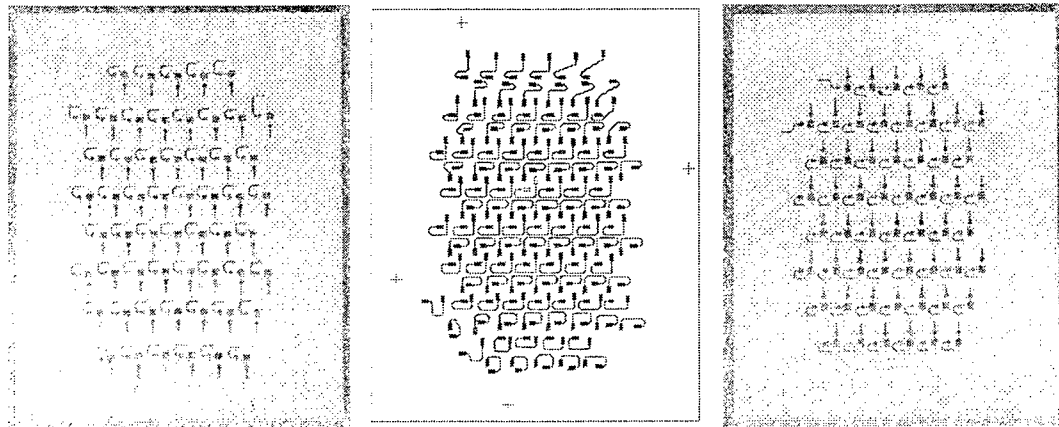

Figure 8. Photographs of the two sides of the 64-element DLA and layout of the sandwiched stripline delay line layer.

Figure 9(a) shows the radiation patterns measured at 26.7GHz at University of Colorado for five different positions of a waveguide feed along the focal arc.

Figure 9(b) shows the simulated versus measured single beam pattern at -25 degrees.

The lens array performs a discrete Fourier transform, in analogy to an optical dielectric lens performing a Fourier transform. Because of this property of DLAs, amplitude variations at the feed on the focal surface correspond to phase shifts at the non-feed side, which in turn correspond to a steering of the beam. Each feed of the dual-beam array was implemented with a 2-element array of patch antennas, spaced λ apart. The power radiated/received by each element is controlled with variable-gain attenuators or amplifiers so that the ratio between them can be varied to steer the beam, as illustrated in Figure 10(a). The measurement for a power ratio between 0.13 and 0.96 is shown in Figure 10(b).

(a)   (b)
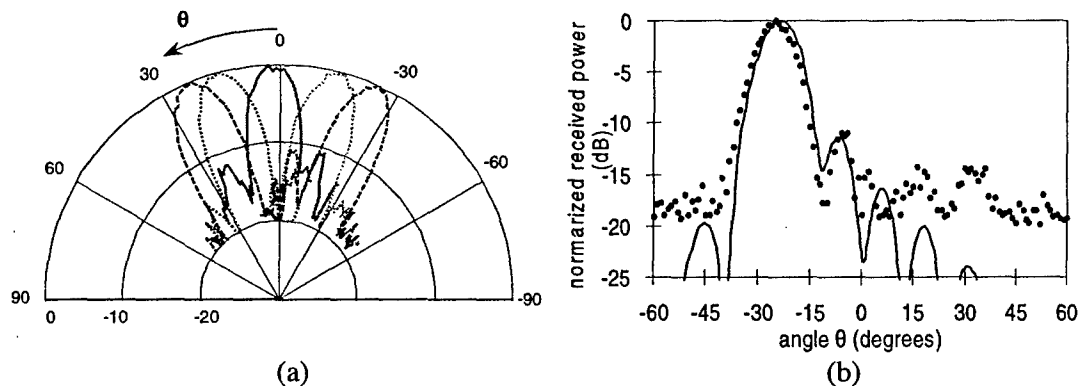
Figure 9. (a) Measured 5-beam pattern at 26.7GHz (the patterns at the lower frequency look very similar). (b) Measured and simulated pattern steered at -25 degrees off broadside.

4. DISCUSSION AND CONTINUED WORK

This paper describes a front end discrete lens antenna array as it applies to: (1) wireless communications with more than one diversity type and (2) low-cost phase-shifterless beamforming. The lens array is shown to be a multibeam array that can be designed to have low loss for large numbers of elements for two orthogonal well-isolated (30dB) polarizations. In a transmitter, where each element can have a power amplifier, the powers will add coherently. In a receiver application where low-noise amplifiers are integrated in each antenna element, the noises add incoherently, while the signals add coherently at the receivers along the focal arc, therefore increasing the RF dynamic range by $10\log N$. Loss in the lens will degrade the noise figure, and a loss budget for DLAs needs to be

performed. Measurements with a calibrated "thru" as described above in Section 2 give an indication of how efficient the system is in collecting RF power relative to the system without the lens array. Since the effective area is increased with the presence of the lens array we would expect to be able to collect more power. However, due to a variety of loss mechanisms, such as spill-over loss, nonuniform illumination loss, mismatch loss and ohmic loss, the total received power is in most cases bellow the level that we would receive using the receiver antenna alone. The main contributor is the spill-over loss, meaning that power is lost due to the fact that the effective area of the feed antenna on the focal surface is not large enough to collect all the power of the image. This loss can be significantly reduced if the lens array and the receiving antenna are designed as a system, which was attempted in the case of the 10-GHz lens described in Section 2, giving as low as 0.7dB "thru" loss. This means that the total DLA loss is roughly equal to the array gain, and this can be compensated with a pre-amplifier in transmission, and some added LNA gain in reception.
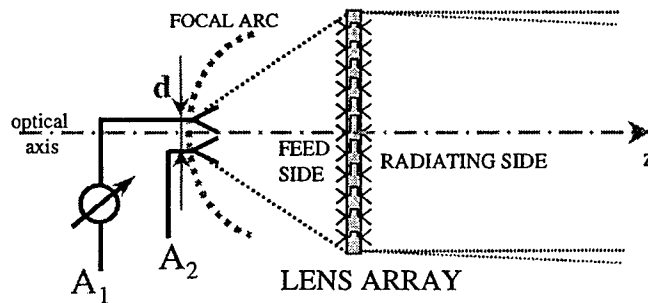
(a)
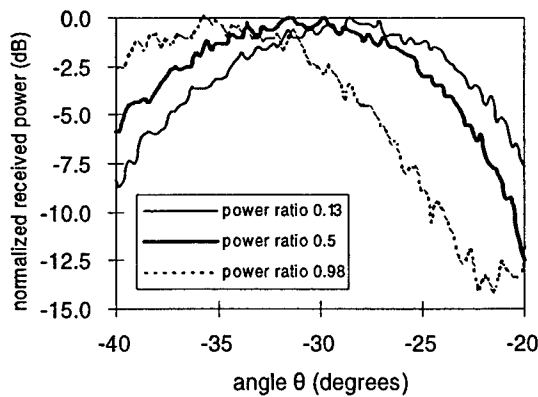
(b)

Figure 10. (a) Setup for amplitude controlled fine beam steering. (b) Measured beam steering using an amplitude ratio of

35

The lens array is a multibeam array with a single spatial feed, and an important parameter is isolation between the beams. In the angle diversity application, the "crosstalk" between the beams will result in correlated diversity orders, reducing ultimately channel capacity. In a multibeam system, the crosstalk will determine how many independent beams can be reasonably used for an N-element DLA. Theoretically, an N-element lens has N independent beams, but in practice this number will be limited by the coupling between the beams and the scan angle. Figure 11 shows measured coupling between two feed antennas positioned for -30 degree and +30 degree beams, along with coupling of the two feeds on the same dual frequency feed antenna of the Ka-band DLA.
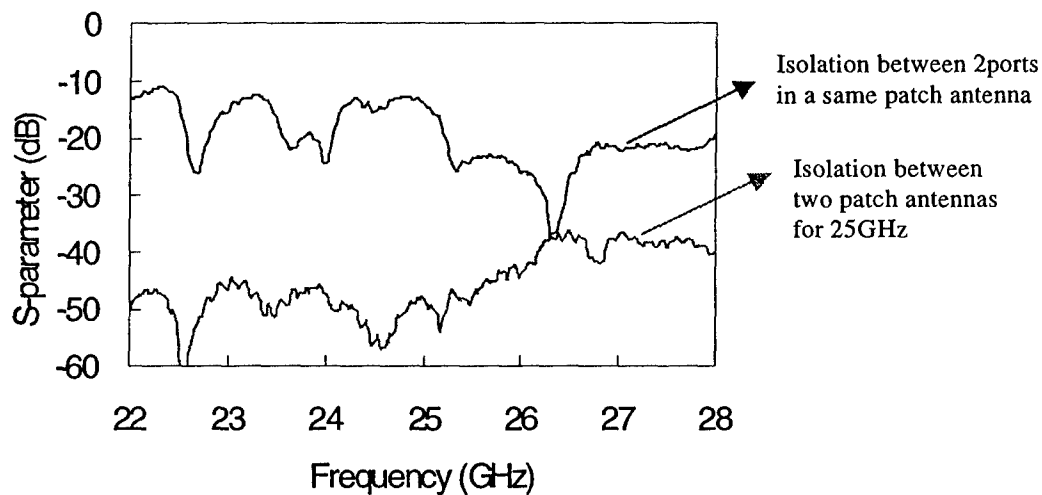
Figure 11. Measured isolation (s21) between two ports on the same antenna and two ports on the two different feed antennas for the Ka-band dual-frequency DLA with feed antennas positioned at -30 degrees and +30 degrees off broadside.

It is important to note here one advantage of the discrete lens arrays over phased arrays. The phased array feeds for large number of beams and elements become very complex and contribute to a huge increase in cost and losses. In lenses, however, the feed network complexity and losses scale favorably [18].

ACKNOWLEDGEMENT

REFERENCES

[1] D.T. McGrath, "Planar three-dimensional constrained lenses," *IEEE Trans. Antennas Propag.,* vol.AP-34, pp. 46-50, Jan.1986.

[2] S. Hollung, A. Cox, Z. Popovic, "A quasi-optical bi-directional lens amplifier," *IEEE Trans. on Microwave Theory and Techniques, Vol. 47, No. 12,* pp. 2352-2357, Dec. 1997.

[3] Z. Popovic, A. Mortazawi, "Quasi-optical transmit/receive front ends, " *invited paper, IEEE Trans. on Microwave Theory and Techniques, Vol. 48, No. 11,* pp. 1964-1975, Nov. 1998.

[4] D. Z. Anderson, V. Damiao, E. Fotheringham, D. Popovic, S. Romisch, Z. Popovic, "Optically smart active antenna arrays," *IEEE Trans. on Antennas and Propagations, Vol.50, No5.,* pp.607-617, May 2001.

[5] J. Vain, Z. Popovic, "Smart lens antenna arrays," *IEEE 2001 IMS Symposium Digest,* pp. 129 – 132, Phoenix, Arizona, May 2001.

[6] D. Popovic, Z. Popovic, "Multibeam antennas with polarization and angle diversity," *IEEE Trans. on Antenna and Propagation, Vol.50, No.5,* Special Issue on Wireless Communications, pp. 651-657, May 2002.

[7] Microwave mobile communications, W. C. Jakes, ed., reprinted by IEEE Press, Piscataway, NJ, 1994.

[8] W. L. Stutzman, J. H. Reed, C. B. Dietrich, B. K. Kim and D. G. Sweeney, "Recent results from smart antenna experiments – base station and handheld terminals," Proceedings RAWCON, September 2000, pp. 139-142

[9] P. L. Perini and C. L. Holloway, "Angle and space diversity comparisons in different mobile radio environments," IEEE Transactions on Antennas and Propagation, Vol. 46, No. 6, June 1998, pp. 764-775

[10] B. S. Collins, "Polarization diversity antennas for compact base stations", Microwave Journal, Vol. 43, No. 1, January 2000, pp. 76-88.

[11] C. Beckman and U. Wahlberg, "Antenna systems for polarization diversity," Microwave Journal, Vol. 40, No. 5, May 1997, pp. 330-334.

[12] *Microstrip antennas: the analysis and design of microstrip antennas and arrays,* D. M. Pozar and D. H. Schaubert, IEEE Press, Piscataway, NJ, 1995.

[14] S. Hollung, *Quasi-Optical Transmit/ Receive Lens Amplifier Arrays,* Ph.D. Thesis Dissertation, University of Colorado, Boulder, 1998.

[16] R.Q. Lee, S. Romisch and Z. Popovic, "Multi-Beam Phased Array Antennas," 26th Annual Antenna Applications Symposium, Sept. 2002, Monticello, Illinois.

[17] Hansen R. C., Phased array antennas, Wiley Series in Microwave and Optical Engineering, Kai Chang Series Editor, Ch. 10, 1998.

[18] S. Römisch, N. Shino, D. Popović, P. Bell, Z. Popović, "Multibeam planar discrete millimeter-wave discrete lens for fixed formation satellites," *2002 URSI General Assembly Digest,* Maastricht, The Netherlands, August 2002.

Rectenna Arrays for Recycling Statistical Broadband Radiation

Joseph A. Hagerty, Zoya Popovic
Department of Electrical and Computer Engineering
University of Colorado at Boulder, Boulder CO 80309
zoya@colorado.edu

This paper discusses a study of rectification of broadband statistically time-varying low-power microwave radiation. Polarization, spectral content and power levels of incident radiation of the array are allowed to vary randomly over a broad range. The applications for this work are in wireless powering of indoor industrial sensors, sensor arrays in areas of low solar radiation, and recycling of ambient RF energy. A 64-element dual-polarized spiral rectenna array is designed and characterized over a frequency range of 2-18GHz. In the design, nonlinear harmonic balance simulations are combined with full-wave field analysis. The nonlinear simulations are compared with source-pull diode nonlinear measurements in order to establish a reliable design methodology. The rectifier diodes are directly matched to the antenna over a broad frequency range and a large range of input power density levels from 10^{-5} to 10^{-1}mW/cm^2. This eliminates matching and filtering circuits, thereby maximizing effective area. The rectified DC power and efficiency are characterized as a function of DC load impedance and DC circuit topology, polarization, incident power density, and incidence angle.

1. INTRODUCTION

Rectification of microwave signals for supplying DC power through wireless transmission has been proposed and researched in the context of high power beaming since the 1950's, a good review of which is given in [1]. In microwave power transmission, the antennas have well-defined polarization and high rectification efficiency enabled by single-frequency, high microwave power densities incident on an array of antennas and rectifying circuits. Applications for this type of power transfer have been proposed for helicopter powering [1], solar-powered satellite-to-ground transmission [2], inter-satellite power transmission [3] [4] including utility power satellites [5], mechanical actuators for space-based telescopes [6], small DC motor driving [7], and short range wireless power

transfer, e.g. between two parts of a satellite. Both linear [8] ,[9] dual-linear [6], [10] and circular polarization [2], [11] of the receiving antennas were used for demonstrations of efficiencies ranging from around 85-90% at lower microwave frequencies to around 60% at X-band and around 40% at Ka-band [5].

In the above referenced work, rectification was performed for narrow-band, essentially single-frequency, incident microwave radiation with relatively high power densities. A survey of the typical power densities associated with high-power rectennas is given in Table 1, along with the corresponding operating rectification efficiencies. Also shown in the table are expected power densities near a typical base station tower operating at 880 and 1990 MHz [12]. The typcial solar radiation level is shown for comparison.

Topic	Power density (mW/cm^2)	Reported efficiency	Ref.	Frequency	Polarization
50-m from basestation	0.0001		[13]	900 MHz	Any
	0.005	40-50%	[8]	2.45 GHz	Linear
SPST-WPT	0.1-10	65-92%	[3],[4] [13]	5.8 GHz	Circular, linear
FCC exposure limit	0.5			880 MHz	Any
FCC exposure limit	1.5			1990 MHz	Any
ANSII/IEEE standard	1			3-30GHz	Any
	10	80%	[3]	5.8GHz	
50-V output	25	52%	[6]	8.51 GHz	Dual linear
Sunlight	~100			Optical	Elliptical
This work	0.000015 – 0.08	0.1-20%	[this work]	2-18 GHz range	Random, arbitrary

Table 1. Typical power densities over the microwave frequency range. The power density operating points and frequencies of several rectenna designs found in the literature and their corresponding efficiencies [8], [3], [6] are given. Also shown is the range of expected power densities used in the Solar Power Satellite (SPS) and Wireless Power Transmission (WPT) applications. The range of power densities measured in this paper is indicated for comparison. Measured ambient levels in our lab (no high power equipment) are in the 10^{-6} to 10^{-5} mW/cm^2 range. The solar power density is shown for comparison.

Concerns have been expressed in terms of possible health hazards [13]. In [8], rectification of low power levels was discussed for battery-free transponders, with

power densities on the order of 0.01mW/cm^2. More recently, broadband rectification of very low-power incident radiation (less than 1mW/cm^2) was demonstrated in [14]. This paper focuses on incident power densities and input power levels that are orders of magnitude lower than those associated with the projects in the literature cited above, as shown in Table 1.
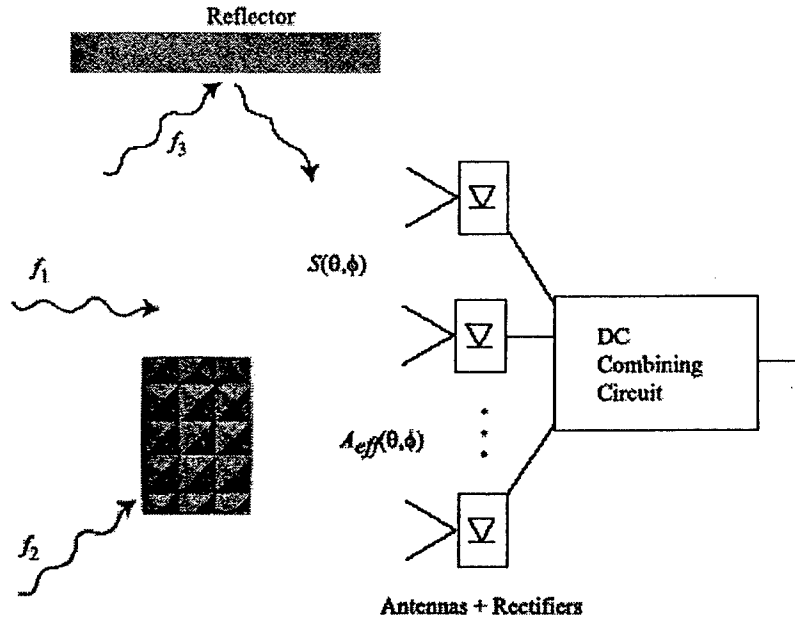
Figure 1. Block diagram of rectenna array for ambient energy recycling. Waves of different frequencies and power levels propagate through a complex environment before they are received by a dual-polarized array of antennas. Each element in the array is integrated with a rectifying device. The resulting DC outputs are combined

The general block-diagram of the rectenna array discussed in this paper is shown in Figure 1. Multiple sources of different frequencies are radiating power in all directions in a rich scattering environment. The DC powers from many rectenna elements are added by current and voltage summing with a conversion efficiency

$$\eta = P_{DC}/P_{RF},$$

which is a function of statistically varying incident RF power. The received average RF power over a range of frequencies, at any instant in time is given by

$$P_{RF}(t) = \frac{1}{f_2 - f_1} \int_{f_1}^{f_2} \int_0^{4\pi} S(\Omega, f, t) A_{eff}(\Omega, f) d\Omega df$$

where Ω is the solid angle in steradians and $S(\Omega, f, t)$ is the time varying frequency and angle dependent incident power density. A_{eff} is the angle, frequency, and polarization dependent effective area of the antenna. Because of the nonlinearity of the diode, the mismatch between the antenna and the rectifying diode is dependent on power as well as frequency. The diode is driven as a half-wave rectifier with an efficiency limited to

$$\eta_{max} = \frac{1}{1 + \frac{V_D}{2V_{out}}}$$

where V_{out} is the output DC voltage and V_D is the drop across the conducting diode. In this work it is more appropriate to measure the efficiency defined abve through power, which includes the loss due to reflected power. For low power applications, as is the case for collected ambient energy, there is generally not enough power to drive the diode in a high efficiency mode. Furthermore, rectification over multiple octaves requires a different approach from standard matching techniques. In a rectenna application, the antenna itself can be used as the matching mechanism instead of using a transmission-line matching circuit as in [5]–[11]. The antenna design is therefore heavily dependent on the diode characteristics.

2. DESIGN OF INTEGRATED RECTIFIER DIODE AND ANTENNA ELEMENT

The design of a broadband nonlinear active antenna element starts with the determination of the active element impedance over a range of frequencies and power levels. This analysis is performed using nonlinear Harmonic Balance simulations in Agilent ADS with the nonlinear diode model provided by the manufacturer. Nonlinear analysis is required since the nonlinear capacitance of the diode needs to be taken into account past a few GHz for most devices. In addition, harmonics are produced by the diode and the reflected harmonic energy from the input or output side of the diode can alter the voltage across the diode. Another important effect that linear analysis cannot take into account is the fact that the diode self-biases as it produces more DC current, thus moving the DC operating point of the IV curve in a nonlinear fashion.

Figure 2 shows the range of impedances for the Schottky diode used in this work, for a frequency range from 1-16GHz and a power range from -30dBm to 10dBm.The magnitude of the optimal source impedance becomes smaller with increasing incident power. The same occurs as the DC load approaches the optimal value, however the effect is not as dramatic. More significantly, the

optimal source impedance moves counter-clockwise along a constant admittance circle with increasing frequency due to the junction capacitance. This needs to be taken into account when designing the antenna element, since most antennas have impedance traces that move clockwise with increasing frequency on the Smith chart.
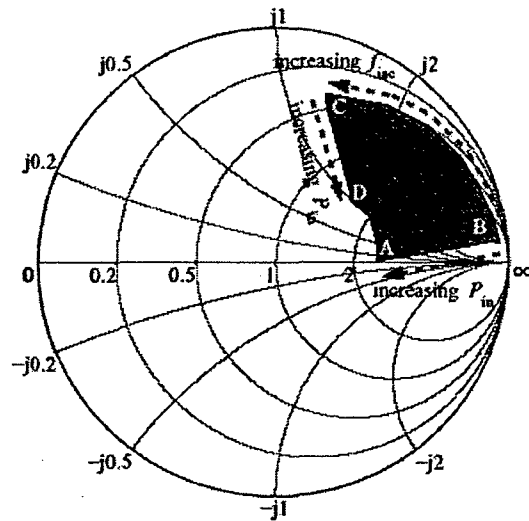
Figure 2. Simulated range of optimal source impedances for the SMS7630 Schottky diode as the incident wave frequency and input power are varied from 1 to 16 GHz and -30dBm to 10dBm, respectively. Within the shaded area, region A corresponds to high input power and low frequency, B to low power and low frequency, C to low power and high frequency, D to high power and high frequency.

In most rectenna designs, a narrow band antenna is used to feed a transmission line followed by space-consuming, traditional matching and filtering sections. In the work presented here the diode is integrated directly into the antenna, reducing the required area and increasing the bandwidth. The antenna impedance is either obtained from simulations using a full-wave solver, or by measurements, and then included in the HB simulation as the internal impedance of the power source used to drive the circuit. The major problem in broadband rectenna design lies in the nature of the antenna and diode frequency dependent impedances. For maximal power transfer, the antenna impedance would match the optimal diode impedance for all frequencies. Our approach is to present a constant impedance to the diode by using a frequency independent antenna element.

In order to verify the design method, we chose a well-known antipodal Vivaldi tapered slot antenna, Figure 3a, for which we had both simulated and measured input impedance available [15]. The packaged Schottky diode is soldered to the

microstrip feed line near the connector. Figure 3b shows the agreement between Harmonic Balance simulations using measured antenna return loss, and measurements of the DC output voltage into a 660-ohm load.
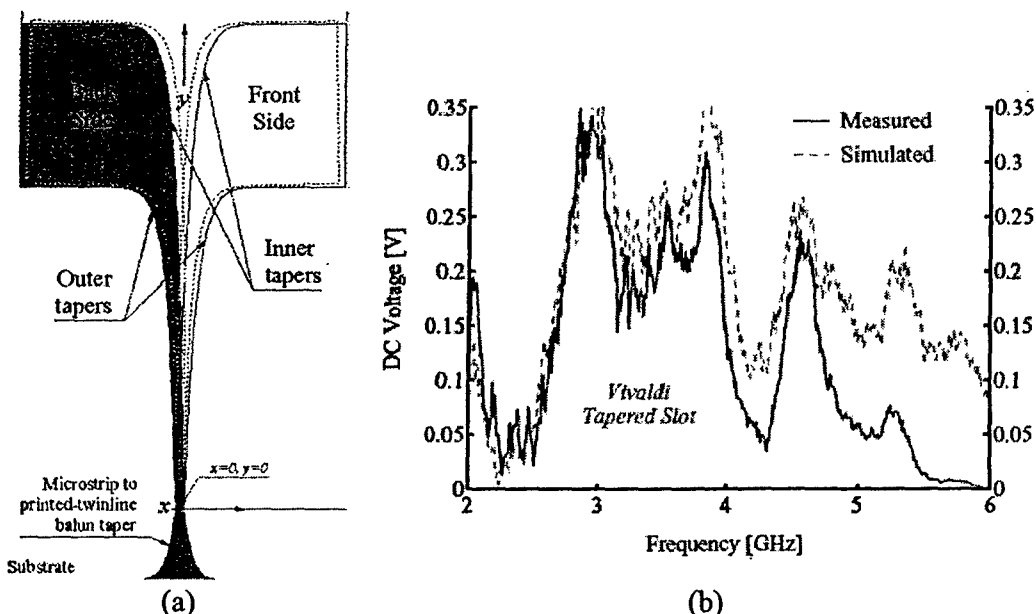

Figure 3. (a) Layout of test Vivaldi antenna. A Schottky diode is connected to the microstrip feed line, and the obtained simulated and measured DC voltage from 2 to 6 GHz is shown in (b).

For a large printed rectenna array, the tapered slot is not a convenient element. An equiangular spiral, Figure 4a, was chosen as the array element for the following reasons: (1) uniplanar with convenient feed point for diode connection, (2) possible dual polarization, (3) convenient connection of dc lines at the tips of the spiral arms. The spiral element was simulated with full-wave CAD tools (Ansoft's *Ensemble* and Zeland's *IE3D*) resulting in a one-port frequency dependent impedance that becomes the diode load in the rectenna.

The measured impedance of a passive spiral with a coaxial feed-line positioned at the center of the spiral is shown in Figure 4b. A diode is then connected at the antenna feed and the resulting rectenna element performance is shown in Figure 5. The disagreement around 4 GHz is believed to be caused by the 1-cm long unbalanced coax feed which was needed to do a single-element measurement, but does not exist in the final array.
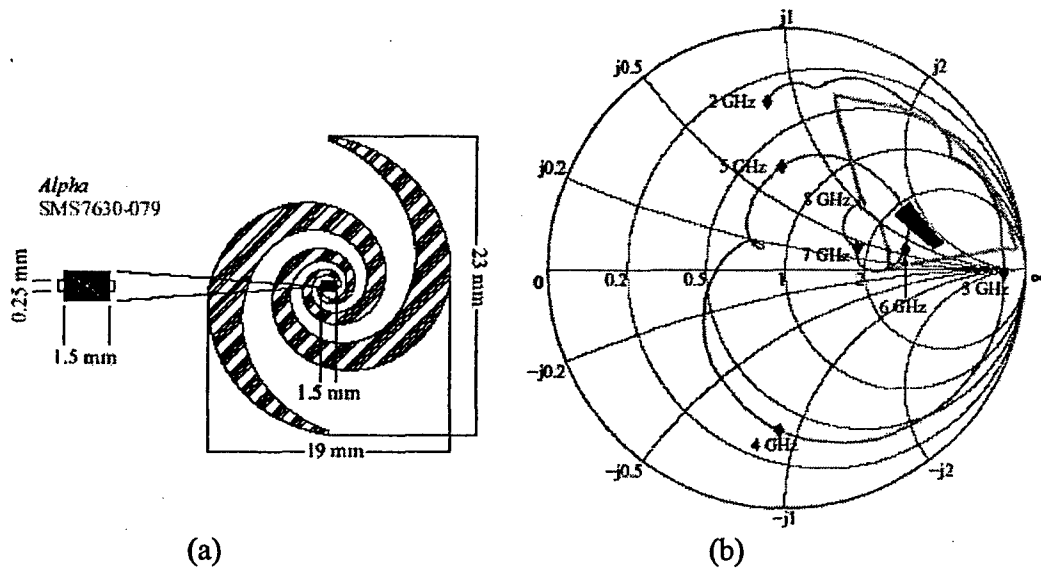
Figure 4. (a) Layout of spiral rectenna element with a packaged Schottky diode connected at the feed point. (b) Simulated input impedance of the spiral element normalized to 50 ohms. The optimal region of impedances from Figure 2 is outlined in gray, and the frequencies and range of input power levels used for this measurement are represented by the black region.
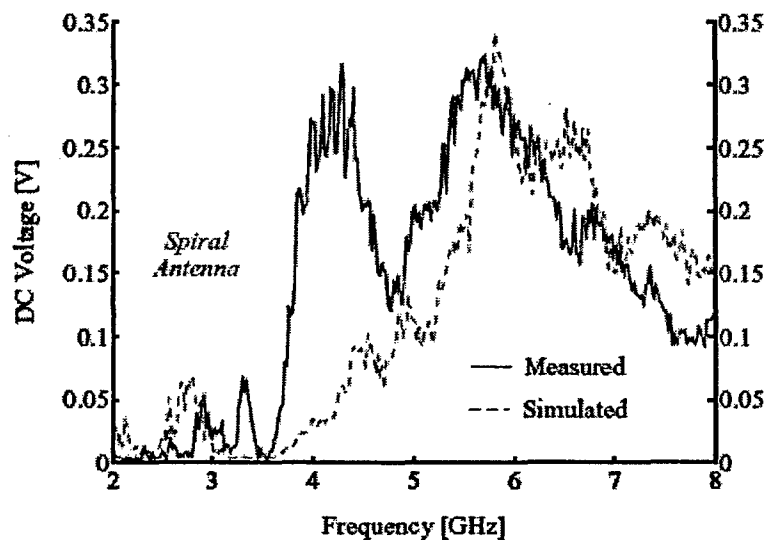
Figure 5. Measured and simulated DC voltage response of a single spiral element with an unbalanced coaxial feed used to extract the C voltage into a 600-ohm load. The disagreement at 4GHz is attributed to the unbalance feed.
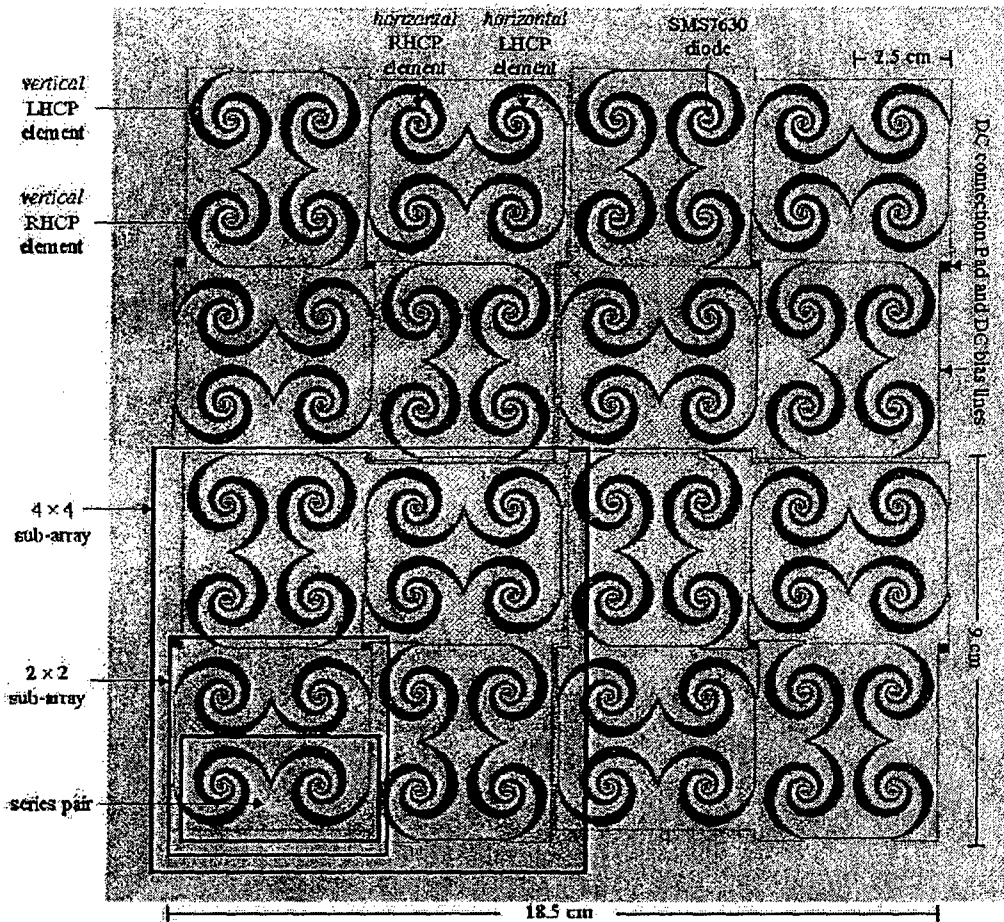
Figure 6. Layout of 64-element rectenna array with alternating RHCP and LHCP spirals.

3. RECTENNA ARRAY DESIGN AND CHARACTERIZATION

A 64-element array of left and right hand circularly polarized spiral elements, Figure 6, is designed so that each spiral element is directly connected to a rectifier diode. Therefore, the RF powers received independently by each element are summed upon rectification as DC currents and/or voltage of total rectified power from the array depends on the angle of incidence of the RF plane wave(s). The angle-dependent rectified DC power of a single element can be used to define an *element DC radiation pattern*:

$$G_{DC}(\theta, \phi) = \eta(P_{RF}) \frac{4\pi \cdot P_{RF}}{S(\theta, \phi)\lambda^2} = \eta(P_{RF})G(\theta, \phi)$$

where $G(\theta, \phi)$ is the RF radiation pattern. The *DC radiation pattern*, $G_{DC}(\theta, \phi)$, is different from the RF radiation pattern due to the nonlinear dependence of efficiency on RF power. The resulting pattern obtained by measuring the DC voltage across an optimal load exhibits lower gain at larger angles θ and ϕ. The radiation pattern for the n-element array is the same as the element pattern, with an additional multiplier factor that is a function of the DC connections in the array, and to first order is not a function of angle.
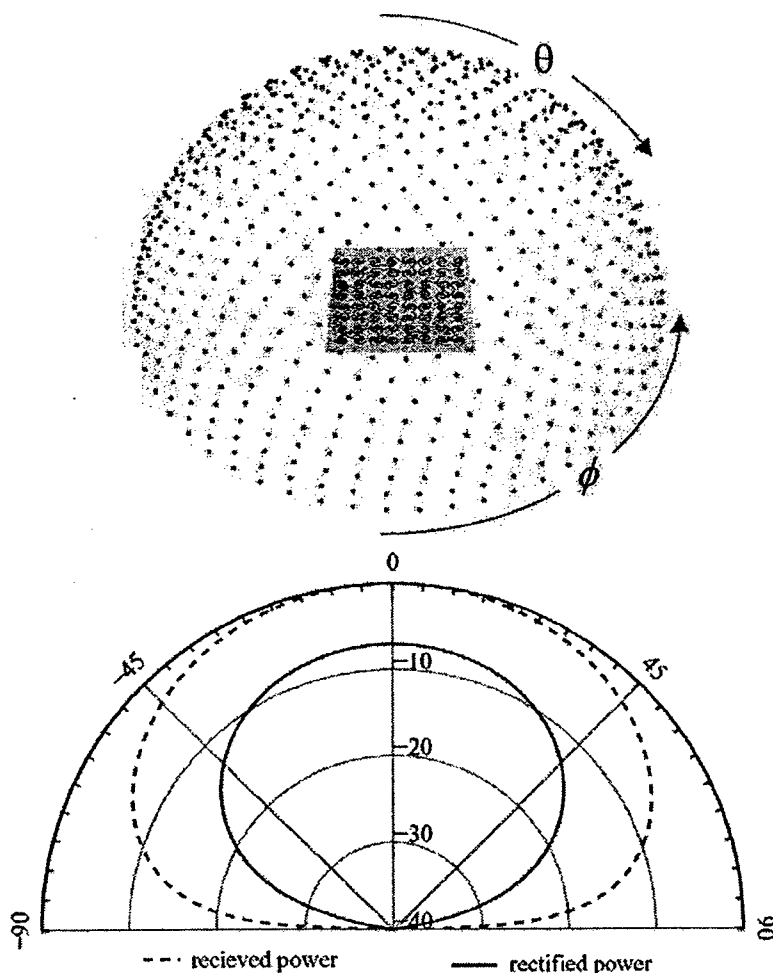
Figure 7. Layout of 1024 points from which the array was illuminated during the pattern measurements (top). Measured DC radiation pattern compared to received RF power shows the expected narrowing in pattern due to nonlinearity (bottom).

The patterns of the rectenna array are found by measuring the output DC rectified power over a hemisphere sampled at 1012 points, Figure 7a. One cross-section of a pattern is shown in Figure 7b to point out the relationship of the rectified to the actual received power by the array. Figure 8 shows measured radiation patterns, which are a superposition of the response to two orthogonally linearly polarized incident waves. This means that the array suffers an average 3 dB input polarization loss for *every* possible polarization of the incident energy. However, this strategy ensures a flat polarization response. At higher frequencies the spiral element is predominately circularly polarized. In order to design a broadband array with as uniform a pattern in space and polarization as possible, RHCP and LHCP spirals are alternated in the layout.
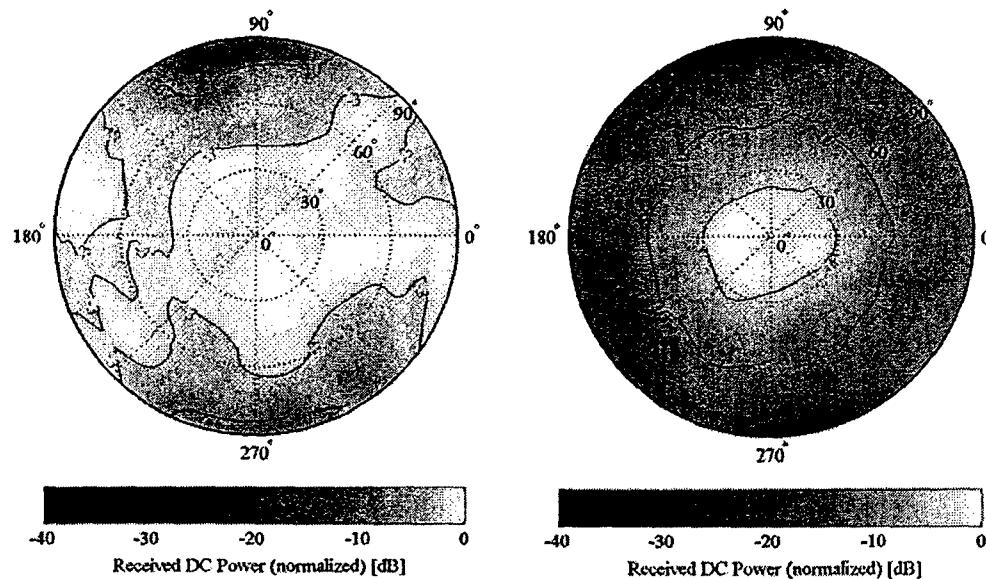
Figure 8. Measured DC power as a function of angle of incidence over a hemisphere for two orthogonally linearly polarized input waves at 2 GHz (left) and 4.6 GHz (right).

The planar layout of the array places certain limits on the polarization and reception at azimuth angles. Figure 8 shows that the radiation pattern has low directivity and is similar to that of a single element. Note that the size of the array is $1.5 \lambda_0^2$ at 2 GHz, and $116 \lambda_0^2$ at 18 GHz. However, by observing the patterns in Figure 8 it is seen that the array receives from all directions over a broad frequency range.

The crucial design step for the array is to achieve optimal DC combining efficiency. Previous work shows that predominately parallel connections (current-summing) lead to smaller matched loads for the rectenna [16]. For a series connected array (voltage-summed), the matched load is much higher. This can be seen by reducing the array to a combination of DC Thevenin sources where the matched load corresponds to the total source resistance. The nonlinear performance of the diodes must again be considered when considering the DC connections. Increased current or voltage in a predominately series or parallel-connected array can lead to over-biasing of the 64 element array is connected using 2 × 1 parallel pairs connected in series to form a 2×2 sub-subarray: four of these are connected in parallel to create a 4×4 subarray: four more of these are then left as units to comprise the 8×8 array with reconfigurable connectivity.
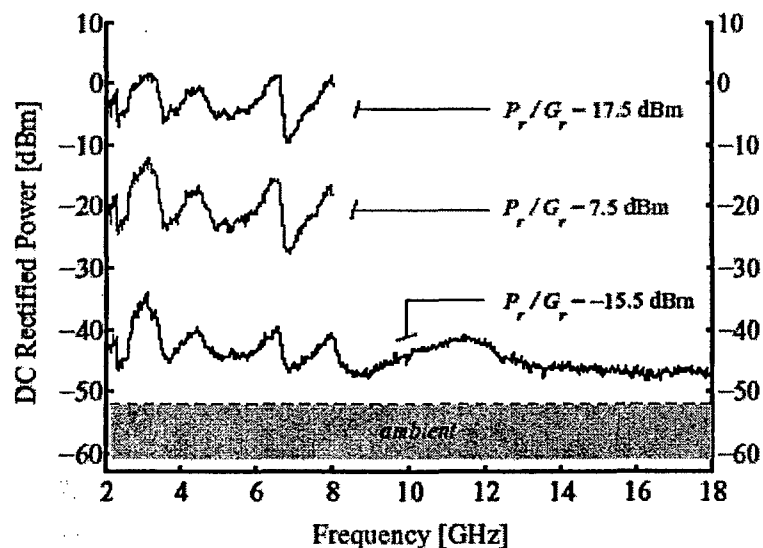
Figure 9. Measured broadband frequency response for various incident power levels related to the power density, S, by $P/G = S\lambda_0^2/(4\pi)$. The shaded area represents the range of rectified power levels resulting from ambient RF background signal present in the building.

The frequency dependence is measured in two ways: three dimensional patterns are integrated from 2 to 8 GHz where sufficient power was available for the measurement. Since the radiation patterns are reasonably smooth, only the broadside frequency response was measured. Higher input powers were used for 2 to 8 GHz and a low power level was used for the broad range from 2 to 18 GHz. The broadside frequency response was also measured using a uniform incident

power density to synthesize constant input power to the diodes. The results for three input power levels are shown in Figure 9.

4. DISCUSSION AND CONTINUED WORK

A study of reception and rectification of broadband statistically-varying rf radiation is presented in this paper. The experimental results show that the combined electromagnetic field analysis of the antenna element and harmonic balance nonlinear circuit simulations for the integrated diode result in predictable rectenna performance. The work focuses on arbitrary polarized low incident power density reception and rectification and shows that rectification efficiencies with average 20% over time, frequency and polarization are achieved. If one of these requirements is relaxed, i.e., highpower, narrow-band, linearly-polarized and/or time-constant power is transmitted, higher efficiencies up to 60% at X-band [5] can be expected. The motivation for considering the low-power multipath channel case are applications in ambient energy recycling and low-power batteryless sensors.

The first type of application addresses using otherwise wasted power, which in some cases can also help reduce health hazards. For example, the rooftops of buildings in city centers are often leased to a number of wireless providers and technical staff has reported health problems when servicing a transmitter in the presence of other operating transmitters [14]. In this environment, a variety of output powers, frequencies, and polarizations are present, and interference between a number of antennas in each other's near fields changes their radiation properties, accounting for more *wasted* power. The results of this paper show that this power can be absorbed (received), rectified and stored for future use.

It can be shown that a simple sensor that requires a small energy packet to perform the sensory function, and one packet to transmit data, it would be able to transmit new data around 20 times per second in the best case under the wireless power delivery of low power levels such as the ones described in this paper. An example of such an application is a manufacturing environment, where a large number of sensors occasionally transmit data such as stress, temperature, pressure, light level, etc. A large number of such sensors with no batteries that need replacing (or recycling) can be charged with a low-power transmitter overnight. In such an indoor multipath propagation environment, the spatial distribution of polarization and power varies statistically. The results of this paper show that it is possible to efficiently collect such energy by receiving and

rectifying two orthogonal polarizations independently and adding the power upon rectification.

Finally, a third future application of the described systems which will present a more difficult antenna design problem is delivery of low power levels to sensors implanted in live bodies. In this case, the antenna is embedded in a lossy inhomogeneous dielectric and the heating due to the limited diode efficiency and absorption of the tissue is a relevant and interesting topic of research.

ACKNOWLEDGEMENT

REFERENCES

[1] W.C. Brown, "The history of power transmission by radio waves," *IEEE Transactions on Microwave Theory and Techniques*, vol. 32, no. 9, pp. 1230–1242, Sept. 1984.

[2] N. Shinohara and H. Matsumoto, "Experimental study of large rectenna array for microwave energy transmission," *IEEE Transactions on Microwave Theory and Techniques*, vol. 46, no. 3, pp. 261–267, Mar.1998.

[3] J.O. McSpadden, F.E. Little, M.B Duke, and A. Ignatiev, "An in-space wireless energy transmission experiment," *IECEC Energy Conversion Engineering Conference Proceedings.*, vol. 1, pp. 468–473, Aug. 1996.

[4] Kai Chang, *Microwave Ring Circuits and Antennas*, John Wiley & Sons, New York, NY, 1996.

[5] T. Yoo and K. Chang, "Theoretical and experimental development of 10 and 35 GHz rectennas," *IEEE Transactions on Microwave Theory and Techniques*, vol. 40, no. 6, pp. 1259–1266, June 1992.

[6] L.W. Epp, A.R. Khan, H.K. Smith, and R.P Smith, "A compact dualpolarized 8.51-GHz rectenna for high-voltage (50 V) actuator applications," *IEEE Transactions on Microwave Theory and Techniques*, vol. 48, no. 1, pp. 111–120, Jan. 2000.

[7] Y. Fujino, T. Ito, M. Fujita, N. Kaya, H. Matsumoto, K. Kawabata, H. Sawada, and T. Onodera, "A driving test of a small DC motor with a rectenna array," *IEICE Trans. Commun.*, vol. E77-B, no. 4, pp. 526–528, Apr. 1994.

[8] W.C. Brown, "An experimental low power density rectenna," *IEEE MTTS International Microwave Symposium Digest*, pp. 197–200, 1991.

[9] J.O McSpadden, R.M. Dickinson, L. Fan, and Kai Chang, "Design and experiments of a high-conversion-efficiency 5.8-GHz rectenna," *IEEE MTT-S International Microwave Symposium Digest*, vol. 2, pp. 1161–1164, 1998.

[10] J.O. McSpadden and K. Chang, "A dual polarized circular patch rectifying antenna at 2.45 GHz for microwave power conversion and detection," *IEEE MTT-S International Microwave Symposium Digest*, pp. 1749–1752, 1994.

[11] B. Strassner and K. Chang, "A circularly polarized rectifying antenna array for wireless microwave power transmission with over 78% efficiency," *IEEE MTT-S International Microwave Symposium Digest*, pp. 1535–1538, 2002.

[12] J. C. Lin, "Radio frequency exposure and safety associated with base stations used for personal wireless communication," *IEEE Antennas and Propagation Magazine*, vol. 44, no. 1, pp. 180–183, Feb. 2002.

[13] J. C. Lin, "Space solar-power stations, wireless power transmissions, and biological implications," *IEEE Microwave Magizine*, pp. 36–42, Mar. 2002.

[14] J.A Hagerty and Z. Popovi'c, "An experimental and theoretical characterization of a broadband arbitrarily-polarized rectenna array," *IEEE MTT-S International Microwave Symposium Digest*, vol. 3, pp. 1855–1858, 2001.

[15] H. Loui, J. Peeters Weem, Z. Popovic, "A dual-band dual-polarized nested Vivaldi slot array with multilevel ground plane," *to appear in IEEE Trans. Antennas and Propagation*, Sept. 2003.

[16] N. Shinohara and H. Matsumoto, "Dependence of dc output of a rectenna array on the method of interconnection of its array elements," *Electrical Engineering in Japan*, vol. 125, no. 1, pp. 9–17, 1998.

SPACE-BASED E-TEXTILE ARRAYS

Michael A. Deaett, Pierre A. Dufilie and William H. Weedon
Applied Radar, Inc.
210 Airport Street
N. Kingstown, RI 02852

Abstract: Next-generation space-based radar and communications arrays require very large apertures in order to achieve the required gain and resolution. The implementation of these very large apertures poses several challenges in order to reduce the cost and weight while improving manufacturability. As system requirements have grown more stringent and required arrays have increased in size, new forms of antenna implementation are desirable. Electronic textiles, or E-textiles, is a candidate new technology that promises lighter weight and lower cost flexible options for satisfying a wide range of array applications. In this paper, we discuss the design of an L band array partitioned into subarrays to realize a total aperture of more than 100 meters in length. Multilayer designs utilizing embroidered antenna patches, knitted polyester spacers and woven ground planes are examined. We discuss the requirements for building a one meter by one meter subarray panel for a precision radar demonstration prototype. Array issues including subarray partitioning, beamwidths, beamsteering, antenna manufacturing tolerances and material electromagnetic property variations as they affect the final system performance are addressed. We summarize by showing that significant array advances are feasible and illustrate the development challenges that this technology faces.

1. Introduction

Early radar satellites were deployed in a variety of LEO orbits at altitudes of less than 1000 km [1, 2]. As the throw weights of launch vehicles has increased and system requirements have become more demanding, satellites are being deployed in MEO altitudes to 10,000 km. These higher orbits require larger antenna apertures to maintain system capabilities [3]. For example, an aircraft surveillance radar with a seven meter aperture has been projected to translate to a 57 meter aperture for a LEO orbit satellite of the same capability and to a 320 meter aperture for a MEO orbit [4]. The manufacturing of very large aperture antennas within realistic cost and weight constraints is a very challenging problem. There

have been several technologies suggested for implementation. These include inflatable reflector antennas [5] and extensions of conventional printed microcircuit antennas. Another technology that has significant cost and weight advantages over conventional plated microcircuit technology is Electronic Textiles or E-Textiles [6]. The application of this technology to space-based arrays is therefore being investigated. In our paper we first review the impact of higher altitude orbits on the size of the deployed arrays. We then seek to simplify the implementation of these arrays through the use of subarray beamforming. We use several examples to establish the context for real radar and communication applications of our array technology.

In section 3, we review the patch level technology that has proven feasibility. Here a key aspect is to transition from hand constructed antenna prototypes to an automated, computer controlled manufacturing process that produces a predictable, high performance product. In section 4 we cover current progress in developing a one meter square subarray that can enable space-based large aperture deployments.

2.0 Space-Based Very Large Aperture Radar Ranging

Previous earth satellites employed for radar surveillance purposes have utilized LEO orbits. For example, the Seasat and RadarSat satellites as well as the envisioned Space Based Radar and TerraSar satellites all employ orbits with heights of less than 1000 km. However, future missions will employ higher orbits to reduce the number of system satellites, to simplify control and orbital maintenance and to improve mission flexibility and performance. For these missions, orbital heights of from 1000 to 10000 km are planned. Missions include both radar surveillance and communications relay objectives. One of the most important contributors to the success of these missions is the availability of larger, low-cost, lightweight antenna apertures to support the more stringent beamforming and beam pointing requirements.

To extrapolate aperture performance to other ranges, we can employ a simplified model of satellite-based illumination and use the equation,

$$X_{cr} = (\lambda/D_{aperture})*R, \tag{1}$$

where X_{cr} is the desired cross range resolution, $D_{aperture}$ is the aperture length, λ is the wavelength of the radar or communication system and R is the distance from the imaged surface to the imaging radar. Using this equation, we can see that

a radar that has a cross range illumination of 600 meters at a nominal 10 GHz using a 10 meter aperture at an altitude of 200 km will require a 100 meter aperture at a range of 2000 km. These are large apertures but we note that radio astronomy routinely uses even greater apertures so the issue is how to build and deploy these large antenna arrays in space.

Another significant determinant of array construction complexity is the feed network that connects the array antennas with the system transceiver. Note that this transceiver can in fact be composed of a multiplicity of transceivers where each transceiver may be connected to only a portion of the total number of array antennas. For comparison purposes, we consider here the single transceiver case and examine the use of subarrays to simplify array construction. If a single array consisting of N_e antenna elements is connected to an analog summation beamformer, then a single aperture with an angular resolution of φ is formed where $\varphi = \lambda/D_{aperture}$. If this same array is divided into two nonoverlapping subarrays each of which incorporates a separate analog summation beamformer, then the outputs of these two subarrays may be steered to cover a field of view that to a first approximation is equal to $2*\varphi$. Likewise, if the array is divided into N equal, separate subarrays, then the field-of-view is approximately $N*\varphi$. When the array consists of N_e individual steerable antenna elements, then the full field - of-view of 120 to 180 degrees can be scanned electronically. The subarray beamformers may be digitally switched phase shifters or they may be fully digital and implemented in the time or the frequency domain. Of importance to E-Textile array construction is that the additional subarray beamformers can lead to a less complex implementation so that the total field-of-view to be scanned is an important design variable.

The total field-of-view is dependent on the mission that the array supports [7]. For an earth surveillance satellite, a fixed aperture that is scanned across the earth by the motion of the satellite may be sufficient. Any greater resolution than that provided by the real physical aperture may be provided by introducing a phase stable correction and synthetic aperture formation. However, in the case of spot beam radars or communications systems, a single beam covering the entire area of interest may not provide a sufficient SNR. Spot beam steering is then required. Earth coverage from an orbital height of 2000 km requires a total scan capability of about 100 degrees while scanning from 20000 km requires a scan of about 28 degrees. For comparison, a satellite could operate from a geosynchronous 35,784 km orbit where the total earth coverage scan would be approximately 18 degrees. It can be seen that since the field-of-view of higher orbit satellites is less than that

of LEO satellites, the use of subarray beamforming to reduce the complexity of an array implementation becomes more important. We are therefore including the use of subarrays in our investigations.

A prototyping benchmark is necessary is focus our development efforts and to provide tradeoffs that will lead to deployed systems. A reasonable array size, compatible with early large aperture array requirements incorporates a 100 meter aperture divided into individual one meter square subarrays as shown below. The initial design frequency of operation is 2.435 GHz. This frequency was chosen so that early implementations would be tolerant of textile fabrication tolerances. The implementation of the one meter square subarrays enables those subarrays to use additional, smaller subarrays to meet system requirements in an efficient manner.

3. E-Textile Patch Antenna Technology

In assembling larges subarrays from individual patches we rely on an established hierarchy of textile industry fabrication [8], [9]. This hierarchy considers fibers to be the first and fundamental material from which threads, yarns and rope are made. The threads and yarns are then woven or knit into fabrics which are quasi-planer; that is, they have a significant thickness but are generally produced as flat or sheet goods. From the fabrics, finished products such as garments are produced through a process that incorporates cutting, stitching, gluing and coating. It is also true that more recent processes construct nonwoven fabrics directly from the fibers and binder materials. We note here that every level of the product construction process, from the fiber level to the garment level, can be used for electronic textile antenna construction. The most advantageous selection of available methods and the integration of these methods into the best antenna construction process is the subject of our current research.

To explore E-Textile antenna construction methods, we first designed a prototype antenna patch. The top view of the patch antenna is shown in Figure 1. The design of this patch is based on a transmission line model in which the energy is transferred from the feed point to free space radiation. There are three stacked E-Textile patch antenna elements - a ground plane, a spacer layer and a conductive antenna patch Energy is radiated in transveral mode. To effectively radiate, the antenna is impedance matched to the drive line through a microstrip transformer which consists of a thin patch that connects the bonding pad to the antenna patch.

The usual construction method is to employ a sandwich of two copper layers bonded to a high performance microwave substrate such as Rogers 5880. One of the copper layers is then etched to form the antenna patch. This form of construction produces a heavy, rigid, planar patch antenna. Such an antenna has limited potential to our space-based antenna array objectives. However, it is a current standard because precise construction techniques are available that produce predictable performance.

W2
8 mm

W1
1.7 mm

W
41.4 mm

L1
29.3 mm

L
54.2 mm

f_R = 2.5 GHz.   h = 2.0 mm

λ = 120 mm ε_r = 1.1
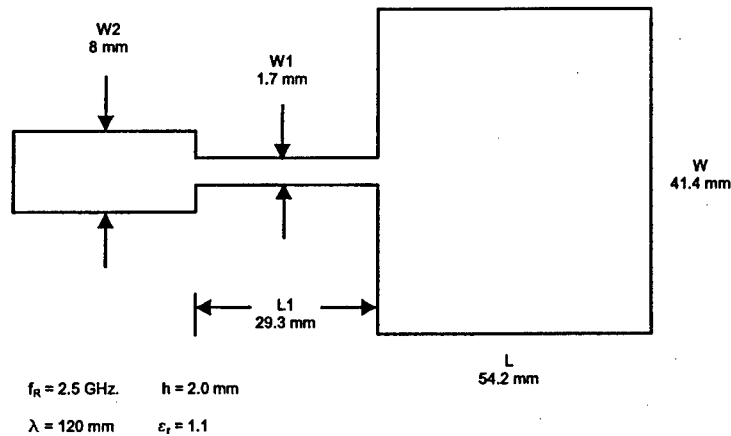
Figure 1: Microwave Patch Antenna Design

We have investigated several alternative E-Textile patch construction methods. These were in two classes of material composition. The first was consists of flexible antennas assembled from fabric components. The second were fabric component antennas which were assembled into rigid structures using epoxy resin. A total of eight patch antennas and several prototype transmission lines were constructed. These transmission lines constitute an RF interconnect. We focus on the antennas shown below.

There are at least two methods of constructing E-Textile antenna patches. The first method is to weave, sew or embroider the wire or conductive yarn into the fabric. We conducted numerous experiments in sewing and embroidering wire. Initial experiments utilized patterns of wire sewn by hand into a fabric. Using this process we stitched antenna patches into a flexible nylon fabric (Figure 2a) and vinyl upholstery fabric (Figure 2b) and (Figure 2c). We found that these fabrics were dimensionally stable even when tensioned and they did not tear away from

the wire when flexed. For spacer materials we used urethane foam and several knit spacer fabrics. Finally, we used both copper cloth and copper polyester tape
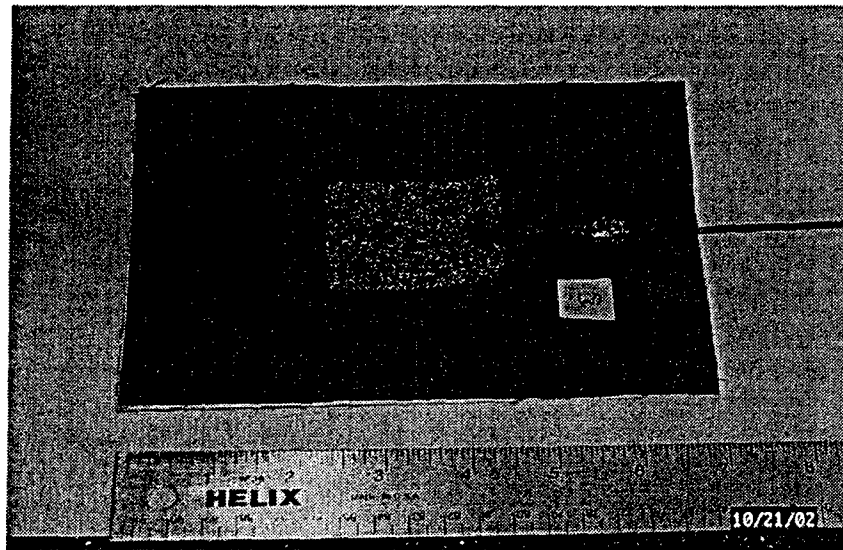

Figure 2a: E-Textile Flexible Patch Antenna
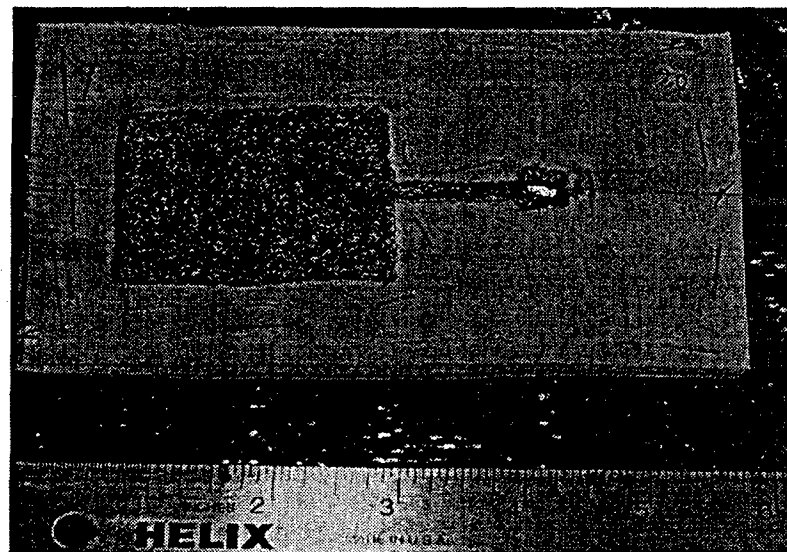
Figure 2b: Foam and Vinyl Sandwich Antenna
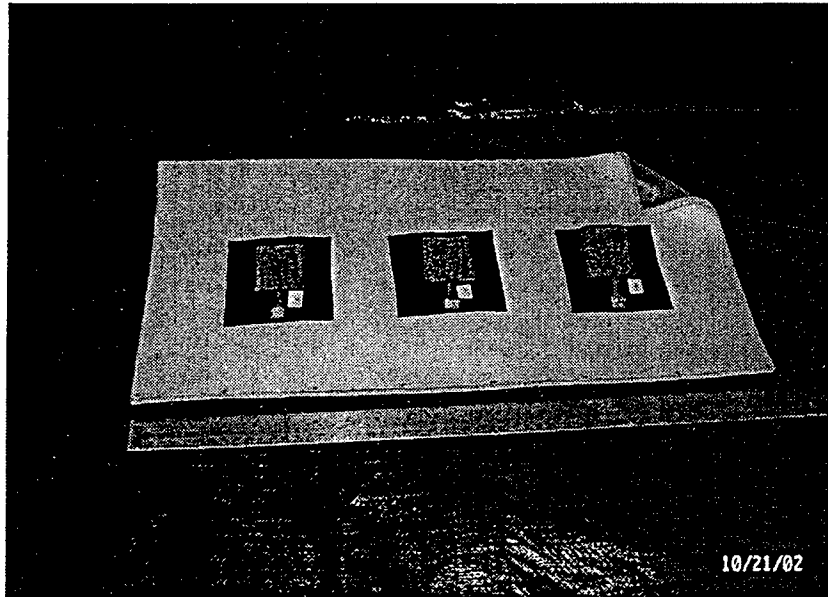
Figure 2c: Multiple Patch Antenna Array

materials for the ground plane layer. These layers were then stitched together with very light thread tension so that the antenna was not distorted. The microwave feed was thin coax which was attached to the stainless steel feed pads. We have also constructed a preliminary three patch array prototype by stitching three patches onto one textile substrate as shown in Figure 2c.

A second method of antenna construction attaches a wire antenna patch made of copper cloth onto a fabric. The patches are cut out of conductive cloth and sewn onto the carrier fabric. We have constructed experimental prototypes by cutting antenna patches out of copper wire cloth and then sewing these patches onto heavy nylon fabric. The dimensional tolerances that can be held with this method may exceed those possible with the wire sewing method. Since the sewing process is so precise with preassembly cutting and since a lock-stitch machine can be used to attach the patch to the fabric, the manufacturing yield of this method is greater than with the wire sewing method. However, the antenna is less integrated with the host fabric and possibly more subject to degradation upon flexure and abrasion. An example of an antenna patch sewn by this method is shown below in Figure 3.

As mentioned above, the fabric antenna patches can be incorporated into composite structures. We produced two patch antennas using stainless steel wire embroidered into heavy (36 and 24 Oz.) industrial grade fiberglass. This fiberglass is used to make airplane fuselages and boat hulls. The ground plane was a graphite fabric and a honeycomb spacer layer was used. This spacer is rigid and the entire composite structure is rigid and load bearing when completed. We believe that the over stitching method of patch incorporation has promise here as well. The inclusion of graphite ground planes and wire antenna structures may be compatible with the structural requirements of several spacecraft.
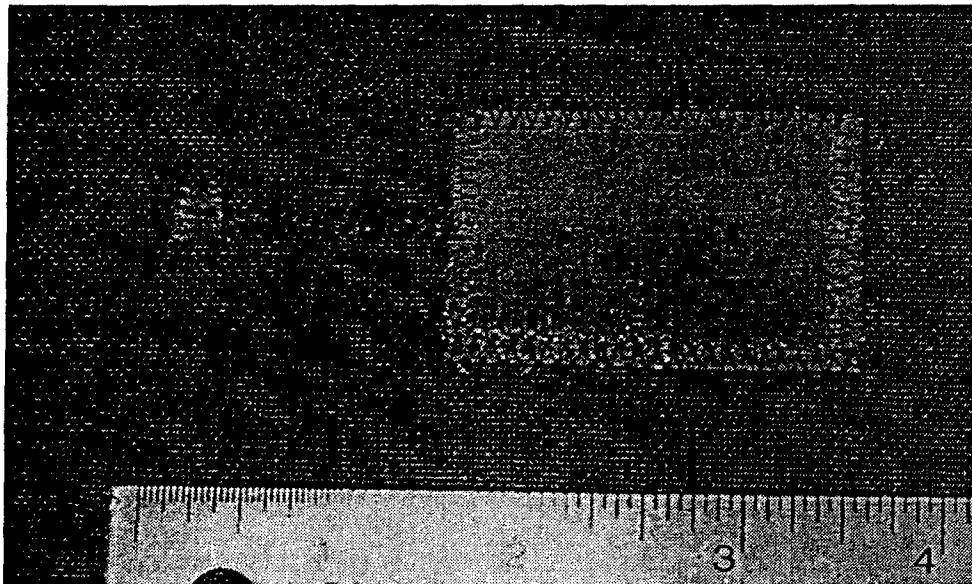

Figure 3: Copper Cloth Antenna Patch Stitched Over Fabric

4. Space-Based Subarray Design

To design a full subarray we are employing multiple patch antenna configurations with a variety of complex feeds and interconnection structures. Figure 4 below shows the initial design for the patch panel that is being used as a benchmark prototype for our E-textile designs. For the initial design, a corporate feed was chosen for implementation. One disadvantage of the corporate feed is that it occupies a large amount of real estate. This places a restriction on the possible variations in the design due to the need to minimize coupling and achieve a

desired element spacing. With larger corporate feeds, the loss increases more rapidly than for series-fed arrays, however, for small 2 by 2 arrays, the loss of a corporate feed is comparable to that of a series feed configuration. The corporate feed does offer a major advantage in that it simplifies the design by ensuring both the phase and amplitude of the patch excitations are all equal. Since the phase excitations of the elements are all the same with respect to frequency, the corporate feed helps to broaden the array's pattern bandwidth, i.e. helps to maintain the radiation pattern at frequencies off from the center frequency.
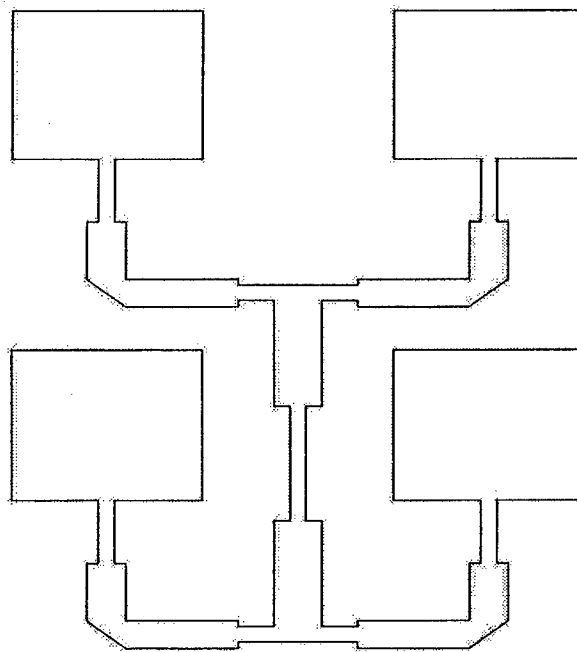
Figure 4: Microstrip E-Textile Patch Panel Layout

In constructing these subarray patch antennas, we are investigating a variety of existing textile materials. Among these are conductive fabrics that are typically used in shielding applications. One would expect that the price structure of such materials would be a function of the shielding effectiveness. Figure 5 below shows a plot of shielding vs. price for various conductive fabrics under consideration. The trend line indicates that the prices of materials increase as the shielding effectiveness increases. It should be noted that shielding is not the only factor that influences the cost of the material, which leads to the somewhat loose correlation.
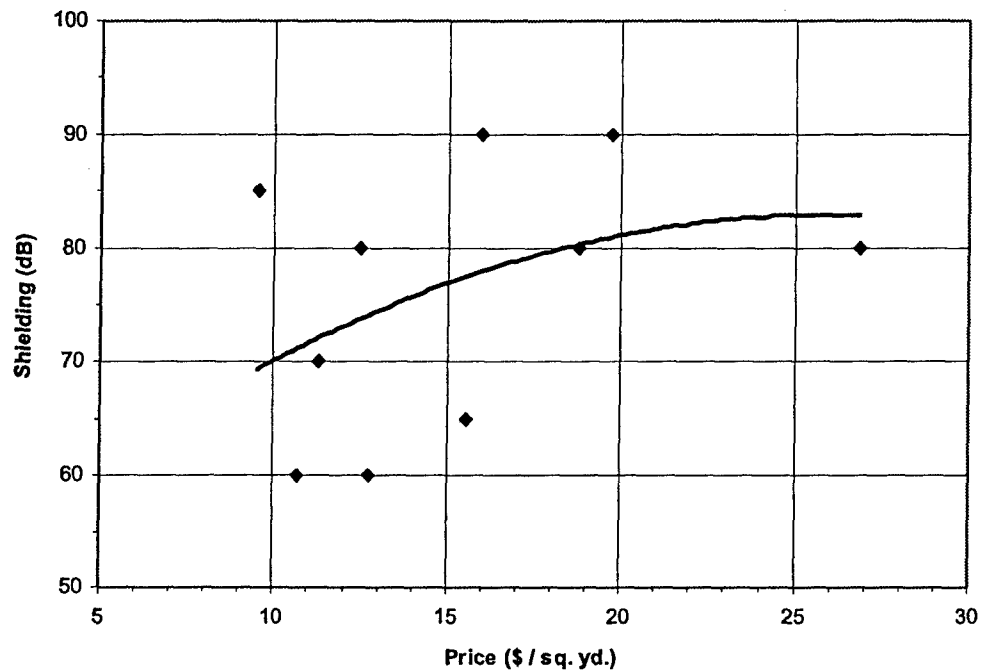
Figure 5: Shielding vs. Price of Various Conductive Fabrics

Shielding is not a critical property of the material when used in a planar antenna array. From a design viewpoint, loss is a major consideration among other properties in choosing a conductive layer. Figure 6 below shows a graph of loss vs. price for the same fabrics used in Figure 5.

It should be noted that the correlation has become even looser than in the previous case when shielding was the property of interest. The various fabrics appear to be grouped into two ranges of loss, one from approximately 160 to 190 dB / 100 meters and the other from 40 to 70 dB / 100 meters. The two groups are separated by approximately a factor of 3 on a dB scale. It should also be noted that the materials exhibiting lower loss have a trend line that is almost independent of price over the range shown. The designer is then left with several options: 1) a low-cost solution with high loss, 2) a high-cost solution with low loss, and 3) a low-cost solution with low loss. The materials of option 3 will be the first ones to be examined for the design.
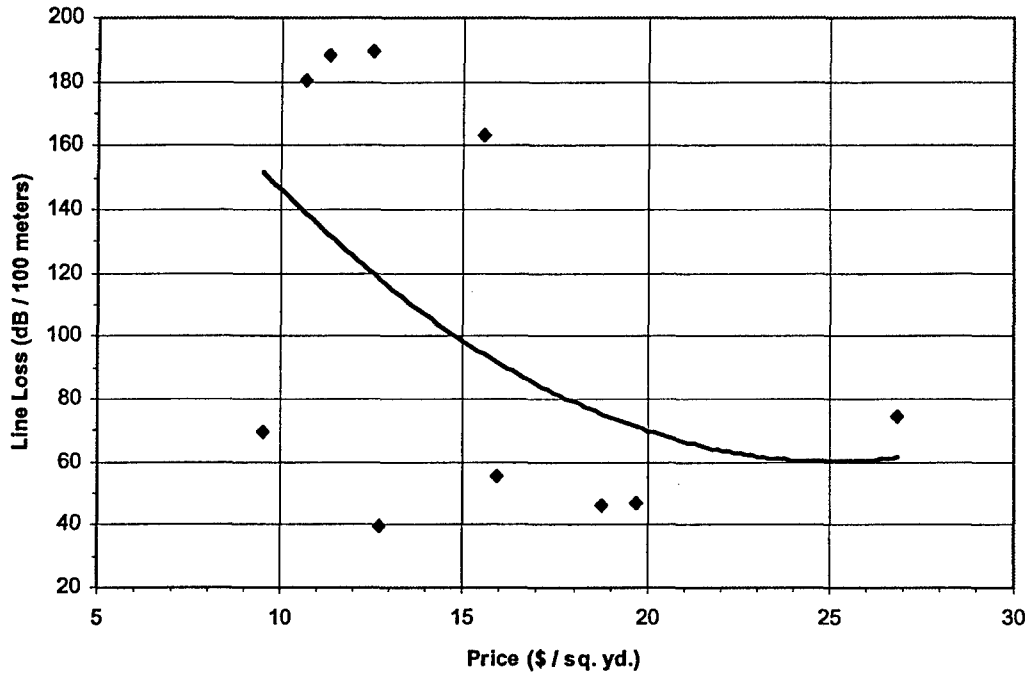
Figure 6: Loss vs. Price of Various Conductive Fabrics

It is important to estimate the performance of the quad patch panel using the characteristics of the textile materials from which it will be constructed. The two by two E-Textile patch panel array was modeled in computer simulation to predict its performance. Figure 7 below shows a plot of the input reflection coefficient. The goal for the center frequency of operation was 2.435 GHz, which is labeled as point 1 in Figure 2. Markers 2 and 3 show the bounding edges of the −10 dB impedance bandwidth of the array, which is approximately 6 % or 146 MHz. The predicted loss in the feed network was approximately 0.25 dB.

Figure 8 below shows the expected radiation pattern of the 2 by 2 array in both the E and H-Planes. As expected, the H-Plane pattern is symmetric while the E-Plane pattern is somewhat asymmetric due to the lines of physical symmetry along the E and H-Planes respectively. The half-power (-3 dB) beamwidth was approximately 28° in both planes. The predicted gain of the antenna was nearly 14.5 dB.

| X1= 2.44GHz	X2= 2.37GHz	X3= 2.51GHz
Y1= -19.92	Y2= -10.72	Y3= -10.67
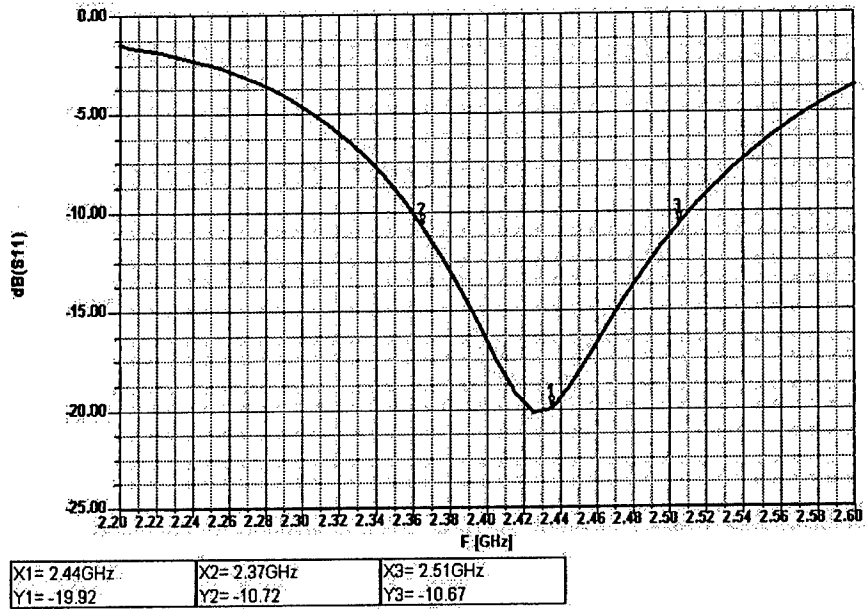
Figure 7: Predicted Input Reflection Coefficient of the 2 by 2 Patch Array
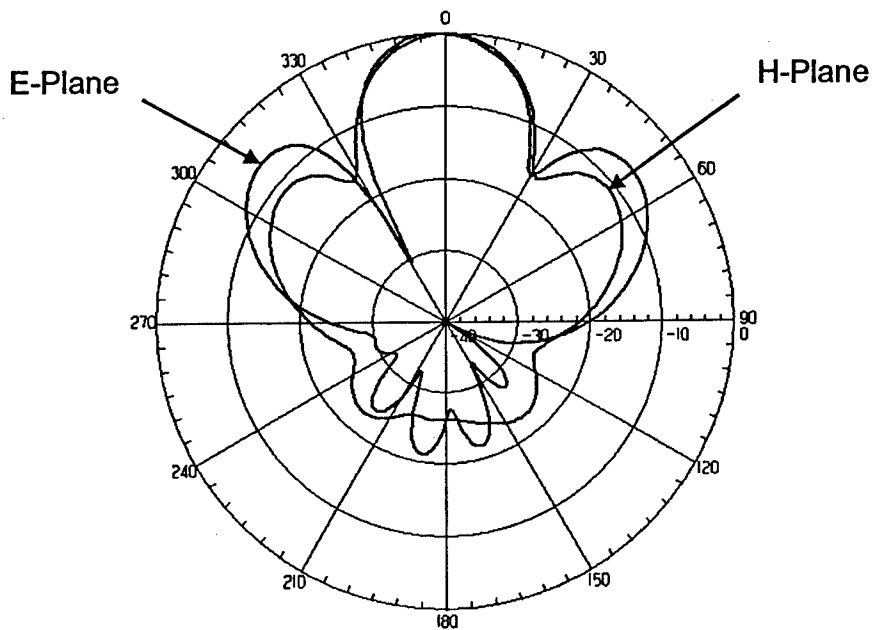
Figure 8: Predicted E and H-Plane Radiation Patterns of the 2 by 2 Patch Array

63

5. Component Antenna Subarray Design

Once the 2 by 2 element subarray has been designed, larger arrays can follow by patterning the sub-array and connecting them together. Figure 9 below shows the layout of a square meter size panel of patches. The sub-arrays are connected together by a corporate feed on a lower trace layer behind a ground plane. Vias are used in order to connect the top trace layer that contains the patches to the bottom trace layer below the ground plane. The reason for using separate feed layers is to ensure that enough space will be available to construct the corporate feed that connects the sub-arrays together. The same procedure could be used to physically separate the four patches in the sub-array design from the corporate feed that connects them together, however, this would require an additional trace layer, and it would further complicate the manufacturing process.
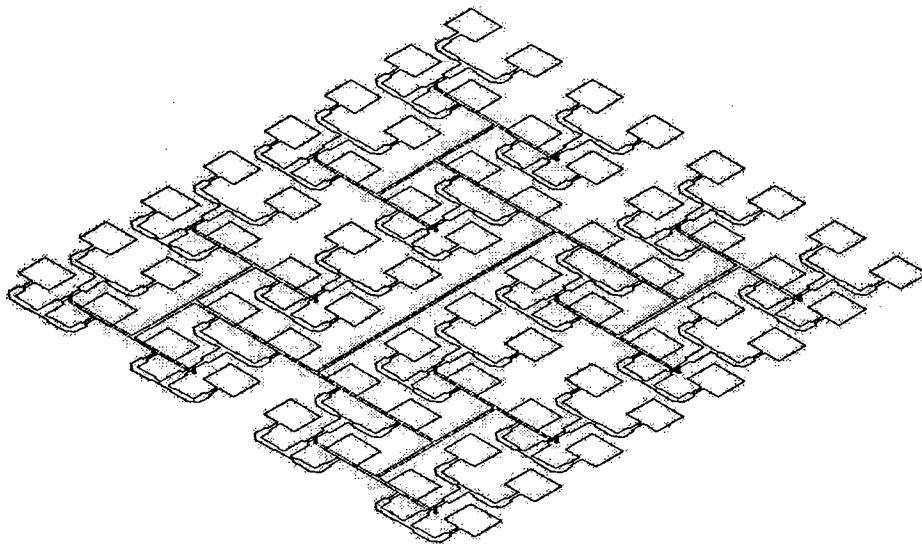
Figure 9: Initial Layout for a Square Meter Subarray of Patch Antennas

6. Summary

Investigations to date have shown that it is indeed possible to build one meter square E-Textile subarrays from which very large space-based arrays can be constructed. Significant challenges remain for the successful deployment of these arrays in space. Among these is to establish the textile construction method tolerances which in turn determine the maximum frequency at which this technology can be employed. The consistent reproducability of a uniform array product must also be demonstrated so that manufacturing yields with acceptable cost burdens can be realized. Finally, the best construction methods for individual satellite apertures must be established so that performance is maintained over the entire mission duration.

7. Acknowledgement:

8. References

[1] John C. Curlander and Robert McDonough, Synthetic Aperture Radar Systems and Signal Processing, New York: Wiley, 1991.

[2] Fred Nathanson, J. Reilly and M. Cohen, Radar Design Principles, New Jersey: Scitech Publishing, 1999.

[3] Mark E. Davis, "Space Based Radar Core Technology Challenges for Affordability", Colorado Springs, Colorado:Core Technologies for Space Systems Conference, 2001, http://www.spacecoretech.org/coretech2001/.

[4] J. Guerci, "Innovative Space-Based Radar Antenna Technology Program, DARPATech 2002, http://www.darpa.mil.darpatech2002/presentations/spo.pdf.

[5] William H. Weedon, W. C. Chew, T. J. Cui and L. Poles, "Error Compensation for Very Large Inflatable Reflector Antennas", 2000 Allerton Antenna Applications Symposium, Allerton Park, Monticello, IL, Sept. 20-22, 2000.

[6] Michael A. Deaett and William H. Weedon, "Novel E-Textile Antennas for Homeland Defense Applications", Government Microcircuit and Critical Technology Conference (GOMACTech), Tampa Fl., 2003.

[7] James J. Spilker, Jr., Digital Communications by Satellite, New York: Prentice Hall, 1977.

[8] Sabit Adanur, Handbook of Weaving, Technomic Publishing Co, 2001.

[9] Pat Earnshaw, Lace Machines and Machine Laces, London, UK: B. T. Batsford Ltd. 1986.

A Computer-Aided Approach for Designing Edge-Slot Waveguide Arrays

R.B. Gosselin
Microwave Instrument Technology Branch, Code 555
NASA - Goddard Space Flight Center
Greenbelt, MD 20771, U.S.A.

Abstract: Traditional techniques for designing resonant edge-slot waveguide arrays have required an iterative trial-and-error process of measuring slot data from several prototypes. Since very little meaningful data has been published, this technology remains relatively immature and prohibitive for many smaller programs that could benefit from some advantages this antenna has to offer. A new Computer-Aided Design technique for designing resonant edge-slot waveguide arrays was used to successfully design such an X-band radiometer antenna for the NASA Light Rainfall Radiometer (LRR) instrument. Having the ability to rapidly create such an extremely accurate and efficient antenna design without the need to manufacture prototypes has also enabled inexpensive research that promises to improve the system-level performance of microwave radiometers for upcoming space-flight missions. This paper will present details of the LRR antenna design and describe some other current edge-slot array accomplishments at Goddard Space Flight Center.

1. Introduction

The recent success of NASA's Light Rainfall Radiometer (LRR) aircraft mission has demonstrated some tremendous advantages of resonant edge-slot waveguide arrays for passive microwave Synthetic Aperture Interferometric Radiometry (SAIR) applications [1, 2]. The quality of science data received during several test flights can be attributed in part to the very high-performance of the fourteen X-band antenna elements mounted beneath the aircraft. Because of their incredible mechanical integrity it was possible to fly them using only a very thin layer of Kapton tape over the openings and a dry-nitrogen purge to remove potential accumulations of moisture. Achieving such high-quality antenna performance using a computer-aided approach and eliminating the effects of a radome was an important accomplishment for passive microwave radiometry and has it renewed interest in exploring edge-slot waveguide array technology for future space-flight missions.

Despite what these antennas have to offer, they have never emerged as an off-the-shelf technology primarily because it remains very difficult to determine the precise slot depths and angles to produce an optimized design. The choice of this antenna on a previous L-band program proved to be a very expensive one especially when burdened with some of the common design issues and the absence of literature offering reliable engineering guidelines [3,4]. In many cases the huge benefits of having an extremely low-loss, integrated waveguide combiner network have been lost to the accumulated design inaccuracies.

LRR was an example of a small project with very limited funding that leveraged from a commercially available electromagnetic software package to overcome these past obstacles. In this case the commercial software used was Ansoft HFSS (http://www.ansoft.com). It replaced the expensive and time-consuming empirical techniques from the past with virtual models that simply required a moderate amount of computer resources. No longer was it necessary to manufacture and measure numerous prototype antennas to characterize slot performance The time to derive the set of design curves for resonant slot characteristics at X-band was less than the time spent on a previous program to achieve just one data-point at a more forgiving L-Band frequency.

2. Basic Design Principles [7, 8, 9, 10]:

A section from a typical resonant edge-slot waveguide array is shown in **Figure 1**. The basic approach for designing them has remained unchanged since the first radar applications of WWII [3,5]. Slots are machined across the narrow face of the waveguide at some alternating fixed angles $\pm\theta$ to interrupt the currents along the inside skin so radiation propagates from an electric field vector bridging that gap. The resulting slot also penetrates into each of the broad-walls by some depth d; which LRR defined in accordance with the typical convention as measured with respect to the outside surface of the narrow wall being cut.

Figure 2 shows a graphical visualization using Ansoft HFSS to display radiation from a slot in terms of electric field vectors. Slots are located at half-guide-wavelength intervals where standing-wave energy inside the waveguide is peaked between the shorting plates at each end. **Figure 3** shows a cross-sectional contour plot of radiation inside the waveguide and slots using HFSS post-processing of the antenna; and this graphical representation was an especially useful diagnostic tool to provide confidence that microwave propagation inside the waveguide was correctly aligned with the slot locations.

Adjusting slot angle is the common technique for controlling the amount of radiation from a slot. For example, a tapered array design requires placement of the largest slot angles at the array center since these excitations are the greatest, and the angles must be progressively decreased towards each end. Different slot depths are necessary for each slot angle in order to maintain resonance. The analogy between slots and the complimentary dipole provides a good explanation why maintaining some constant resonant slot length requires that the contribution from the wrap-around depth penetrating into the broad-wall must decrease as slot angle increases and vice-versa [6].

Some interesting work has been done by others to achieve variable radiation from a slot by adjusting obstacles and irises inside the waveguide; however the possibility of further reducing bandwidth and adding to the mechanical complexity of the LRR array made this option less attractive for LRR. This past work emphasizes the fact that these types of antennas incorporate the internal RF combiner network as part of the external radiating structure and there is essentially no isolation allowing a partition between the two designs.

3. Design Approach Used for LRR Antennas:

Using data from resonant slots and applying the basic concept of pure conductances in parallel (as described by the ladder-line model shown in **Figure 4**) was the fundamental approach for the LRR design effort. To derive individual slot conductance directly from the array S11, the average individual slot conductance was calculated as the conductance measured for the entire array divided by the number of slots.

A series of models having progressive increments of deeper slots were created and analyzed until the admittance (derived from the S11) for the array had only a very small contribution from the susceptance term and crossed over the line of pure conductance when plotted on a Smith Chart. This technique was used to derive a summary of slot data from several uniform 36-slot array models using HFSS, and the results for first resonances at various angles are documented in the design curves of **Figure 5** and **Figure 6**.

Using the HFSS modeling approach had the advantage that S11 was provided from a single waveguide port definition as shown in **Figures 7 and 8** and therefore the slot characteristics were not masked by the sometimes complicated electrical effects of a probe assembly. This departs from the traditional feed-point shown for the ladder line in **Figure 5**; which is based on the actual hardware representation with a feed shown in **Figure 9**. Past laboratory techniques

typically only measured incremental slot conductance of an array by covering a single slot with copper tape and subtracting this value from what was measured previously with the slot uncovered [10].

Once a database of slot characteristics (as represented by the curves shown in **Figures 5** and **6** was established, any array design could easily be created using a spreadsheet with the desired voltage distribution coefficients as input. Embedded in this approach is the assumption that mutual coupling changes between neighboring slots of slightly differing angles will have negligible impact. To minimize the potential impact of errors caused by mutual coupling, the uniform array models created to derive the design curves used the same number of slots (36) as the final tapered design.

Creating a well-matched array of uniform linear voltage excitations is usually somewhat simple since there is only one common value of angle theta and depth d for each and every slot. To achieve a reasonable match to the waveguide characteristic impedance, each resonant slot in a uniform array must have a normalized conductance value close to 1/N where N equals the number of slots in the array. This follows from the general rule that to achieve a good array match the sum of the normalized conductances must sum to 1.0 [7]. Making a Uniform array is especially easy if there is no firm length requirement so the number of slots can be adjusted.

The array excitations for the final LRR antenna slots were defined using the Villeneuve array equations to create a-Taylor 25 dB, nBar=4 [11]. The desired slot conductances g_n for each array element were applied to a spreadsheet (**Table 1**) that used data from **Fig. 5 and Fig. 6** to compute each of the 36 resonant slot angles and depths. Some design limitations did occur for two end-elements where the curves are not defined for smaller values of slot angle since resonance was no longer achievable. The slot angle and depth for the third and thirty-forth slots were simply copied for those adjacent end locations since only small errors were anticipated because they were not contributing much radiation. This deviation also seemed acceptable since these edge-elements may have been prone to small errors from mutual coupling effects anyway. It is interesting to consider, however, the mutual coupling effects between slots of shallower angles (lower conductance) should be less pronounced and may be the reason why the curve for slot depth in **Figure 6** has a sharply increase. Likewise, at these small angles there is closer agreement between the curves in **Figure 10** labeled "HFSS Resonant Uniform Array of 36 slots" and "Watson's Ordinary Conductance" which was intended for characterization of end-slots [7].

Table 1 uses **Equation 1** to define the normalized conductances for each slot from the desired aperture taper voltage coefficients [7].

$$g_n = \frac{a_n^2}{\sum_{i=1}^{t} a_i^2} \tag{1}$$

Where g_n is the individual normalized slot conductance, t is the total number of slots, n is the slot number, and a_n is the coefficient for slot excitation voltage defined by the taper. **Equation 1** is derived from the relationship that the square of the voltage excitation at each slot is proportional to the normalized conductance, and enforces the requirement that for a matched end-fed array as shown in **Figure 9** the sum of those slot conductances must equal one to properly match the slots to the characteristic impedance of the waveguide.

4. LRR Antenna Performance:

The first LRR antenna produced used a typical probe though the broad-wall with tuning screws on the opposite side. To adjust these screws to match the probe, the slots were sealed with copper foil tape and a terminating load was used in place of the shorting plate at the end furthest from the probe. The two tuning screws were adjusted and locked once VSWR displayed on the Network Analyzer indicated an excellent match. The tape was removed from the slots and the load was replaced by the shorting plate. The evidence of a well optimized array design was indicated by the excellent match at the center frequency; which remained unchanged. Typical VSWR performance for two adjacent waveguide arrays is shown in **Figure 11.** . The VSWR typically did shift slightly when the LRR arrays are placed in the instrument-array environment with identical neighboring elements in close proximity; however for all fourteen sticks it typically remained less than 1.16:1 over the band of 10.65 GHz to 10.85 GHz.

Typical cross-polarized and co-polarized azimuth patterns for the series of manufactured LRR arrays are shown in **Figure 12** and **Figure 13,** respectively. The resulting side-lobe level was very close to the goal of -25 dB. It was fortunate that the slot angles for most of the 36 slots were very small since this minimized the cross-polarized lobes at approximately 42 degrees and therefore none of the typical techniques for reducing cross-pol. radiation were necessary for LRR **[4,10,12].**

5. Historical Comparison:

Prior to validation from the hardware fabrication and successful performance it was understood that comparison and agreement with past data was very important. **Figures 5 and 6** include resonant slot data for the LRR frequency of 10.7 GHz using both WR-75 and WR-90 waveguide, and for 9.375 GHz using only WR-90 waveguide. The 9.375 GHz case was constructed since it offers an interesting comparison with the WR-90 at 10.7 GHz case, and is a benchmark from what has often been published. **Figure 10** offers a direct comparison with some commonly published data and includes an overlay of the same HFSS curve for 9.375 GHz taken from **Figure 5. [7]**

6. Array Layout:

To minimize the accumulation of small errors, some special consideration was given to using several significant digits when defining array length and the precise location of the slots. The center frequency of 10.7 GHz translated into a guide-wavelength of roughly 1.63 inches inside the WR-75 tubing and meant the half-wave spacing between slots should be approximately 0.739 times the free-space wavelength. This unavoidable, but typical, violation of the Nyquist criteria was not an issue because the main beam remains stationary. Since the HFSS models assumed a perfectly square corner, the value for guide-wavelength which the software computed was extremely close to the standard text-book equation. This consistently close agreement gave some confidence to using that standard value for all the HFSS models. In the transition from software model to hardware, the value for lambda-guide and resulting slot spacing was recalculated to take into account some small effects of the radius at the waveguide edges that were not practical to model using HFSS **[13, 14]**.

The beamwidth requirements of the LRR instrument dictated that mechanical layout of the LRR array be determined prior to starting any electrical analyses and achieving a linear aperture of approximately 1 meter was a priority. The decision was made to use WR-75 waveguide since the alternative WR-90 type had a wider narrow-wall which exceeded the tight allowance for some of the interferometer spacings between adjacent linear arrays. From these factors it was calculated that 36 slots were necessary to adequately populate the aperture with some distance left between the feed probe and the first slot. One of the potential effects from a probe assembly is the presence of modes other than TE_{10}. To minimize any potential problems from moding that will alter the nearby slot conductances, a spacing distance of 3 guide-wavelengths from the probe to the first slot was part of the final LRR design shown in **Figure 9 [10, 16].**

In computing the necessary slot conductances it was somewhat fortunate that only two end-slots were outside the range of achievable values found in the derived curves of **Figures 5 and 6**. Such a limitation to the lowest value of resonant slot conductance can also be a restriction to maximum number of slots and overall length of the array.

7. Limitations and Future Work:

Some current investigations are attempting to better understand what influences the achievable range of slot conductances so compensations can be made when necessary. For example, the optimal slot width and waveguide wall thickness has been totally ignored by the literature but some experience using HFSS indicates they both very critical to slot performance. The Microwave Instrument Technology Branch at Goddard Space Flight Center is currently leading the design effort for a much more complicated edge-slot array operating at 36.5 GHz. Controlling the values for slot conductance has been a primary challenge driven by the requirement that the K_a-band array length must be 1.12 Meters; which is electrically much longer than the LRR X-band model that was at approximately 1 Meter. It has already been concluded that the nominal 40 Mil wall thickness of WR-22 must be reduced to 10 Mils to achieve any slot resonance at this higher frequency.

Larger array lengths inherently have narrower bandwidths, and this can lead to some interesting trade-offs when one considers the prospects of subdividing the array into sub-arrays. An HFSS analysis of the entire array of 184 slots has confirmed that for a maximum VSWR of 1.2:1, the bandwidth was approximately 20 MHz and fell short of the goal of 100 MHz. Breaking the antenna into two sub-arrays should offer some improvements; however implementing an external combiner network will add some complexity to the design. The simplest approach of using coaxial components is not an option because of the losses incurred. Center-feeding the antenna introduces the difficulty of disturbing slot performance near the feed probe assembly and the detrimental effect of sidelobes caused by simply removing them from the center of the array. Some complex arrangements of a waveguide feed network behind the array to feed each sub-array at the very ends seems to be most promising approach to ensure there is no gap between slots at the overall array center.

Looking ahead to the possibility of further subdividing the array into 4 sub-arrays presents some even greater engineering challenges. **Figure 14** is a plot of the conductance values necessary for a 25 dB, nBar=4 Taylor distribution applied over 4 sub-arrays using a power divider of equal amplitude and phase. The

unequal division of slots must be made to satisfy all the basic criteria for matching each sub-array design and the constraints defined by the taper including minimizing the discontinuity in conductance values between the middle and end sub-arrays. In this example, an overall array of 184 slots as shown in **Figure 14** would require a sub-array of 66 slots on each end; which may still be a large enough number to present some bandwidth issues. An alternative to this approach would be an unequal split in power that would allow the number of slots to be partitioned more evenly.

8. Conclusion:

The successful delivery of a low-cost, but very well-optimized antenna has proven that commercial computer tools have evolved to accurately predict the performance of edge-slot waveguide arrays. The knowledge gained from the LRR program has enabled some very accurate research that promises to improve passive microwave radiometry performance for an upcoming space-flight mission and should benefit edge-slot waveguide array technology in general.
The future of edge-slot technology seems very promising. A simple cut to form a slot through a piece of waveguide was at the threshold of technology during WWII, but there is reason for speculation that an evolution to more complex shapes and sizes could offer some performance improvements. The continued advances in computing power, Genetic Algorithm approaches [15], and commercially available software offer some interesting prospects.

9. Acknowledgment:

References

[1] C. Ruf, et al., "Lightweight Rainfall Radiometer STAR Aircraft Sensor", International Geoscience and Remote Sensing Symposium, 2002.IEEE, Volume: 2 , 2002.

[2] R. B. Gosselin, S. E. Seufert, L.R. Dod, "Design of a Resonant Edge-Slot Waveguide Array for the Lightweight Rainfall Radiometer (LRR)", International Geoscience and Remote Sensing Symposium, 2003.IEEE

[3] S. R. Rengarajan, ., L. G. Josefsson, , R. S. Elliott "Waveguide-fed Slot Antennas and Arrays: A Review", Electromagnetics, Vol. 19, No. 1, January/February, 1999.

[4] M. M. Brady, "Single Slotted-Waveguide Linear Arrays" in Advances in Microwaves, L. Young, ed. New York: Academic Press, 1971.

[5] W. H.Watson, "The Physical Principles of Waveguide Transmission and Antenna Systems", Oxford University Press, London and New York, 1947.

[6] H. G. Booker, "Slot Aerials", J. Inst. Elect. Eng., Part 3 **93**, 42 (1946).

[7] H. Y. Yee, R. C. Voges, "Slot-Antenna Arrays", Chapter 9 in Antenna Engineering Handbook, 3rd Edition, eds. R. C Johnson, H. Jasik, New York: McGraw Hill, Inc.

[8] R. S. Elliott, "The Design of Waveguide-Fed Slot Arrays', Chapter 12 in Antenna Handbook, eds. Y. T. Lo, S. W. Lee, New York, Van Nostrand Reinhold Company, Inc.

[9] R. C. Hansen, "Linear Arrays", Chapter 9 in The Handbook of Antenna Design, Volume 2, eds. A. W. Rudge, K. Milne, A. D. Olver, P. Knight, London, UK., Peter Peregrinus Ltd.

[10] M .J. Ehrlich, "Slot-Antenna Arrays", Chapter 9 in Antenna Engineering Handbook, 1st Edition, ed. H. Jasik, New York: McGraw Hill Book Co., Inc.

[11]   A. T. Villeneuve, "Taylor Patterns for Discrete Arrays", Antennas and Propagation, IEEE Transactions, Volume: 32 No. 10 , Oct 1984, Page(s): 1089 -1093.

[12]   S. Matsuda, T. Takeshima, and Y. Isogai, "Crosspolarized Radiation Beams of Slot Array Antennas", Elec. Commun. Jap. 47, 77-84 (1964).

[13]   D. M. Kerns and W. T. Grandy, "Pertubation Theorums for Waveguide Junctions, with Applications", IEEE Trans., Vol. MTT-14, No. 2. pp. 85-92 (February 1966).

[14]   M. M. Brady, "Tables of Constants for Standard Rectangular Waveguides" in Microwave engineers' handbook. Volume 1. Compiled and edited by T. S. Saad. Co-editors: R. C. Hansen [and] G. J. Wheeler, T. S Saad, ed., pp. 38-71, Dedham, Mass., Artech House [1971].

[15]   P. James, and S. J. Vetterlein, "A Wideband Resonant Slotted Waveguide Array for Space SAR Applications", NCAP 1998

[16]   M.C. Bailey, Private Communication, NASA Langley Research Center, 1996
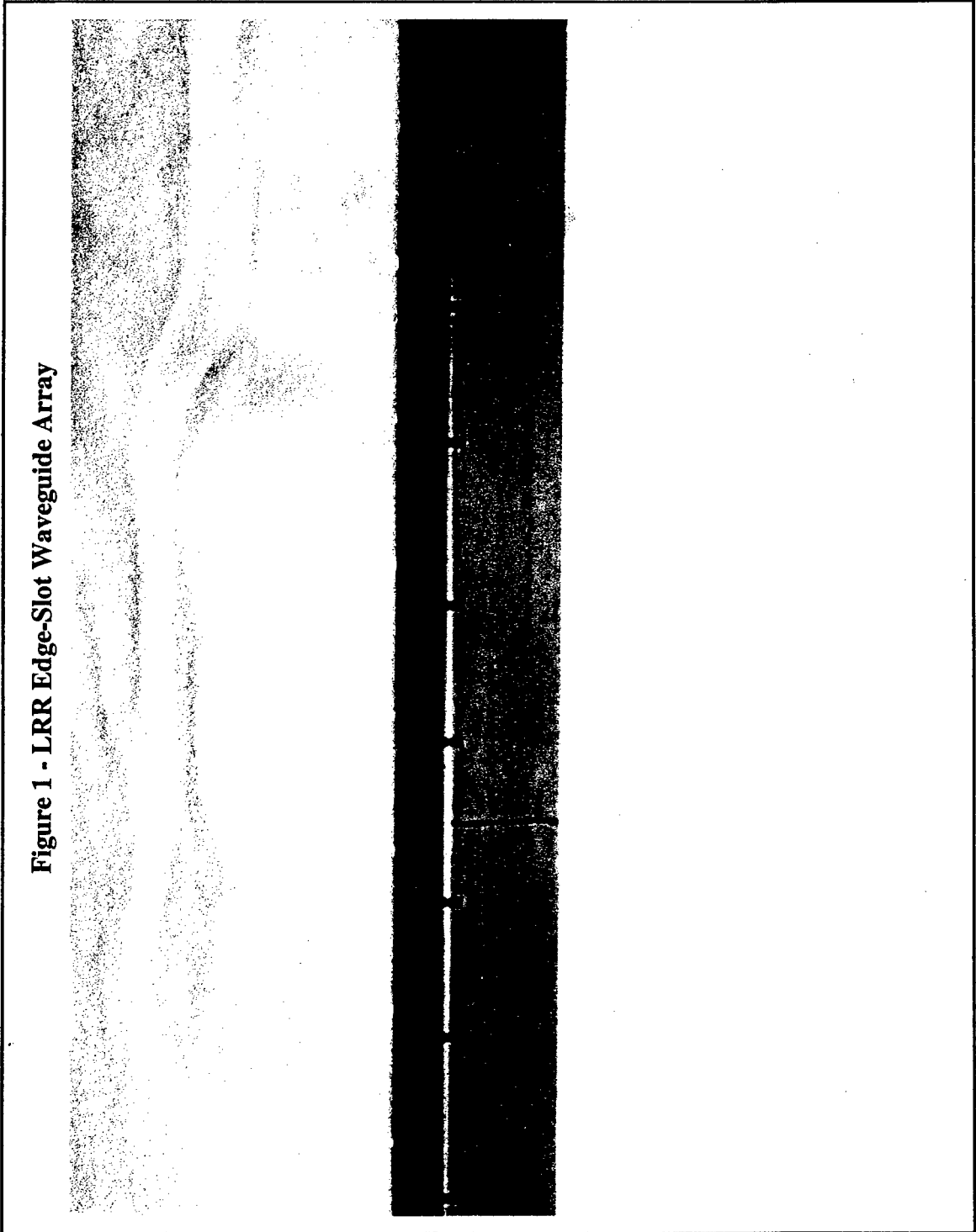
Figure 1 - LRR Edge-Slot Waveguide Array

Figure 2 - HFSS Graphic of Slot Radiation
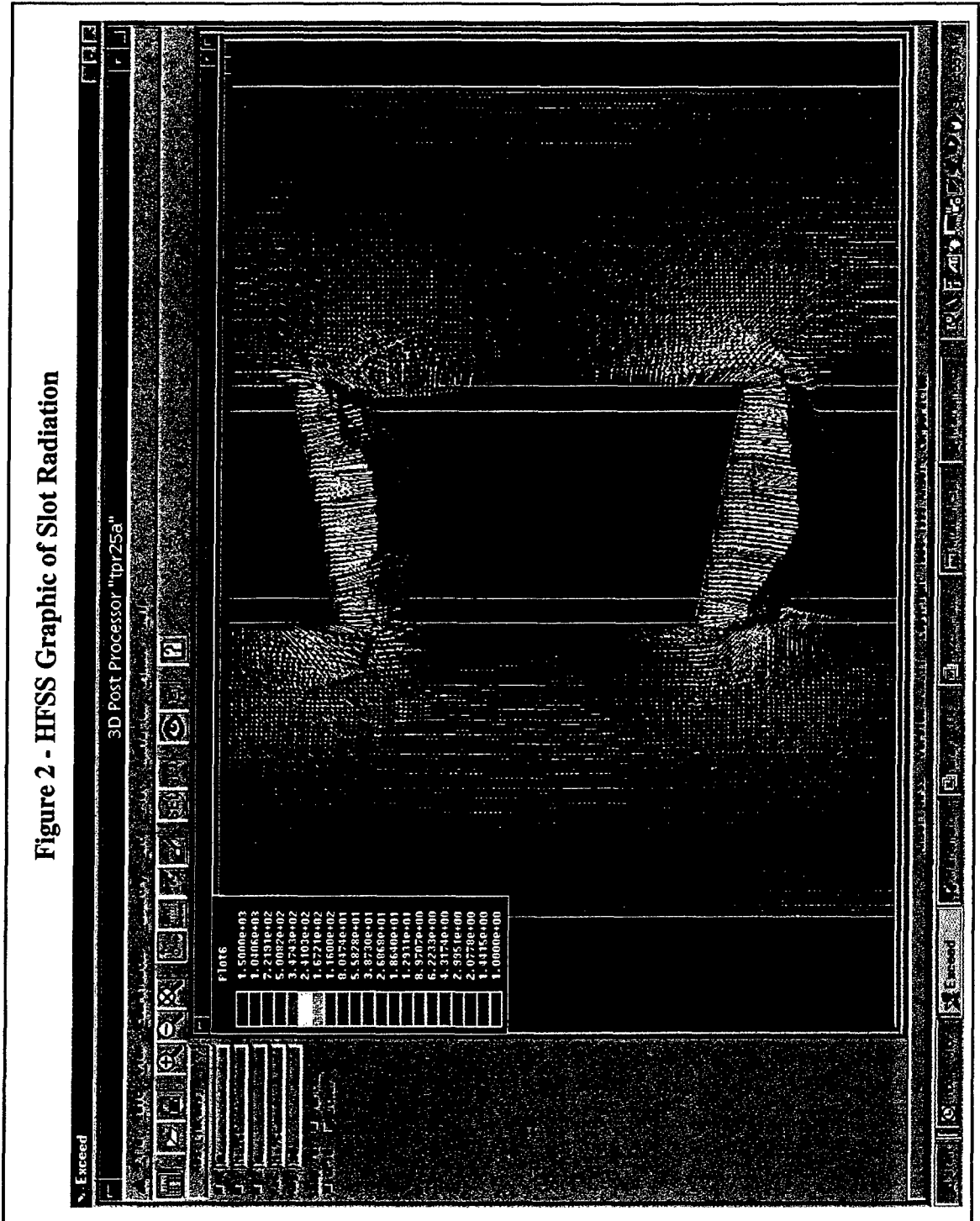
**Figure 3 – HFSS-generated Contour Plot showing internal E-field Alignment with Slots**

Contour Plot with cross-sectional view through center of narrow-walls. The radiation within slot openings are located at tips of arrows.
Arrows are drawn within HFSS-defined radiation boundary surrounding the waveguide.
Standing-wave energy inside waveguide is properly aligned to left of slot openings.

Figure 4 - Wire-line model of Slot Conductance in Parallel

80

Figure 5 - Normalized Resonant Slot Conductance vs. Angle
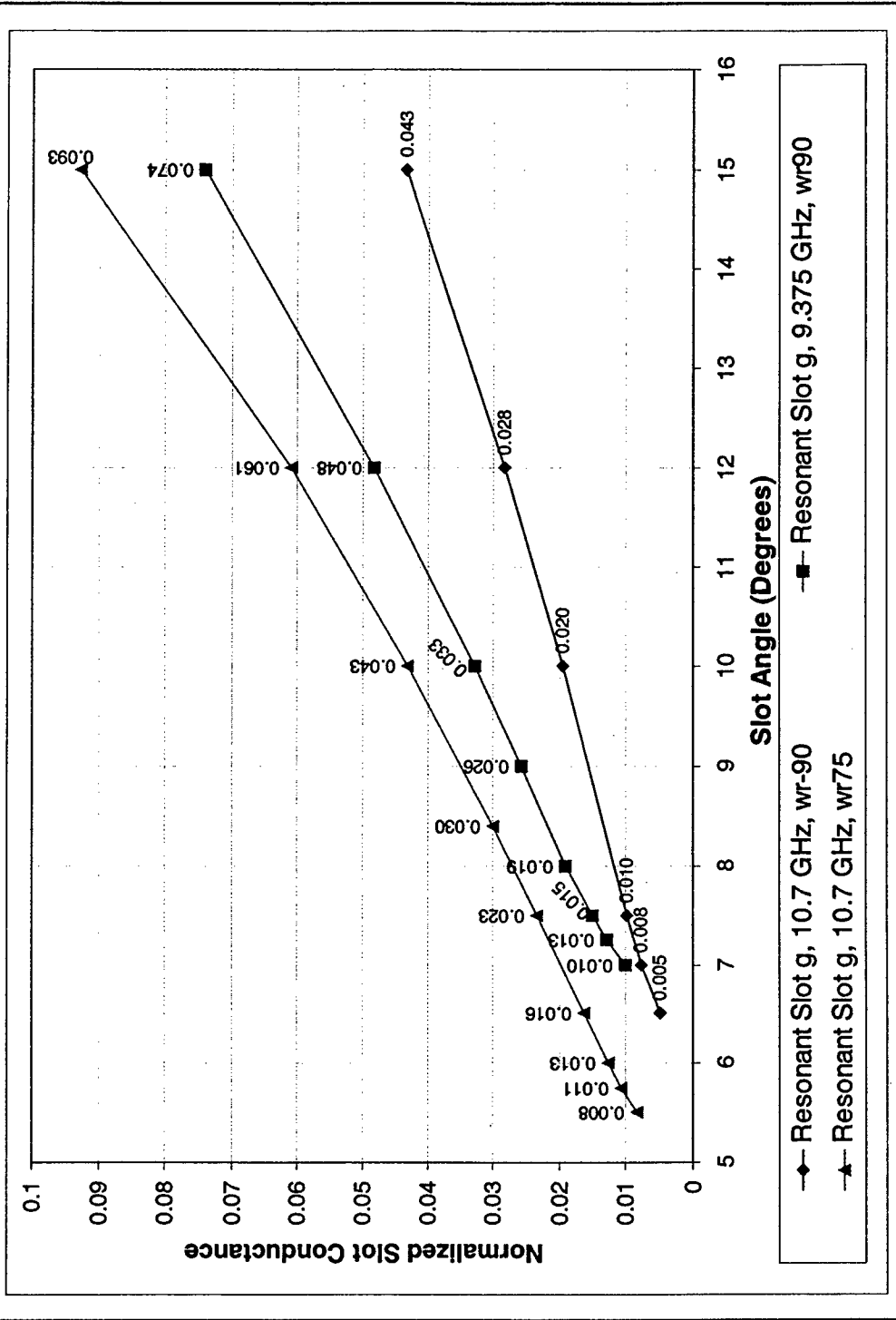
Figure 6 - Resonant Slot Depth vs. Angle

Resonant Slot Depths 10.7 GHz, wr-90
Resonant Slot Depths, 9.375GHz, wr90
Resonant Slot Depths 10.7 GHz, wr75

82
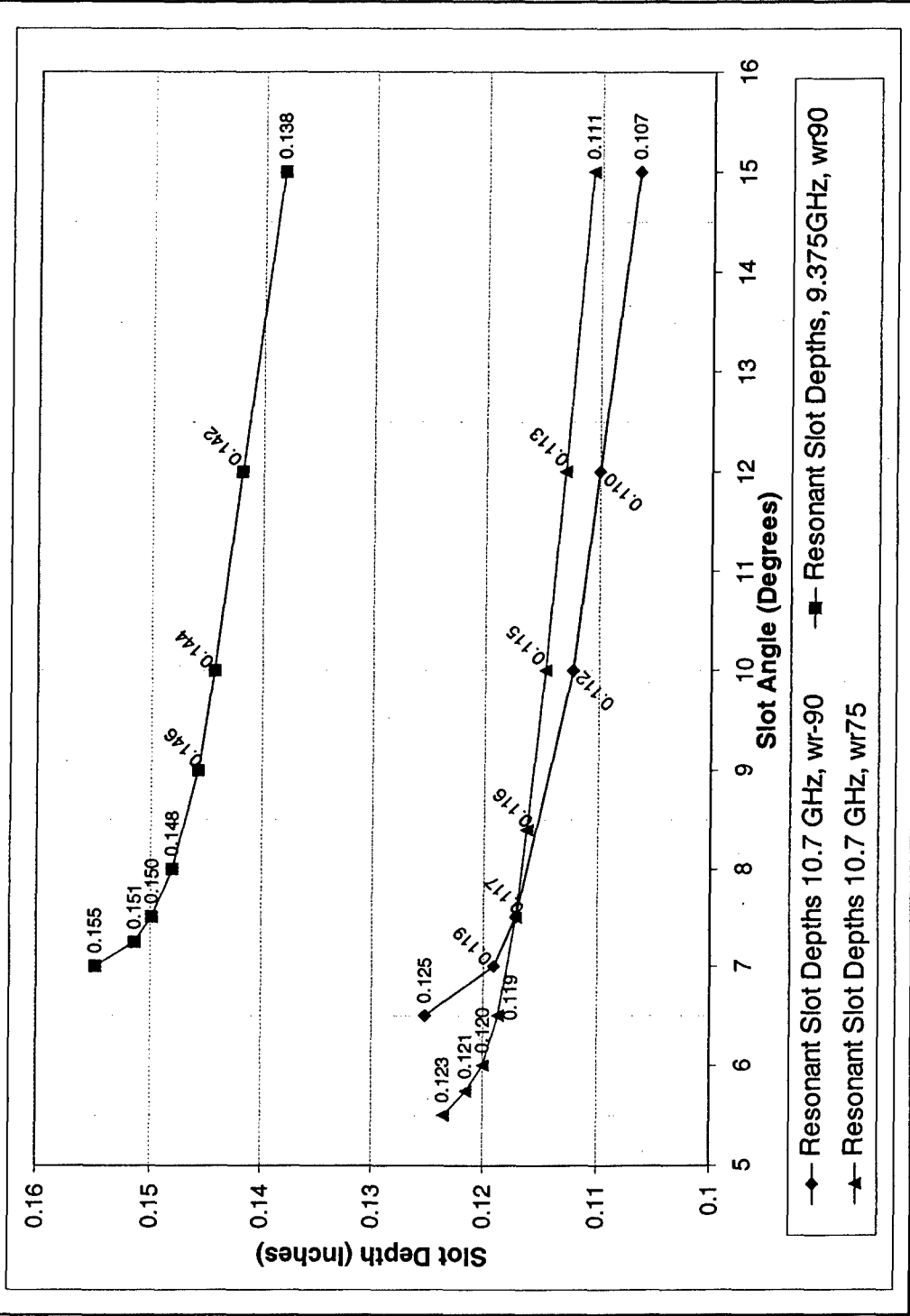
Figure 7 - Typical HFSS Model for LRR Development

- 36 Slots cut into wall of metal tube

- Radiation boundary surrounds tube and slots.

- Single feed Port defined at open end appears as infinitely long waveguide tube.
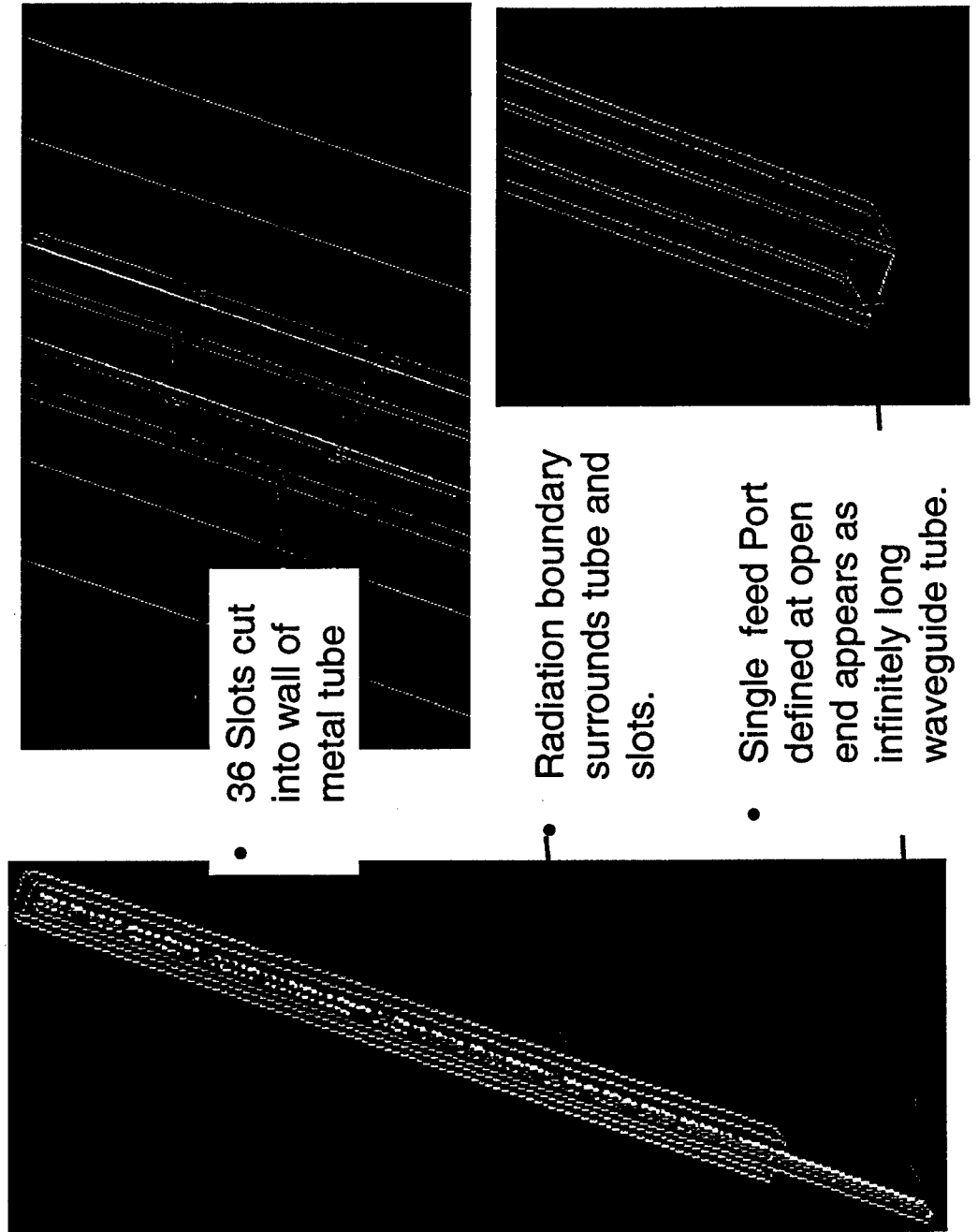
Figure 8 - HFSS Model Definitions

Slot depth is w.r.t. top outside of Narrow-wall

Slot Depth

Shorting Plate

$\lambda g/4$

Slot n

Slot Angle

Break

Slot 4

Slot 3

Slot 2

Slot 1

λg

$\lambda g/2$

HFSS PORT

- Waveguide Port definition for HFSS model was at $\lambda g/2$ from the first slot.

- HFSS simulates a perfect TE10 mode launched from an infinitely long waveguide.
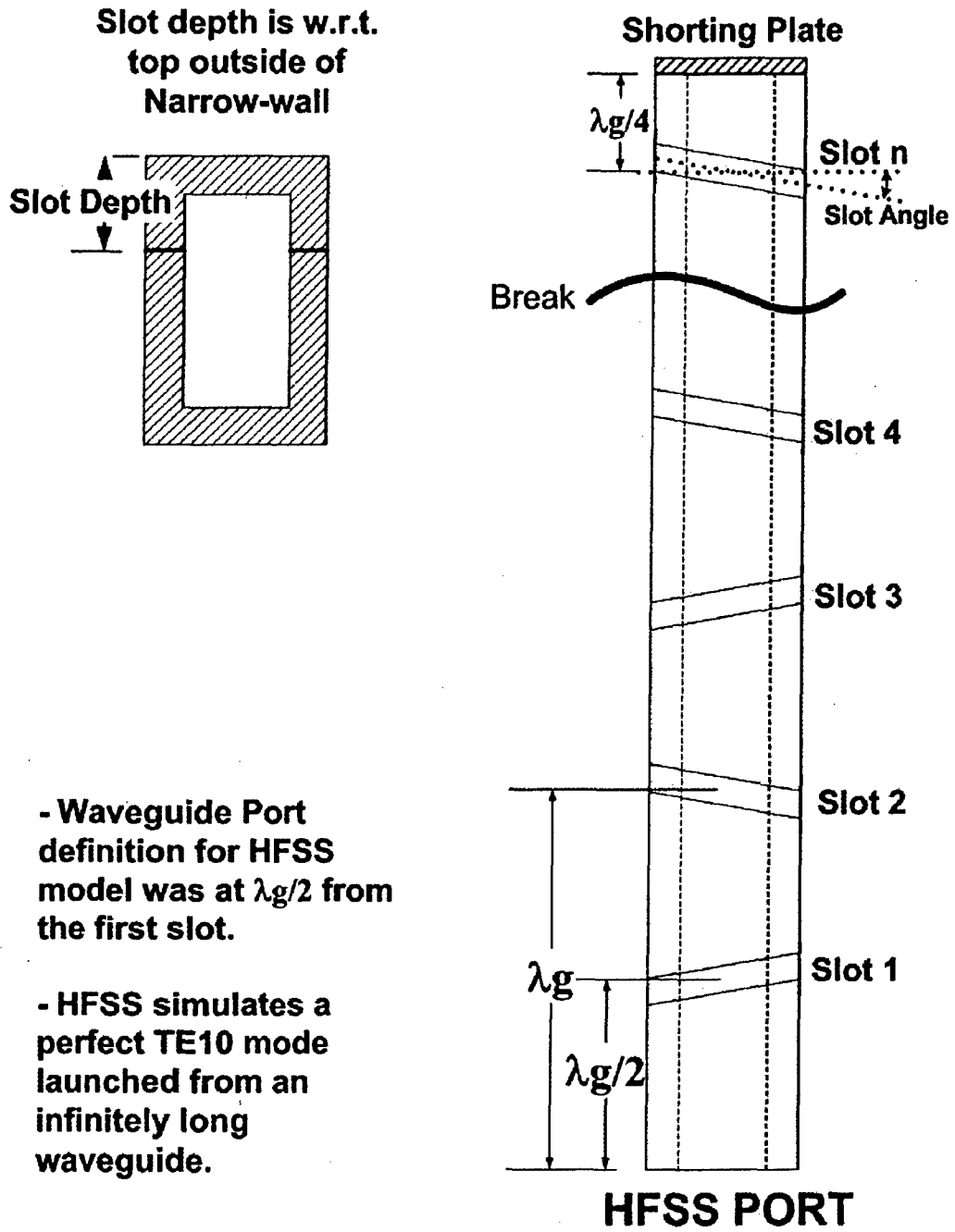
Figure 9 - Hardware Definitions

Shorting Plate

$\lambda g/4$

Slot n

Slot Angle

Break

Slot 4

Slot 3

Slot 2

$\lambda g/2$

Slot 1

Relative Dimensions of actual LRR Waveguide Array

$3\lambda g$

Voltage Probe Location

$\lambda g/4$

Shorting Plate
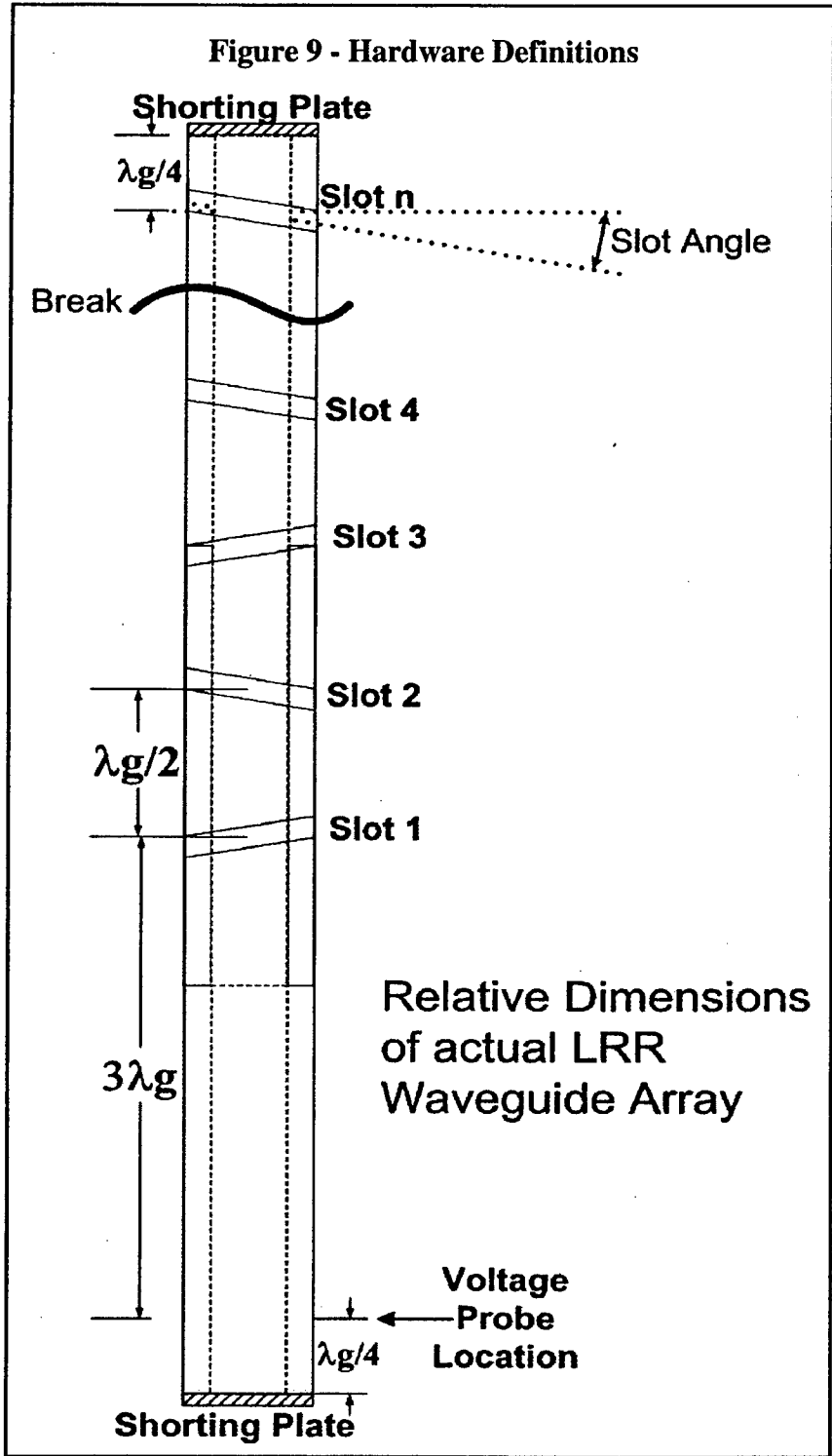
Figure 10 - Comparison of Watson's Slot Data with HFSS results

Comparison of Data from HFSS model with Watson's Published Data
WR-90 Waveguide, 9.375 GHz; Single Slot is 62.5 Mils Wide, 3.5 mm Deep

W.H. Watson's data from:
H.Y. Yee, R.C. Voges,
"Slot-Antenna Arrays", Chapter 9 in
Antenna Engineering Handbook, 3rd
Edition, eds. R.C. Johnson, H. Jasik,
New York: McGraw Hill, Inc.

Watson's Incremental Conductance
Watson's Ordinary Conductance
HFSS Data Single Slot Constant 3.5mm Deep
HFSS Resonant Uniform Arrays of 36 Slots,
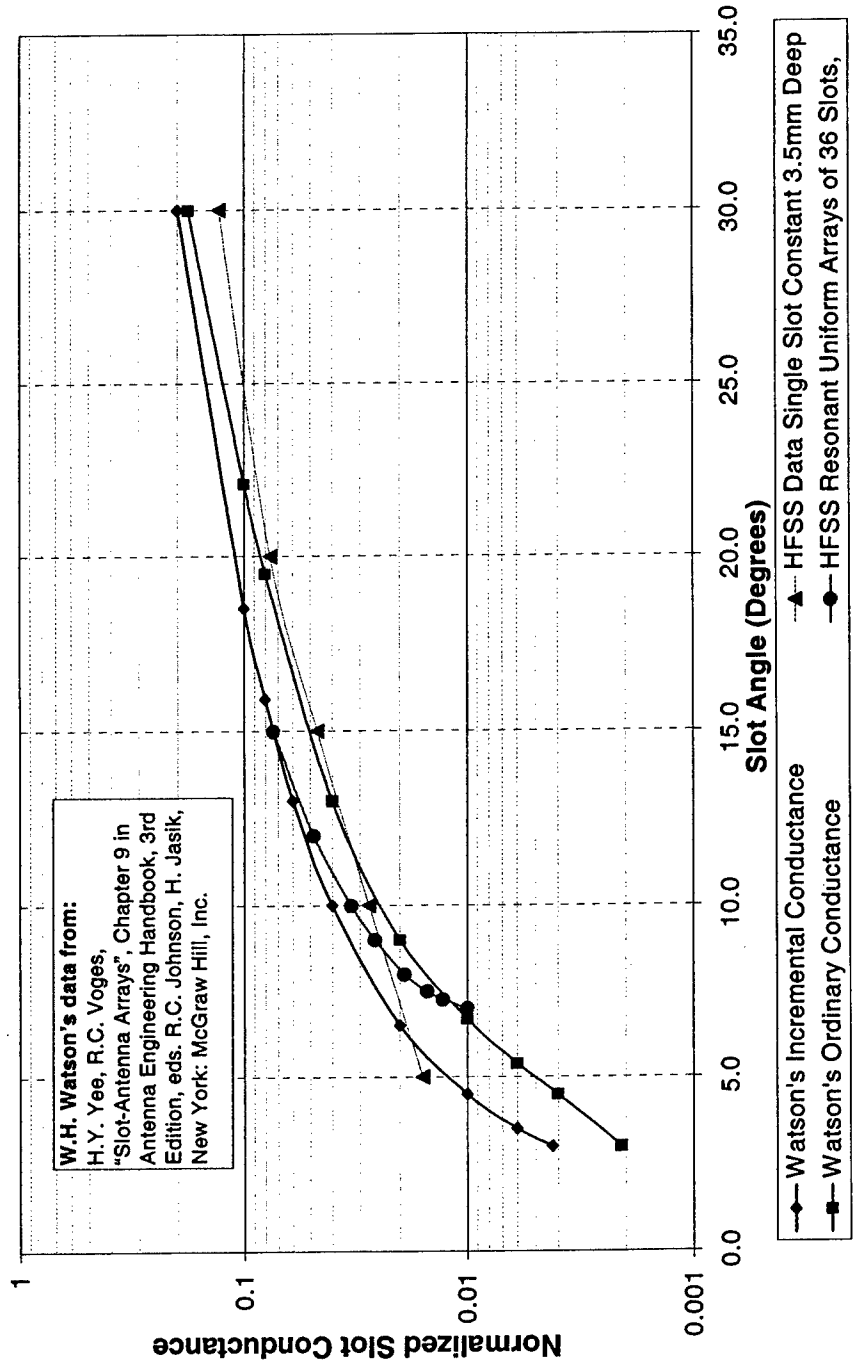
Typical measured VSWR for LRR waveguide array
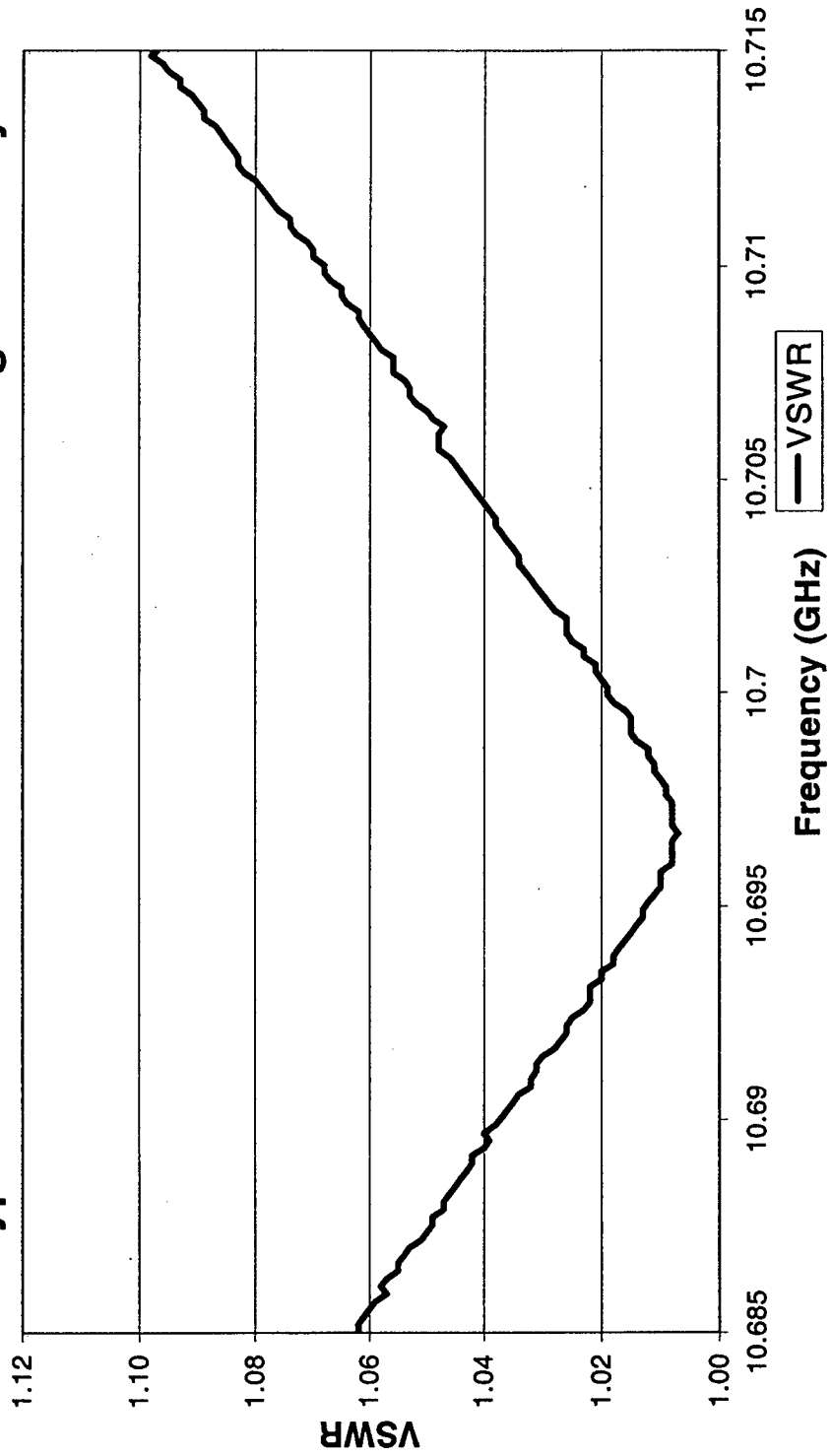
Figure 12 - Co-Polarized Pattern Comparison between HFSS and Measured

Peak Gain of Measured Is 21.5 dBi

Angle (degrees)

Linear Directivity (dB)

—— Measured Co-Pol ······ HFSS Co-Pol
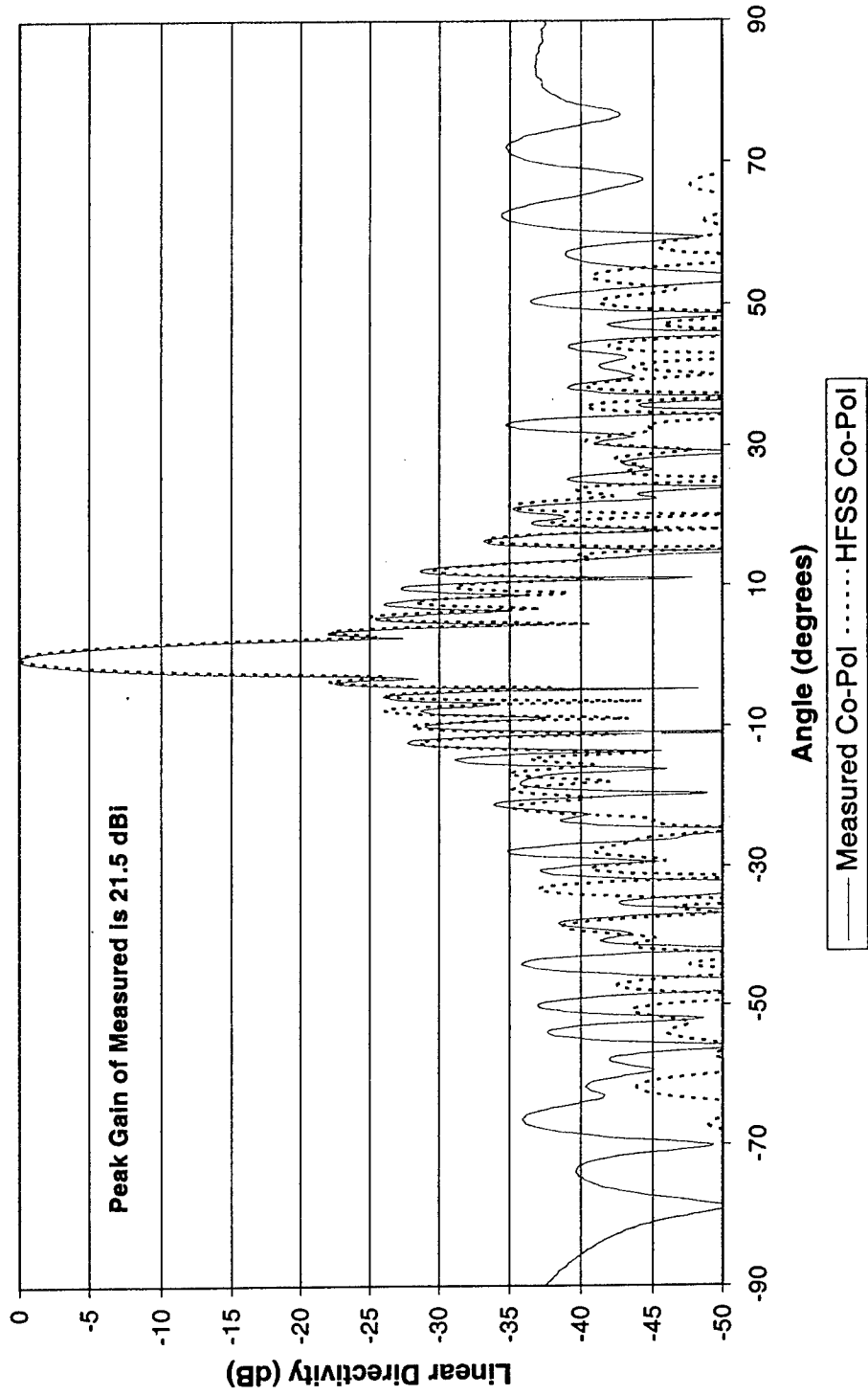
Figure 13 - Cross-Polarized Pattern Comparison between HFSS and Measured

——— Measured Cross-Pol ········· HFSS Cross-Pol

Angle (degrees)

Linear Directivity (dB from Peak of Beam)
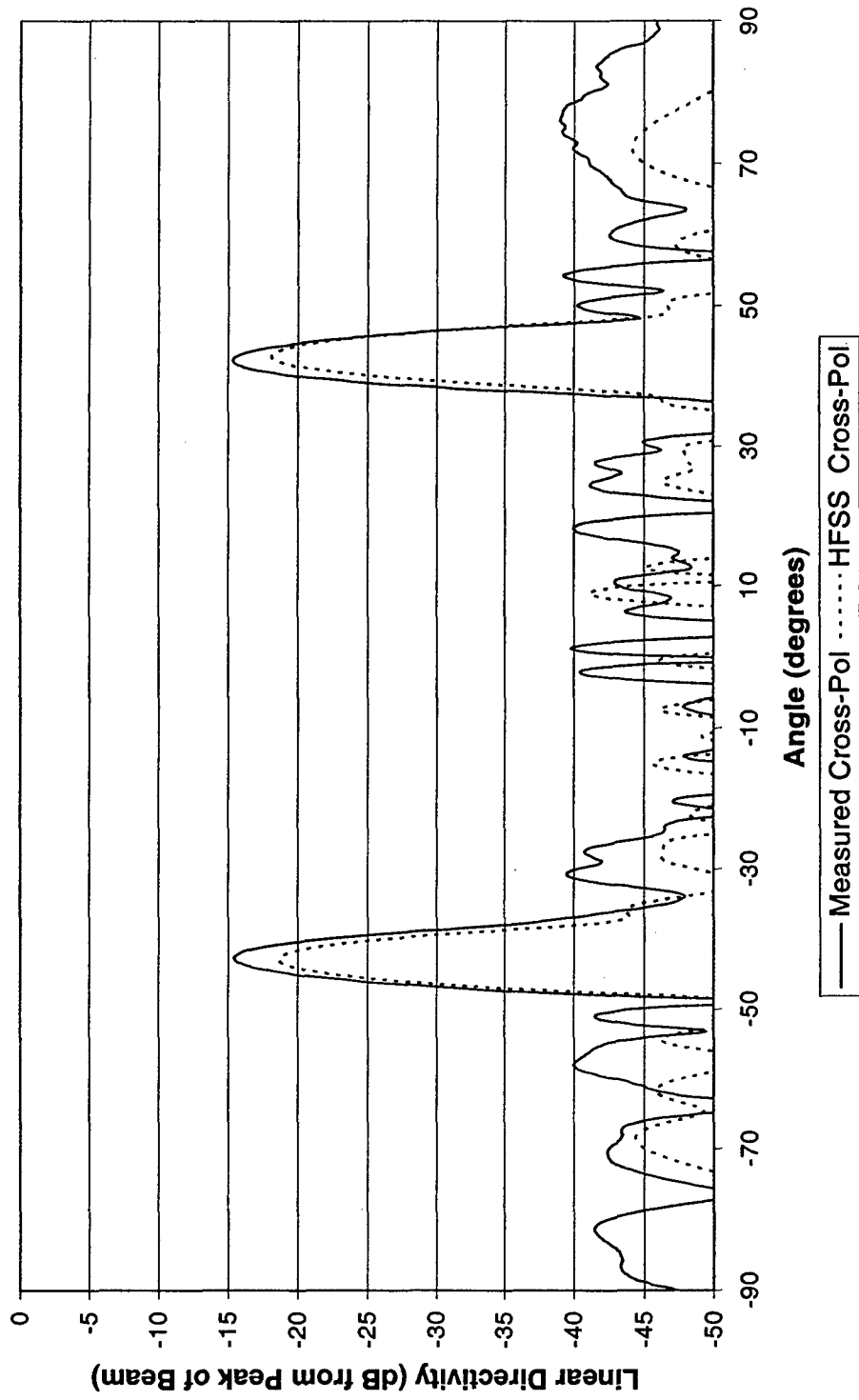
Figure 14 - Plot of Slot Conductance for Taper applied over 4 Sub-arrays using equal power division.
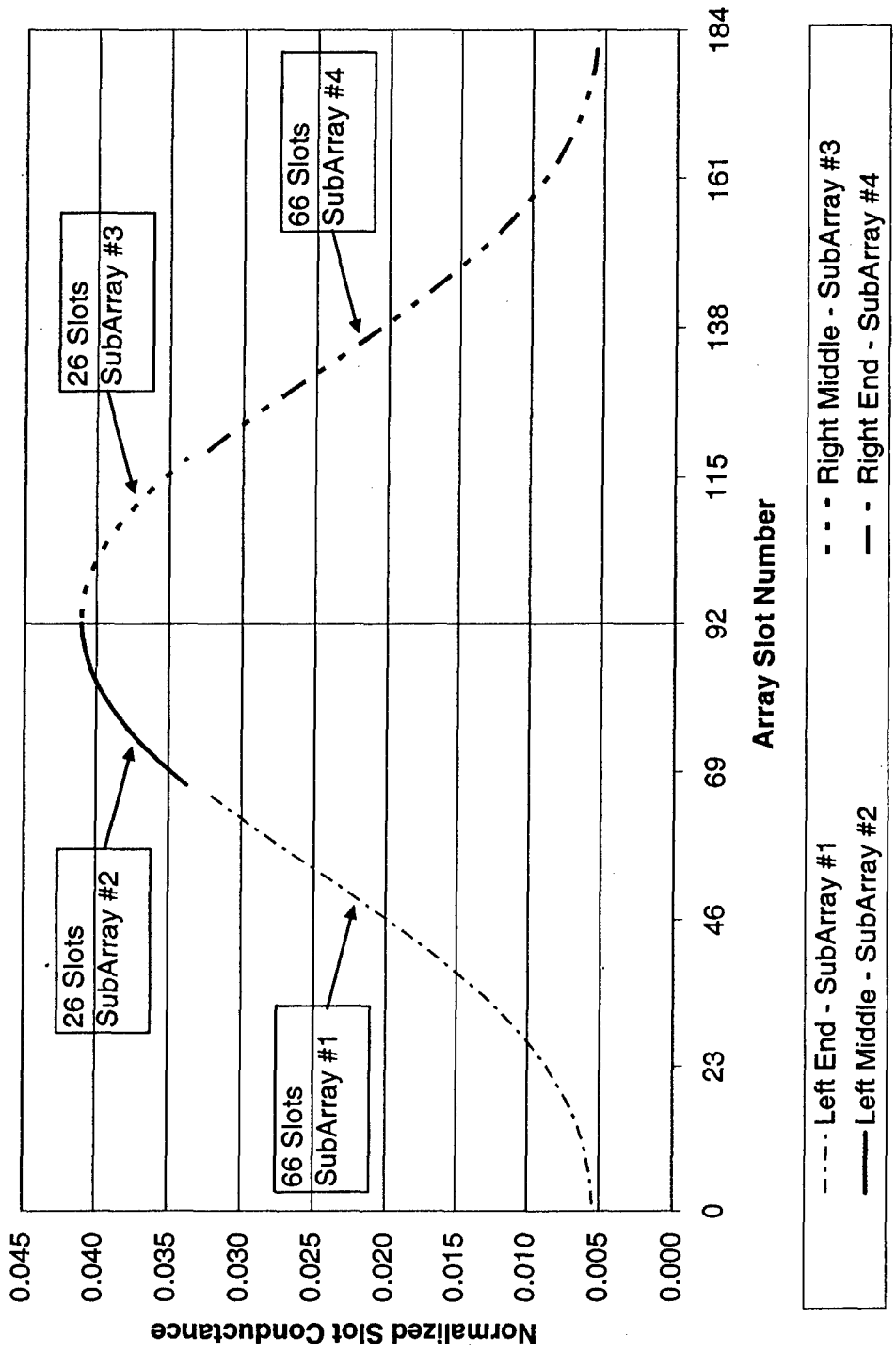
Table 1 Applying Villeneuve [11] Distribution for LRR 36-slot Array

Voltages from Analysis Data for 25 dB Taylor nbar=4	V**2 for 25 dB Taylor nbar=4	Normalized Slot Conductance g	Slot Angle Theta (degrees)	Slot Depth d (Inches)
0.370362	0.137168	0.007093694		#N/A
0.380648	0.1448929	0.007493189		#N/A
0.400971	0.1607777	0.00831468		0.12347
0.430809	0.1855964	0.009598185		0.12243
0.469316	0.2202575	0.011390698		0.12098
0.515286	0.2655197	0.013731446		0.11960
0.567139	0.3216466	0.016634074		0.11864
0.62297	0.3880916	0.0200703		0.11790
0.680637	0.4632667	0.023958008		0.11711
0.737919	0.5445245	0.028160281		0.11650
0.79268	0.6283416	0.032494915		0.11596
0.843048	0.7107299	0.036755658		0.11549
0.887542	0.7877308	0.040737786		0.11505
0.925143	0.8558896	0.044262642		0.11468
0.955281	0.9125618	0.047193467		0.11441
0.97776	0.9560146	0.049440645		0.11420
0.992621	0.9852964	0.050954966		0.11406
1	1	0.051715366		0.11399
1	1	0.051715366		0.11399
0.992621	0.9852964	0.050954966		0.11406
0.97776	0.9560146	0.049440645		0.11420
0.955281	0.9125618	0.047193467		0.11441
0.925143	0.8558896	0.044262642		0.11468
0.887542	0.7877308	0.040737786		0.11505
0.843048	0.7107299	0.036755658		0.11549
0.79268	0.6283416	0.032494915		0.11596
0.737919	0.5445245	0.028160281		0.11650
0.680637	0.4632667	0.023958008		0.11711
0.62297	0.3880916	0.0200703		0.11790
0.567139	0.3216466	0.016634074		0.11864
0.515286	0.2655197	0.013731446		0.11960
0.469316	0.2202575	0.011390698		0.12098
0.430809	0.1855964	0.009598185		0.12243
0.400971	0.1607777	0.00831468		0.12347
0.380648	0.1448929	0.007493189		#N/A
0.370362	0.137168	0.007093694		#N/A
Sums	9.336618			

NEW VARIABLE FOR FRESNEL ZONE PLATE ANTENNAS

G. W. Webb
Institute for Pure and Applied Physical Sciences,
University of California, San Diego
San Diego, CA 92093

Abstract - I present experimental results and analysis on the application of a new variable in the design of zone plate antennas. This variable is the choice of phase reference used in the definition of the Fresnel zones from which zone plates are constructed. The standard zone plate construction assumes a specific choice for this reference phase which, however, can be chosen to have any value between 0° and 360°. When the reference phase is varied, antenna pattern measurements reveal small systematic changes in the main lobe gain accompanied by large improvements in the overall sidelobe level and position in both the E- and H-planes. Measurements also show that through variation of the reference phase, the phase of the main lobe can be varied controllably through 360°. I conclude that reference phase is a useful new tool available to the zone plate antenna designer.

1. Introduction

Fresnel zone plates are a type of diffractive antenna. The concept of a focusing zone plate grew out of Fresnel's analysis of the diffraction of radiation through an aperture [1,2]. Fresnel analyzed radiation emitted from a source which passed through an aperture and arrived at a detection point. He called attention to zones in the aperture of constructively and destructively interfering radiation at the detection point. In defining these zones of constructive and destructive radiation, he assigned a specific phase origin or reference phase of 0° to *the shortest ray* connecting the source and detection point in order to simplify the analysis. Based on Fresnel's analysis, Soret later demonstrated focusing in half opaque zone plates which blocked radiation from what was defined as the destructively interfering zones [3]; the same choice of phase origin as Fresnel was used. Later work has shown that the out-of-phase zones need not be blocked if selective phase shifts are introduced into the zone plate [2,4,5]. However the same special choice of phase origin as Fresnel has been made.

Here we consider varying the reference phase in zone plates. The choice of phase reference in Fresnel zone construction does not of course affect the

diffractive properties of the aperture. However when zone plates for the aperture are made using the Fresnel zone construction, then their resultant diffracted beams depend on the choice of phase reference. In this work [6] we examine the effect of variable reference phase on beam amplitude, beam phase, and antenna pattern.

2. Reference Phase

Fig. 1a shows rays from a source (S) which pass through an aperture (A) in an opaque screen to a detection point (P). Time dependence is suppressed. The rays have a phase at P which depends on the positions of S and of P, the distance between them, and on the point where they went through the aperture. The path length of the *shortest ray* connecting S and P, sometimes called the direct ray, is $R=f+h$. Historically the phase of a general ray with path length $r=r1+r2$ has been computed by subtracting R from r, implicitly assuming that the distance R of the shortest ray defines the phase origin $\theta_{ref}=0°$ or reference phase. All rays with phase in the range $-90°<phase<90°$ are defined as constructive and a zone plate of the blocking type is designed to block all rays whose phase fall outside this range.

We use a definition of phase generalized to include θ_{ref} explicitly

$$\text{phase} = (r1 + r2 - R)\frac{360°}{\lambda} - \theta_{ref} \qquad (1)$$

where λ is the wave length. Fig.1b assumes the usual choice $\theta_{ref}=0°$ and shows the relative phase at P of rays plotted with a gray scale on the plane of the aperture at the point where the ray passed through the aperture. If, however, a different reference phase is chosen, for example $\theta_{ref}=60°$ in Fig. 1c, then the relative phase distribution across the aperture is changed [7].

Fig. 1d displays the sine of the phase plotted vs. radius for the two choices $\theta_{ref}=0°$ and $\theta_{ref}=60°$; $0<\sin(phase)<1$ corresponds to gray to white, while $-1<\sin(phase)<0$ corresponds to black to gray in Figs.1b,c. All $\sin(phase)>0$ rays can be taken as in-phase and $\sin(phase)<0$ rays as out-of-phase. As before, a zone plate is designed to have a geometry that blocks the out-of-phase rays at P so that the only rays arriving are in-phase and thus a beam of radiation is focused. It is evident that changing the reference phase re-defines which rays in the aperture will be in constructive interference at P.

3. Model Analysis

For analysis we assume the specific set of parameters for wavelength, S, A, and P as in Fig. 1, but allow θ_{ref} to vary. The same analysis applies, however,

to other parameter values and to the usual types of phase correcting zone plates without loss of generality. The resultant zone plate constructions are displayed in Fig. 2 and are shown numbered ZP=0-11 (ZP#) with corresponding θ_{ref}=0°-330° in increments of 30°. It can be seen that zone plate features change smoothly with ZP#, or θ_{ref}. This choice of parameters gives an equal number of in-phase and out-of-phase zones for θ_{ref}=0° so that the total area of in-phase zones does not change significantly as θ_{ref} is varied. In this context note that in the series ZP0-5, as the center constructive zone becomes progressively more destructive, the outermost destructive zone becomes increasingly more constructive.

The amplitude $|U_{calc}|$ and phase θ_{calc} of the focused radiation at P can be calculated in the scalar approximation of Fresnel - Kirchhoff [8]:

$$U_P = -\frac{ike^{-i\omega t}}{4\pi} \iint_A U_0 \frac{e^{ik(r1+r2)}}{r1r2}[\cos(n,r1)-\cos(n,r2)]dA \qquad (2)$$

U_P is the "optical disturbance" at P, n is the normal to the aperture, and the other quantities have the same meaning as Fig. 1a. Eq. 2 was first solved for ZP=0-11 assuming a constant (uniform) feed pattern, U_0, for simplicity. The results $|U_{calc}|$ and θ_{calc} are plotted in Fig. 3 as a function of ZP# and its corresponding θ_{ref}. Time dependence is suppressed. Note that $|U_{calc}|$ is nearly constant across ZP0-11 while θ_{calc} varies nearly linearly with ZP# and θ_{ref}.

4. Experimental Details

A set of experimental zone plates was fabricated to fulfill the conditions of Fig.2. They consisted of 15μ (ca) thick copper rings on a low-loss dielectric substrate of 168μ thickness [9]. They were fabricated using printed circuit board materials and techniques. These zone plates were attached to flat, low-loss, low refractive index dielectric foam substrates of 6.3mm thickness. Fabrication techniques and materials were the same for all zone plates.

The experimental zone plates were measured in the apparatus shown schematically in Fig. 4a,b. The feed (F) is an open ended waveguide positioned behind the zone plate at the design focusing point. The power P_{beam} reaching the detector (D) was measured for each zone plate under identical conditions in Fig.4a. Beam amplitude, $|U|$, was defined through $P_{beam}=|U|^2$. For pattern measurements, the zone plate and feed assembly were rotated with respect to the source. Beam phase was measured with the apparatus in Fig. 4b.

5. Measured Beam Phase and Amplitude vs. θ_{ref} and Comparison with Model

Fig. 5 displays measured beam amplitude data |U| for ZP0-11 as points. The feed pattern of F was determined in an independent measurement of F and parameterized; this parameterized function was included as U_0 in the calculation of Eq.2. The solid line shows resultant calculated values for |U|. Note that the calculation qualitatively reproduces the magnitude of the overall variation across ZP0-11 (about 1.7dB in power), the existence of a slight maximum in amplitude for ZP=11, and the minimum near ZP=6.

The phase of the focused beam for ZP0-11 was measured with the phase apparatus of Fig. 4b. These measured beam phase data, θ_{beam}, are plotted vs. θ_{ref} as points in Fig.6 for comparison. The measured phase data are plotted relative to that of ZP0. The calculated phase of the focused beam was also determined from Eq. 2 using the parameterized feed function and is shown in Fig. 6 by the solid line. The calculated phase data are also plotted relative to ZP0. Note that measured and calculated phases both vary close to linearly with θ_{ref}. It is evident that the choice of θ_{ref} in the design of a zone plate allows the beam phase to be varied over a full $360°$.

6. Measured Antenna Patterns vs. θ_{ref}

Antenna patterns for ZP0-11 were also measured by mounting the antenna zone plate and receiver feed assembly on a rotation stage that could be turned relative to the transmit horn. The patterns obtained by rotating the antenna in the H-plane are shown in Figure 7a and for rotation in the E-plane in Figure 7b. The value of θ_{ref} for the particular zone plate is shown in the upper right corner of each panel. (The slight asymmetry at low power in some panels is thought to be due to the experimental setup rather be of fundamental significance.) It is seen that as θ_{ref} is varied from $0°$ through $330°$ the patterns change smoothly and systematically. It is also evident that the magnitude and position of the maximum side lobe varies with θ_{ref}. A model calculation of antenna pattern has not yet been carried out.

The antenna pattern results are summarized in Figure 8 where plots are displayed for the peak to side lobe ratio (PSL) in dB vs. θ_{ref} in the two cardinal planes. It is seen that the variation of PSL with θ_{ref} tracks approximately for the two directions. It is interesting that the PSL is maximized for the non-standard value of $\theta_{ref}=60°$ and exceeds that of the standard value for a range of θ_{ref}.

7. Discussion and Conclusions

This work[*] has shown that reference phase θ_{ref}, relative to the direct ray, is an intrinsic and useful property of a Fresnel zone plate. It was seen that changing the reference phase re-defines which set of rays in the aperture will be in constructive interference later. This also has the important property that it controls

the path length through constructive zones in the zone plate and thus the phase of the focused beam. In particular, the beam phase θ_{beam}, varies close to linearly with θ_{ref}. It is inferred that the small deviations from the predicted almost-linear relationship between θ_{beam} and θ_{ref} of a zone plate arise here primarily from a departure of the feed function from uniform. Conversely, it has been shown that the design choice for θ_{ref} from $0°$ to $330°$ does not strongly affect the amplitude of the focused beam; it is inferred that the small variations in amplitude that are observed are also due primarily to the feed function. A main conclusion is that the choice of θ_{ref} provides a full $360°$ control over beam phase with only minor variation in beam amplitude.

It has been shown that the antenna angular patterns are functions of θ_{ref} and that the peak to sidelobe ratio can be optimized for selected values of θ_{ref}. It is not known yet if other feed functions would require different values of θ_{ref} for optimum PSL. It is of potential interest that the position and depth of nulls of an antenna pattern might be controlled through θ_{ref}. If the geometry of the zone plate can varied in real-time [10,11] then the phase of the focused beam and the antenna pattern can also be controlled in real-time.

Finally, since Fresnel zone plates can exist in a variety of arbitrarily curved shapes [2] as well as planar, it seems likely that the phase of focused beams diffracted from arbitrarily curved shapes can also be controlled through the reference phase.

* Note added in proof – Another work [I.V. Minin and O.V. Minin, Sov. J. Quantum Electron. 20, 198 (1990)] treats the radius of the central zone, called "reference radius", as a free parameter. Reference radius is closely related to our reference phase. They investigated the effect of varying the reference radius numerically. I thank I.V. Minin for calling this paper to my attention.

References

[1] A. Fresnel, "CALCUL DE L'INTENSITE DE LA LUMIERE AU CENTRE DE L'OMBRE D'UN ECRAN ET D'UNE OUVERTURE CIRCULARAIRES ECLAIRES PAR UN POINT RADIEUX," Oeuvres d'Augustin Fresnel, Vol. 1, Note 1, pp.365-372 (1866). Reprinted in J. Ojeda-Castanada and C. Gomez-Reino, Selected Papers on ZONE PLATES, SPIE Milestone Series VOL. MS 128 (1996).

[2] J. Ojeda-Castanada and C. Gomez-Reino, *ibid*. This work also contains extensive references to zone plate literature.

[3] J.L. Soret, "Ueber die durch Kreisgitter erzeugten Diffractionsphanomene," Annalen der Physic und Chemie, Vol. 156, pp. 99-113 (1875). Reprinted in J. Ojeda-Castanada and C. Gomez-Reino, *ibid*. Soret also demonstrated the existence of focusing by blocking the "constructive" zones instead of the "destructive" ones.

[4] Lord Rayleigh, reprinted in Lord Rayleigh Scientific Papers, Vol. 3, pp. 74-79 (1887-1892). R.W. Wood, "Phase Reversal Zone Plates and Diffraction Telescope," Phil. Mag. Series 5, Vol.45, 511 (1898).

[5] H.D. Hristov, Fresnel Zones in wireless links, zone plate lenses, and antennas, Artech House Boston, 2000 contains extensive references to zone plate literature. Also see J.C. Wiltse, "History and Evolution of Fresnel Zone Plate Antennas for Microwaves and Millimeter Waves," IEEE Antennas and Propagation Int. Symp. 1999, Special Section "Status and Future of Fresnel Zone Plate Antennas," Orlando FL, July 11-16, 1999, Symp. Digest Vol. 2, pp. 722-725.

[6] See also G.W. Webb, "Reference Phase of Fresnel Zone Plates," arXiv:physics/0303002 28 Feb 2003 and G.W. Webb, to be published.

[7] It is a trivial alternative to leave the definition of phase of the direct ray as $0°$ and re-define the phase interval for constructive interference, however nothing new is gained.

[8] G.R. Fowles, Introduction to Modern Optics, 2nd Ed. Dover Publ. New York, 1975.

[9] Rogers RO4350B 5E/5E 6.6mil ½ oz Cu. Rohacell polymethacrylimide foam.

[10] G.W. Webb, S.C. Rose, M.S Sanchez, J.M. Osterwalder, "Experiments on an Optically Controlled 2-D Scanning Antenna," 1998 Antenna Applications Symposium, Allerton Park, Monticello, IL, September 16-18, 1998, p. 99.

[11] G.W. Webb, S. Angello, W. Vernon, M.S. Sanchez, and S.C. Rose, "Novel Photonically Controlled Antenna for MMW Communications," Proc. Int. Topical Meeting on Microwave Photonics MWP2000, Oxford UK, September 11-13, 2000, p. 97.

Figure Captions

Fig. 1. a) Schematic of rays which leave source (S) pass through circular aperture (A) in opaque screen (SC) and arrive at detection point (P), not to scale. S, A, and P are co-axial. $R=f+h$ is the shortest path length between S and P. Path length R defines what is sometimes called the direct ray. Path length of a general ray is $r=r1+r2$; b) Example gray scale plot of phase at P of rays going through different parts of the aperture with reference phase $\theta_{ref}=0°$ and c) $\theta_{ref}=60°$; d) Sine of the phase from Eq. 1 for $\theta_{ref}=0°$ (solid) and $\theta_{ref}=60°$ (dots) plotted along a radius from center to edge of aperture. $0<\sin(\text{phase})<1$ corresponds to gray to white and $-1<\sin(\text{phase})<0$ corresponds to black to gray in b,c. Specific parameters used here and below are: Frequency $\nu=39\text{GHz}$, $f=7.04\text{cm}$, aperture radius=7.91cm, and $R=3.05\text{m}$.

Fig. 2. Zone plates ZP=0, 1, 2, …11, corresponding to reference ray choice of $\theta_{ref}=0°$, 30°, 60°, …330°, as indicated and to scale. Specific parameters are those of Fig. 1. Transparent zones are shown as white and opaque zones as black. The set ZP=0-5 and ZP=6-11 are mirror images of each other which differ in θ_{ref} by 180°. ZP=0 and its inverse ZP=6 correspond qualitatively to the two used by Soret.

Fig. 3. Calculated amplitude $|U_{calc}|$ from Eq. 2 (diamonds) and resultant phase, θ_{calc}, (squares) for ZP0-11. Amplitude and phase results are plotted relative to ZP0. The solid line is a guide for the eye and the dashed line is a straight line connecting 0° to 360°. $|U_{calc}|$ and θ_{calc} are plotted vs. ZP# and corresponding reference phase θ_{ref}.

Fig. 4. Schematic of apparatus (not to scale) to measure (a) amplitude and (b) phase. Source S emits linearly polarized 39GHz radiation through horn (H_1), zone plate (ZP) focuses incident radiation on feed (F); distance from H_1 to F is the same in both a) and b). The phase apparatus in 4b has arms defined, by F and horn H2, which are connected by a -10dB directional coupler (DC). Relative amplitude between arms is adjusted by attenuator (A) and relative phase (θ) by translating horn H2 toward H1under micrometer control. Interferometer of (b) is nulled through the relative phase adjustment (θ) in upper arm and attenuator (A) adjustment in lower arm. In these measurements, ZP=0 was mounted first and θ and A adjusted for null; θ was adjusted by the position of H2. The change in the null position of H2 from ZP0 was converted to phase for ZP1-11 using the known wavelength.

Fig. 5. Focused beam amplitude |U| as a function of θ_{ref}. Points are measured data and solid line is calculated from Eq. 2 using measured feed function. The dashed line shows the calculated results with a uniform feed function for comparison.

Fig. 6. Focused beam phase vs. reference phase θ_{ref} for the set ZP0-11 relative to ZP0. Points are measured data with the apparatus of Fig. 4b and the solid line is the calculated phase from Eq. 2 with the same feed function of Fig. 5

Fig. 7. Power (dBm) vs. angle (degrees) a) H-plane antenna pattern; b) E-plane antenna pattern. The value of θ_{ref} in degrees for the zone plate is shown in the upper right corner of each panel.

Fig. 8. Peak to side lobe ratio (PSL) for H-plane (diamonds) and E-plane (squares) scans. Note that the optimum PSL occurs for the non-standard value of $\theta_{ref} = 60°$.

a)

SC

r1   r2

S   h   A   f   P

b) $\theta_{ref}=0^{o}$ **c) $\theta_{ref}=60^{o}$**

d) Sine of phase vs. radius (cm)

$\sin(\phi 0(r))$

$\sin(\phi 60(r))$
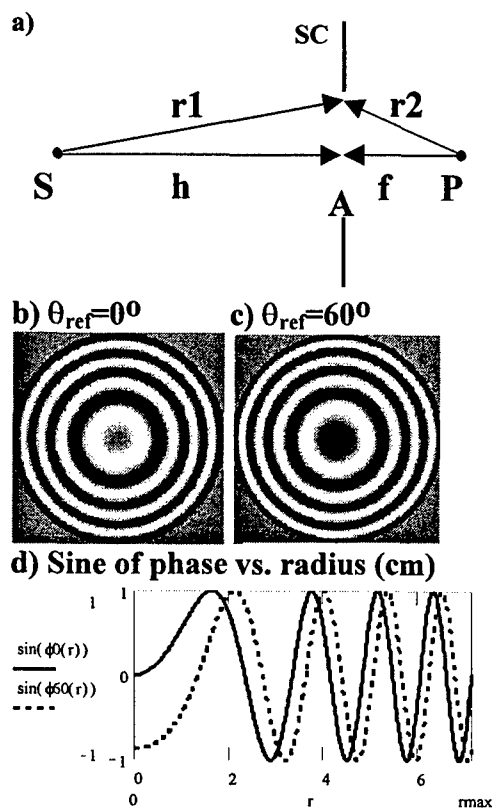
Fig. 1.
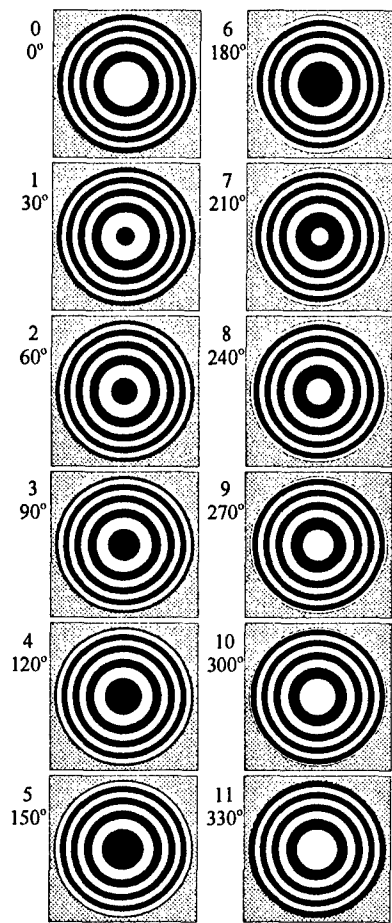
Fig. 2.
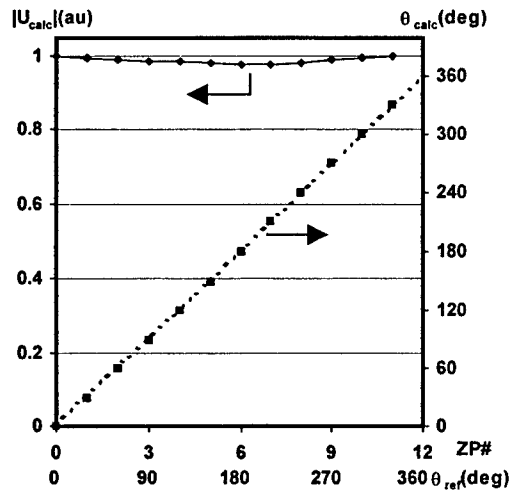
Fig. 3.
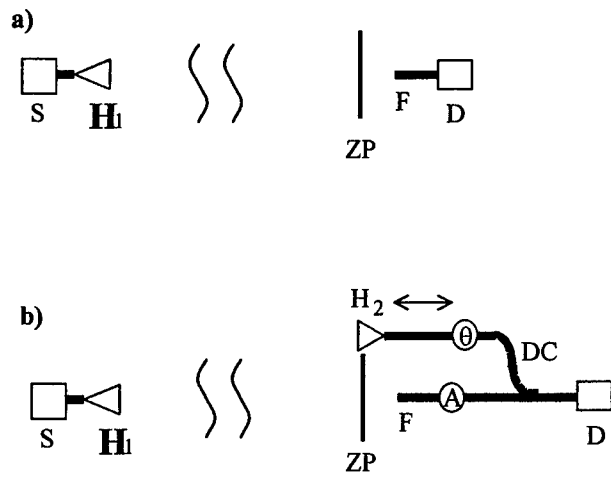
Fig. 4.
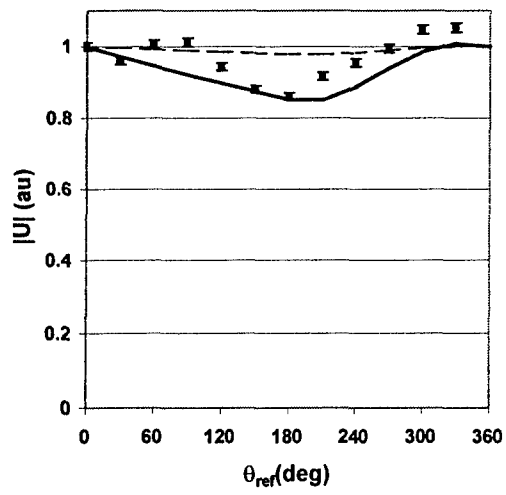
Fig. 5.
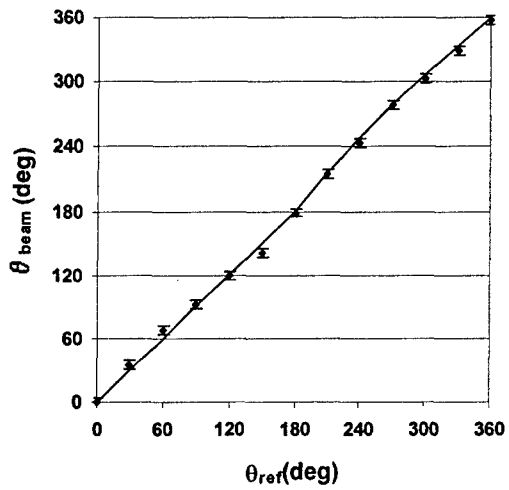

Fig. 6.
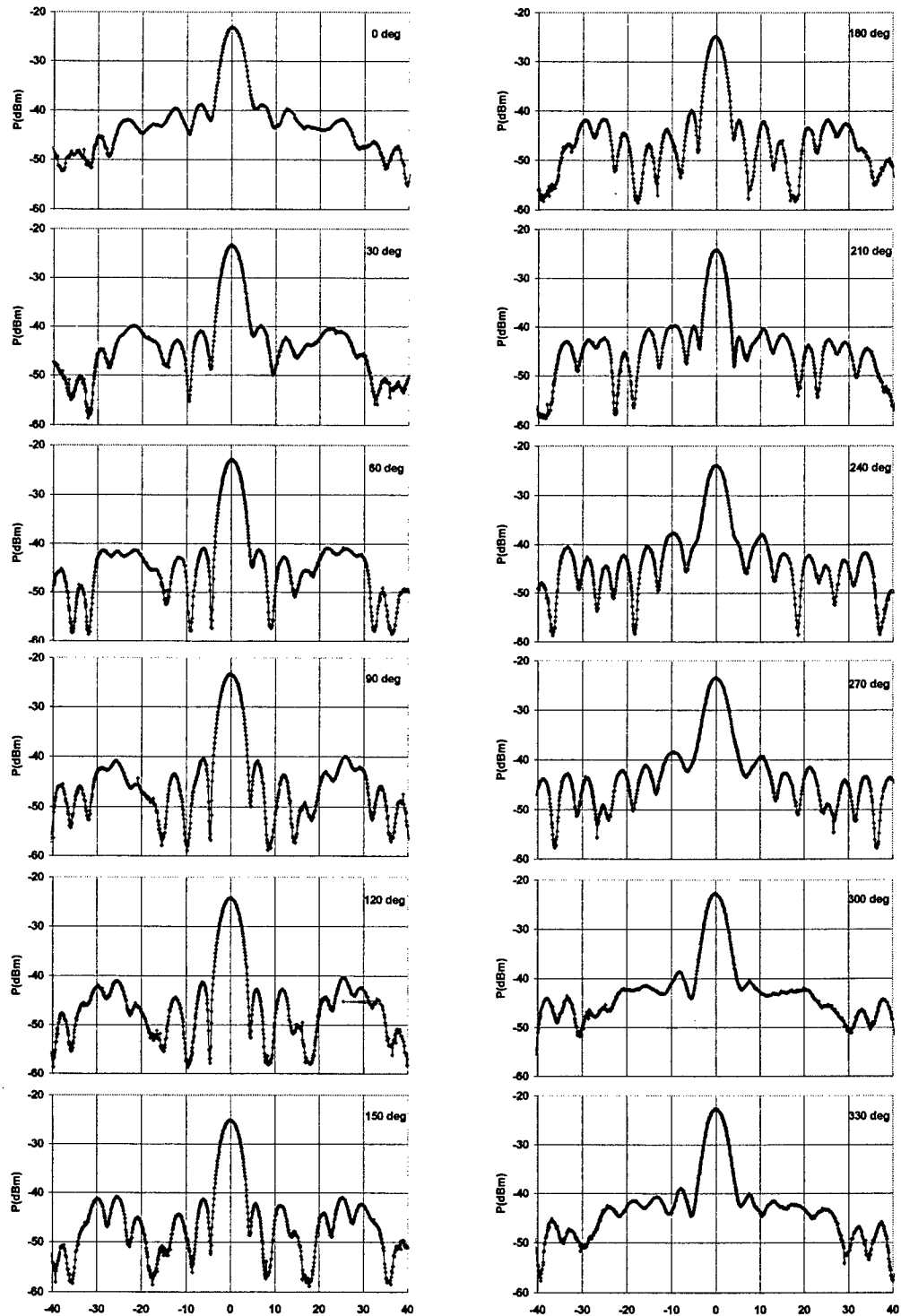
Fig. 7a.
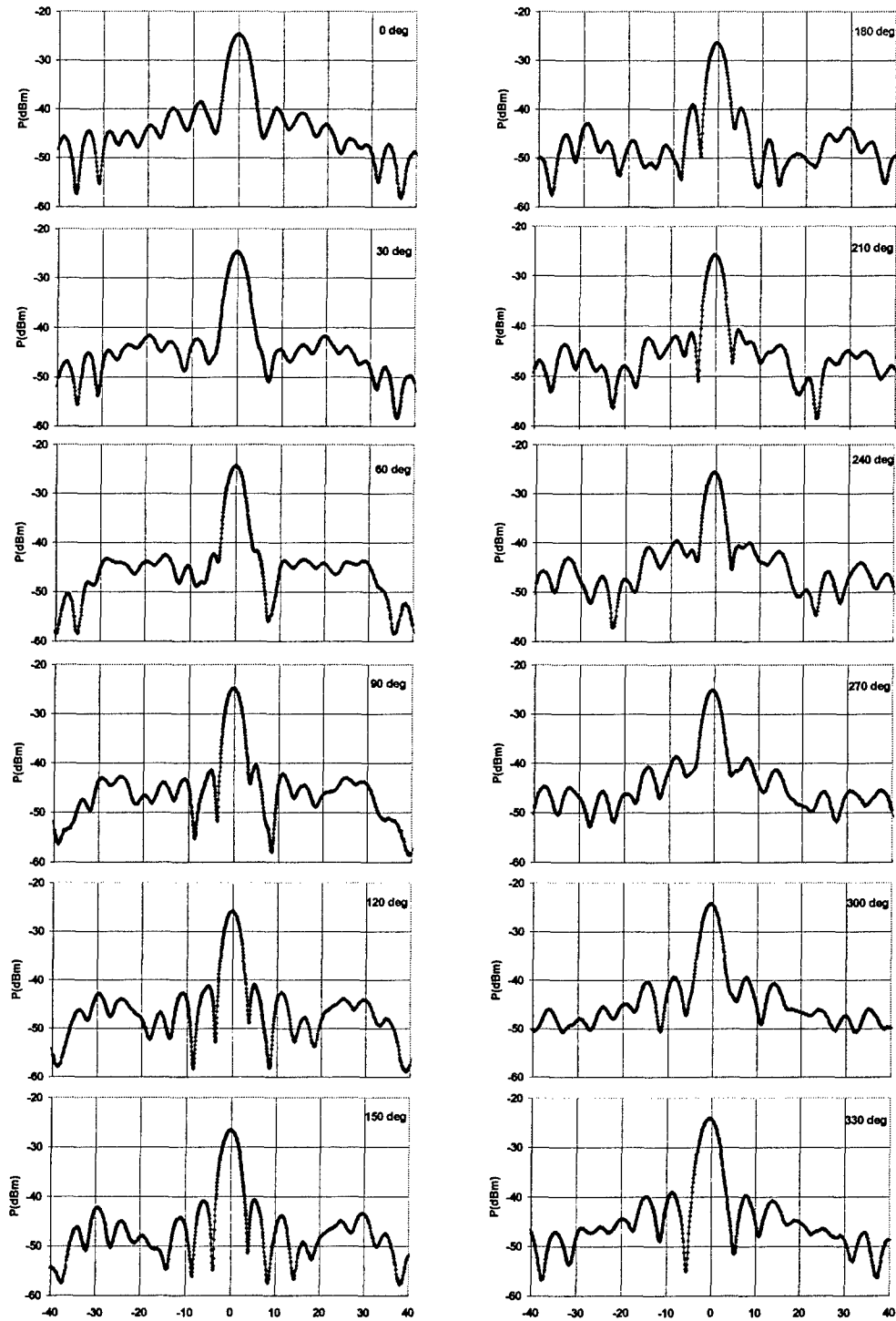
Fig. 7b.

Peak to Side Lobe Ratio vs θref
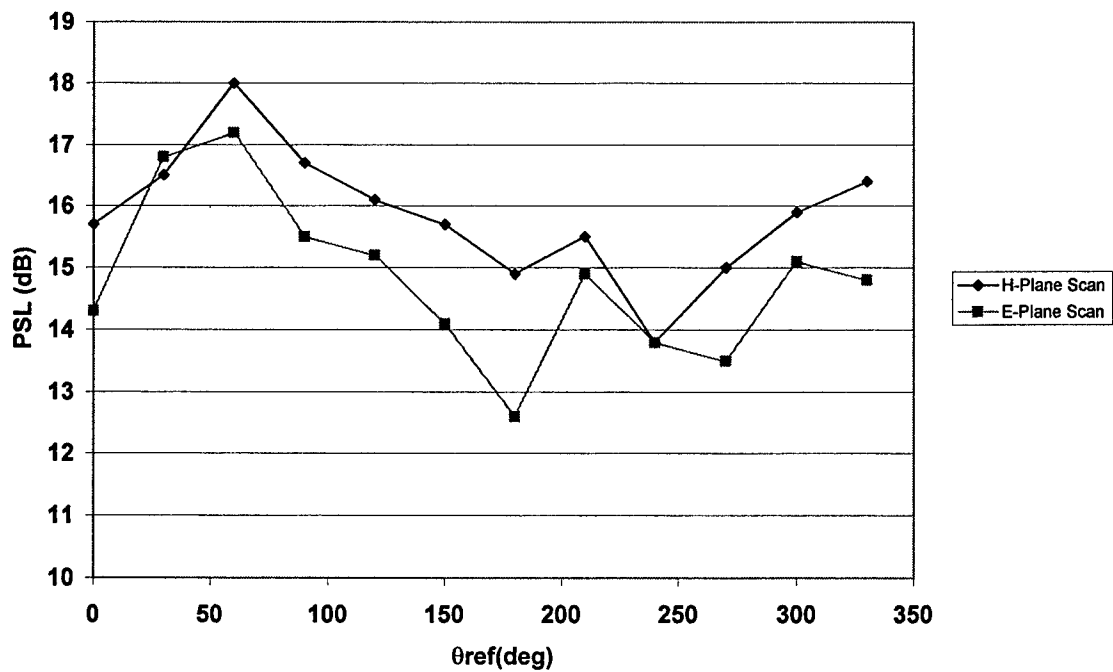
Fig. 8.
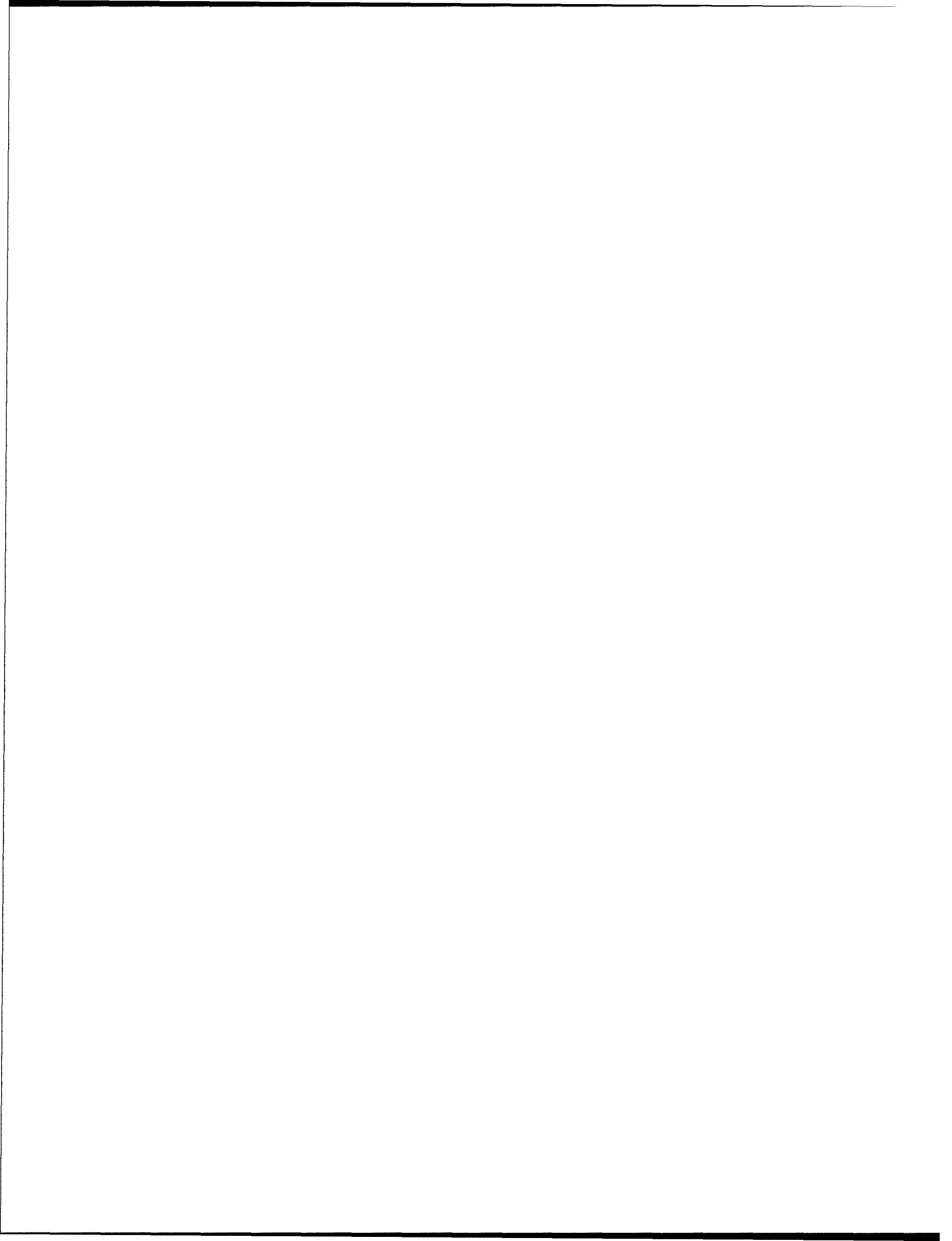
FREQUENCY SELECTIVE SURFACES: DESIGN OF BROADBAND ELEMENTS AND NEW FREQUENCY STABILIZATION TECHNIQUES

Adriano P. Raiva*, Frances J. Harackiewicz*, and Jefferson Lindsey III**
*Department of Electrical and Computer Engineering
**Department of Technology
Southern Illinois University Carbondale
Carbondale, Illinois 62901

Abstract: Two important features of a frequency selective surface (FSS) are bandwidth and frequency stability. Methods of increasing FSS bandwidth include, among others, decreasing inter-element spacing and increasing the thickness of the supporting dielectric layer. The shape of the FSS element also determines its bandwidth. To achieve any desired bandwidth, a combination of these methods is often required. The present work focuses on designing an FSS element where shape alone is the most important feature in determining its bandwidth. The elements are a combination of two known FSS elements with close resonant frequencies but not located in the same frequency band. The FSS's are designed to act as reflectors. The second part of this paper discusses frequency stabilization techniques, focusing on rectangular arrays of tripoles and cross dipoles. These elements have poor frequency stability with angle of incidence for parallel polarization. Dielectric loading and skewed arrays help minimize the problem. In the present work, a new method based on varying the element's impedance by partially removing the conducting patch at the center of the element is introduced.

1. Introduction

Broadband frequency selective surfaces often require the design of closely packed arrays of FSS elements or the increase of thickness of the supporting dielectric material [1, 2]. New techniques such as genetic algorithm [3] can deliver an FSS with a desired bandwidth at the expense of higher computation time. In the present work, an FSS element with broadband characteristics designed as a combination of known elements is presented. At first, multiband frequency selective surfaces are discussed. Double-Ring (DR) and Double Square Loop (DSL) FSS [1] have proven to be good single layer, dual band FSS. More recently the use of fractal geometries [4-7] in FSS applications has made possible the design of single layer dual or tri-band FSS, which is a great advantage since multiband FSS were designed using multiple layer frequency selective surfaces. However, resonant frequencies of fractal, double ring, or double square loop frequency selective surfaces are not closely located. This is because most designs require that these frequencies be located at different frequency bands and the design of fractal, DR or DSL FSS with close resonant frequencies is not possible. However, these FSS's are important when making a comparative study of resonant frequency placement in a dual band FSS.

107

The design of broadband elements begins with a comparative study of dual-band FSS's made of elements of different shapes. Later the elements are chosen according to features such as how close their resonant frequencies can be, their resonant frequency stability, and their bandwidth. At the end, a new FSS element is created.

The second part of this paper analyzes the frequency stabilization of rectangular arrays of tripole and cross dipole FSS with the angle of incidence. The goal is to show that even without skewed arrays it is possible to avoid frequency drift with the angle of incidence provided that part of the patch at the center of elements is removed. Skewed and closely packed arrays create very large bandwidths which may not be desirable if the FSS is to be used as subreflector at frequencies that are not too far apart. Numerical and experimental results will be discussed in both cases.

2. From Multiband to Broadband FSS. A Comparative Study of Resonant Frequency Location.

We begin our analysis with the study of fractal FSS. For our purpose, only one type of fractal structure will be discussed, and it is shown in Figure 1. Figure 1 shows a fractal structure of inset cross dipoles. It is important to emphasize that this fractal structure is a combination of two arrays: one formed by the larger cross dipoles of the 0th iteration, and the second array formed by the smaller cross dipoles of the 1st iteration. Each array can be analyzed separately as an FSS, which allows us to change the properties of elements of one iteration leaving the elements of the other iteration unchanged. Fractal geometries such as Sierpinski carpet, Sierpinski gasket or Koch patch would not serve our purposes since the different stages cannot be analyzed and manipulated separately.
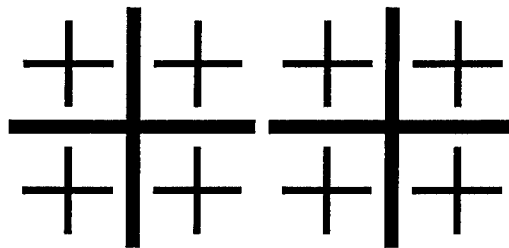

Figure 1. Inset cross dipole fractal FSS.

Fractal structures such as the shown in Figure 1 have been extensively analyzed [4] and their features as dual band FSS have been verified. Therefore they will not be analyzed in this paper. Due to space limitation, the size of cross dipole of the 1st iteration on Figure 1 can not be increased such that its resonant frequency is close to that of the cross dipole of the 0th iteration. The lowest resonant frequency of the 1st iteration can be at least twice of the resonant frequency of the 0th iteration. It is therefore necessary to change the elements of the 1st iteration if we want to bring its resonant frequency close to that of the first stage cross dipole. The changes of elements in the 1st iteration will be made such that their resonant frequency decreases gradually in order to analyze carefully their influence on transmission properties of the FSS. At this stage of our analysis, the shape of the element is irrelevant and only the location of the second resonant frequency is of the utmost importance.

We start by replacing the smaller cross dipoles of the 1st iteration in Figure 1 by tripoles, and the resulting non-fractal structure is shown in Figure 2.
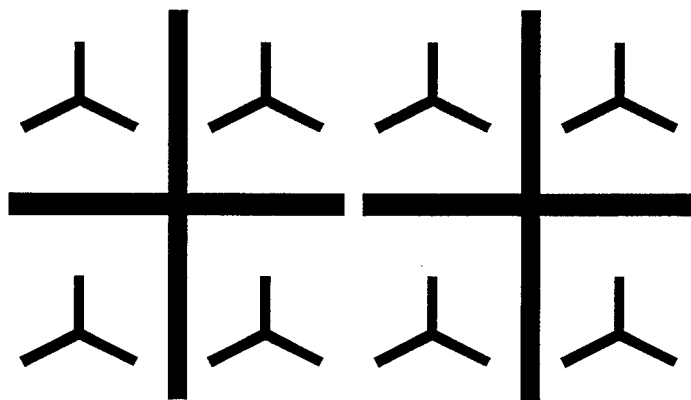
Figure 2. Modified structure from Figure 1 with the smaller cross dipoles replaced by tripoles.

The FSS shown in Figure 2 was analyzed for the dimensions shown in Table 1. The computed results in Figure 3 are for normal incidence and parallel polarization. The two resonant frequencies are not close, but at least the resonant frequency of the tripole is less than twice the frequency of cross dipole. This could not be achieved with fractal structures since we do not want to increase the FSS's cell size.

Table 1. Parameters of the arrays in Figure 2.

Element	length L, mm	Width w, mm	periodicity in x direction Tx, mm	periodicity in y direction Ty, mm
cross dipole	11	0.5	16.4	16.4
tripole	3.5	0.3	8.2	7.4

The array of Figure 2 is printed on a dielectric material with $\varepsilon_r = 4.5$ and thickness $t = 30$ mil (0.762 mm). The transmission characteristics are shown in Figure 3, and the transmission coefficients of each array as a separate FSS are also shown. The transmission characteristics of the tripole FSS alone, cross dipole FSS alone, and the combination of both elements as in Figure 3 are similar to the transmission characteristics of fractal structures shown in [4].
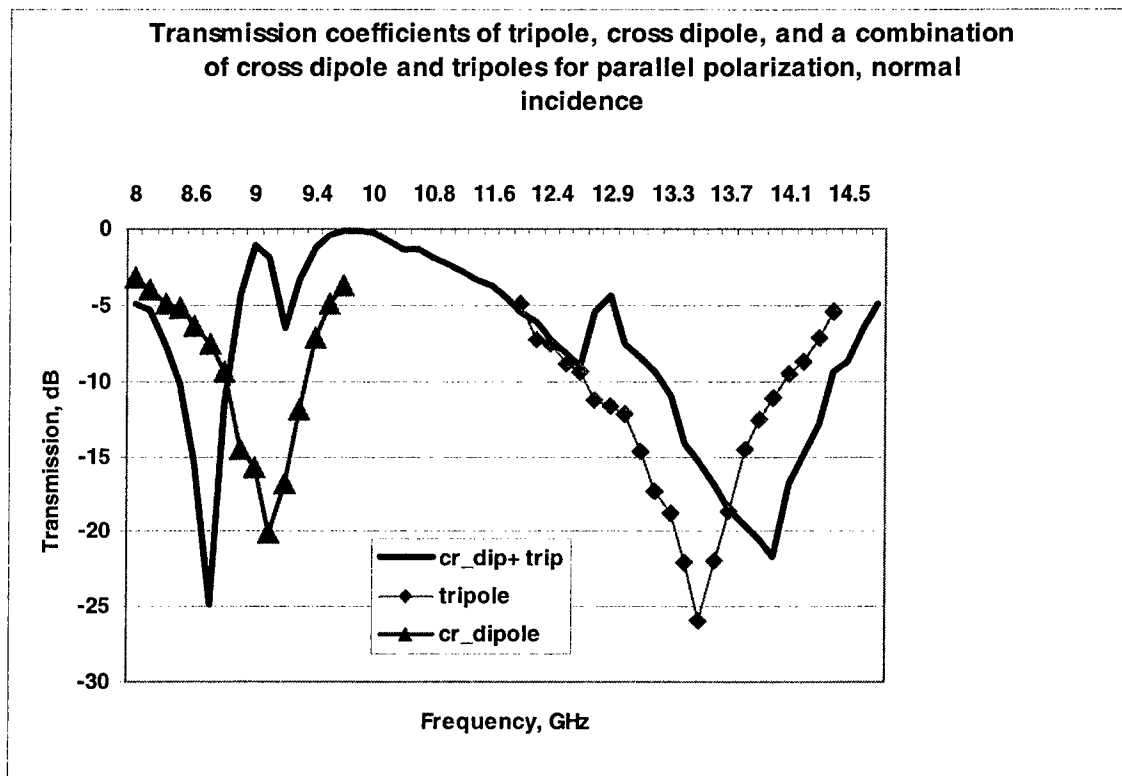
Figure 3. Computed transmission coefficients of tripole, cross dipole, and the combination of both as shown in Figure 2.

110

The graph shows that combining tripoles and cross dipoles in the same unit cell gives similar transmission characteristics to those of FSS made of each element separately. The graphs are for normal incidence, parallel polarization. Ansoft HFSS was used to compute the transmission coefficients.

If we want the two resonant frequencies to be even closer to each other, we need to change the tripole with an element of much lower resonant frequency. In Figure 4 the tripoles of Figure 2 have been replaced by Jerusalem crosses and the transmission characteristics have been computed similarly to Figure 3.
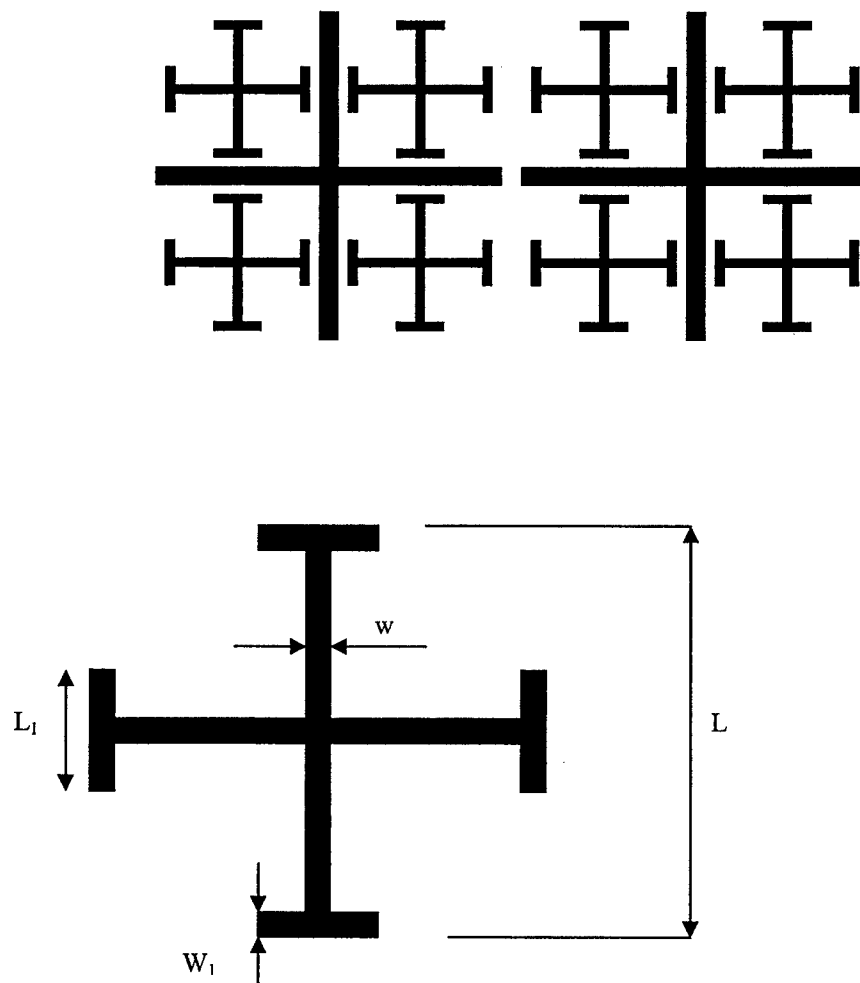
Figure 4. *Top.* Modified structure from Figure 2 with the second stage tripoles replaced by Jerusalem crosses. *Bottom:* Jerusalem cross.

111

Figure 5 shows the transmission coefficients of cross dipole, Jerusalem cross and the combination of both as shown in Figure 4. The parameters of the array of Figure 4 are given in Table 2, and like in Figure 2, the computation was made for a supporting dielectric layer of ε_r = 4.5 and thickness of 30 mil (0.762 mm). It is important to notice that the resonant frequency of the tripole is 13.5 GHz and that of Jerusalem cross is 12.5 GHz as shown in figures 3 and 5, respectively. The Jerusalem cross did manage to drop the second resonant frequency. The first resonant frequency for the combined elements in Figure 2 is 8.7 GHz while the same frequency for the arrangement in Figure 4 is 7.5 GHz as it is shown in figures 3 and 5, respectively. The difference between the second and the first resonant frequencies drops from 5.2 GHz in Figure 3 to 4.7 GHz in Figure 5 for the combined elements.

Table 2. Parameters of the arrays in Figure 4.

Element	length L, mm	Width w, mm	periodicity in x direction Tx, mm	periodicity in y direction Ty, mm
cross dipole	11	0.5	16.4	16.4
Jerusalem cross*	6.4	0.6	8.2	8.2

*Jerusalem cross end loading bars dimensions are w_l = 0.2 mm L_l = 2.0 mm
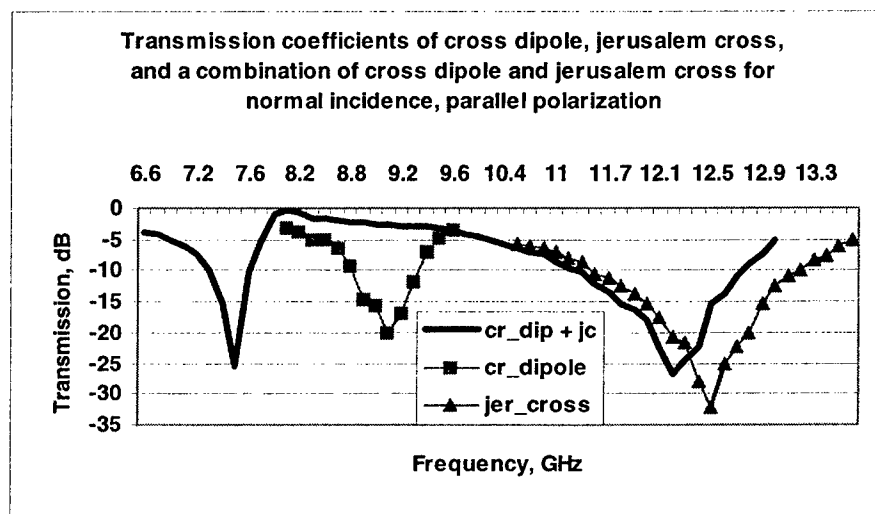
Figure 5. Computed transmission coefficients of cross dipole, Jerusalem cross and the combination of both. The first and second resonant frequencies of the arrangement in Figure 4 get slightly closer, but the results are still far from the desired.

112

From the arrangement in Figure 4 and the corresponding graph in Figure 5 it is clear that the first and the second resonant frequencies are as close as possible for this geometry. To overcome the problem, another change on element shape is needed. We replace the cross dipole with a ring, and the arrangement is shown in Figure 6. Also the dielectric material was changed to ε_r = 10.2 and thickness = 25 mil (0.64 mm). The change of dielectric constant was made in order to reduce the size of the ring needed to obtain a resonant frequency similar to that of the replaced cross dipole. The inner and the outer radiuses of the ring are 3 mm and 3.5 mm respectively. The length and width of the Jerusalem cross are L = 5.4 mm and w = 0.5 mm, and the Jerusalem cross end loading bars dimensions are w_1 = 0.2 mm, and L_1 = 1.9 mm.
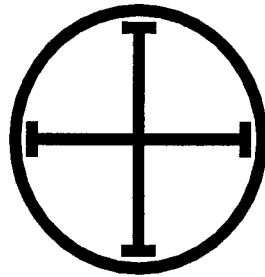
Figure 6. Ring and Jerusalem cross are the elements that have the closest resonant frequencies.

Figure 7 shows the transmission coefficients of ring, Jerusalem cross, and the combination of both. Analyzing the graphs of Figure 7, we can notice that as the resonant frequencies of the elements get closer, the resonant frequencies of the combined elements do not get closer. They actually are farther apart compared to the arrangements of Figures 2 and 4. The difference between the second and the first resonant frequencies of the combined ring and Jerusalem cross arrangement is 6.6 GHz, which is more that the differences of the previous arrangements of Figures 2 and 4. This is because since the two resonant frequencies are not in the same reflection band the Foster's reactance theorem [2] must apply. This theorem states that between two nulls there must be a pole and vice versa. That explains why the resonant frequencies of the ring and Jerusalem cross are much different to their values in a combination ring-Jerusalem cross. If the resonant frequencies of ring and Jerusalem cross were located in the same frequency band we could immediately have a broadband FSS [8], but due to the size restrictions, we cannot make the frequencies any closer. However, we can notice that the second reflection band is becoming much larger than in the previous cases, and we need to use this characteristic to make our broadband FSS. One way to accomplish our objective is to connect the ring and the Jerusalem cross, forming one single element as shown in Figure 8. The transmission coefficient of the element of Figure 8 is shown in Figure 9,

and it is compared with the second reflection band of the combination ring-Jerusalem cross. As it can be seen from the graphs in Figure 9, our new element has a much larger bandwidth compared to the unconnected ring-Jerusalem cross pair. Note: The ring plus the Jerusalem cross FSS is found to be transparent at 6.5 GHz while acting as a reflector at 5.7 and 12.5 GHz. Figure 10 shows the numerical and measured transmission characteristics of the new element, and Figure 11 shows the FSS board used for measurement results on Figure 10.
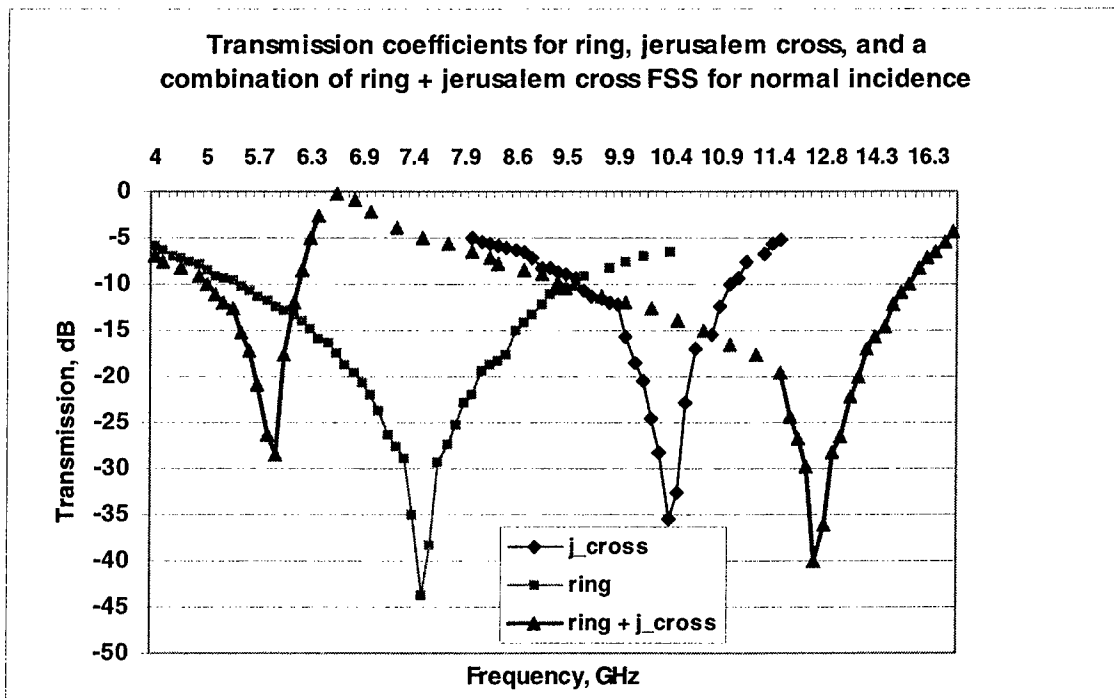
Figure 7. Computed transmission coefficients of ring, Jerusalem cross, and a combination ring-Jerusalem cross. The periodicity of the elements is 7.5 mm in both x and y directions.

114
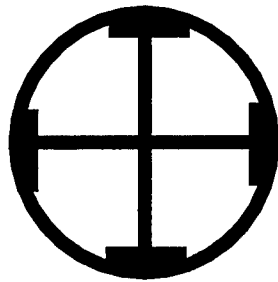
Figure 8. Ring and Jerusalem connected to form one single element in order to get broadband characteristics.
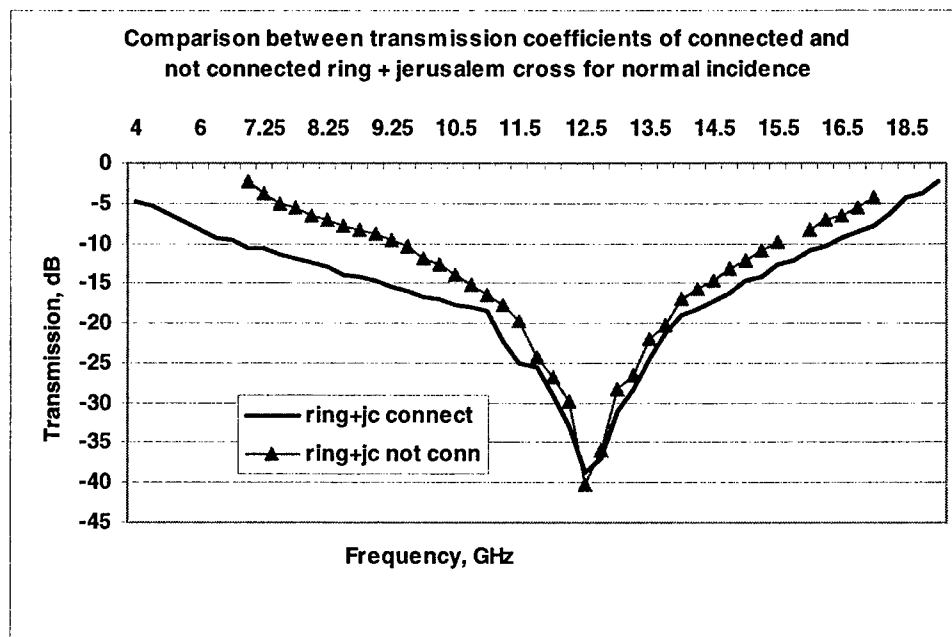
Figure 9. Comparison of computed transmission coefficients of unconnected ring + Jerusalem cross (second reflection band) and the same elements connected. From the graphs, it is clear that connecting both elements increases the bandwidth of the reflection band.
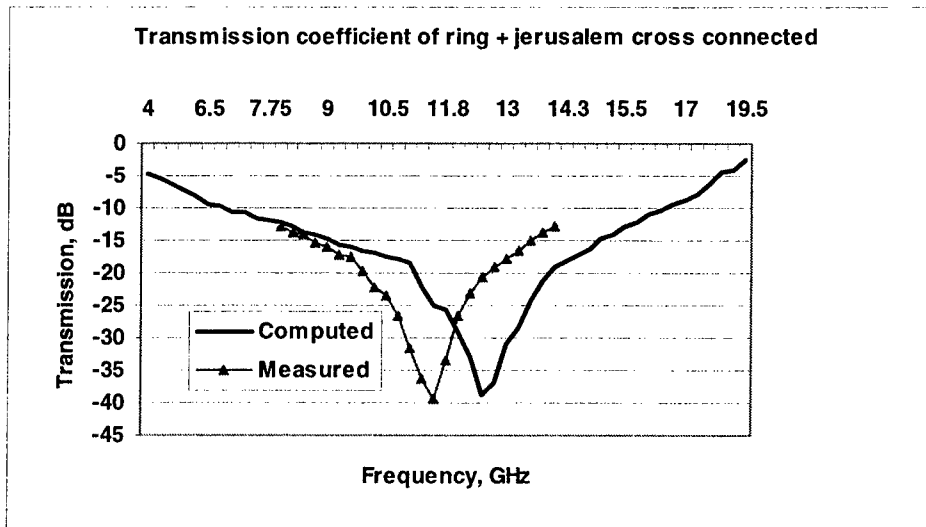
Figure 10. Computed and measured transmission coefficients of the new element shown in Figure 8. .
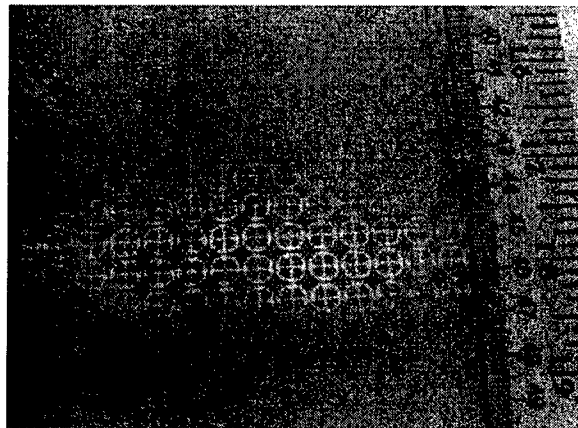
Figure 11. FSS used for measurement results shown in Figure 10. The dielectric material is RT/Duroid with $\varepsilon_r = 10.2$, and thickness = 25 mil (0.64 mm). The size of the FSS is 18 inches x 18 inches.

Table 3 shows a comparison of the bandwidths between the Jerusalem cross, ring, combination ring-Jerusalem cross, and the new element.

116

Table 3. Comparison of the frequency characteristics of elements used in the making of the new FSS element.

	Center Frequency (GHz)	Bandwidth (GHz)	Bandwidth (%)
Jerusalem Cross	10.4	1.5	14.42
Ring	7.5	4	53.3
Ring + Jerusalem Cross Disconnected	11.5	6	52.17
Ring + Jerusalem Cross Connected	11.5	9.5	82.6

As seen in Table 3 the new element has a bandwidth of 9.5 GHz which is 2.375 times the bandwidth of the ring element, 6.3 times the bandwidth of Jerusalem cross, and 1.58 times the bandwidth of the combination ring-Jerusalem cross. These properties are remarkable, since most of the common elements would require a sandwich FSS to achieve such a large bandwidth.

2.1. Broadband Element Based on Combination of Square Loop and Jerusalem Cross

Based on the analysis previously formulated, another element with broadband characteristics similar to the element of connected ring-Jerusalem cross was obtained. This element is the combination of square loop and Jerusalem cross. Figure 12 shows the broadband element, and Figure 13 shows its transmission coefficient for normal incidence.
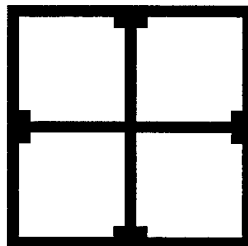

Figure 12. Square loop and Jerusalem cross connected in order to from a broadband element. The approach is similar to the presented in figure 8. The dimensions used for computation coefficients are: the outer and inner dimensions of the loop are 6mm and 5.4 mm, respectively. The length of the Jerusalem cross is 5.2 mm, width $w = 0.5$ mm, and the end loading bars dimensions are $L_1 = 1.9$ mm, $w_1 = 0.2$ mm.

117

Transmission versus frequency. Connected square loop and jerusalem cross for normal incidence, parallel polarization
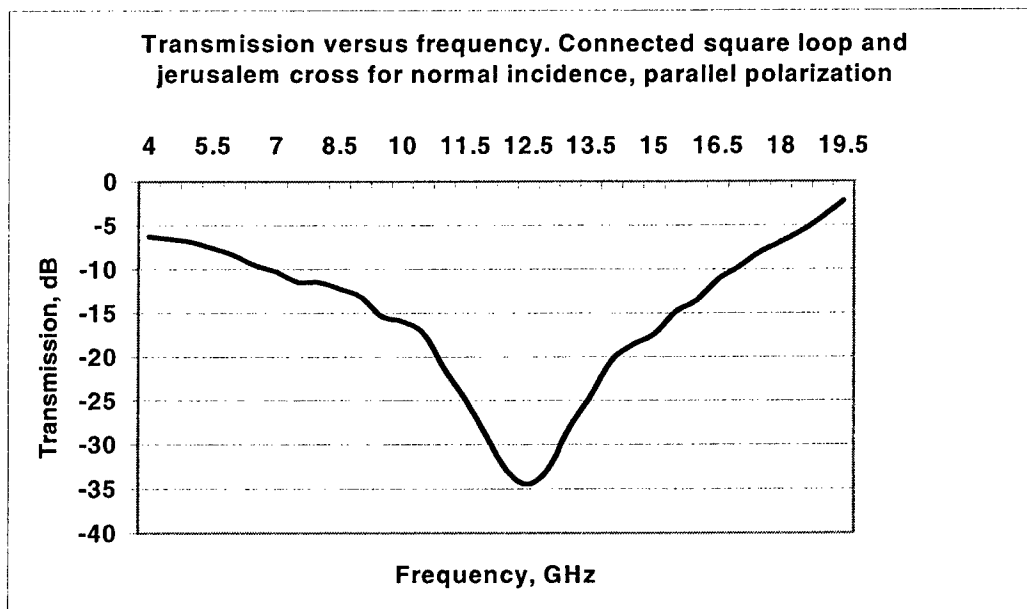
Figure 13. Computed transmission coefficient of the element shown in figure 12 for normal incidence. The dielectric material is RT/Duroid with thickness 0.64 mm and ε_r = 10.2.

3. Frequency Stabilization Technique for FSS made of Rectangular Arrays of Tripoles and Cross Dipoles

Tripoles and cross dipoles have the following principal characteristics:

a) The fundamental mode is strongly excited when the element length is about $\lambda/2$, and the incident E-field has a component parallel to the elements.

b) An odd mode is excited only for oblique angles of incidence, and when the element length is approximately λ.

c) The inter-element spacing plays a big role. Decreasing the inter-element spacing increases the bandwidth and delays the onset of grating lobes. This feature is common for every type of FSS elements.

For the tripole FSS in particular, a skewed array is highly recommended since it not only increases frequency stability with angle of incidence but also solves the problem of cross polarization making the cross polarization frequency identical to the parallel polarization.

The analysis on frequency stabilization will be centered on tripole and cross dipole rectangular arrays of FSS. Studies on skewed arrays did not bring good results especially for cross polarization on tripole arrays where the cross polarization transmission coefficient was not lower than −10 dB over the entire reflection band. One of the

118

objectives was to keep the dual polarization characteristics of the elements. The design parameters were chosen as follows:

i) The inter-element spacing was made as large as possible without generating grating lobes. That would reduce the bandwidth and allow a better analysis of resonant frequency drift with angle of incidence for parallel incident E-fields.

ii) The remaining parameters such as resonant frequency, length and width of the elements, dielectric constant and thickness of the supporting dielectric materials, were chosen such that experiments could be performed with the existing measurement facilities at Southern Illinois University.

The frequency stabilization method presented is based on the theory of variable surface impedance [9] used to change the transmission and reflection properties of an FSS. Once the shape, array element and the unit cell dimensions are fixed, an additional method of changing the frequency response is through the application of a varying surface impedance as shown in Figure 14. The addition of element losses began with the application of a constant resistive boundary condition on the tangential electric fields at the surface of the conductor, and this was later applied to periodic surfaces. The resistive boundary condition evolved from the application of the boundary condition to thin metallic surfaces. The general equation is

$$\vec{E}^{inc} + \vec{E}^{scat} = Z_s \vec{J}_s \tag{1}$$

where the surface impedance is given by Z_s. The two limiting cases of this equation occur when $Z_s = 0$ and Z_s approaches infinity. When $Z_s = 0$ the boundary condition enforced by equation (1) is a PEC boundary, and when $Z_s \rightarrow \infty$ the surface currents are forced to zero, and the surface no longer scatters energy. In the current analysis the case of $Z_s \rightarrow \infty$ is applied given that for both tripole and cross dipole the surface impedance of the element is changed by removing the conducting material at its center as shown in Figure 15.
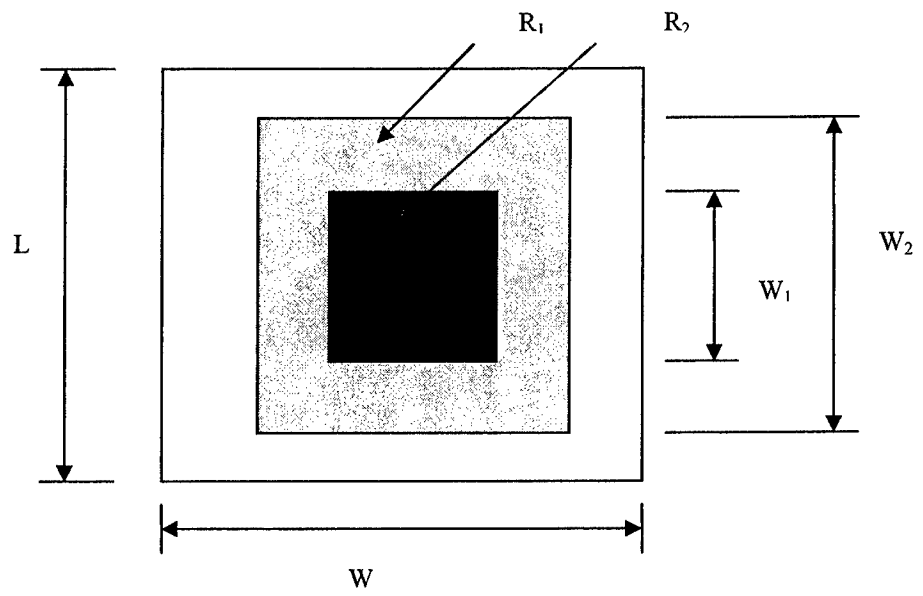
Figure 14.   Example of a unit cell geometry showing varying surface impedances R_1 and R_2.
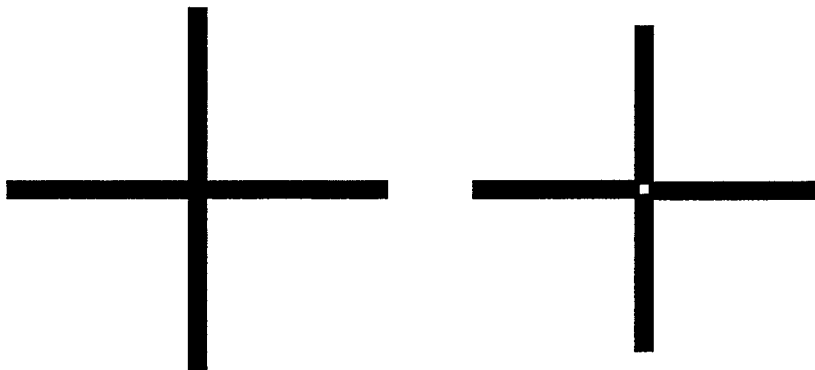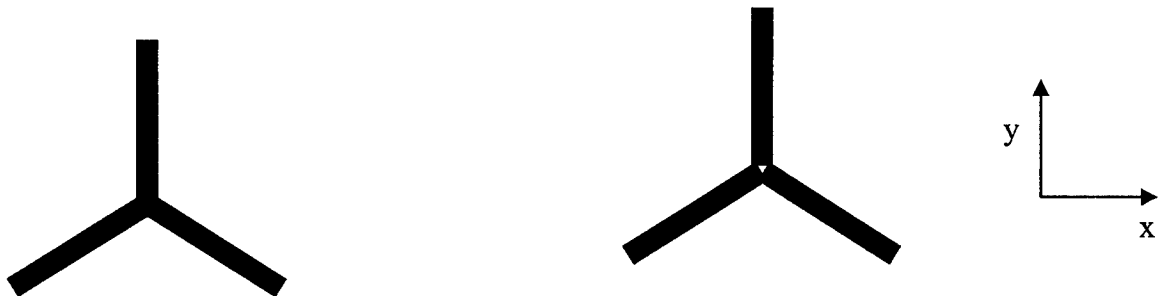
Figure 15. a) Cross dipole and b) tripole with and without removed conducting patch at the center. Removing the conducting material at the center of element implies a variation of impedance from $Z_s = 0$ to $Z_s \to \infty$.

3.1. Analysis of Tripole Array

Theoretical and measured results were obtained for tripole arrays [2, 10] and for tripole arrays with removed conducting material at its center. The length and width of the tripoles were 4 mm and 0.6 mm respectively, and the area of the removed conducting material is a triangle with side length 0.6 mm. The performances of the arrays have been examined for two principal orientations relative to the incident plane wave. In the first orientation, the tangential component of the electric field is parallel to the top arm of the tripole (y-axis), and in the second orientation, they are perpendicular to each other. The resonant frequency is within the X-band frequency. The tripole array was printed on a dielectric substrate with thickness of 20 mil (0.508 mm), $\varepsilon_r = 4.5$, and inter-element spacing of 12 mm. A second dielectric with the same parameters was placed on top of the arrays forming a sandwich FSS. Figure 16 shows the transmission response of a tripole array. Ansoft HFSS was used for computation of the transmission responses.

The graphs on Figure 16 show that for parallel polarization the resonant frequency drifts when the angle of incidence varies from 0^0 to 45^0. Figure 17 shows comparison of transmission coefficients of tripole FSS rectangular arrays with and without removed conducting patch. Other studies conducted by the authors show that the resonant frequency drifts downwards when part of the conducting material is removed. The amount of drift depends on the area and shape of the conducting material removed. Removing large areas of conducting material can result in greater resonant frequency drift.
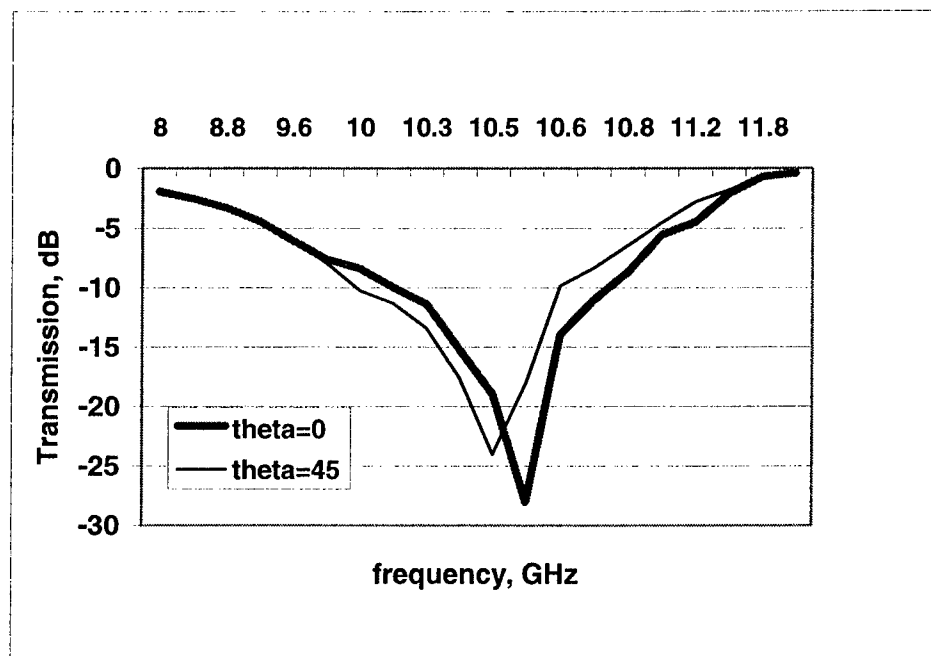

Figure 16. Computed transmission coefficient of rectangular arrays of tripole FSS, parallel polarization for angles of incidence of 0^0 and 45^0.

Transmission coefficient of tripole. Parallel and perpendicular polarization with and without removed patch. Normal incidence.
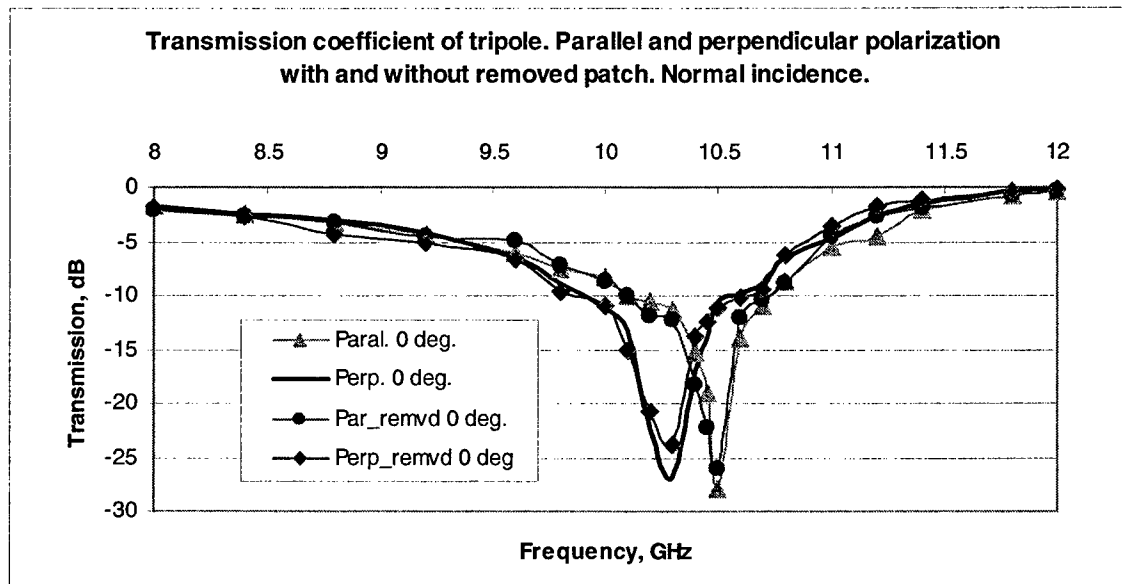

Figure 17. Comparison of computed transmission coefficients of tripole and tripole with removed conducting material for normal incidence, parallel and perpendicular polarization. The graphs are very similar since the area removed is small

Figure 18 shows transmission coefficient for parallel polarization for angles of incidence of 0^0 and 45^0. As it is shown in Figure 18 and in contrast with the tripole shown in Figure 16, there is no frequency drift when the angle of incidence is shifted from 0^0 to 45^0. Transmission coefficient for perpendicular polarization differs from that of parallel polarization for rectangular arrays as shown in Figure 19. To compensate the difference the length of the upper arm of the tripole was increased in order to lower the resonant frequency of the parallel polarization and make it equal to that of perpendicular polarization as shown in Figure 20. This is because increasing the length of the tripole's upper arm only influences parallel polarization keeping the perpendicular polarization unchanged. Figure 21 shows the FSS used for measurements, and it uses modified tripoles shown in Figure 20.

Transmission coeff. for tripole with removed patch, parallel polarization.

| | 8 | 8.8 | 9.6 | 10 | 10.2 | 10.4 | 10.6 | 10.8 | 11 | 11.4 | 12 |

Transmission, dB

theta=0
theta=45
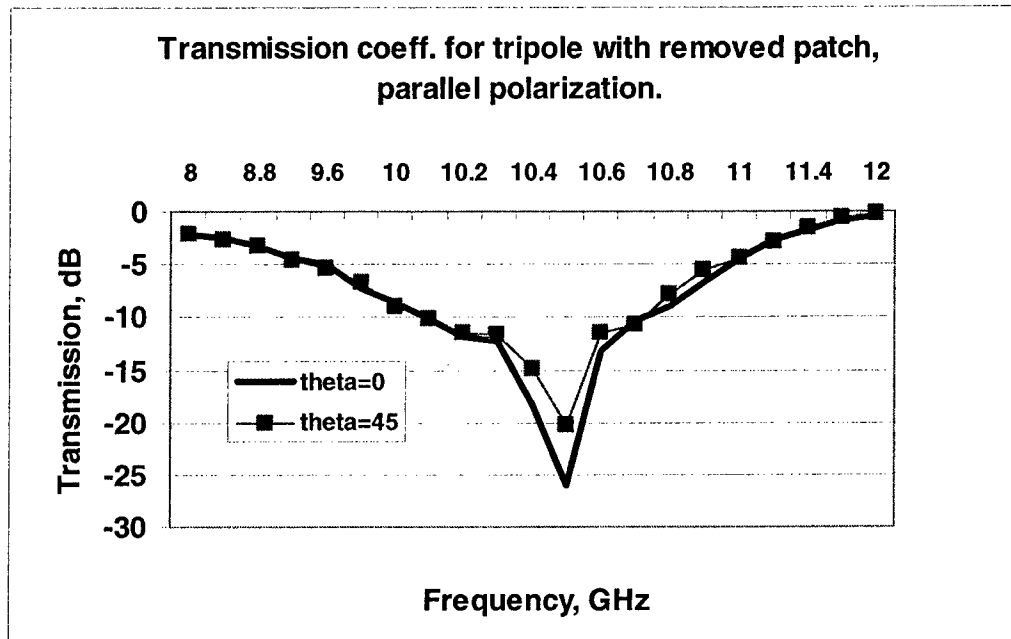
Frequency, GHz

Figure 18. Computed transmission coefficients of tripole with removed conducting patch, parallel polarization, incidence angles of 0^0 and 45^0. The figure shows that there is no frequency drift with the change of incidence angle as in Figure 16.

Parallel and perpendicular polarization for tripole with removed patch

| | 8 | 8.8 | 9.5 | 9.8 | 10.1 | 10.3 | 10.5 | 10.7 | 10.9 | 11.2 | 11.8 |

Transmission, dB

phi=0
phi=90

Frequency, GHz
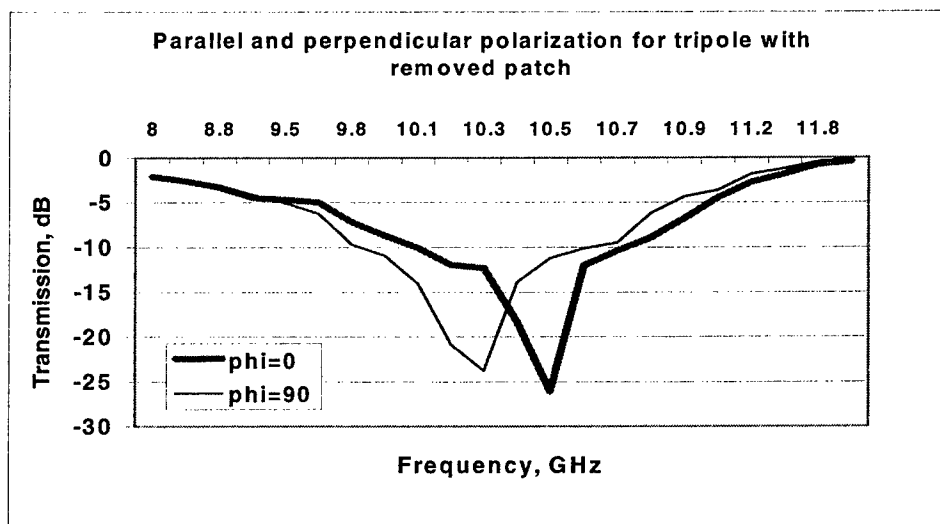
Figure 19. Transmission coefficients for parallel (phi=0) and perpendicular (phi=90) polarizations, normal incidence of tripole with removed patch.
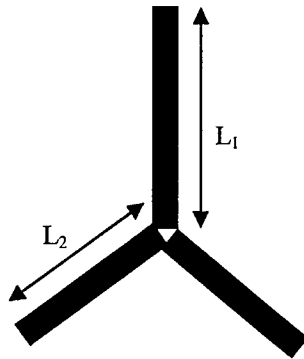
Figure 20. Modified tripole with removed patch. Increasing properly the length of the upper arm of the tripole drops the resonant frequency of parallel polarization to a value equal to that of the perpendicular polarization.
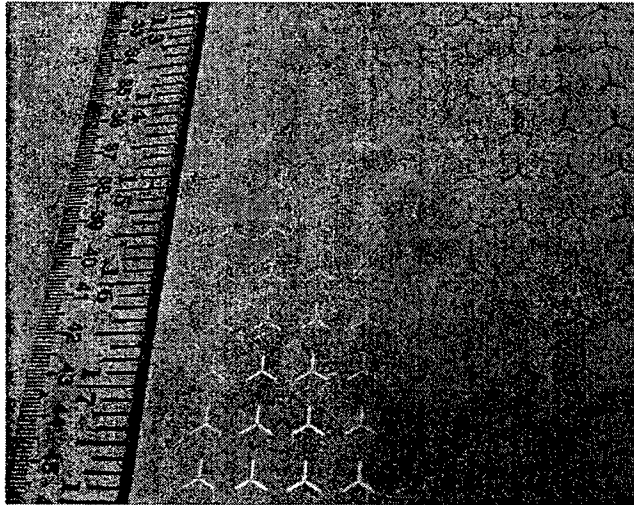

Figure 21. Printed tripoles with removed patch on a dielectric substrate used for measurements. The shown FSS was covered by a dielectric with similar properties. The array covers an area of 18"x18". The inter-element spacing is 12mm, the tripole length is: upper arm L_1 = 4.1 mm, other arms L = 4 mm, width = 0.6 mm. Dielectric thickness = 20 mil (0.508 mm), ε_r = 4.5.

Figure 22 a) shows the computed transmission coefficient of the modified tripole with removed patch for both parallel and perpendicular polarization. As it is shown there is no more difference between the parallel and perpendicular polarization frequencies. The length of the upper arm of the tripole has been increased by 0.1 mm. Figure 22 b) shows the measured results for the same case. As it is shown, there is little difference between computed and measured results.
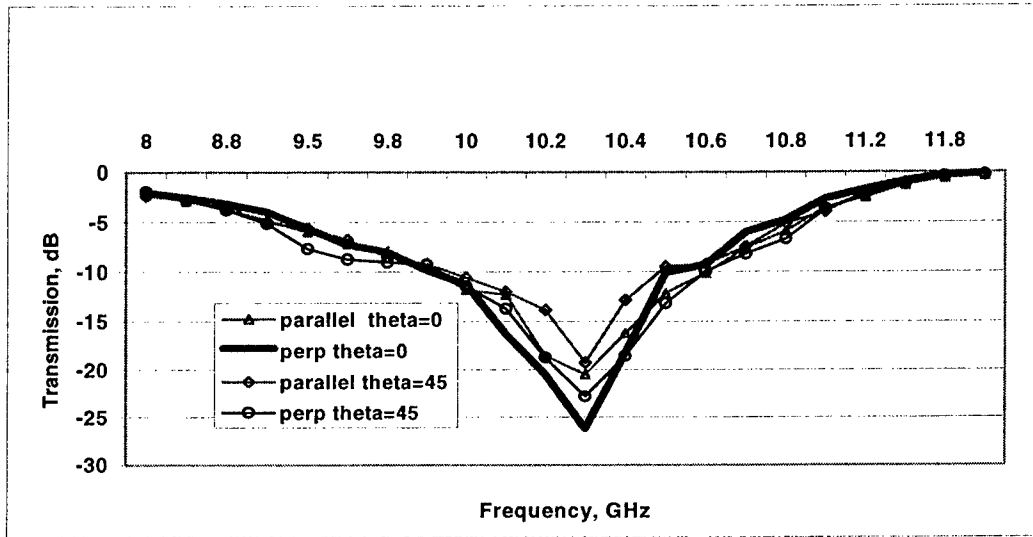
a)
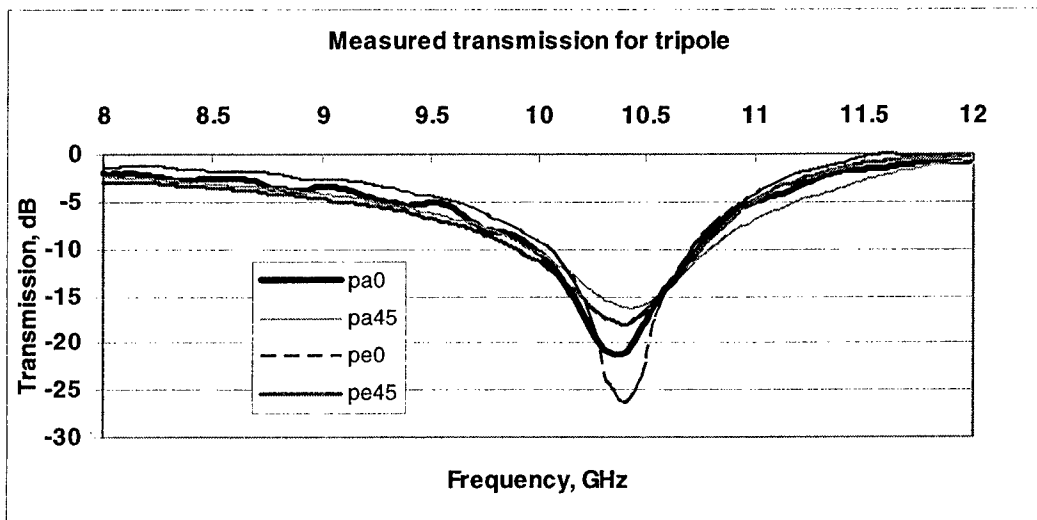
b)

Figure 22. a) Computed and b) measured results for modified tripole with removed patch.

126

3.2. Analysis of Cross Dipole Array

Similar analysis was made for cross dipole array. The cross dipole length and width were 6 mm and 0.6 mm respectively, and the inter-element spacing was 10 mm. As with the tripole arrays, the array of cross dipoles was printed on a dielectric material with thickness of 20 mil (0.508 mm) and $\varepsilon_r = 4.5$. Another dielectric with the same properties was placed on top forming a sandwiched FSS. Figure 23 shows computed transmission coefficients of cross dipole for angles of incidence of 0^0 and 45^0. As shown in this figure, there is a frequency drift when the angle of incidence is changed from 0^0 to 45^0. Figure 24 shows the transmission coefficients of cross dipole and cross dipole with removed patch, and the area removed is a square with sides of 0.2 mm. In this figure, it is clear that the resonant frequency drops when part of the conducting patch is removed. Figure 25 shows the transmission coefficients of cross dipole with removed patch for incident angles of 0^0 and 45^0. Similarly to the tripole case there is no frequency drift when part of conducting patch at the center of cross dipoles is removed.
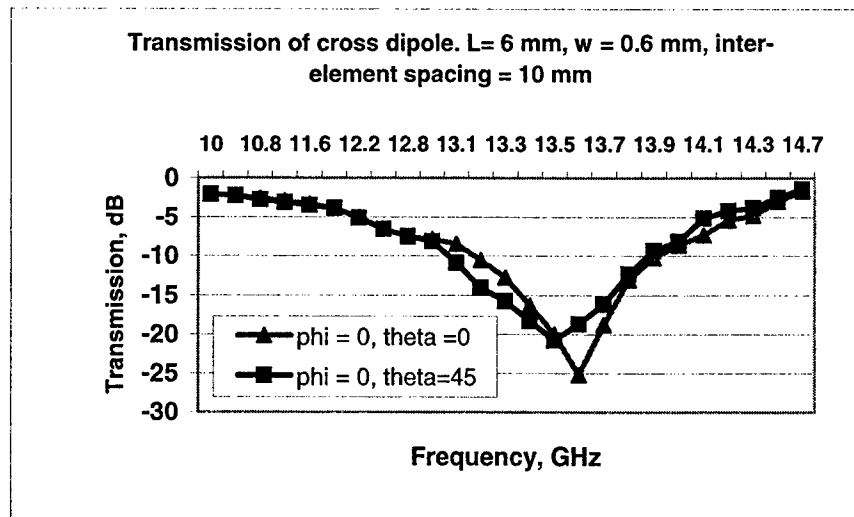
Figure 23. Computed transmission coefficients of cross dipole FSS for incidence angles of 0^0 and 45^0.

127
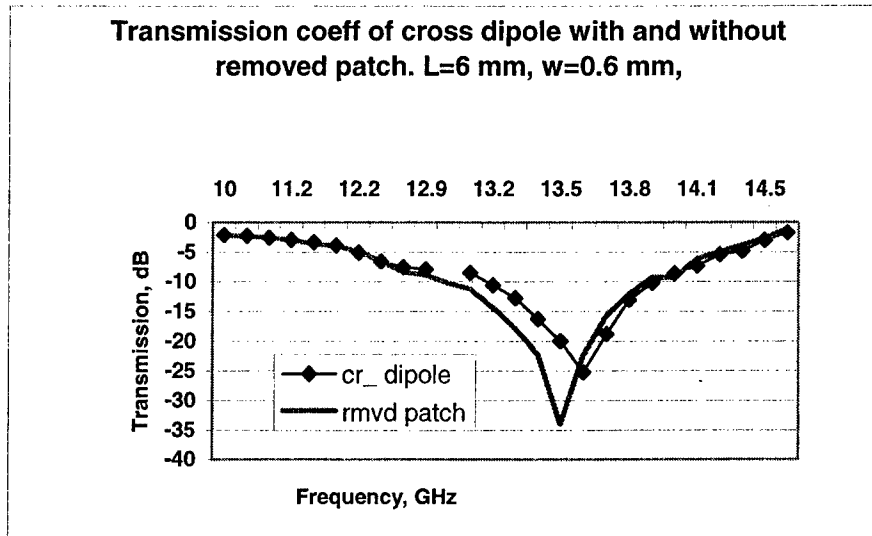
Figure 24. Computed transmission coefficients of cross dipoles with and without removed conducting patch for normal incidence.
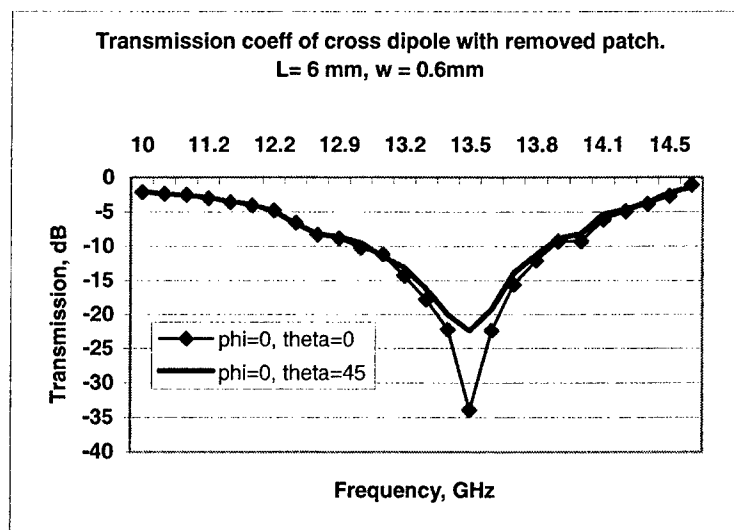

Figure 25. Computed transmission coefficients of cross dipole with removed conducting patch for angles of incidence 0^0 and 45^0.

128

4. CONCLUSIONS

In this paper two different topics were discussed: design of single layer broadband FSS element, and a frequency stabilization technique for tripole and cross dipole rectangular arrays of FSS. The broadband FSS design was based on analysis of transmission characteristics of double band, single layer FSS. Special attention was focused on the study of how the transmission characteristics of the double band FSS behave when the resonant frequencies of the two reflection bands are placed close to each other. It was found that as the two resonant frequencies get closer, the second reflection band gets wider. Due to the Foster's reactance theorem, the lower resonant frequency drifts to a lower value in order to get a pole between the two nulls. This particular feature was used to create a broadband FSS by connecting together two elements to form a single element with desirable broadband characteristics. Two broadband elements were formed by first connecting a Jerusalem cross with a ring, and later connecting a Jerusalem cross with a square loop. Their transmission characteristics were presented, and some measured results were shown.

With regards to the frequency stabilization technique it was found that removing part of the conducting patch at the center of tripoles and cross dipoles could prevent frequency drift with the angle of incidence. By removing part of the conducting patch of the element, the surface impedance of the element varies and this produces the change in the transmission characteristics. For tripole elements the upper arm must be increased to match the resonant frequencies of parallel and perpendicular polarizations.

REFERENCES

[1]   T. K. Wu, *Frequency selective surfaces and grid Array*, John Wiley & Sons INC, 1995.

[2]   Ben A. Munk, *Frequency Selective Surfaces. Theory and Design*, John Wiley & Sons, INC, 2000

[3]   Sourav Chakravarty, Raj Mittra, "Application of Microgenetic Algorithm (MGA) to the Design of Broad-band Microwave Absorbers using Multiple Frequency Selective Surface screens buried in Dielectrics", *IEEE Transactions on Antennas and Propagation,* vol. 30 no. 3 pp 284-296, March 2002

[4]   John P. Gianvittorio, Yahya Rahmat-Samii, and Jordi Romeu, "Various self-Similar Geometries Used for Dual-Band and Dual-Polarized FSS", *www.ee.ucla.edu/~johng/research.html,* accessed 11/10/2002

[5]   Jordi Romeu and Yahia Rahmat-Samii, "Fractal Based FSS with Dual Band Characteristics, *IEEE Antennas and Propagation Society International Symposium*, Vol. 3 pp 1734-1737, 1999

[6]   Jordi Romeu and Yahia Rahmat-Samii, "Fractal FSS: A Novel Dual-Band Frequency Selective Surface", *IEEE Transactions on Antennas and Propagation,* Vol. 48 No. 7 pp1097-1105, July 2000.

[7]   Douglas H. Werner, Suman Ganguly, "An Overview of Fractal Antenna Engineering Research", *IEEE Antennas and Propagation Magazine,* Vol. 45   No. 1, pp 38-57, February 2003

[8]   D. Sarkar, P. P. Sarkar, S. Das, and K.Chowdhury, "An Array of Stagger-Tuned Printed Dipoles as a Broadband Frequency Selective Surface" *Microwave and Optical Technology letters,* Vol. 35 No. 2, October, 2002

[9]   Larry W. Epp, *Frequency Selective Surfaces with Lumped and Time Varying Loads, Variable Surface Impedance, and Multiple Screens,* Ph.D Dissertation, University of Illinois at Urbana-Champaign, 1990

[10]   P. W. B. Au, L. S. Musa, E. A. Parker, R. J. Langley, "Parametric Study of Tripole and Tripole loop arrays as Frequency Selective Surfaces", *IEE Proceedings,* Vol. 137, Pt. H, No. 5 pp. 263-268, October 1990.

GENETIC ANTENNA OPTIMIZATION:
A TALE OF TWO CHROMOSOMES

Terry O'Donnell[1], Steven Best[2], Edward Altshuler[2],
Jim Hunter[3], Terry Bullett[3], and Richard Barton[3]
Air Force Research Laboratory
AFRL/SNHA and AFRL/VSBXI
Hanscom AFB, MA 01731

Abstract: In this paper, we describe how to apply genetic algorithm (GA) optimization techniques to two diverse antenna optimization problems: electrically-small bent-wire antennas and a digital ionosonde transmit antenna. For each of these we present a description of the problem and one or more ways in which it can be modeled for genetic algorithm optimization. The goal of this paper is not to present optimal results for each of these antenna design areas, but rather to illustrate how antenna optimization problems can be translated into chromosome representations for genetic algorithm optimization. Lessons learned from using different chromosome representations are presented, along with simulated and measured results as available.

1. Introduction

Genetic algorithms (GAs) have been demonstrated as a useful tool for both designing and optimizing many different types of antennas, ranging from electrically small antennas to loaded monopoles and ultra wide-band antennas. [1,2,3,4,5,6]. However, it is not always clear how to translate one's antenna problem into a representation suitable for genetic optimization. This can be a major drawback towards the greater use of genetic algorithms for antenna design or optimization. ·

We differentiate the terms *genetic antenna design* and *optimization* as follows. In *genetic antenna design*, it is not necessary to have a pre-conceived notion as to the basic antenna shape. We start with a set of parameters that this shape must lie

---

[1] Lt Col Terry O'Donnell is an IMA (reservist) with AFRL/VSB and an on-site contractor (ARCON Corporation) for AFRL/SNHA.
[2] Dr. Best and Dr. Altshuler are from the Antenna Technology Branch of the AFRL Sensors Directorate (AFRL/SNHA).
[3] Major Hunter, Dr. Bullett, and 1Lt Barton are with the Space Weather Center of Excellence of the AFRL Space Vehicles Directorate (AFRL/VSBXI).

within and the materials that make up the antenna. The final shape and design of the antenna may vary widely, depending on the chromosome representation and how the genetic algorithm progresses. In some genetic algorithm designs, we may converge to a new nonintuitive antenna shape; in others, the GA continually reaches a well-known existing antenna design.

In *genetic antenna optimization*, we attempt to optimize the parameters of an existing antenna design for a particular electromagnetic environment to obtain the best customization of that design for the particular conditions of the problem. The role of the genetic algorithm in this case is searching through the parameters within that antenna design to find a good or optimal solution that meets our particular criteria.

We have shown in [6] that the genetic representation itself is key to how well a genetic algorithm can optimize a problem. Different representations yield different subsets of possible solutions, some of which are more-general than others. A good representation will allow for a large portion of the function space to be explored. A poor genetic representation will limit the type of antenna which may be expressed and only allow for pieces of space of all possible solutions to be explored. In this latter case, the solution found by the genetic algorithm may not truly be the optimal solution to the problem, but only the optimal answer which can be expressed by this chromosome representation.

In this paper, we illustrate chromosome representations for two very different types of antenna designs and optimizations. In the first, we revisit the problem of electrically-small bent-wire genetic antenna design and illustrate how different antenna models and chromosome designs affect convergence to an optimized solution. In the second, we explore genetic algorithm optimization of a hybrid digital ionosonde transmit antenna having a more complicated figure of merit. While we present simulated and measured results as currently available, the goal of this paper is not to present optimal results for each of these antenna types, but rather to illustrate how antenna optimization problems can be translated into a GA chromosome representation. In our discussion, we present lessons-learned in translation to chromosome representation and the limits inherent in these representations.

2. Genetic Algorithm Overview

A full discussion of genetic algorithms (GAs) is well beyond the scope of this paper; however, we present a limited overview here for the reader's benefit. The

132

literature abounds with many detailed discussions of simple and competent genetic algorithms; an excellent resource can be found in [7].

The genetic antenna designs and optimizations presented in this paper are created using what is known as a *simple* genetic algorithm, shown in Fig. 1. This is the type most widely used in the literature and what is generally thought of as a genetic algorithm.


Figure 1: Genetic algorithm overview. After determining a chromosome representation and developing a cost function, the genetic algorithm optimization loop is applied until convergence occurs.

First, a *chromosome* is designed to encode potential problem solutions, usually as a string of binary values. A *cost function* is developed so that different solutions may be compared against each other to determine which are better. After these are both developed, the genetic algorithm begins with an initial (usually random) *population*. The solutions represented by the population are evaluated and ranked using the cost function to determine which are better. Good parents are *selected* and then used in *recombination* to create children, which then have some probability of *mutation*. After mutation, the next population is evaluated and ranked. The process continues until an acceptable solution is found or convergence occurs (solutions do not continue to improve).

The simple operations of selection, recombination, and mutation act to combine pieces of salient information (called *schema)* from multiple "good" solutions together. Chromosomes with some of these good schema should perform better than other chromosomes without them and therefore be selected as parents. Through recombination, good schema representing different parts of a "good" solution have the chance of occurring simultaneously within the same chromosome to create an even better solution. Mutations allow for small changes to occur in the schema and new genetic material to be introduced which may not be present in the initial population.

Over time, we would like the GA to generate a chromosome which contains all the best schema and which represents the best possible solution to the problem. In a simple GA, that sometimes happens. Other times, especially in multi-modal problems, the GA converges prematurely to a non-optimal solution which represents a local minimum. Depending on the problem, the solution represented by one of these local minima might still be quite acceptable as an antenna solution; however, one should be careful about declaring this to be an optimal solution to the problem.

To help a simple GA work effectively, *it is important to encode one's chromosome so that pieces of schema which relate strongly to each other, such as those representing a certain physical characteristic of the solution, be somewhat close together in the chromosome.* This increases the probability that these schema will cross-over together during recombination[4]. In the following two examples, you will note our chromosomes have been developed with this principal in mind to allow the simple genetic algorithm to work as effectively as possible.

---

[4] Note that this is not so critical in competent GAs [7], where genes within a chromosome may be reordered dynamically or linked together to make sure that schema which are relevant to each other stick together during recombination.

3. Electrically Small Bent-Wire Antenna Optimization

The crooked wire genetic antenna design problem was first introduced by Altshuler and Linden [5] and the electrically-small bent wire antenna subsequently pursued by Altshuler in [1]. In this latter problem, the genetic algorithm was used to design new shapes of electrically small bent wire antennas. The goal of the genetic algorithm was to determine the lowest VSWR obtainable for a single wire antenna matched to 50Ω and fitting within a given physical cube size. Other constraints were that the antenna consisted of only a single wire and that pieces of the antenna within the cube could not touch the ground plane nor each other.

3.1 Coordinate Chromosome Representation

One method of encoding this antenna design for a genetic algorithm represents the antenna as a fixed number of straight wire segments connected in series at their
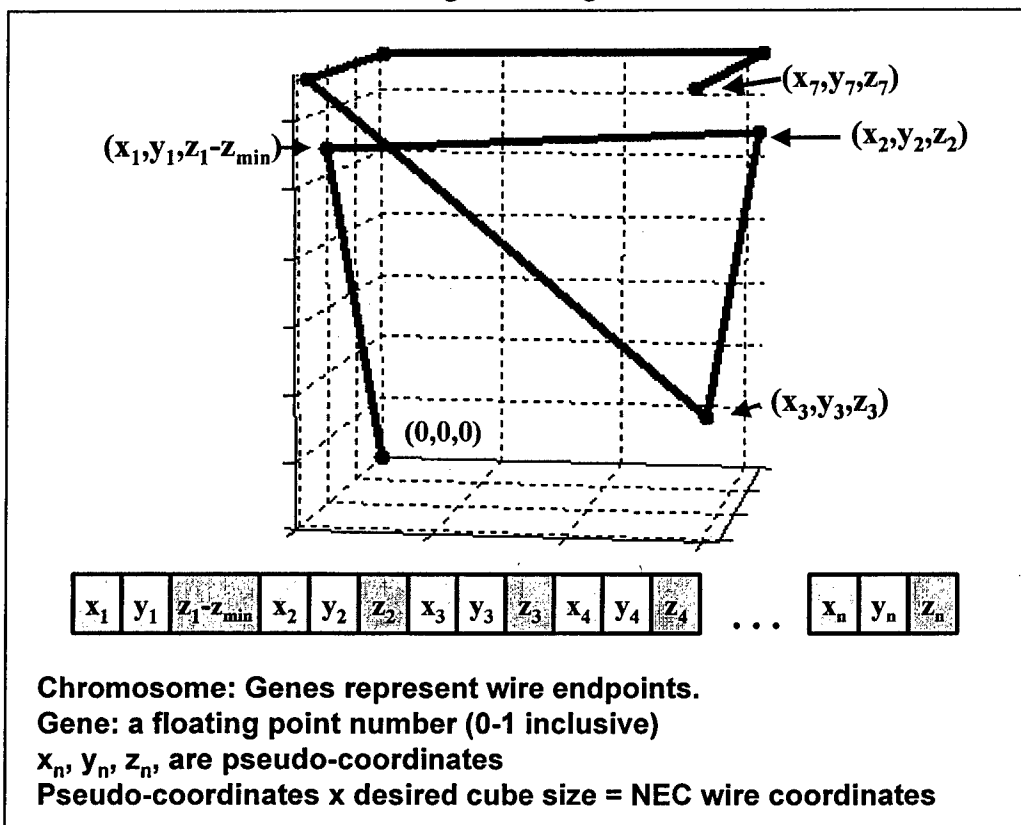
Figure 2. Coordinate-based genetic antenna chromosome and a typical resulting antenna.

endpoints (called "nodes"). The chromosome representation for this model then consists of a string of x, y, and z Cartesian-space coordinates for each of these nodes, as shown in Fig. 2. In the physical implementation of this chromosome, the nodes were originally coded using 5-bits for each coordinate [5]. However, in subsequent research, a real-valued GA was utilized and the coordinates represented by positive real values [1].

3.2 Angular Chromosome Representations

An alternative way to think of this problem is to model the antenna as a single piece of wire, subdivided into many fixed-length straight segments. The chromosome representation of an antenna would then be the angular orientation of each segment.

It is immediately obvious that there are two ways to represent these angular orientations. In the first sub-model, shown in Fig 3., we can represent them in an *absolute* fixed cylindrical coordinate system. In the second sub-model, the


$(x_{13}, y_{13}, z_{13}) = (x_{12}, y_{12}, z_{12}) + (\cos \alpha_{13} \cos \beta_{13}, \cos \alpha_{13} \sin \beta_{13}, \sin \alpha_{13})$

$(x_1, y_1, z_1) = (\cos \alpha_1, 0, \sin \alpha_1)$

$(0,0,0)$

| α_1 | α_2 | β_2 | α_3 | β_3 | α_4 | β_4 | ... | α_N | β_N |

Chromosome: 2N - 1 genes, Az/El angles of N equal-length wire pieces
(connected in series) comprising antenna of fixed length, L (in λ)
Gene: a n-bit, binary cyclic gray-coded angle (0-2π)
α_n are elevation angles, β_n are azimuth angles.
Pseudo-coord. offsets $[\Delta x_n, \Delta y_n, \Delta z_n] = ([\cos \alpha_n \cos \beta_n, \cos \alpha_n \sin \beta_n, \sin \alpha_n])$
NEC wire coordinates $= [x_{n-1}, y_{n-1}, z_{n-1}] + [\Delta x_n, \Delta y_n, \Delta z_n] \lambda$ L/N

Figure 3. The absolute angle genetic antenna chromosome and a typical resulting antenna.

136

$(x_{30}, y_{30}, z_{30}) = (x_{29}, y_{29}, z_{29}) +$
$(\cos \alpha_{30} \cos \beta_{30}, \cos \alpha_{30} \sin \beta_{30}, \sin \alpha_{30})$

$(x_2, y_2, z_2) = (x_1, y_1, z_1) +$
$(\cos \alpha_2 \cos \beta_2, \cos \alpha_2 \sin \beta_2, \sin \alpha_2)$

$(x_1, y_1, z_1) = (\cos \alpha_1, 0, \sin \alpha_1)$

$(0, 0, 0)$

$\Delta\alpha_1$	$\Delta\alpha_2$	$\Delta\beta_2$	$\Delta\alpha_3$	$\Delta\beta_3$	$\Delta\alpha_4$	$\Delta\beta_4$	$\cdots$	$\Delta\alpha_N$	$\Delta\beta_N$

Chromosome: 2N - 1 genes, representing Δ Az/El angles of N equal-length wire pieces (connected in series) comprising antenna of fixed length, L (in λ)
Gene: a n-bit, binary cyclic gray-coded angle (within +/- θ)
$\Delta \alpha_n$ are changes in elevation angle, $\Delta \beta_n$ are changes azimuth angles.
$\alpha_n = \alpha_{n-1} + \Delta\alpha_n \qquad \beta_n = \beta_{n-1} + \Delta\beta_n$
Pseudo-coord. offsets $[\Delta x_n, \Delta y_n, \Delta z_n] = ([\cos \alpha_n \cos \beta_n, \cos \alpha_n \sin \beta_n, \sin \alpha_n])$
NEC wire coordinates $= [x_{n-1}, y_{n-1}, z_{n-1}] + [\Delta x_n, \Delta y_n, \Delta z_n] \lambda$ L/N

Figure 4. The relative angle genetic antenna chromosome and a typical resulting antenna.

orientations may be represented *relative* to a cylindrical coordinate system centered on the vector orientation of the previous wire segment, with the z-axis lying along the segment, shown in Fig. 4.[5]

There are intuitive pros and cons to each of these sub-models. Supporting the first representation, one might consider that the electrical properties of a wire segment have some strong relationship to it's orientation to the ground-plane (and hence to its mirror image). This would favor the absolute angle representation.

However, a counter argument follows the logic of what happens during genetic algorithm mating (or *recombination*), where a piece of one chromosome (or antenna) is merged with pieces of another parent chromosome to create children for the next generation. In such mating, the schema might be better preserved in

---

[5] For both sub-models, the first azimuth angle was removed from the chromosome and fixed to be zero, to avoid competing identical solutions rotated around the z-axis. Also, for the relative angle chromosome, the first segment was represented relative to the z-axis of an initial reference frame.

the relative angle representation of the segments (relative to each other), rather than in absolute terms.

Rather than a real-valued chromosome, we encoded the angular chromosome representations into a cyclic gray-code binary representation. This has the benefit of allowing standard binary cross-over recombination operators, while eliminating the Hamming cliffs that occur in traditional binary representations. An additional benefit of a cyclic gray-code representation is the seamless cross-over in angular representation from the highest to the lowest values in this case from 2π back to 0.

3.3 Comparison of Chromosome Representations

We have illustrated three possible chromosome representations for the same antenna design problem. While a full discussion of the pros and cons of each approach has already been presented and may be found in [6], we provide a short summary here to illustrate the importance of good chromosome design.

First, not all of these representations are capable of representing all possible bent-wire antennas. In both the coordinate and angular chromosome representations, the number of straight wire pieces needs to be determined apriority. One could argue that if a sufficiently large number of small pieces were used, a general solution would be possible. However, experimentation showed that only the relative angle chromosome representation benefited from using many small pieces. The performance of both the coordinate and absolute angle chromosome representations deteriorated when the number of wire pieces or number of endpoint "nodes" exceeded a relatively small number (like 7-12 pieces). The relative angle representation, however, was successful with pieces as small as we were able to model with the limits imposed by the NEC thin-wire approximation methods. Hence this representation was best-able to model antennas closest to a general solution

Also notable is the fact that the angular representations require the antenna pieces to all be of equal-length and the total antenna length to be determined apriori, while the coordinate representation does not fix the length of the wire pieces or the total length of the antenna. These limitations could both be mitigated by expanding the angular chromosomes to include segment length information, which may be pursued in the future. However, note that the equal-length segments become only a very minor limitation when many very-small wire pieces are used: short pieces of antenna structure may be represented by only one or two of our short segments, while longer pieces are created by aligning the vectors many short segments to form one longer wire piece.
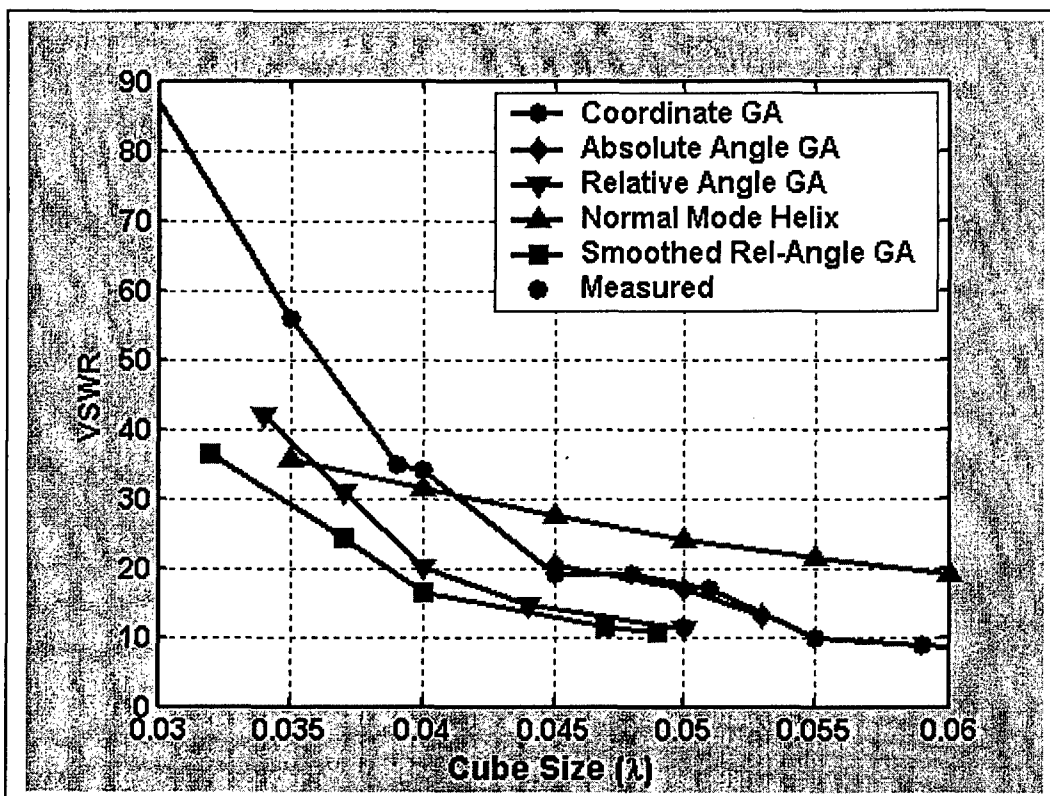
Figure 5: Comparison of lowest VSWRs obtained for a bent-wire antennas created by different chromosome representations for a desired cube size, of edge length λ.

Aside from the above discussion, other comparisons between and limitations of these three chromosomes can be made and are presented more completely in [6].

3.4 Results for Electrically-Small Bent Wire Chromosomes

In Fig. 5, we show results to date comparing antennas obtained using the coordinate, absolute-angle and relative-angle chromosomes. These results are more comprehensive than presently previous in [6], mainly because more GA runs have been completed.

We see that the absolute angle and coordinate chromosome representations performed similarly. The relative angle chromosome, using many small pieces, was able to create curving antenna structures which better met our criteria for low VSWR for a give cube-size. For comparison, we have included an electrically-

139

small normal-mode helix on our curve. To date, only one of the antennas (the relative-angle solution for the .05λ cube-size) has been built and measured; however, the measured VSWR was as predicted by NEC.

We must point out that none of these antennas may represent the *optimal* single bent wire electrically small antenna for these cube sizes. As described earlier, all of these chromosomes limit the resulting antenna shape somewhat from a general solution. In fact, when the shapes resulting from the relative angle genetic algorithm design are "smoothed" by hand with no limitations on segment size or angle, even better results are achieved, as also shown in Fig. 5.

We hope that this discussion of chromosomes for the small antenna problem has provided a useful backdrop for illustrating the importance of chromosome representation. We now move on to discuss an antenna optimization problem we are also currently applying genetic algorithms to.

4. DISS Ionosonde Optimization

The Digital Ionospheric Sounding System (DISS) network is operated by the US Air Force Weather Agency (AFWA) in order to observe and specify the global ionosphere in real time. There are over a dozen fully automated digital ionosondes deployed worldwide to perform this function. Within the Air Force, the DISS network provides data for many products, including specification and forecasts of primary and secondary HF radio propagation characteristics, ionospheric electron density, and total electron content, ionospheric scintillation, environmental conditions for spacecraft anomalies, and sunspot number.

The system basically consists of a transmitting antenna that sends radio signals of different frequencies across a specified sweep (usually between 2 and 30 MHz) in a vertical direction that are then reflected, absorbed, or distorted by the ionosphere. Receive antennas then intercept the returning signals, for processing by various analysis algorithms.

The current transmitting antenna, an off-the-shelf model TCI-613F (shown schematically in Fig. 6a) was not designed for ionospheric measurements and does not exhibit the consistent gain in the vertical direction for all of the desired frequencies. We explored adding a standard log period array (LPA) antenna to the TCI (Fig. 6b); however, for the desired electromagnetic coverage, the resulting structure was mechanically difficult to deploy and maintain in isolated areas with extreme weather. We therefore began an investigation to determine if
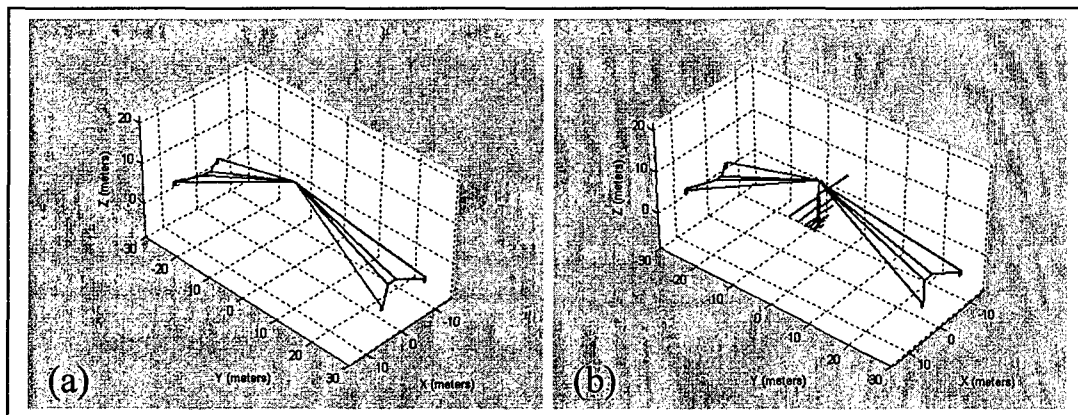
Figure 6: Schematic of TCI transmit antenna (a) and TCI with added LPA (b).

a modified antenna design could be optimized by a genetic algorithm for the DISS transmitting function.

4.1 Hybrid Folded-dipole / TCI Antenna Configuration

It was clear that we needed to add something resembling a log periodic array (LPA) or a folded dipole array to the TCI transmit antenna to provide additional frequency coverage. Since the mechanical structure of a standard LPA was unfeasible, we explored a folded wire design, using active elements folded down to additional ground stakes. We initially considered adding six parallel folded wires per side. However, since the addition of fourteen ground stakes per antenna was undesirable, we chose to modify the design to use only four additional stakes, two per side. This led to the hybrid antenna configuration shown in Fig. 7.

The hybrid antenna consists of some or all of the existing TCI antenna plus six pairs of new antenna wires. The wires are connected to the feed line, which runs up the tower, and are at various angles so that they may be mechanically connected to either part of the existing TCI curtain or two new ground stakes. Note that the entire length of each wire to the stake is not actively radiating – after the active length as been established, we transition to an insulator which then completes the mechanical connection.

The wires are currently arranged so that the highest new wire is connected out at an azimuth angle which allows it to be mechanically secured to the TCI curtain. The next two highest wires are connected to stake 1, with the lowest three wires are connected to stake 2.
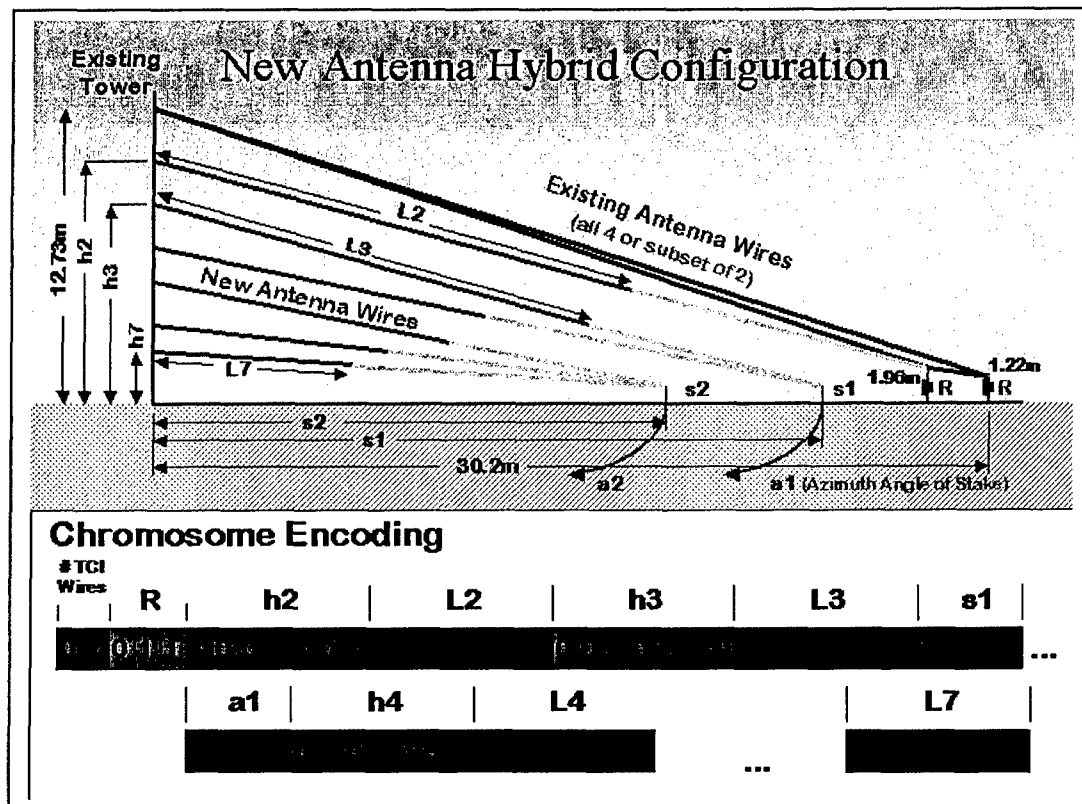
Figure 7: Hybrid antenna, using some or all of the existing TCI antenna, plus seven pairs of wires running down to either the TCI curtain or two new stakes.

The distances of the stakes from the tower and their azimuth angles relative to the TCI antenna are variable and part of the optimization, as are the active lengths of each wire and the height of the wire on the tower.

This basic hybrid antenna shape was based on: 1) the realization that an LPA-like structure would be a beneficial addition to the TCI, and 2) mechanical, fabrication, and implementation constraints that required us to create a robust solution that was low-cost, easy to implement, and used as much of the existing system as possible. However, there were a number of parameters in this solution that needed to be optimized in order to achieve a satisfactory electromagnetic solution.

142

4.2 Hybrid DISS Antenna Chromosome

As shown in Fig. 7, the chromosome we created to optimize this hybrid antenna design consists of a number of parameters. First of all, we were undecided on whether all the TCI wires (4 / side) were necessary or if the total antenna would be better if only a subset of the existing wires were used. Thus, the first 2-bit gene of the chromosome addresses these choices. The next gene of 3 bits addresses the value of the load resistance on the TCI antenna – it was initially 600Ω; however, we felt that it may need to be varied once the additional antenna structure was added.

Following this, we have genes addressing the heights and lengths of the six new wires (labeled L2 through L7[6]) and the two stake distances and azimuth angles (S1, A1, S2, and A2). The locations of these genes within the chromosome is somewhat important due to the necessity of keeping relevant genes together. For our current chromosome, we have embedded the stake distance and angle information for stake 1 (to which wires L3 and L4 connect) in-between the length and height genes for new wires 3 and 4. The angle and distance genes for stake 2 are located after the height/length genes for wire 5 (and before wires 6 and 7).

4.3 Figure of Merit

Our figure of merit for this optimization includes both an effective gain curve over the desired ionospheric measuring range from 2-30 MHz, and a desired VSWR (<= 3 when matched to 450Ω). We would ideally like a desired gain curve which is a constant 3dBi across our frequency range. However, given the reality of our lowest frequency (2MHz) and the physical area we are working in (within a 30 meter radius, roughly the existing footprint of the TCI antenna), we allow the desired gain curve to drop off somewhat at the low end, as shown in the graphs in Fig. 8. We may increase the desired gain curve at the low end in the future if we determine that our hybrid antenna design is capable of producing it.

Thus, our figure of merit, *FOM,* for this optimization consists of a weighted sum of the total effective gain error, Ge_{tot_err} (that which is less than our desired curve), the standard deviation of this error, Ge_{std_err}, the total VSWR error, $VSWR_{tot\_err}$ (that which is greater than 3) and the standard deviation of this error, $VSWR_{std\_err}$, such that:

---

[6] We consider the TCI antenna wires to be an implicit "wire 1" in the antenna, thus starting our new wire labeling with wire 2, having length L2 and height on the tower of H2.

143

$$FOM = Ge_{tot\_err} + 10 * Ge_{std\_err} + VSWR_{tot\_err} + 10 * VSWR_{std\_error} \qquad (1)$$

The standard deviation is important to avoid large error spikes in either effective gain or VSWR; however, it needs to be multiplied by 10 for it to have sufficient weight in the sum.

4.4 Initial Simulated Results for the Hybrid GA DISS Antenna

Our initial results using this chromosome to optimize the proposed hybrid DISS antenna using this figure of merit are extremely encouraging. Fig. 8a shows the effective gain and VSWR curves for the existing TCI antenna solution, simulated via NEC 4, and shown graphically in Fig. 6a. In Fig. 8b, we show similar curves that were obtained from simulations of the standard hybrid TCI / LPA solution shown earlier in Fig. 6b. In Fig. 9, we show one solution which has resulted from our genetic optimization of this hybrid folded-dipole design. While this is only a preliminary result, it shows that the genetic optimization was successful at using this chromosome to create an antenna which appears to be both mechanically
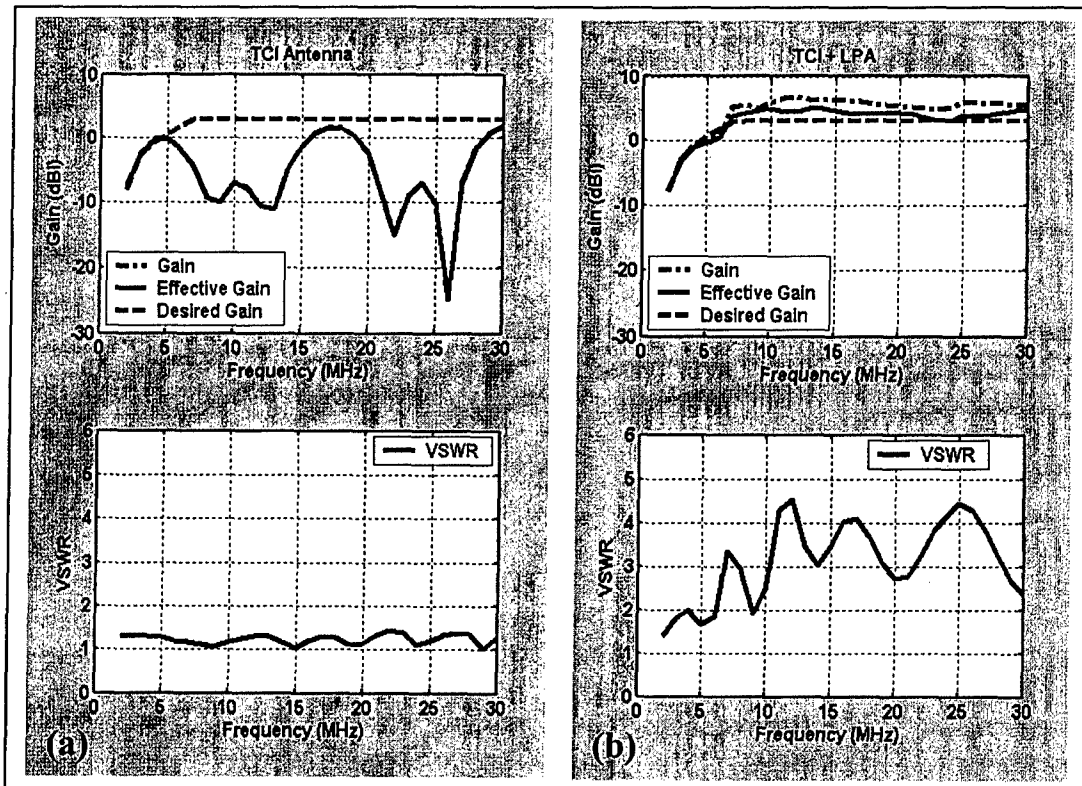
Figure 8: The modeled effective gain and VSWR of the existing TCI antenna (a) and the initial TCI+LPA configuration (b).

144
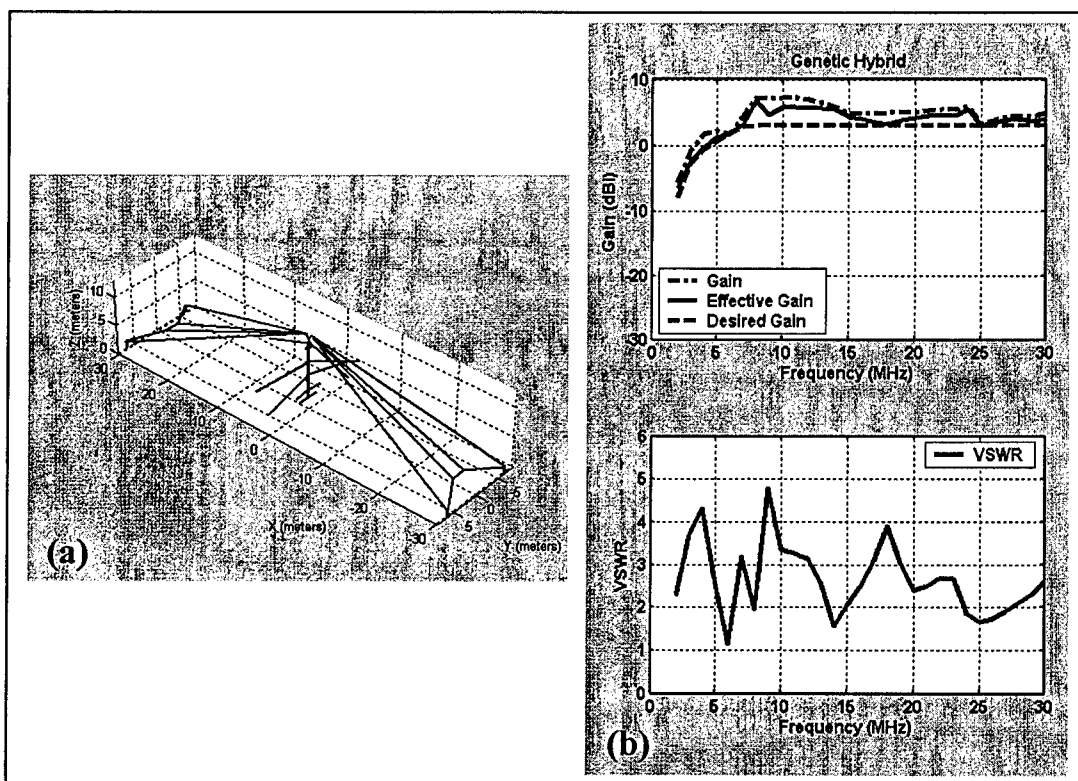
Figure 9: A schematic representation (a) and the modeled effective gain and VSWR (b) of the Hybrid GA DISS antenna.

feasible for our environment while presenting fairly uniform gain across the desired bandwidth and a VSWR that (while not as good as the TCI alone) is similar to that of the TCI+LPA solution that was not mechanically suitable.

5. Conclusions

We have presented chromosome representations for two very different types of antenna designs and optimizations. For the electrically-small bent-wire antenna design, we illustrated how the problem could be modeled in three different ways, yielding three different chromosome encodings. Our optimizations for each of these show that some encodings were more effective than others. In the second example, we described how genetic algorithm optimization was applied to a hybrid digital ionosonde transmit antenna with a more complicated figure of merit. While this research is still on-going, our initial results indicate that genetic antenna optimization of this hybrid antenna design will yield an acceptable solution.

145

Our hope is that this paper and our experiences presented therein will be of use to you in analyzing your own antenna design or optimization problem and in creating a chromosome representation that is suitable and effective for genetic antenna optimization.

6. Acknowledgments

7. References

[1] E. Altshuler, "Electrically Small Self-Resonant Wire Antennas Optimized Using a Genetic Algorithm, " IEEE Trans. Ant & Prop., Vol. 50, No 3, pp 297 – 300, March 2002.

[2] E. E. Altshuler and D. S. Linden, "Design of a Loaded Monopole Having Hemispherical Coverage Using a Genetic Algorithm", IEEE Trans. Ant. & Prop., Vol 45, No. 1, January 1997, pp. 1 – 4.

[3] A. Boag, A. Boag, E. Michielssen, and R. Mittra, "Design of Electrically Loaded Wire Antennas Using Genetic Algorithms", IEEE Trans Ant. & Prop., Vol 44., No 5., May 1996, pp. 687 – 695.

[4] Z. Altman, R. Mittra, and A. Boag, "New Designs of Ultra Wide-Band Communication Antennas Using a Genetic Algorithm", IEEE Trans.Ant.& Prop., Vol 45, No. 10, Oct. 1997, pp. 1494 – 1501.

[5] E. Altshuler, and D. Linden, "Wire-Antenna Designs Using Genetic Algorithms", IEEE Antennas and Propagation Magazine, Vol. 39, No. 2, April 1997.

[6] T. O'Donnell, E. Altshuler, and S. Best, "The Significance of Genetic Representation in Genetic Antenna Design", 2003 IEEE Antennas and Propagation Symposium, Vol.1, Section 7-3, June 2003.

[7] D. E. Goldberg, The Design of Innovation: Lessons from and for Competent Genetic Algorithms, Kluwer Academic Publishers, Boston, MA. 2002.

A Small Array of Boresight to Endfire Radiation Reconfigurable Antennas[1]

G. H. Huff, J. Feng, and J. T. Bernhard

Electromagnetics Laboratory
Department of Electrical and Computer Engineering
University of Illinois at Urbana-Champaign
Urbana, IL 61801

Abstract

This work describes the development of a 2x2 array of pattern reconfigurable antennas, capable of switching between boresight and endfire radiation patterns over a common impedance bandwidth. The reconfigurable element for the array is a single turn square spiral microstrip antenna on an electrically thin substrate, and is capable of reconfiguring its radiation pattern from boresight to endfire using two surface-mounted switching elements. An outline of the theory developed for standing wave devices to generate reconfigurable pattern behavior is also included. Application of the antenna array to geosynchronous satellites is also provided.

1. Introduction

Reconfigurable behavior of an antenna can manifest itself in a variety of different and useful forms. The desired properties of such an antenna may range from manipulation of the frequency response all the way to changing the radiation characteristics (such as pattern or polarization). Coinciding with the development and practicality of the reconfigurable antenna, reliable switching technologies continue to advance, providing endless possibilities for their application to future integrated antenna designs. As a result, systems that these antennas support are

likely to advance as well, or simply become smaller, lighter and considerably less expensive due to the increased functionality that comes with reconfigurability.

For the array of reconfigurable radiation elements discussed in this work, the pattern is reconfigured from boresight to endfire over a common impedance bandwidth. To develop a pattern reconfigurable array, the single element is discussed first and a model is presented that outlines the reconfigured radiation characteristics and geometry of the antenna. Measurements of the single element's radiation patterns and impedance are given next. Following this, the settings needed for the array to recover the reconfigured radiation characteristics of the single element are determined using pattern multiplication of the array factor and the individual element patterns. After the proper array settings have been determined, the 2x2 array is fabricated and measurements of the radiation patterns and the VSWR of the individual elements are presented. The final two sections provide a brief discussion on the application of the small array of reconfigurable elements to geosynchronous satellites and mobile communications and a summary of the work and possibilities for future work.

2. Element Characteristics

With an increasing amount of reconfigurable antennas under development, only a limited amount of research has been presented to characterize their operation. As a result, many of these devices become a challenge to formalize into a specific design process, making them somewhat enigmatic to scale and tune for individual applications. To develop a better understanding of the electromagnetics driving the pattern reconfigurable antenna discussed in this work, and gain insight into the fundamental operation of the device, an effective model of a standing wave reconfigurable antenna is presented.

2.1 Model Outline

To develop an effective model for the radiation reconfigurable antenna, the reconfigured pattern characteristics of the antenna become the defining parameter. For the antenna in this work, the desired radiation pattern is to be switched between boresight and endfire directions (relative to the antenna), and is to occur over a common impedance bandwidth. To capture this functionality, the model begins with a few observations about the geometry (shown in Figure 1) and operation of the antenna; a) the antenna is a standing wave device, b) the standing surface current distribution occurs only along the length of the line, and c) the standing current density that facilitates radiation can be replaced by a set of equivalent dipoles. The resulting reconfigured pattern behavior may be predicted

via pattern superposition of the equivalent dipole patterns. Using these guidelines, a model can be developed to enable this class of devices to reconfigure themselves for almost any type of operation.

The analysis begins with an examination of the standing current density for a given geometry. Using this distribution, the modal structure of the current density is replaced by an appropriate series of dipoles positioned appropriately at the location of the anti-nodes. Given a geometry that supports this modal current distribution, the linear separation of these equivalent dipoles is a half wavelength. Utilizing the geometry as a degree of freedom, these dipole moments are then given a specific orientation and phase provided by the sign of the anti-node. For a well designed geometry and placement of anti-nodes, array theory can simplify the characterization of the radiation pattern. Then, assuming the means are available through alteration of geometric character, the reconfigured pattern is achieved by modifying the current distribution, resulting in a phase shift between the equivalent dipoles that can then facilitate changes in radiation characteristics.

2.2 Antenna Geometry

The base geometry for the antenna is a single turn square microstrip spiral antenna [1, 2], which supports a standing wave on an electrically thin substrate. and is similar to the antenna in [3, 4, 5]. The antenna geometry along with the accompanying switching element positions can be seen in Figure 1 with the associated parameters in Table 1. The linear dimension of the antenna is 81 mm, approximately two wavelengths at the desired frequency and is fabricated on Duroid 5880 substrate ($\varepsilon_r = 2.2$) with height h = 3.175 mm (~0.072λ @ 6.8 GHz). A vertical SMA probe feed of diameter 1.23 mm is used to feed the antenna, which is shorted to ground at the opposing linear dimension using a via of diameter 1.23 mm. To alter the current distribution on the structure and reconfigure the radiation pattern, two surface mountable in-line switching elements of dimension 1.0mm x 1.0mm (currently hard wired for proof of concept) are incorporated into the design. For impedance tuning, the location of these switching elements can be carefully adjusted to achieve the correct impedance. To fully describe the reconfigured radiation, the antenna is examined for the two configurations used to reconfigure the radiation pattern from boresight to endfire over a shared impedance bandwidth. The first configuration discussed is that for the endfire radiation characteristics, followed by the boresight radiation configuration.

2.2.1 Endfire Configuration

In the endfire configuration, the switch at c' is closed and the switch at e' is open, yielding a total linear length of 81 mm. At this length, the antenna is approximately two wavelengths long at the design frequency of 6.8 GHz, and represents the second full standing wave mode of the antenna. Examination of the current distribution at this frequency places the resulting equivalent dipoles approximately at the corners of the structure (with a slight offset generated by the probe feed through the substrate). Since the standing current density lies on the corners, the resulting dipoles can be split into the two principle polarizations in the E-plane (xz) and H-plane (yz). With these current distributions representing the different polarizations, the equivalent sets of dipoles can be viewed as an array of dipoles that are spaced one half wavelength apart with a progressive phase difference of 180 degrees. The resulting radiation pattern can then be easily approximated as having endfire radiation characteristics using pattern multiplication.

2.2.2 Boresight Configuration

In the broadside configuration, the switch at c' is open and the switch at e' is closed, yielding a total linear length of 41 mm connected to the SMA probe feed, and 42.25 mm connected to the via to ground. In this configuration the antenna appears as two coupled single wavelength resonators, where the overlap between the two sections resembles a variation on a quarter wave coupled line filter. The SMA probe fed portion of the antenna acts as the driven portion of the coupled structure, with the grounded parasitic arm coupling the energy through the overlapping section, which is approximately one quarter of a guided wavelength. Since the coupling across the separation 's' represents a differential mode transfer of energy, the phase of the resulting currents on the parasitic arm are reversed and are 180 degrees out of phase from the probe fed section. By changing the phase of these currents on the parasitic arm, the resulting dipole arrangement is reversed, and hence the pattern is reconfigured. The analysis of the radiation characteristics is slightly different from the endfire configuration due to the standing current density being slightly shifted away from the corners on the parasitic section, but can be simplified to gain understanding of the radiation characteristics. With this slight shift off the corners and the increased magnitude of the currents on the parasitic section due to the coupling effects, a different distribution of magnitudes for the resulting set of dipoles occurs. Assuming that the current distribution is much greater on the parasitic arm, the currents on the driven section can be neglected, leaving only two orthogonal dipole orientations. This resulting dipole representation then yields an approximate boresight pattern.

150

2.3 Single Element Measurements

Measurements of the input impedance, VSWR, and radiation characteristics can be seen in Figures 3, 4, and 5 respectively (of the single element). Examining the plot of the VSWR for both configurations shows a shared impedance bandwidth of 96 MHz (1.39% BW), centered at 6.913 GHz. Examination of the radiation characteristics shows good agreement with the predicted pattern behavior from the dipole representation. In the boresight configuration, a tilt in the pattern is attributed to the relative magnitude difference in the dipole approximation (in which the contribution from the driven section was neglected), but the boresight characteristics are still maintained.

3. Array Configuration

For the array of reconfigurable antennas, several factors were examined to provide the necessary conditions needed by the two configurations in order to recover the functionality of the reconfigured antennas in an array setting. For this, the array factors for several different spacing and phasing scenarios were considered. Among these, two different array settings are considered along with the ground plane dimensions of the array.

3.1 Array Spacing

The array factors for each of the two array settings can be seen in Figure 6. To determine the relative performance tradeoffs of the two configurations, pattern multiplication between the single element pattern and the array factor has been used. The first array setting (Figure 6a) has a spacing that provides major lobes in the boresight and endfire directions, and uses the element pattern to dictate the peak and null directions. This spacing has several drawbacks however, including a full wavelength spacing (leading to a sparse array), and poor pattern control due to the onset of grating lobes from spacing and non-ideal pattern characteristics of the single element. To avoid these pitfalls, a better solution is found by spacing the elements one-half a wavelength apart (Figure 6b), and progressively phasing the elements in the endfire configuration 180° (Figure 6c). Doing so will result in an endfire pattern in the direction of progressive phasing, which will be addressed separately in both the E-plane and H-plane measurements. Although this array setting incorporates the additional complexity of phase shifters, both radiation configurations can be recovered. Consequently, the inter-element spacing in the array is quite small in the E-plane and H-plane, 3.8 mm (0.087λ) and 1.55 mm

(0.036λ) respectively, which will generate considerable effects on the performance of the array elements.

3.2 Ground Plane Dimensions

Along with the primary operating conditions (spacing, phasing, inter-element coupling, etc.), the ground plane dimensions are also examined and have shown significant effects on the performance of the array. Initial considerations of the ground plane dimensions arise from the desired performance of the array. For this particular antenna and array, a squinting of the endfire radiation away from the plane of the antenna has been seen in the single element when the ground plane dimension exceeds half a wavelength from all edges of the element, and is attributed to the far field beam forming restraints placed on it by the ground plane, similar to the squinted radiation pattern of a monopole over a finite ground plane. Therefore, effects from the asymmetrical placement of the elements on the larger ground plane of the array are also likely to influence the overall radiation characteristics of the array.

4. Experimental Results of the 2x2 Array

4.1 Common Impedance Bandwidth

Measurements of the VSWR for the endfire and boresight configurations can be seen in Figures 7 and 8 for the array. Earlier predictions of performance issues arising from inter-element coupling can be seen in the shifting and expansion of the VSWR bandwidths for the individual elements. Specifically, the upper and lower elements in the array show trends for each configuration depending on the row in which they reside. Since the dimension between rows (y-direction) is several times smaller than the column spacing (x-direction), the effect is much more pronounced in the rows of elements. This trend is especially evident in the boresight configuration where the quarter wave coupling section plays a key role in the operation of the individual elements. In total, the common impedance bandwidth is slightly broadened to 98.0 MHz (1.43% BW) with a shifted center frequency of 6.845 GHz.

4.2 Radiation Characteristics

Measurements of the radiation patterns for the endfire and boresight configurations can be seen in Figures 9 and 10 for the array. In the boresight configuration, the array performs well with minimal side lobes and an overall gain of 12.4 dBi. For all of the measured patterns, the maximum radiation occurs in

this configuration, and all endfire patterns are shown relative to this maximum. In the endfire configuration, the phasing in the E-plane and H-plane both generate well formed endfire radiation characteristics. The effect of ground plane dimensions can be seen in the radiation patterns for the endfire configuration for both the E-plane and H-plane phasing. For each of these patterns (Figure 10a and 10d), the maximum radiation occurs off of true endfire $\left(\theta = 90°, \phi = 0°, 180° \left(E - plane \right) \text{ and } 90°, 270° \left(H - plane \right) \right)$, at approximately $\theta = 60°$ with a gain of 9.52 dBi and 9.42 dBi for the E-plane and H-plane phasing respectively (also where the single element experiences a maximum endfire gain). For the total reconfigured pattern characteristics, the best operation is found in the phased E-plane setting where the resulting reconfigured pattern is linearly polarized in the cross-polarization and has a broad coverage.

5. Application

For the reconfigurable antenna presented, application to communication with geosynchronous satellites is considered as a possible application. Using the antenna in a small array setting, the coverage possible extends across the horizon and can be shifted towards the appropriate horizontal direction via the phasing in the x or y- directions. In doing so, communication through tunnels and during steep inclines or grades can be improved by reconfiguring the main beam towards the best possible reception which may not be directly overhead. Several drawbacks also arise from using an antenna with predominantly linear radiation characteristics because most down linked signals are broadcast in circular polarization. However, for linearly polarized signals the effects of multi-path should allow the antenna to operate effectively in most settings.

6. Conclusions

In this work, a 2x2 array of boresight to endfire pattern reconfigurable elements has been successfully demonstrated. In doing so, it has also been confirmed that the functionality of the individual reconfigurable elements can be recovered through judicious array planning, including spacing and phasing. Along with the array behavior of the individual elements, a model to describe the reconfigured radiation characteristics of the individual elements has also been developed and is in good agreement with the simulated and measured results. Future work for this antenna includes frequency and substrate scaling as well as integration with RF MEMS as well as other switching possibilities. Along with the physical parameters effecting the performance of the antenna, issues such as beam steering and grating lobes are also being considered.

7. Work Cited

[1] G. H. Huff, J. Feng, S. Zhang, J. T. Bernhard, "A Novel Radiation Pattern and Frequency Reconfigurable Single Turn Square Spiral Antenna," IEEE Microwave and Wireless Components Letters, vol.13, no. 2, pp. 57-60, Feb. 2003.

[2] G. H. Huff, J. Feng, J. T. Bernhard, "Theory and Measurement of a Radiation Reconfigurable Antenna," Submitted to IEEE Transactions on Antennas and Propagation.

[3] H. Nakano, S. Okuzawa, K. Ohishi, H. Mimaki, and J. Yamauchi, " A curl antenna," *IEEE Trans. Antennas Propagat.*, vol. 41, pp. 1570-1575, Nov. 1993.

[4] H. Nakano and H. Mimaki, " Axial ratio of a curl antenna," *IEE Proc.- Microw. Antennas Propag.*, vol. 144, pp. 488-490, Dec. 1997.

[5] C. Huang and K. Wong, "Stripline-fed printed square spiral slot antenna for circular polarization," *Electronic Letters*, vol. 34, pp. 2290-2292, Nov. 1998.

Via to Ground

Substrate

e'

e

s

w

In-Line
Open/Short
Circuit

b

y

c'

x

c

d

SMA
Probe
Feed

h

z

x, y

	[mm]
a	16
b	18
c	18
c'	7
d	20.25
e	12
e'	8.75
w	1.0
s	1.25
h	3.175
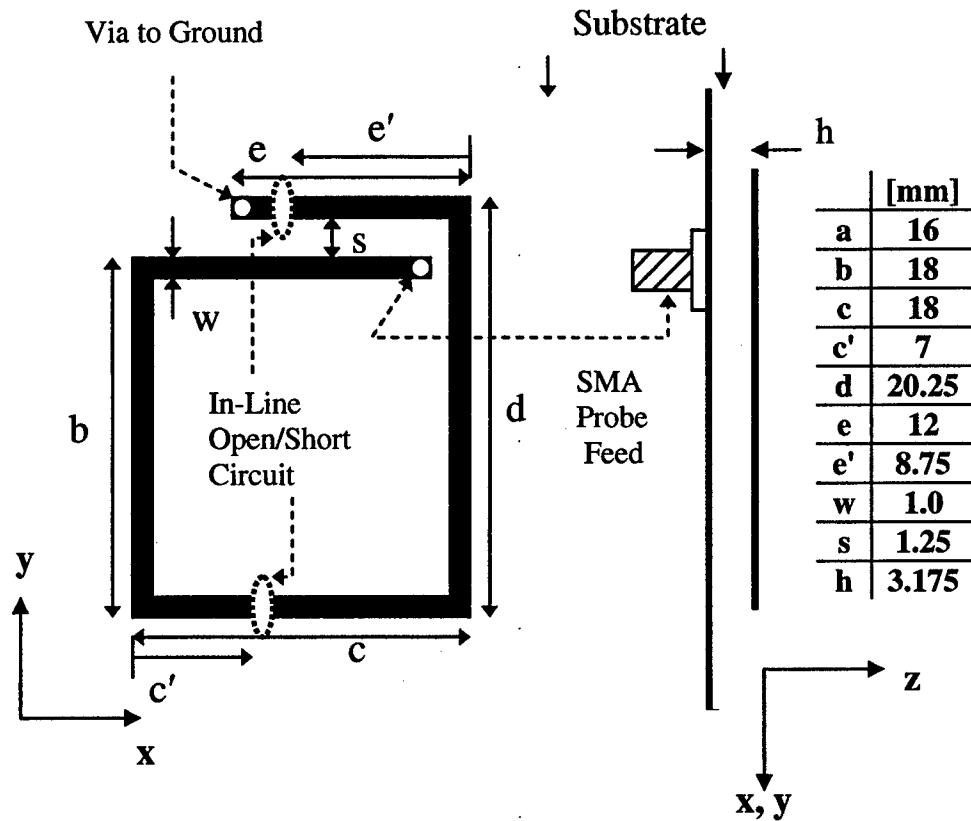
Figure 1. (Left) Antenna geometry and orientation for reconfigured pattern operation, (Right) list of given dimensions for the square spiral antenna. In the endfire configuration, the switch at e' is open and the switch at c' is closed, forming the square spiral geometry. For the boresight configuration the switch at c' is open and the switch at e' is closed, breaking the spiral and shorting the parasitic arm. In the orientation above, the E-plane is the xz-plane and the H-plane is the yz-plane.
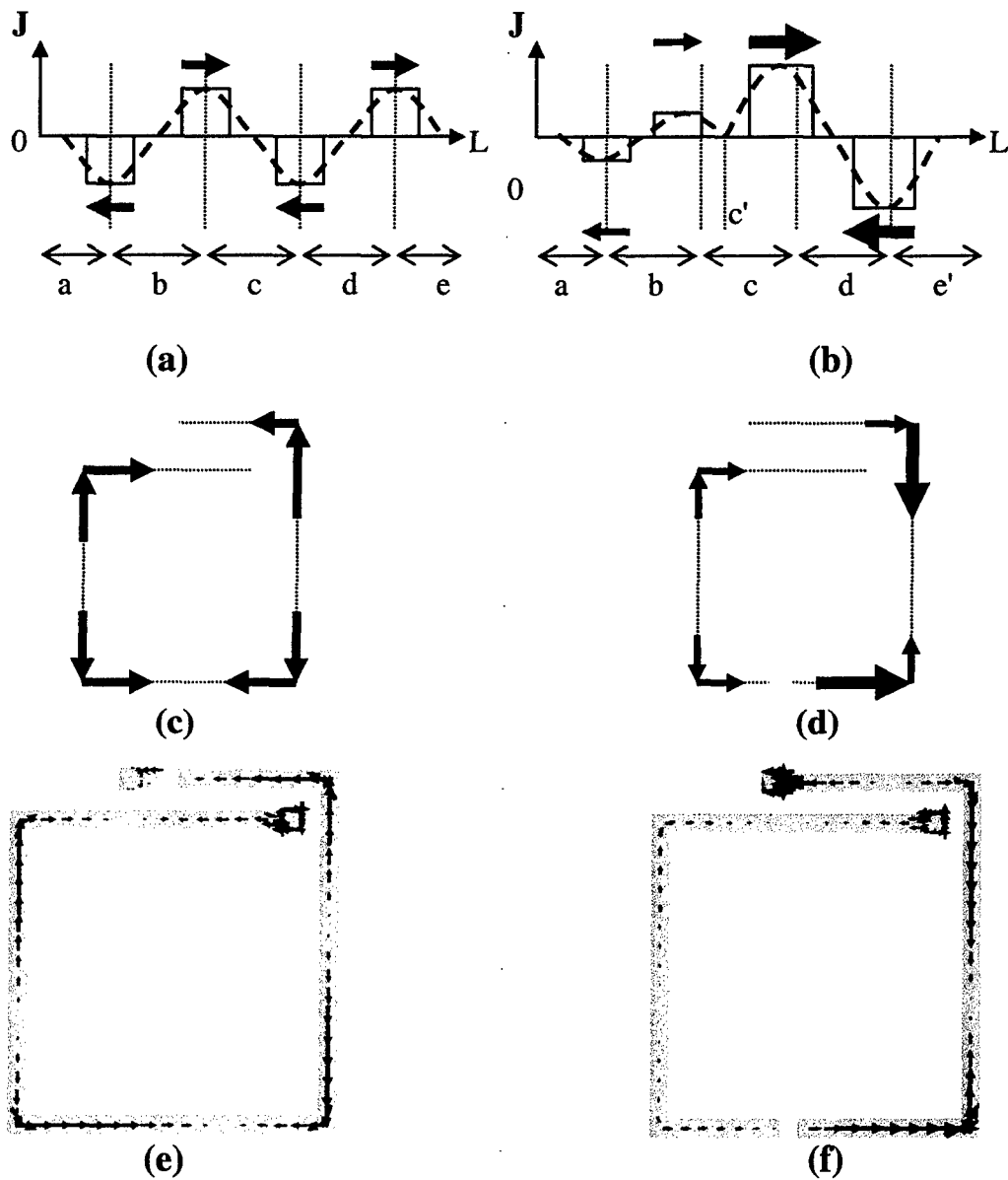
Figure 2. Graphical model for the prediction of radiation patterns via the mode structure of the current density **J** on spiral for the two configurations, endfire on left and boresight on right; (a) and (b) The approximate sinusoidal current distribution behavior of and equivalent set of dipoles, (c) and (d) Currents are mapped to the spiral geometry, resulting in the dipole array for use in the prediction of the radiation characteristics, (e) and (f) IE3D simulations of the surface current density on the two spiral geometries.
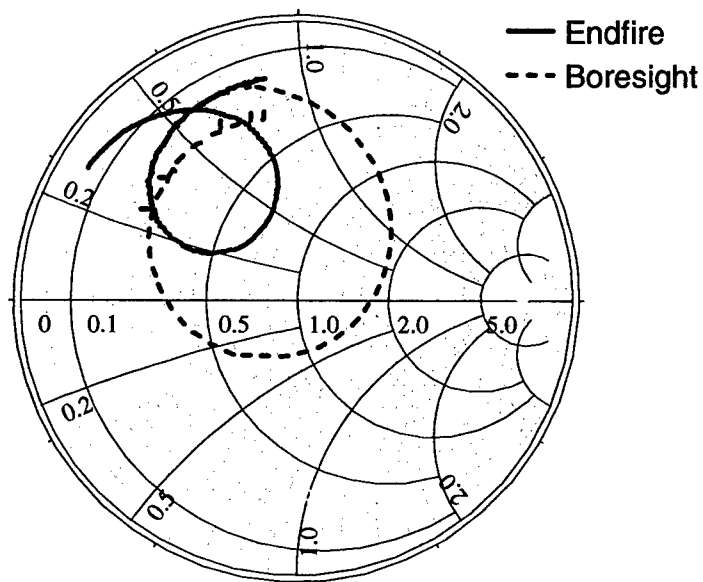
Figure 3. Measured input impedance of the endfire (solid) and boresight (dashed) configurations.
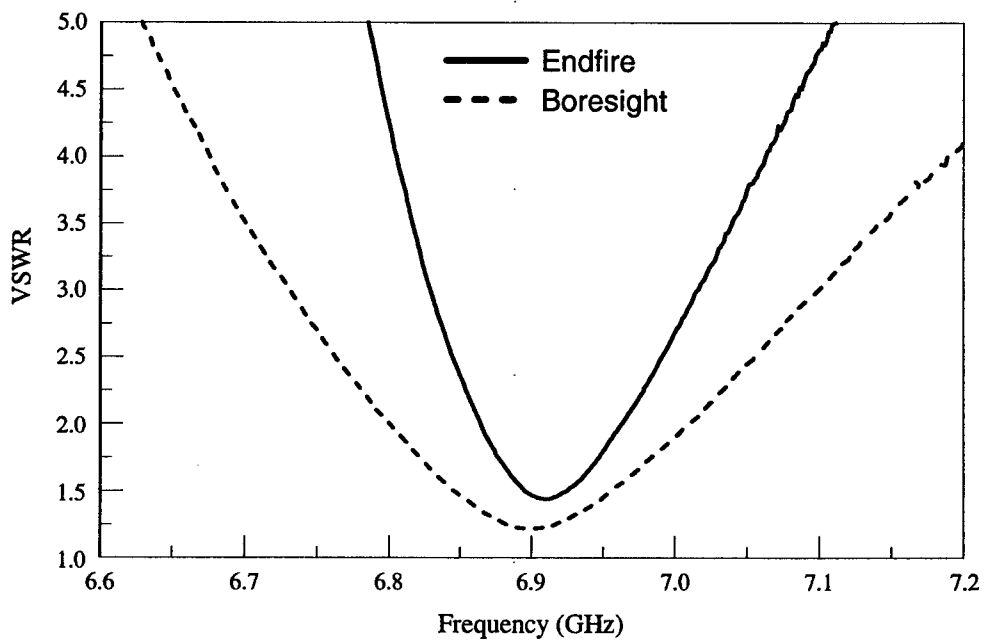
Figure 4. Measured VSWR of endfire (solid) and boresight (dashed) configurations with a common impedance bandwidth of 96 MHz (1.39 % BW) centered at 6.913 GHZ.
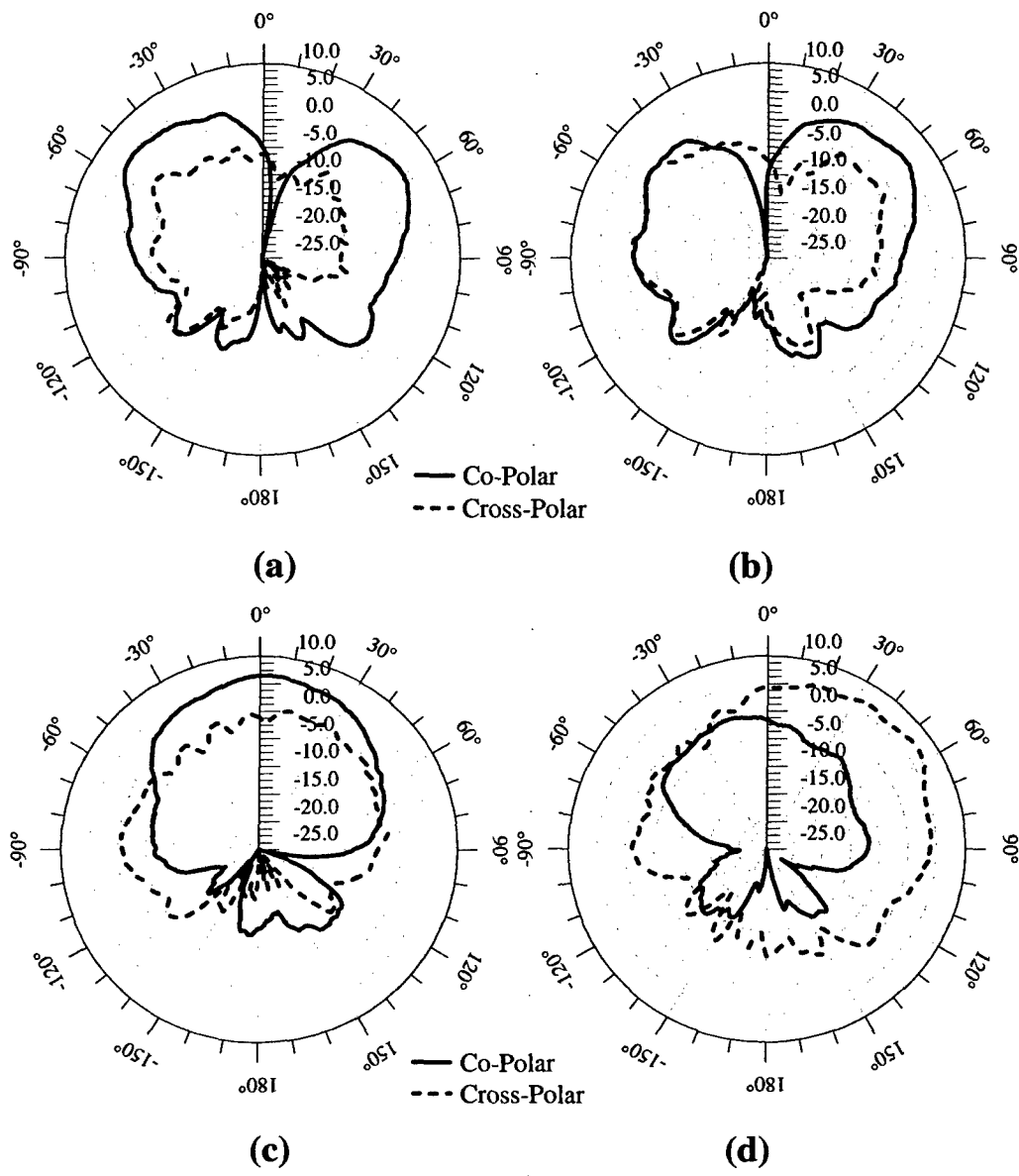
Figure 5. Measured single element radiation patterns for the (a) Endfire E-plane, (b) Endfire H-plane, (c) Boresight E-plane, and (d) Boresight H-plane.

(a)   **(b)**   **(c)**
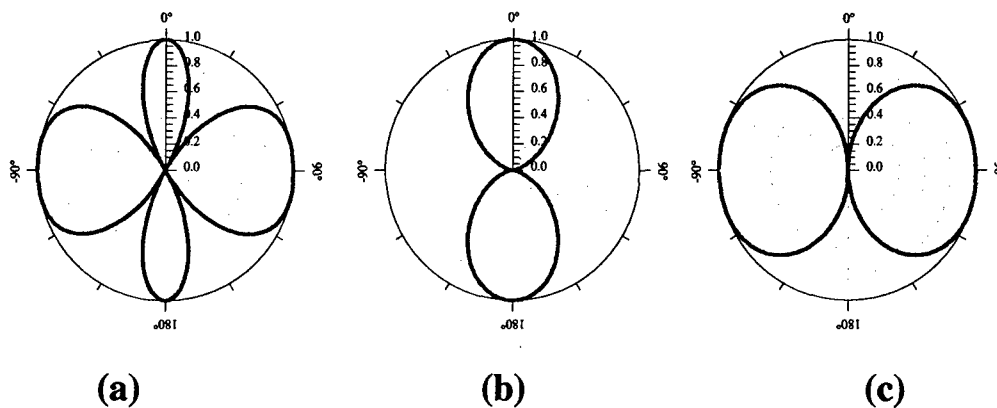
Figure 6. Two element array factors used to determine the operational characteristics of the antenna in an array setting; (a) configuration 1 uses a full wavelength spacing and is un-phased, (b) and (c) configuration 2 uses a half-wavelength spacing and is un-phased and progressively phased 180 degrees for the boresight and endfire configurations respectively.
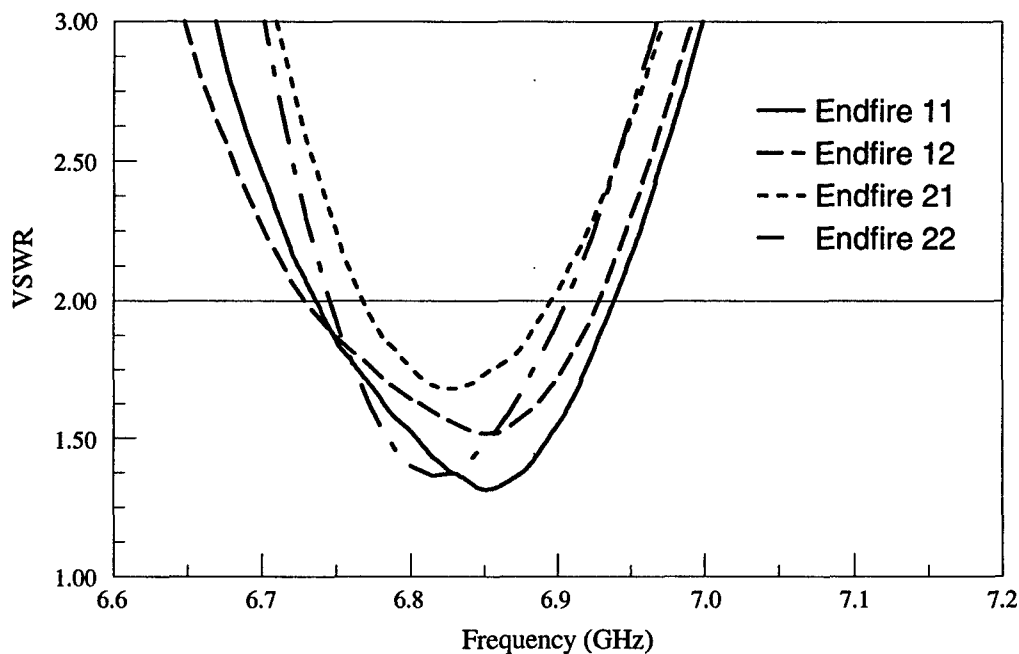
Figure 7. Measured VSWR of the array comprised of endfire configured elements. In the endfire configuration, the upper row of elements (11 and 12) experience a slight broadening of bandwidth, which is more pronounced in the lower row of elements (21 and 22). This is a result of the inter-element coupling.

159
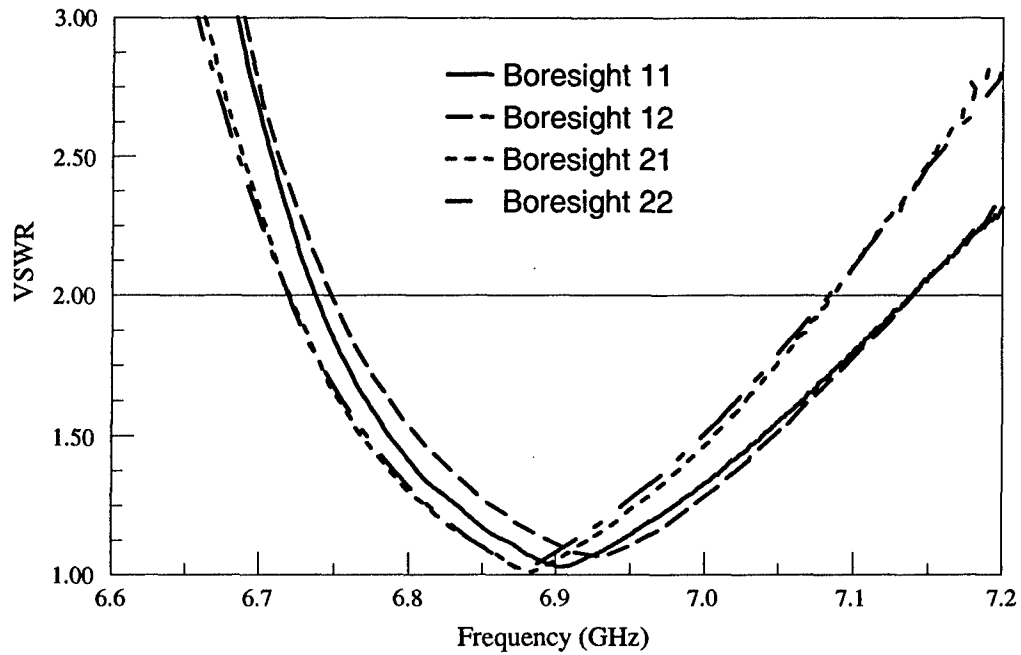
Figure 8. Measured VSWR of the array comprised of boresight configured elements. Note the trends in the upper row of elements (11 and 12) and lower the lower row of elements (21 and 22) due to the inter-element coupling.

(a)   **(b)**
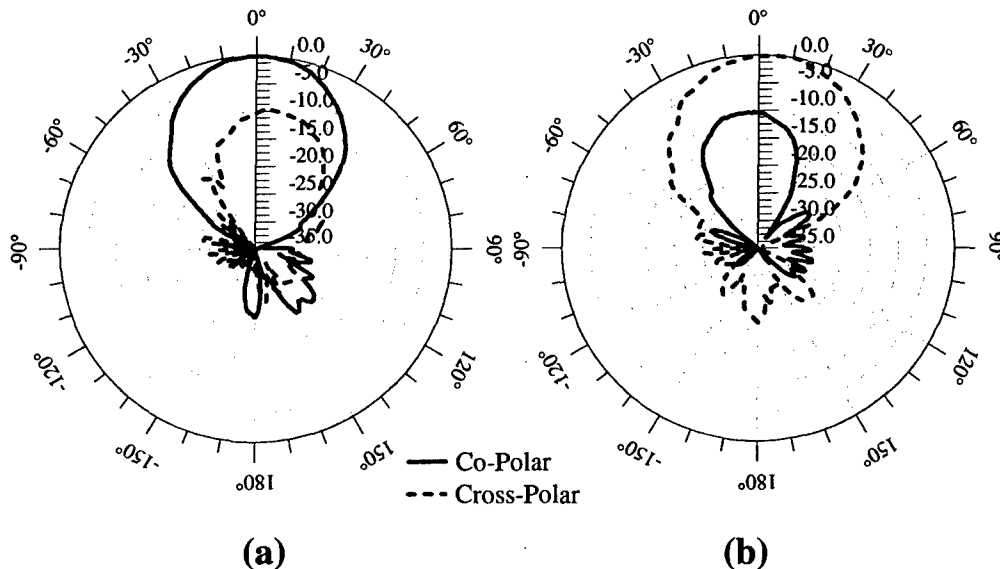
Figure 9. Measured (a) E-plane and (b) H-plane radiation patterns for the boresight configuration. The maximum gain for the array in this configuration is 12.41 dBi.

160
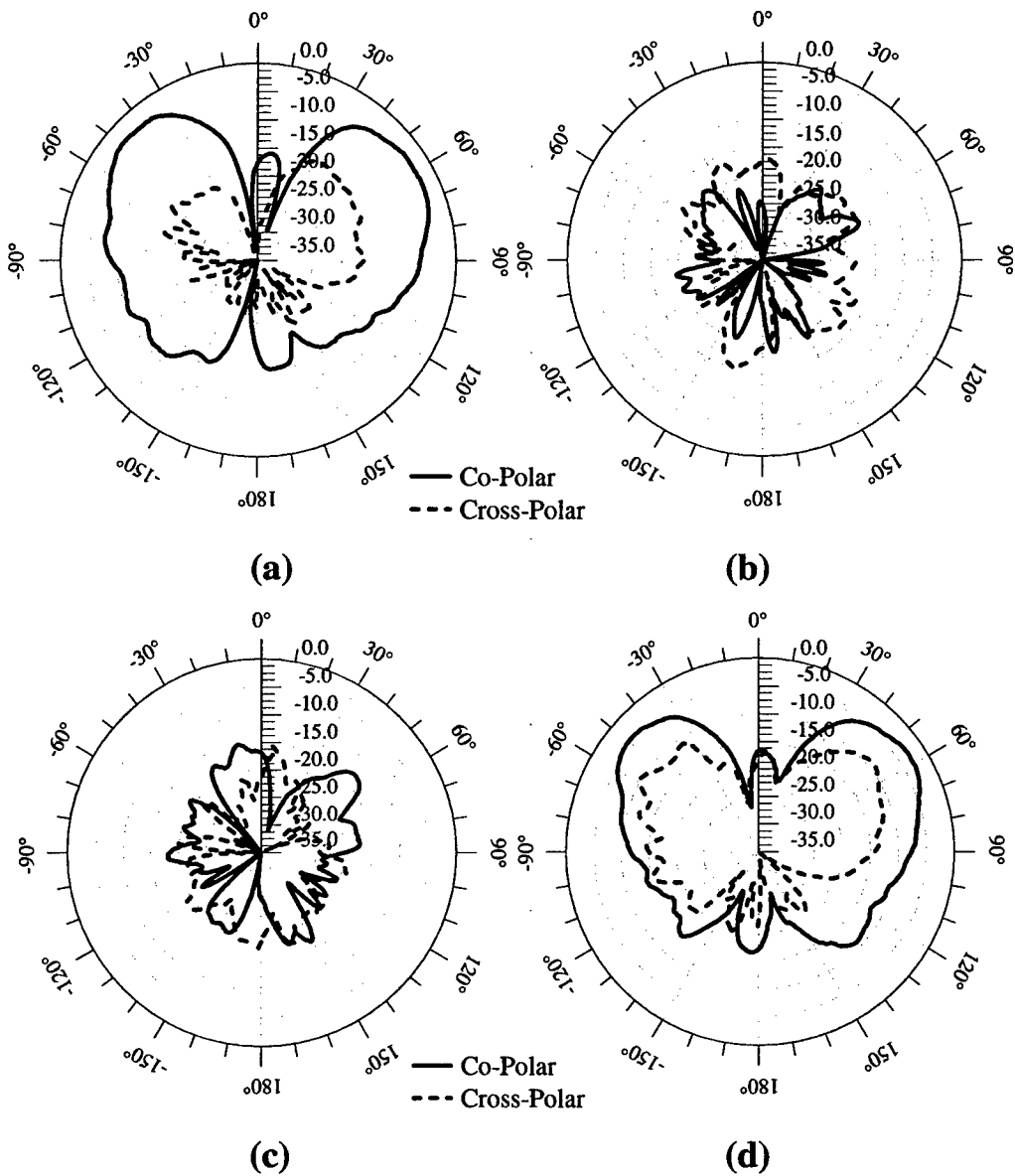
Figure 10. Measured 2x2 array radiation patterns for the endfire radiation configuration using two phasing routines; (a) and (b) are the E-plane and H-plane respectively for a 180° progressive phase shift in the E-plane (xz) and 0° in the H-plane (yx), (c) and (d) are the E-plane and H-plane respectively for a 180° progressive phase shift in the H-plane (yz) and 0° in the E-plane (xx). The maximum gain in (a) is 9.52 dBi and in (d) is 9.42 dBi, and is shown relative to the maximum radiation in the boresight configuration.

161

Effect of Dielectric Substrate on Infinite Arrays of Single-Polarized Vivaldi Antennas

S. Kasturi, D. H. Schaubert
ANTLAB, University of Massachusetts
Amherst, MA 01003

ABSTRACT

The effect of dielectric substrate on the performance of infinite arrays of single-polarized Vivaldi antennas is studied by computing the input impedance of an antenna in an array environment using full wave method of moments techniques. It is found that dielectric permittivity plays an important role in the wideband performance of such arrays, and comparison with dielectric-free cases for similar geometries is also included to bring out the impact of the presence of the substrate. The effect of substrate thickness is also studied. Results are shown to explain the trends and characteristics of parametric variation, which are useful in creating a new design, or in optimizing an existing one involving Vivaldi arrays aimed at wideband performance.

1. Introduction

The Tapered Slot Antenna (TSA) was first introduced by Lewis et al [1] in 1974, followed by Gibson [2] in 1979, who named it 'Vivaldi'. An important characteristic of the Vivaldi or notch antenna as it is also called, is its wide-scan, wide-band performance, when used as an element in a scanning array. These arrays are relatively easy to fabricate using printed circuit techniques, and the feed techniques are also convenient: microstrip or stripline is used, depending on the application and scale. Recognizing the potential of the TSA as an array element, extensive work has been done over the past couple of decades, resulting in a good amount of background on the subject [3]-[8].

An insight into the cause-effect relationship of different design parameters and antenna array performance is necessary to develop a successful design. Preliminary studies [9] have laid the foundation for study of parametric

dependencies in infinite TSA arrays. One important parameter that has been hitherto unexplored is the dielectric substrate. Though many of the designs that have been successfully implemented employ stripline feed circuits [10,11], the effects of varying the dielectric parameters (permittivity and thickness) have not been published. Antennas without substrate, i.e., dielectric-free antennas, have the advantage that they are less bulky, less expensive, and still yield reasonably good results [12]. This necessitated a comparative study of dielectric-free antennas and antennas with similar geometries employing stripline feeds, which was done in [13] using one value of dielectric permittivity. The present paper attempts to evaluate the effect of dielectric substrate by studying the performance for different permittivities, and also the dielectric-free case, over 27 different geometries. Further, the effect of thickness of dielectric is examined. The study was conducted by using the infinite-array analyses [14,15] that have been developed at the University of Massachusetts and verified by comparison to waveguide simulator experiments and to other computational methods.

2. Design Parameters and Method of Analysis

The design parameters of a Vivaldi antenna, called its 'geometry', are defined in Figures 1 - 3. All parameters except the ones under study are fixed based on previous studies [13]. The H-plane spacing is equal to the E-plane spacing, which is 8 cm (equal to half-wavelength at 1.875 GHz). For the permittivity study, each geometry is identified by the combination of three variable metal fin parameters, the opening rate **Ra**, antenna depth **D**, and cavity size **Dsl**. The variation of permittivity is studied for each such geometry (27 in all), with a constant thickness of t=0.32 cm (126 mils). Similarly, the variation of thickness is studied for several geometries, and three values of relative permittivity ε_r. Tables I and II list values of the variable parameters involved.

The several cases that were selected for permittivity study, dielectric-free and stripline-fed with ε_r = 2.2, 4 and 6 (Figure 4(a)), yield sufficiently different results to indicate the impact of ε_r on array performance and they span the range of substrates that are often considered for TSA array fabrication. The dielectric-free cases (Figure 4(b)) are of considerable interest because the cost and weight of microwave substrates used in stripline-fed arrays are too high for many applications. Antennas employing substrate thickness ranging from 30 mils to 150 mils are also studied, for three different dielectric substrates ε_r =2.2, 3.5 and 6.

163

Figure 1. Metal Fin Parameters (All dimensions in cm)
Ra: 0.1, 0.2, 0.3
D: 24, 32, 40
Dsl: 1.5, 2.0, 2.5

Figure 2. Feed – Stub Parameters
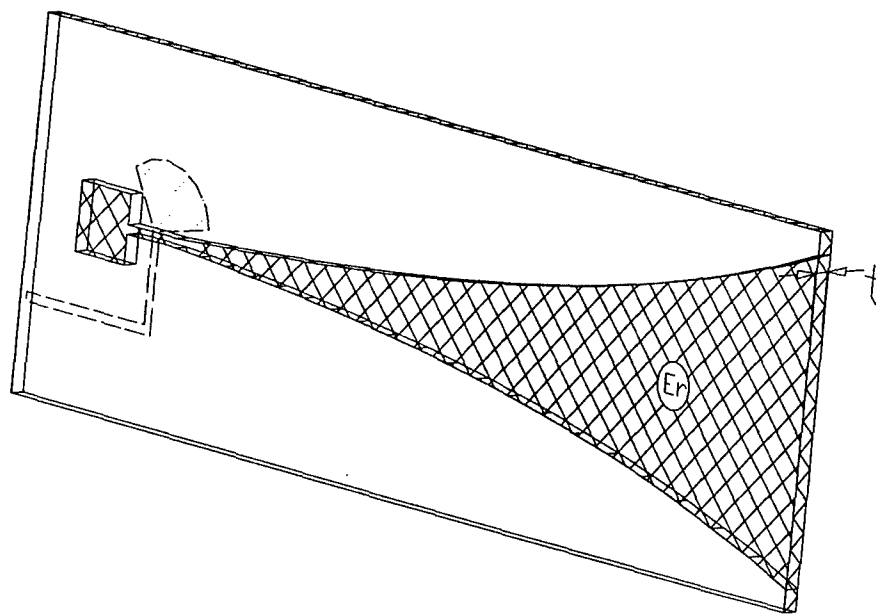
Figure 3. Dielectric Parameters

TABLE I
PARAMETERS FOR PERMITTIVITY STUDY

Relative Permittivity, ε_r	Substrate Thickness, t
2.2	0.32 cm (126 mils)
4.0	0.32 cm (126 mils)
6.0	0.32 cm (126 mils)
9.8*	0.32 cm (126 mils)

* ε_r = 9.8 case is computed only for one geometry (Dsl=1.5, D=24, Ra=0.1).

TABLE II
PARAMETERS FOR THICKNESS STUDY

Substrate Thickness, t	Relative Permittivity, ε_r
0.0762 cm (30 mils)	2.2, 3.5, 6
0.1575 cm (62 mils)	2.2, 3.5, 6
0.254 cm (100 mils)	2.2, 3.5, 6
0.381 cm (150 mils)	2.2, 3.5, 6
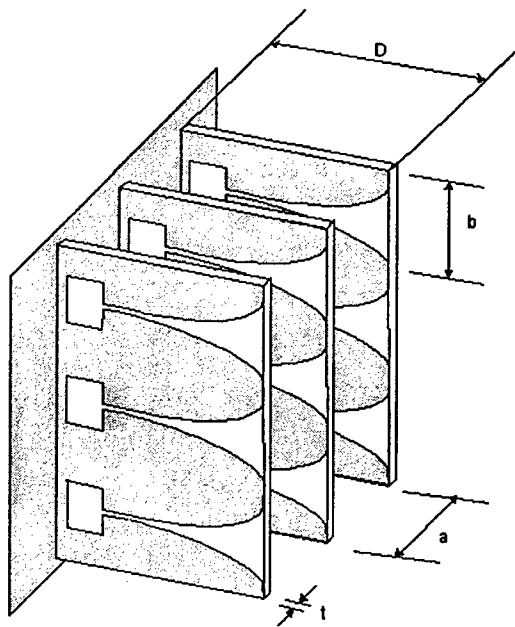
Figure 4. (a) Single-polarized TSA
array with dielectric.
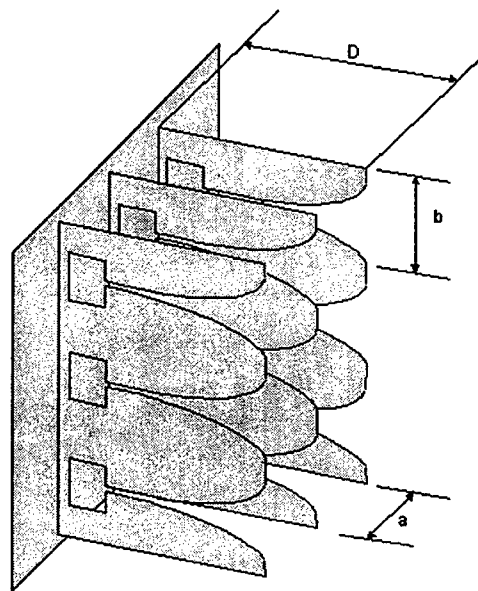
Figure 4. (b) Single-polarized TSA
array without dielectric.

Dielectric-free antennas are comprised of a metal fin and are fed by a balanced circuit or by microstripline on a small piece of substrate covering only a small portion of the antenna near the narrowest part of the slotline.

Two different Frequency – Domain Method of Moments (FD-MoM) computational schemes were employed to compute the input impedance of the dielectric and dielectric-free antennas. Both methods employ the unit cell approach and Floquet modes are used to represent infinite periodicity. The former [14] involves magnetic currents in the slot region while the latter [15] involves calculation of electric surface currents on the metal fin. The magnetic current approach is beneficial to model antennas with a dielectric sandwiched between the two metal fins.

Care was taken to maintain the same electrical point of reference for input impedances calculated by the different computation schemes, which is at the narrowest part of the slotline (the stripline-slotline transition in the case of dielectric). The dielectric-free (AIR) computation scheme directly yields the input impedance at the desired point; the dielectric (stripline-fed) computation yields the input impedance at the start of the stripline, as shown in figure 5 (b). A transmission line model (Figure 6) is used to transform the input impedance from

the start of the stripline to the desired reference plane at the stripline – slotline transition.
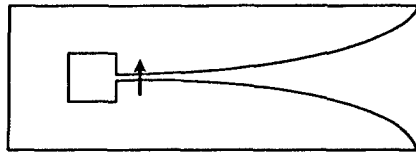
Figure 5(a). Feed mode on AIR
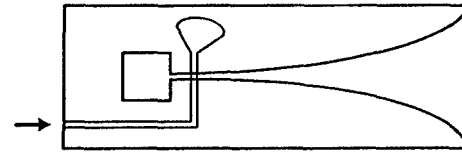
Figure 5(b). Feed mode on stripline-fed

The presence of the capacitive radial stub enhances wideband matching; however, its capacitance is excluded when comparing the input impedance with that of the dielectric case, in which there is no capacitive stub. The reactance of the radial stub is calculated using the MoM code for dielectric antennas but using basis functions *only on the feedline and stub*. This corresponds to analyzing a non-radiating stripline circuit. Previous work has shown that the stub reactance obtained from such an analysis yields good results. After the reactance is computed, it is subtracted from the input impedance at the stripline-slotline transition, which is obtained by employing the equivalent circuit shown in figure 6.
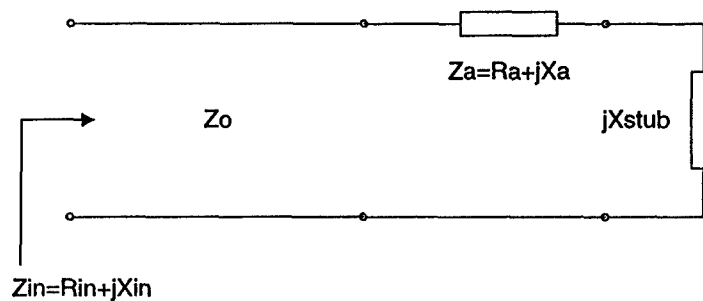
Figure 6. Equivalent circuit for stripline-fed

The following comments are to be noted with respect to the results that follow:

- For the dielectric-free case, the VSWR is calculated with respect to a normalizing impedance of 80Ω, which yields the best wide-band VSWR for most of the geometries.
- For the dielectric case, the VSWR is calculated by normalizing to the impedance value that yields for that case the best VSWR

through the whole band. This normalizing impedance is usually 40-80Ω.

- In the dielectric case, the impedance used to calculate the VSWR includes the radial stub reactance, since the capacitance of the stub is an integral part of the actual antenna and it usually improves the wideband VSWR.

3. Results and Discussion

3.1. Dielectric Permittivity (ε_r):

As stated earlier, the effect of dielectric substrate was studied over twenty-seven different geometries (of the metal fin) and compared against the dielectric-free case of the corresponding same structure. Figures 7, 8 and 9 below depict the impact of dielectric on the input impedance for a particular geometry. All impedances are evaluated for a broadside beam of the infinite array.
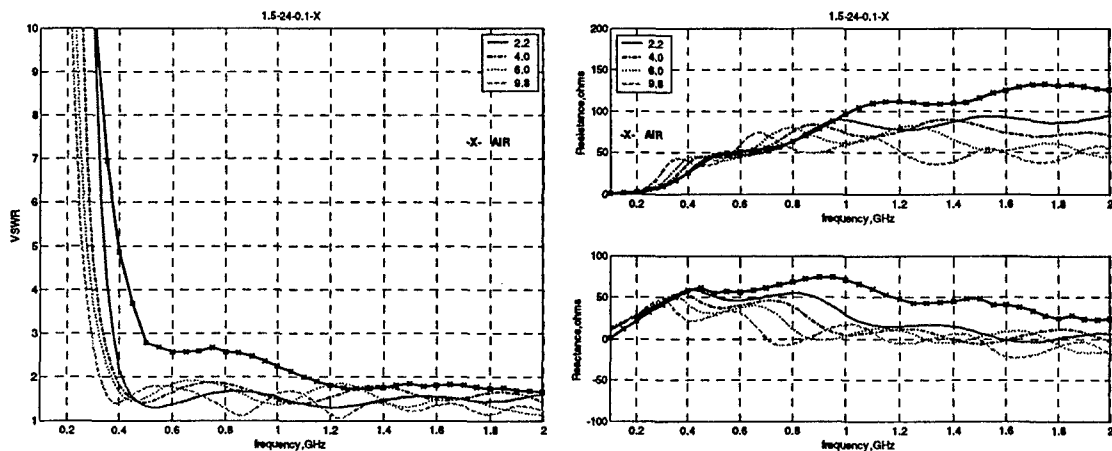
Figure 7. Effect of dielectric permittivity (ε_r =2.2, 4.0, 6.0, 9.8, slotline cavity size=1.5 cm, antenna length=24 cm, rate of exponential taper=0.1 cm^{-1})

168
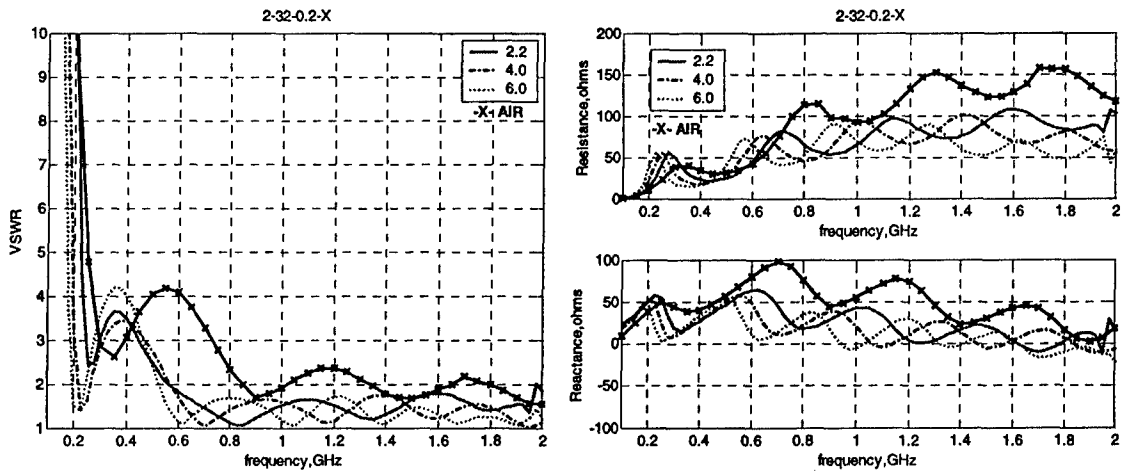
Figure 8. Effect of dielectric permittivity (ε_r =2.2, 4.0, 6.0 slotline cavity size=2 cm, antenna length=32 cm, rate of exponential taper=0.2 cm^{-1})
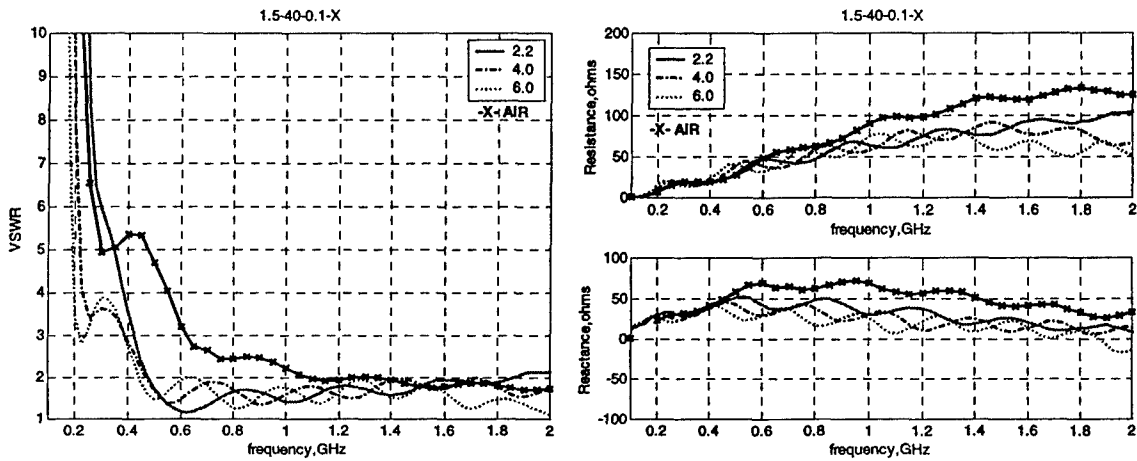
Figure 9. Effect of dielectric permittivity (ε_r =2.2, 4.0, 6.0 slotline cavity size=1.5 cm, antenna length=40 cm, rate of exponential taper=0.1 cm^{-1})

169

The following inferences can be made from the above and other similar comparisons for different geometries:

- The dielectric substrate has a significant impact on the slope and curvature of the average resistance. For the dielectric-free case, the average resistance increases almost monotonically across the operating frequency range. Hence it is difficult to pick a normalizing resistance that would yield reasonable VSWR for a wide band performance. With the presence of dielectric, however, the average resistance appears to increase and stay almost constant through a considerable range of frequencies; as the permittivity increases, the average resistance towards higher frequencies starts to decrease. In fact, for the ε_r =9.8 case (Figure 7), a second degree of oscillation can be discerned by the fact that the average resistance reaches a maximum below midband, then goes to a minimum, and starts to increase again towards the high frequency end. As is evident from the VSWR plot, the antenna with ε_r =9.8 has the widest operating frequency range.
- The antenna with the highest permittivity has its first resistive peak at the lowest frequency. This results in a lower minimum usable frequency, increasing bandwidth. In comparison, the slope of the resistance of the dielectric-free antenna results in a resistive peak at a much higher frequency, inhibiting its bandwidth.
- The number of oscillations (resonances) in resistance and reactance increases with permittivity. This is similar to the effect seen as the depth of the element increases. It appears that the number of oscillations is approximately determined by the depth of the antenna scaled by the dielectric loading of ε_r.

The strong dependence of low-frequency resistance on ε_r might be used in some cases, to overcome one of the drawbacks of Vivaldi arrays - antenna depth. The low-frequency operation of a Vivaldi array is dependent on the antenna depth - for a fixed dielectric permittivity, longer antennas tend to have greater bandwidth [13]. If there is a depth constraint, a short antenna with high permittivity might replace a longer antenna with low permittivity, provided the decrease in depth does not cut off more bandwidth than that which can be compensated by the increase in permittivity. Hence it is a balance that is to be achieved between the two parameters depth and permittivity, to optimize performance.

As shown in Figure 10, the 24-cm antenna with ε_r = 6 operates over a wider bandwidth with VSWR<2 than a well-designed antenna with ε_r = 2.2 that is

40 cm deep. For this particular geometry, the 32-cm antenna operates even better, since it balances the effects of depth and permittivity.
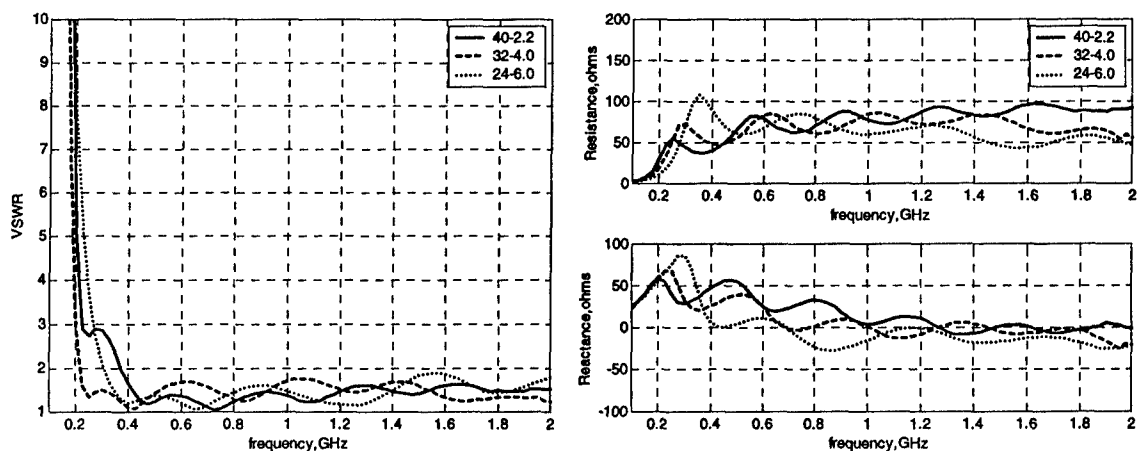

Figure 10. Depth compensation by higher ε_r (slotline cavity size =2.5 cm, opening rate =0.1)

3.2. Substrate thickness (t):

The effect of substrate thickness was examined for a thickness range of 30 mils to 150 mils, over three dielectrics, ε_r =2.2, 3.5 and 6. Other parameters of the geometry are kept constant. Figures 11, 12 and 13 depict the variation of input impedance for one particular geometry.
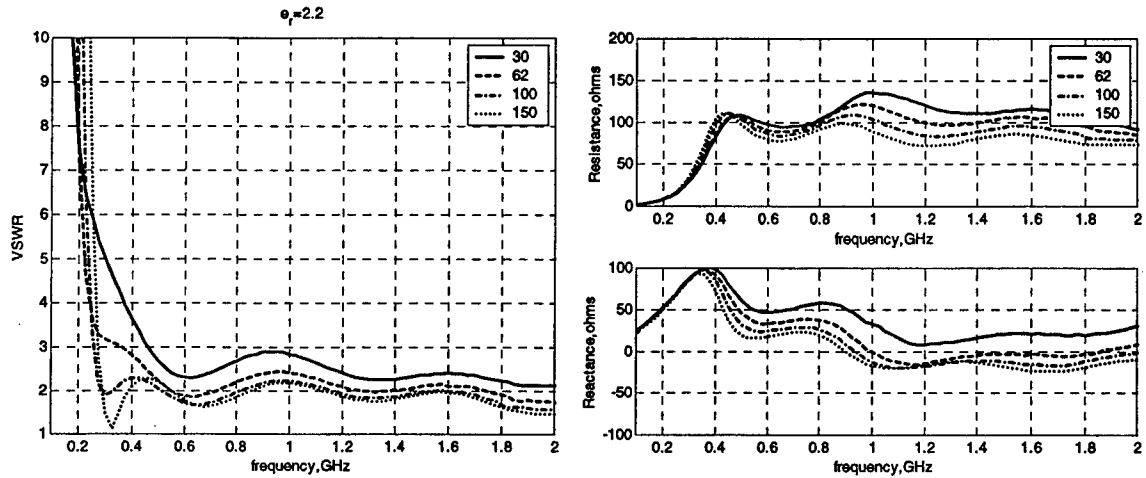
Figure 11. Effect of substrate thickness (t =30, 62, 100, 150 mils, ε_r = 2.2, slotline cavity size=2.5 cm, antenna length=24 cm, rate of exponential taper=0.1 cm^{-1})
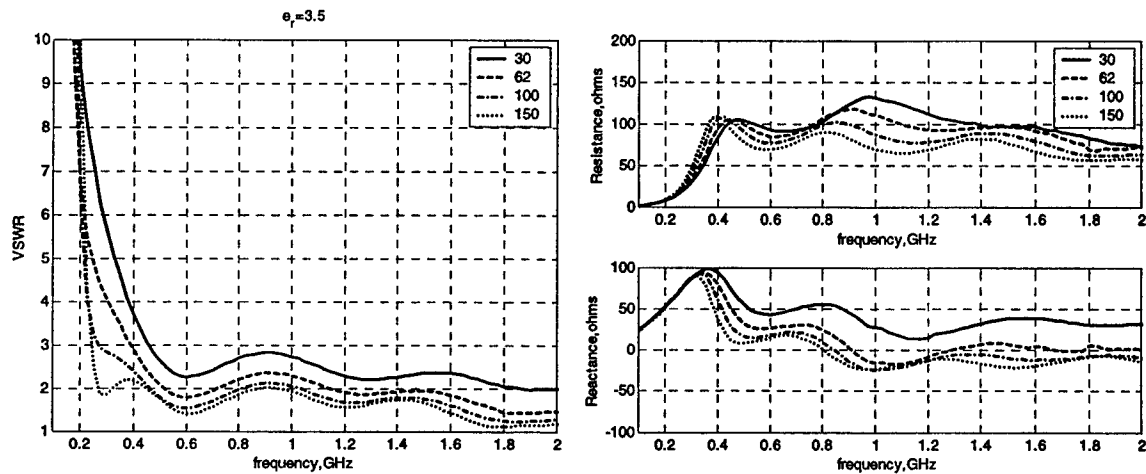
Figure 12. Effect of substrate thickness (t =30, 62, 100, 150 mils, ε_r = 3.5, slotline cavity size=2.5 cm, antenna length=24 cm, rate of exponential taper=0.1 cm^{-1})

172
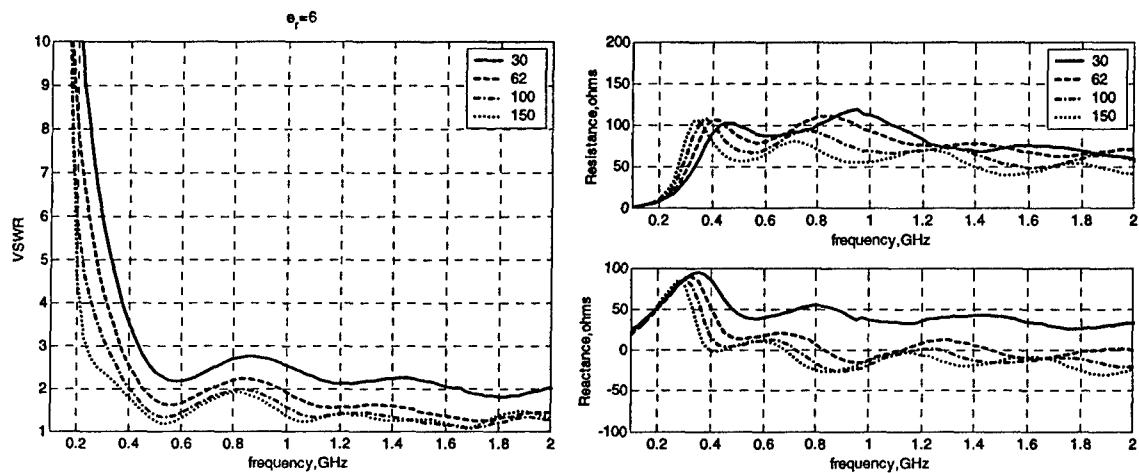
Figure 13. Effect of substrate thickness (t =30, 62, 100, 150 mils, ε_r = 6.0, slotline cavity size=2.5 cm, antenna length=24 cm, rate of exponential taper=0.1 cm^{-1})

The effect of changing substrate thickness can be summarized in the following trends:

- Substrate thickness affects the lower frequency performance of the antenna. With increasing thickness, the minimum usable frequency decreases, thus resulting in a larger band of operation. This effect can be seen especially in Figures 12 and 13, where the high dielectric constant accentuates the trend.
- Thicker substrates result in lower high frequency resistance.
- Thicker substrates result in lower reactance. The low-frequency inductive peak decreases as substrate thickness increases and the high-frequency reactance is near zero.

4. Conclusion

The effect of dielectric substrate is studied and it is found that

- Dielectric loading improves the low-frequency performance considerably in comparison to the dielectric-free case.

173

- Substrates of higher permittivities result in better bandwidths of operation for a given benchmark VSWR.
- The effects of dielectric permittivity can be utilized to counter disadvantages due to variation in other parameters such as changes in the metal fin geometry. For instance, a shorter antenna might be employed to operate over the same frequency range if a higher permittivity substrate is used (shorter antennas tend to have higher minimum usable frequencies).
- Substrate thickness also contributes to bandwidth enhancement-thicker substrates lead to lower frequencies of operation and lower antenna inductance.

5. Acknowledgements

6.Bibliography

[1] L.R. Lewis, M.Fasset and J. Hunt, " A broadband stripline array element", IEEE Antennas & Propag. Symp., pp. 335-337, June 1974.

[2] P. J. Gibson, "The Vivaldi Aerial", Dig. 9th European Microwave Conf., Brighton, UK, pp 120-124, 1979.

[3] D. H. Schaubert., "Endfire slot antennas", Journees Internationales de Nice sur les Antennes, pp 253-265, 13-15 November 1990.

[4] R. C. Hansen., Phased Array Antennas, Wiley-Interscience, 1998.

[5] P.S. Simon, K. McInturff, R.W. Jobsky and D.L. Johnson, "Full-wave analysis of an infinite, planar array of linearly polarized, stripline-fed, tapered notch elements", IEEE Antennas & Propag. Symp., pp. 334-337, 1991.

[6] R.S. Chu, A. Wang, and K.M. Lee, "Analysis of Wideband Tapered Element Phased Array Antennas", IEEE Antennas & Propag. Intl. Symp., June 1994. AP-S Digest, vol.1, pp. 14-17, 1994.

[7] E. Thiele, and A. Taflove, "FD-TD analysis of Vivaldi flared horn antennas and arrays", IEEE Trans. Antennas & Propag., vol. 42, pp. 633-641, May 1994.

[8] M.F. Catedra, J.A. Alcaraz, and J.C. Arredondo, "Analysis of arrays of vivaldi and LTSA antennas", Antennas & Propag, Society Intl Symp., June 1989. AP-S Digest, vol.1, pp. 122-125, 1989.

[9] J. Shin and D.H. Schaubert, "A parameter study of stripline-fed vivaldi notch-antenna arrays", IEEE Trans. Antennas & Propag., vol.47, pp. 879-886, May 1999.

[10] Nick Schuneman, James Irion and Richard Hodges, "Decade bandwidth tapered notch antenna element", Proc.2001, Ant. Appln. Symp., pp. 283-294, Monticello, IL.

[11] M. Kragalott, William R. Pickles, and Michael S. Kluskens, "Design of a 5:1 Bandwidth stripline notch array from FDTD analysis", IEEE Trans. Antennas & Propag., vol. 48, pp. 1733-1741, November 2000.

[12] H. Holter, "Element for wideband and very wide angle phased arrays", IEEE Antennas & Propag. Society Intl. Symp., July 2001. AP-S Digest, vol. 2, pp. 440-443, 2001.

[13] Kasturi S., Boryssenko A. O. and Schaubert D. H., " Infinite arrays of tapered slot antennas with and without dielectric substrate", Proc.2002, Ant. Appln. Symp., pp. 372-390, Monticello, IL.

[14] D.H. Schaubert, Jon Anders Aas, M.E. Cooley and N.E. Buris, "Radiation and scattering analysis of infinite stripline-fed tapered slot antenna arrays with a ground plane", IEEE Trans. Antennas & Propag., vol.42, pp. 1161-1166, Aug 1994.

[15] Michael E. Cooley, D.H. Schaubert, Nicholas E. Buris and Edward A. Urbanik, "Radiation and scattering analysis of infinite arrays of endfire slot antennas with a ground plane", IEEE Trans. Antennas & Propag., vol.39, pp. 1615-1625, November 1991.

A NOVEL APPROACH FOR BANDWIDTH ENHANCEMENT OF SLOT ANTENNAS

Nader Behdad, and Kamal Sarabandi
Department of Electrical Engineering and Computer Science
University of Michigan, Ann Arbor, MI, 48109-2122
behdad@eecs.umich.edu, saraband@eecs.umich.edu

Abstract: **A novel approach is presented to improve the bandwidth of slot antennas. The technique is based on manipulating the field distribution along an ordinary resonant slot structure using the feed line and creating a dual resonance behavior. Hence without changing the length of the antenna its bandwidth is increased by more than 200% relative to a narrow slot. The field distribution along the slot at a frequency slightly above its natural resonance is manipulated by a narrow microstrip line feeding the slot near one of the two edges. By proper choice of the slot width, feed location, and microstrip feed line a fictitious second resonance can be created by establishing a null in the electric field distribution along the slot near the feed line. This null is resulted from the superposition of the microstrip near field and the slot field excited by the displacement current. A prototype is designed and tested at the center frequency 3.4 GHz. A large bandwidth of 37% is achieved without any constraints on impedance matching or complexity in the antenna structure. Also bandwidth enhancement of a miniaturized slot antenna using parasitic coupling is presented. The antenna occupies a small area of $0.15\lambda_0 \times 0.15\lambda_0$ and can have up to 3% bandwidth.**

1. INTRODUCTION

High bandwidth, small size, simplicity, and compatibility to the rest of the RF front-end are desirable factors of an antenna. Enormous effort has been invested on designing frequency independent or very wide band antennas. One of the major drawbacks of such antennas is their relatively large size which can potentially eliminate their use for mobile wireless applications. Therefore, it is desirable to develop other techniques to increase the bandwidth of otherwise narrowband antennas without significantly increasing their sizes. Here we describe two different techniques for enhancing the bandwidth of slot antennas. Microstrip-fed wide slot antennas have been theoretically studied in [1] and experimental investigation on very wide slot antennas that result in wide band antennas has also been performed by various authors [2], [3] but not much effort

has been put into the investigation of the radiation characteristics of the moderately wide slot antennas. Unlike very wide slots, these antennas do not produce high levels of cross polarization and their feeding mechanism is much simpler than the fork shaped [2], [3] or T-shaped microstrip feed [4] normally used in very wide slot antennas. In the following two sections a microstrip-fed wide slot antenna is studied and it is shown that its bandwidth can be more than doubled by creating a fictitious short circuit along the slot or it can be operated in a dual band mode with considerable bandwidth at both frequency bands.

The fundamental limitations on electrically small antennas have been extensively studied by various authors [6]-[8]. Early studies have shown that for a single resonant antenna as the size is decreased its bandwidth (BW), if it can be matched, and efficiency decrease too [6]. This is a fundamental limitation which in general holds true independent of antenna architecture. Recently, there have been a number of studies on different approaches for antenna miniaturization while maintaining a relatively high bandwidth and efficiency. A novel miniaturized slot antenna was recently presented [9]. This element shows good radiation characteristics but has a rather small bandwidth (less than 1%). In the second part of this paper Bandwidth enhancement of this class of miniaturized antennas using a dual resonant topology is examined. Basically the miniaturized slot antenna configuration similar to the one used in [9] is considered to form a dual antenna structure. In this new configuration one of the elements is fed by a microstrip transmission line and the other one is fed parasitically by the first antenna. It is shown that the bandwidth of this new double-element configuration is twice the bandwidth of a single antenna that occupies the same space. In other words by keeping the same space as the single antenna the bandwidth is increased by a factor of two.

In what follows first the design of a microstrip-fed broadband slot antenna is presented in section 2 then dual band characteristics of such antennas is examined in section 3 and in section 4 bandwidth enhancement of miniaturized antennas using parasitic coupling will be studied.

2. WIDEBAND MICROSTRIP-FED SLOT ANTENNA

A resonant narrow slot antenna is equivalent to a magnetic dipole at its first resonant frequency. Its length is $\lambda_g/2$ where λ_g is the guided wavelength in the slot. If the slot antenna is fed near an edge by a very narrow microstrip line and the slot width is properly chosen, at a frequency above the first slot resonance, a fictitious short circuit near the microstrip feed may be created. Basically the tangential electric field created by the narrow microstrip line at a particular distance cancels out the electric field of the slot excited by the return current on

177

the ground plane. A full wave simulation shows the field distribution for this situation in Figure 1(b) whereas Figure 1(a) shows the electric field distribution in the slot at its normal first resonance. The field distribution is shown to have a null along the slot between the two ends at a frequency slightly above the slot resonance.


(a)

(b)
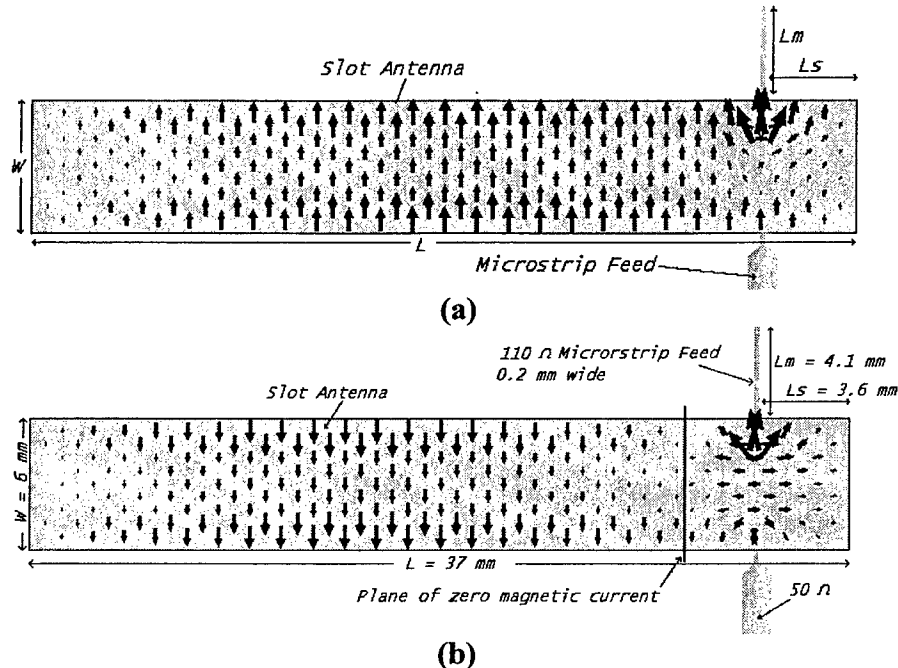
Figure 1. Electric field distribution along a wide slot antenna at the first resonance frequency (a) and the fictitious second resonance (b). (The figures are obtained from full wave simulations)

The width of the microstrip feed, width of the slot, and the distance between the feed and the edge of the slot antenna, L_S, are parameters that affect the existence and location of this fictitious short circuit. As L_S increases, the second resonance frequency also increases therefore by choosing L_S the second resonance frequency can be chosen such that the total antenna bandwidth is increased or a dual band operation is achieved. Matching is achieved by tuning length of the open circuited microstrip line, L_m. Since Ls is being set by the second resonance frequency there is not much flexibility in obtaining a good match by changing the length of Ls.

As can be seen from Figure 1(b), the electric field distribution at this second resonance frequency is similar to that of the first one therefore, it is expected that the radiation patterns of the antenna at the two frequencies be similar. The wideband slot antenna has a length of L=37mm and width of W=6mm and was simulated using IE3D [10] and fabricated on a 500µm thick, RO4350B substrate with dielectric constant of *3.4, tan δ=0.003* and a ground plane area of 15 cm × 11 cm. Figure 2 shows simulated and measured return losses of this antenna. Two

178

different antennas were fabricated and the measured return losses of both of them are shown in Figure 2. The only difference between the two antennas is in the location of the feed. In Antenna #2 L_S is longer than Antenna #1 by 1mm therefore the frequency of second null in S_{11} is higher and the overall bandwidth is larger. The -10 dB bandwidth of Antenna #1 is 1022 MHz (30.3%) and that of Antenna #2 is 1220 MHz. (37%). The slight discrepancy between the simulation and measurement results can be attributed to the finiteness of the ground plane which causes a shift in the resonance frequency and the fact that the response of the system is very sensitive to the exact location of the microstrip feed which is subject to alignment errors in the implementation process.
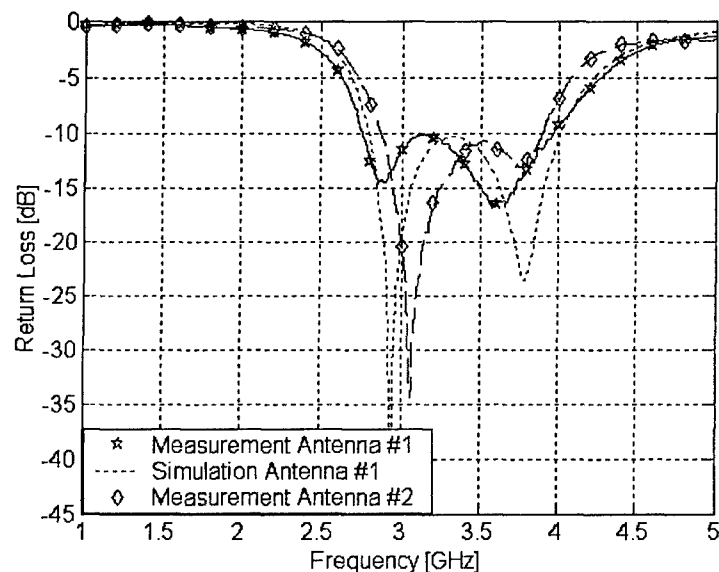
Figure 2. Return losses of the wideband slot antennas.

Radiation patterns of the antenna were measured in the anechoic chamber of the University of Michigan. Figure 3 shows the E- and H-plane co- and cross-polarized patterns at 3.077 GHz and 3.790 GHz. It is shown that the patterns are almost dual of those of an electric dipole of the same length. The deeps in the E-plane at ±90° are caused by the out of phase radiation from the edge of the substrate. It is also seen that the cross polarization level is negligible.

At the second resonance frequency, in addition to the radiation from the edges of the ground plane the oppositely directed magnetic current in one section of the slot can also contribute to the formation of the deep in E-Plane pattern at +90° therefore there will be a deeper null in E-Plane at an azimuth angle of +90°.

179
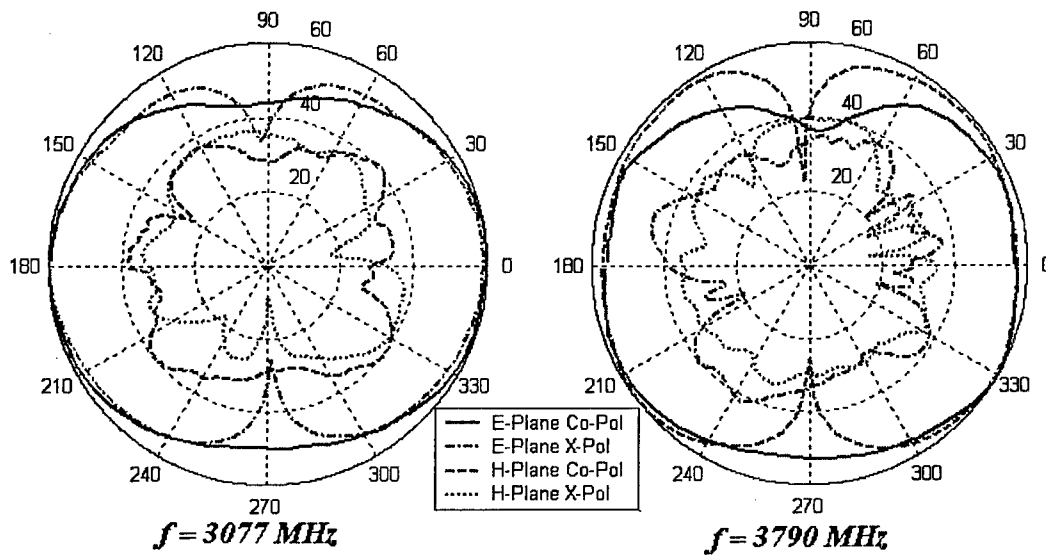
Figure 3. Radiation patterns of the wideband antenna measured at the two resonance frequencies.

The antenna gains were measured at the two resonance frequencies using a reference double ridge horn antenna and are reported in Table I. It is important to note that at f_u the maximum radiation does not take place at bore-sight therefore the gain at bore-sight is lower than the maximum antenna gain.

Type	L, W [mm]	Ls, Lm [mm]	Bandwidth	Gain* @ f_l, f_u
Antenna 1	37, 6	3.6, 4.1	30.3%	2.5 dB, 0.1 dB
Antenna 2	37, 6	4.6, 3.9	37.0%	2.5 dB, 0.0 dB

TABLE I. PHYSICAL AND RADIATION PARAMETERS OF THE BROADBAND SLOT ANTENNA
* Gain is measured at bore-sight.

3. DUAL BAND MICROSTRIP FED SLOT ANTENNA

The wide slot antenna has also the capability of operating in a dual band mode. If the distance L$_S$ is increased the equivalent length of the second resonance decreases therefore the second resonance frequency increases while the location of the first resonance does not change considerably, because it is being set by the overall length of the antenna, therefore the antenna becomes a dual band one. The separation between the two resonance frequencies is a function of the resonant length of the second frequency and as a result of it a function of the distance L$_S$. Figure 4 shows the simulation results of thick slot antenna with L=31 mm and W=6 mm on the RO4350B substrate for different values of L$_S$.
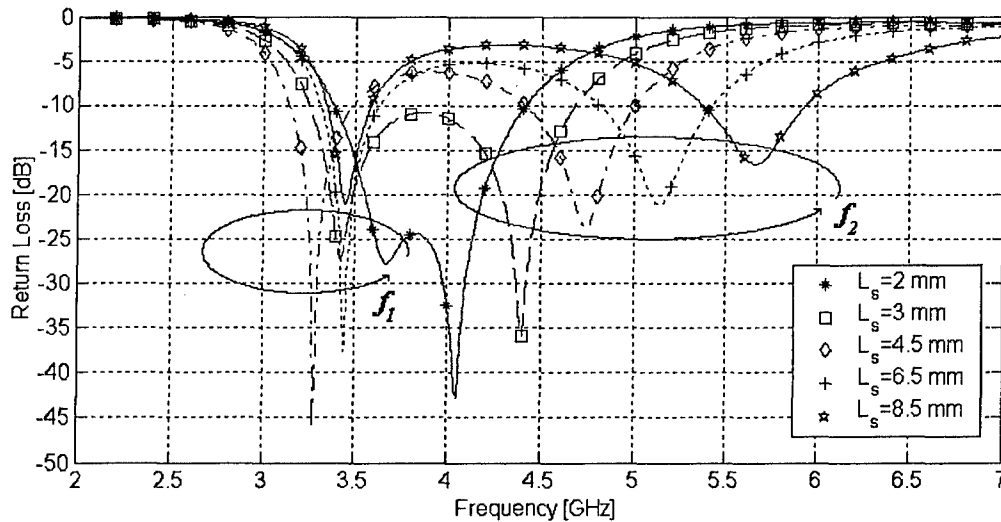
Figure 4. Simulation results of the return loss of the wide slot antenna for different L_s values.

As is observed from this figure, by increasing Ls from 2mm to 8.5 mm, f_l varies between 3.7 GHz and 3.3 GHz and f_u increases from 4GHz to 5.2 GHz. It can be seen that f_u/f_l ratios of 1.6 or more can easily be obtained from this antennas.

The magnetic current distribution at these two different frequencies are similar to each other and result in a similar radiation patterns at the two bands which is expected in a dual-band operation. Figure 5 shows the magnitude of the electric field distribution along the slot for the two resonance frequencies for the case of Ls=8.5 mm. A dual band antenna with L=31mm, W=6mm and Ls=5mm was fabricated on the same RO4350B substrate. The simulated and measured return losses of this antenna are shown in Figure 6. As can be observed, an excellent agreement is observed between the simulation and measurement results. The antenna has f_l and f_u of 3.3 GHz and 4.85 GHz respectively. The bandwidths of the antenna in the first and second bands are 10.6% and 12.1% respectively. It should also be noticed that the antenna has considerable bandwidth in both frequency bands which makes it an excellent choice for wireless communication applications.

The radiation patterns of the antenna were measured in the anechoic chamber of the University of Michigan and the E- and H-Plane, co- and cross-polarized radiation patterns are presented at Figure 7. It is observed that the radiation patterns at both frequencies are similar to each other and the cross polarization level is negligible. As can be seen from Figure 7(b), the maximum radiation in the

181

H-Plane does not occur at bore-sight but rather at around φ=±20° for both frequency bands.
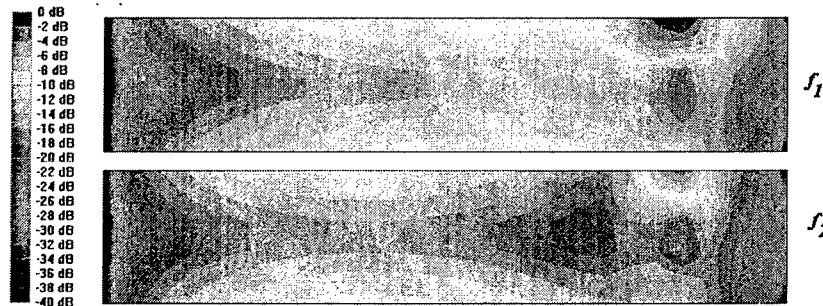
Figure 5. Magnitude of the electric field distribution of the dual band sot antenna at the two resonance frequencies.

L,W [mm]	L_S, L_m [mm]	f_l, f_u [GHz]	BW @ f_l, f_u	Gain* @ f_l, f_u
31, 6	5, 2.3	3.3, 4.85	10.6%, 12.1%	0.5 dBi, 0.3 dBi

TABLE II. A SUMMARY OF THE PHYSICAL AND RADIATION PARAMETERS OF THE DUAL BAND SLOT ANTENNA
* Gain is measured at bore-sight.

The antenna gain at bore-sight is measured using a standard double ridged horn antenna and is reported in Table II. The maximum gain of the antenna in the H-Plane occurs around φ=±20° and is measured to be 2.5 dB and 3.0 dB for f_l and f_u respectively. The efficiency of the antenna can be calculated using the measured values for gain and calculated directivity values. Based on this method efficiency values of 91% and 89% are obtained for the two frequency bands.
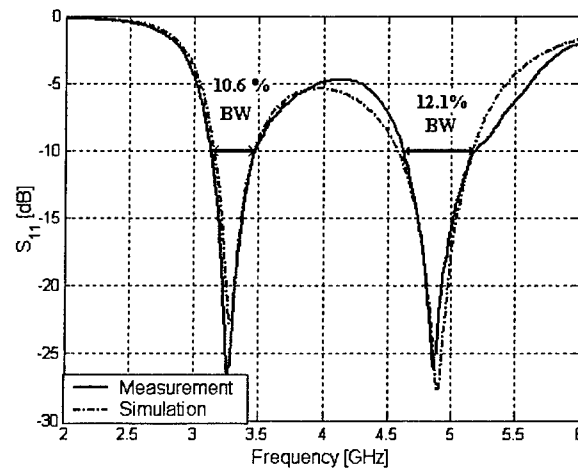
Figure 6. Simulated and measured return losses of a dual band antenna with L=31mm, W=6mm and L_S= 5mm.
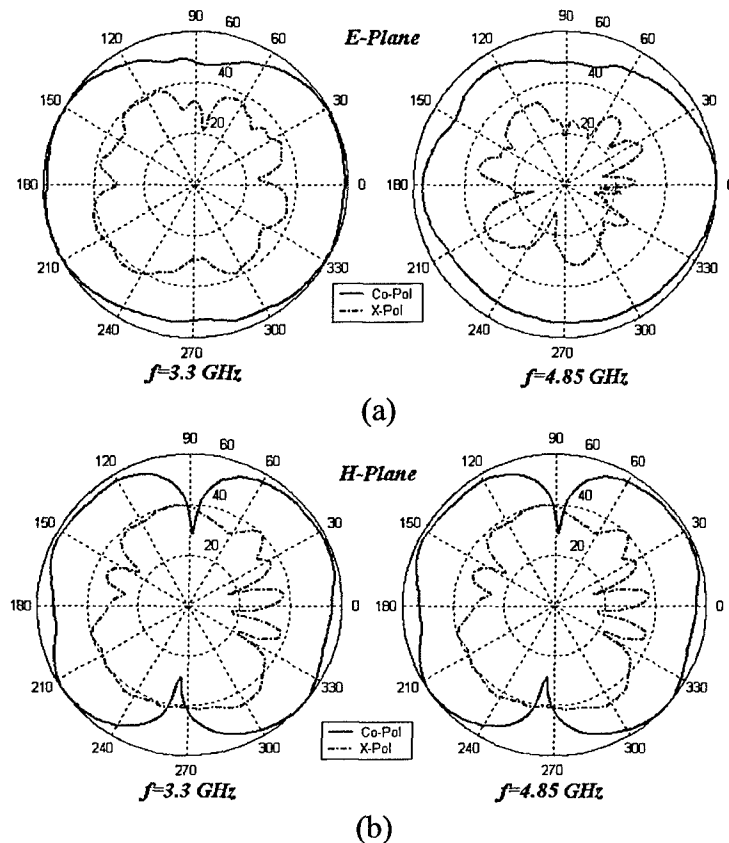
Figure 7. Measured radiation patterns of the dual band slot antenna at f_1=3.3 GHz
and f_2=4.85 GHz. (a) E-Plane (b) H-Plane

4. PARASITICALLY COUPLED MINIATURIZED SLOT ANTENNA

In this section we investigate the design of a double-element miniaturized antenna for bandwidth enhancement. This miniaturized antenna occupies an area of $0.15\lambda_o \times 0.13\lambda_o$ but shows a rather small bandwidth (less than 1%) [9]. A close examination of the antenna topology reveals that the slot structure covers only half of this rectangular area, and therefore another antenna with the same geometry can be placed in the remaining half without significantly increasing the size (Figure 8).

Placing two antennas in such proximity to each other creates significant coupling which can be taken advantage of to increase the total bandwidth of the antenna. In this design the two antennas are tuned to resonate at f_0=850 MHz by adjusting the overall slot length to an effective length of $\lambda_g/2$, where λ_g is the guided wavelength in the slot.
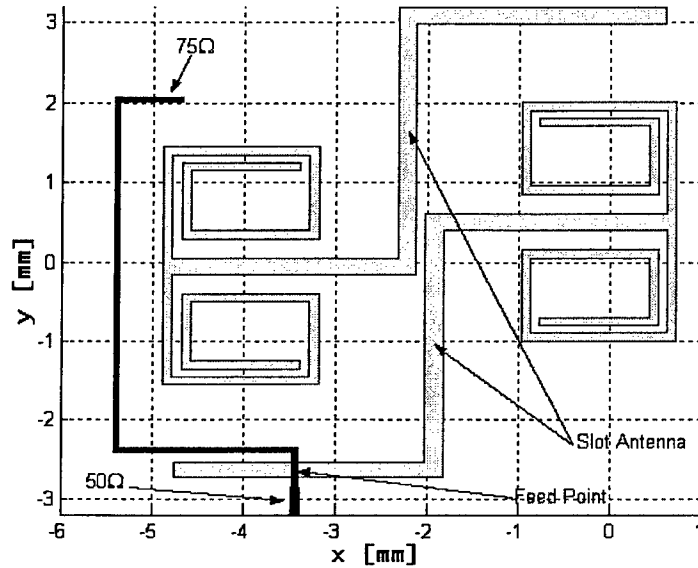
Figure 8. Geometry of the double-element miniaturized slot antenna.

This way, the structure acts like a coupled resonator the bandwidth of which is a function of coupling coefficient between the two resonators. By considering this antenna as a two port network where the second port is in free space, its behavior can be explained using the coupled resonator filter theory. The resonant frequency of the antenna (f_0) determines the center frequency of the operation. The frequency domain reflection coefficient (S_{11}) of this second order system has two distinct zeros with a separation proportional to the coupling coefficient. Bandwidth maximization is accomplished by choosing a coupling coefficient such that S_{11} remains below -10 dB over the entire frequency band as the two zeros are separated. The coupling coefficient which can be controlled by changing the length of the overlap section and the separation between the two antennas (d and s in Figure 10) and is defined as:

$$k_t = \frac{f_u^2 - f_l^2}{f_u^2 + f_l^2} \qquad (1)$$

Where, f_u and f_l are the frequencies of the S_{11} nulls and $f_u > f_l$. The coupling is a mixed electric and magnetic coupling but the electric coupling is stronger in the middle section of both antennas (Figure 10) where the separation, s, is small and the E-Field is large therefore it is the dominant coupling mechanism which results in in-phase magnetic currents in both slot antennas. Figure 9 shows that the two zeros occur at 848MHz and 860 MHz which corresponds to k_t=0.014.

184
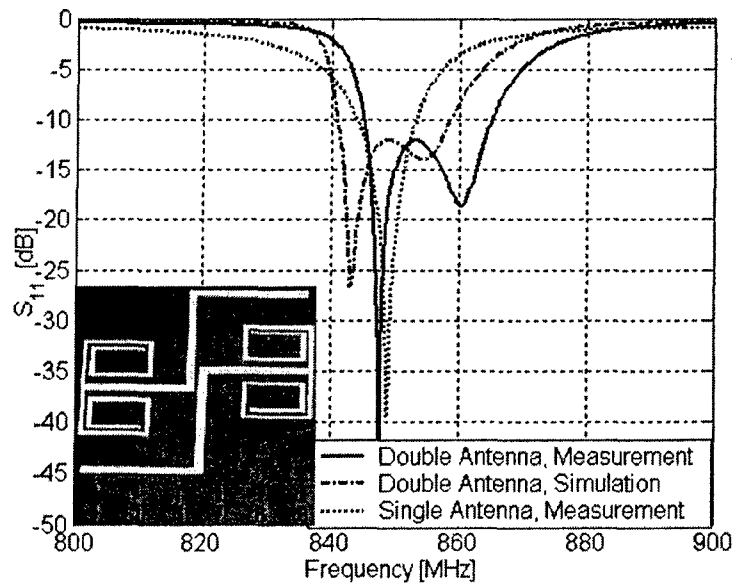
Figure 9. Return losses of the double-element miniaturized antenna and a single element
antenna that constitutes it

The input resistance of a microstrip-fed slot antenna depends on the location of the microstrip feed relative to the slot and varies from zero in the short circuited edge to a high impedance at the center. Therefore an off center feed can be used to match the antenna. Here, the feed is a narrow 75Ω microstrip open circuited transmission line connected to a main $50\ \Omega$ microstrip line. The length of the open circuited microstrip line can be chosen to compensate for the reactive part of the input impedance. Here the input impedance is not purely real therefore the $75\ \Omega$ line is extended by $0.33\lambda_m$ (λ_m is the wavelength in microstrip line) after the strip-slot crossing to compensate for the reactive part of the input impedance.

The double-element slot antenna was simulated using *IE3D* [10] and fabricated on the *500 μm* thick Rogers RO4350B substrate. Figure 9 shows the measured and simulated return losses of the double-element antenna and the measured return loss of a single element that constitutes it. The minute discrepancy between the simulated and measured results can be attributed to the finite size of the ground plane. The antenna shows a -10dB bandwidth of 21 MHz or 2.4% which is more than twice (2.7 times) the bandwidth of a single element antenna (8 MHz or 0.9%). This bandwidth can also be further increased (up to 3%) by increasing the coupling coefficient (Figure 10).

185
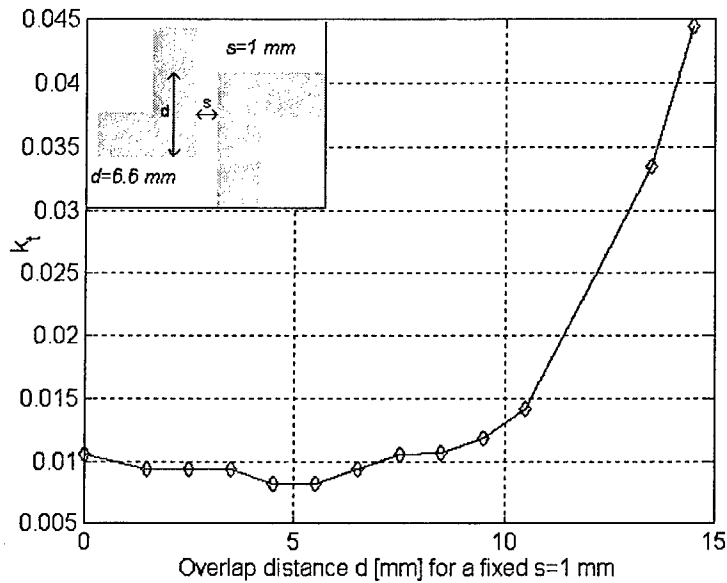
Figure 10. Coupling coefficient of the double-element antenna versus overlap distance, d, obtained from full-wave simulations

Type	Size	Bandwidth	Gain			
Double slot	$0.165\lambda_0$ x $0.157\,\lambda_0$	2.4%	f (MHz)	848	852	860
			G (dB)	1.5	1.7	1.7
Single-Slot	$0.133\,\lambda_0$ x $0.154\,\lambda_0$	0.9%	0.8 dB			

TABLE III. COMPARISON OF DIFFERENT PARAMETERS BETWEEN THE SINGLE ELEMENT ANTENNA AND DOUBLE-ELEMENT ANTENNA.

The radiation patterns of the antenna were measured in the anechoic chamber and the H- and E-plane co- and cross polarized radiation patterns are shown in Figure 11. It is seen that the cross-polarization level is negligible for both cuts. The two slot antennas in the double-element antenna are excited in phase (even mode) therefore their equivalent magnetic currents generate in-phase fields which will add up in the far field. Therefore the overall directivity of the double-element miniaturized antenna is expected to be more than a single element and indeed the measurements verify that (Table III). Gain measurements were performed using a standard log-periodic antenna and it was found that the double-element antenna has a gain of at least 1.5dB whereas the gain of a single element antenna is just 0.8 dB. The current distribution, however, is not the same for different frequencies therefore slight changes in radiation pattern and directivity occur over the bandwidth. The double-element slot antenna is about 25% larger than the single element antenna and features a bandwidth which is 2.7 times that of the single element antenna. In comparison with [11] which uses a folded slot antenna topology to increase the bandwidth, the increase in size is smaller (25% vs. 34%)

and the increase in bandwidth is larger (2.7 vs. 2). If the size of the double-element antenna is reduced to the size of the single antenna a bandwidth increase of 100% can be achieved without increasing the size.
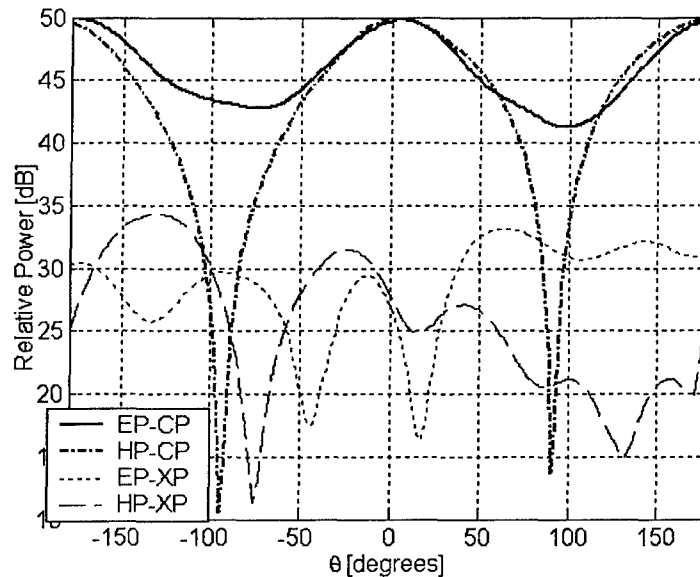
Figure 11. Radiation patterns of the double-element miniaturized slot antenna

5. CONCLUSIONS

Two different methods to enhance the bandwidth of slot antennas were introduced. It was demonstrated that a wide slot antenna, when fed with a narrow microstrip feed, shows a fictitious resonance at a frequency above the first and below the second resonance frequencies. This can be exploited to achieve a high bandwidth or a dual band antenna with similar radiation patterns for both bands.

Parasitic coupling technique when applied to a miniaturized antenna results in an antenna with a very small electrical size and considerable bandwidth compared to equivalent resonant patch antennas. Bandwidth of up to 3% can be achieved for electrical sizes as small as $0.15\lambda_0 \times 0.15\lambda_0$.

REFERENCES

[1] M. Kahrizi, T. Sarkar, and Z. Maricevic, "Analysis of a Wide Radiating Slot in the Ground Plane of a Microstrip Line", IEEE Trans. Microwave Theory and Techniques, Vol. 41, Jan 1993 pp. 29-37.

[2] J. Sze and K. Wong, "Bandwidth Enhancement of a Microstrip-Line-Fed Printed Wide-Slot Antenna", IEEE Trans. Antennas and Prop., Vol. 49, 2001, pp. 1020-1024.

[3] Lee, H. L., H. J. Lee, J. G. Yook, and H. K. Park, "Broadband Planar Antenna Having Round Corner Rectangular Wide Slot", IEEE Antennas. Prop. Sym., Vol. 2, June 2002, pp. 460-463.

[4] Rao, P. H., V. Fusco, and R. Cahill, "A Broadband Antenna for PCN/UMTS Applications", IEEE High Frequency Postgraduate Student Colloquium, 2000 , 7-8 Sept. 2000, pp. 2-5.

[5] D. Llorens, P. Otero, and C. Camacho-Penalosa, "Dual-Band Single CPW Port Planar-Slot Antenna", IEEE Trans. Antennas and Prop. Vol. 51, Jan 2003, pp. 137-139.

[6] L. J. Chu, "Physical limitations on omni-directional Antennas" J. Appl. Phys., vol. 19 pp. 1163-1175, Dec 1948.

[7] H. A. Wheeler, "Fundamental Limitations of small antennas", Proc. IRE. Vol. 35. pp. 1479-1484, Dec, 1947

[8] R. C. Hansen, "Fundamental limitations in antennas", Proc. IEEE, Vol. 69, pp. 170-182, Feb 1981.

[9] K. Sarabandi and R. Azadegan, "Design of an efficient miniaturized UHF planar antenna", IEEE Trans. Ant. & Prop., Vol. 51, June 2003, pp. 1270-1276.

[10] IE3D Electromagnetic Simulation and Optimization Software, Zeland Software, Inc.

[11] R. Azadegan and K. Sarabandi, "Miniaturized Folded-Slot: An Approach to increase the Bandwidth and Efficiency of Miniaturized Slot Antennas", Antennas and Propagation Society, 2002 IEEE International Symposium, Vol. 4, 2002, pp. 14-17.

A COMMEMORATION OF DESCHAMPS' AND SICHAK'S "MICROSTRIP MICROWAVE ANTENNAS": 50 YEARS OF DEVELOPMENT, DIVERGENCE, AND NEW DIRECTIONS

J. T. Bernhard[1], P. E. Mayes[1], D. Schaubert[2], and R. J. Mailloux[3]

[1]Electromagnetics Laboratory, ECE Department,
University of Illinois at Urbana-Champaign, Urbana, IL 61801
[2]Antenna Laboratory, ECE Department,
University of Massachusetts, Amherst, MA 01003
[3]Air Force Research Laboratory, Sensors Directorate
80 Scott Drive, Hanscom AFB, MA, 01731

Abstract: Fifty years ago, the Third Symposium on the USAF Antenna Research and Development Program was held at Robert Allerton Park. During this symposium, Deschamps and Sichak, working for the Federal Telecommunications Laboratory, presented their work entitled "Microstrip Microwave Antennas." Here we commemorate this now declassified work, often cited as the "first microstrip antenna paper," by reflecting upon it in light of the significant advances in microstrip antenna theory and design that have sprung from the pages of the Symposia proceedings since. We conclude with a discussion of the future of microstrip antennas and related structures.

1. Introduction

October 1953: The Armistice agreement formally ending the Korean War has been signed in July, with the DMZ established and manned with U.S. Marines in September. The Brooklyn Dodgers and the New York Yankees have played the World Series, with the Yankees taking it in six games. And, of course, the Symposium at Robert Allerton Park is taking place.

Certainly the impact of each of these events can never be directly measured or compared. However, one can certainly argue that the paper written by Deschamps and Sichak [1] fostered the beginnings of a new discipline within the antenna community that has had significant and long-lasting effects on countless aspects of communication, exploration, and defense. We commemorate the fiftieth anniversary of this work by reflecting upon the emergence of the microstrip microwave antenna and subsequent papers of import that have been

presented at Robert Allerton House over the years. The paper [1] is reprinted here as an appendix for further reference and enjoyment. This work concludes with a brief discussion of the future direction of microstrip antennas and related structures.

2. "Microstrip Microwave Antennas": A Review

Engineers familiar with references to the subject paper [1] may wonder how the name W. Sichak has now become attached to it. In the 1953 Symposium proceedings program, the paper is indeed listed as being by a sole author – Georges Deschamps – and has been referenced as such in a number of highly cited publications [e.g., 2, 3]. However, the annotated copy of the proceedings housed in the Electromagnetics Laboratory at the University of Illinois lists W. Sichak as a co-author on the paper. William Sichak, later named an IRE Fellow, worked at Federal Telecommunication Laboratories with Georges Deschamps and no doubt contributed to the paper, but evidently not in time to have his name on the program or paper officially. Here we correct this oversight, as Deschamps must have done during his presentation.

In [1], the authors detail the development of a high resolution X-band antenna with a shaped vertical pattern and a horizontal beamwidth of less than one degree. Having decided upon a long linear array with a cylindrical reflector to achieve the operational goals, the authors weighed the benefits of using a sectoral lens, a slot array, or an array composed of waveguide-fed horns as a feed mechanism. Given the bulk of such a waveguide system with 300 radiating elements, the authors developed a microstrip feeding system. This is the "microstrip" to which the title refers. Indeed, when one reads the paper, one is struck by the fact that there is, in fact, no microstrip antenna included as we would recognize it today.

What does follow in the rest of the paper is a description of the complete system with measured results. The paper describes the critical issues for each system component – the waveguide-to-microstrip (or stripline) transition, the bends and junctions in the power dividers, and finally, the radiating elements. The radiating elements are either horns created by three-dimensional extensions of the microstrip or lenses.

The microstrip patch we recognize today did not become widely known for another 17 years, through the work of Byron [4], Munson [5, 6], and Howell [7, 8]. However, what the Deschamps and Sichak paper did do was to foster new ways of thinking about complete antenna structures and the subsequent performance benefits and reductions in size, weight, and cost that could be

realized through the use of microstrip or stripline transmission lines. The following sections detail some of the important papers presented through the history of this Symposium that owe, at least in part, their origins to the work of Deschamps and Sichak.

3. "Microstrip Phased Array Antennas" – Munson, 1972

In a paper presented at the Twenty-Second Annual Symposium of the USAF Research and Development Program in 1972, Bob Munson described the first embodiment of the microstrip antenna that quickly captured the attention of the antenna community and grew in popularity and usefulness [5]. The microstrip radiators that Munson used were either metallic strips wrapped around missiles for telemetry systems or flat elements. These antennas differed from a standard "patch" design in that they were several wavelengths long and up to a half wavelength wide with multiple feed points located along the length. Rules of thumb for their design are included along with measured results for a flat version of a wrap-around antenna. Bandwidth was always an issue: Munson states "Several methods are currently being explored...to increase the bandwidth of microstrip antennas [5]." In the same paper, he also mentioned work on arrays of individual microstrip (patch) elements that would use pin diodes for phase shifting. This phased array concept proposed by Munson in the Symposium and later reiterated in a more extensive 1974 *IEEE Transactions on Antennas and Propagation* article [6] is still the baseline configuration for phased arrays today.

Munson's publication in the Symposium Proceedings predates by a few months that of the classical paper by J. Q. Howell at the 1972 International Symposium of the Antennas and Propagation Group of the IEEE in December of 1972 [7]. The latter conference paper and its associated journal article published in 1975 [8] are frequently referenced as the original work on microstrip patches. However, Howell credits Munson with the idea in the reference section of his paper, but only as a private communication. In 1981, Munson returned to Allerton to describe "Advances in Microstrip Antenna Technology." Unfortunately, no printed version of his paper was preserved in the Proceedings.

4. Contributions of John Kerr, 1977-1978

For many years, John Kerr, US Army Electronics Command, Ft Monmouth, NJ, participated in the antenna symposia at Allerton Park. In the 1970's, microstrip antenna technology was advancing at a rapid pace through a combination of simple models (e.g., the cavity model [9]) and empirical development by engineers whose talents were honed before computer simulations contributed

significantly to antenna innovation. At the 1977 and 1978 Symposia, John Kerr presented three papers [10]-[12] that employed and elucidated key properties of microstrip antennas that subsequently have been exploited in a variety of ways. In this section, we recap Kerr's papers and then trace their influence on further developments.

4.1 Summary of Kerr's Papers, 1977-1978

Kerr's 1977 paper [10] introduced the concept of controlling the resonant frequency of a rectangular microstrip patch antenna by removing a portion of the metal in the center of the patch. According to the paper, this discovery came as result of the need to add an inexpensive L-band feed to an existing 4-foot reflector operating at X-band with a shepherd's hook feed. A simple microstrip patch antenna would provide adequate illumination of the reflector, but the X-band shepherd's hook feed could not radiate through the somewhat larger L-band patch and its ground plane. Kerr's solution was to remove the central portion of the patch, the dielectric and the ground plane clearing a pathway for the X-band feed to radiate through the patch while locating both at the reflector's focus, Fig. 1. The dual-frequency reflector problem was solved, and the robustness of microstrip patch antennas to (severe) configuration changes was demonstrated. Kerr noted that removing the one-inch-square region lowered the resonant frequency of the patch from 1370 MHz to 1250 MHz, making the patch electrically smaller at its operating frequency. Three years later, Mink presented a theory that explained Kerr's observations and extended the notion to include ring antennas [13].

Kerr's first paper at the 1978 symposium [11] was a short note that suggested a simple means to add reactance to the usual resonance of a patch antenna and thereby to tune its operating frequency. This result is similar to the well-known techniques for tuning microwave cavities with a lumped reactance, but Kerr employed a length of printed microstrip line, which was easily implemented when the antenna was fabricated, Fig. 2. He showed that a good impedance match is obtained with short-circuit or open-circuit terminations located various distances from the patch, Fig. 3. Kerr noted that the antenna's radiation pattern might limit its useful bandwidth even if its impedance remains acceptable.

His second paper at the 1978 symposium [12] relies on the phenomenon reported in his 1977 paper, but Kerr cleverly employed the change of resonant frequency caused by removal of metalization to create the conditions necessary for circular polarization from a patch with only a single feed port. Kerr observed that creating a narrow slot in the metalization of the patch had little effect on the antenna's

performance if the long axis of the slot was parallel to the dominant currents flowing on the patch, but it significantly lowers the resonant frequency if the slot axis is perpendicular to the current flow. This led to a new variation of the slightly off-square patch to produce circular polarization, Fig 4. Unlike the 1977 paper, Kerr removed metal only from the patch, leaving the ground plane and dielectric intact. He created another version of the antenna that utilizes a perfectly square (or circular) patch and a polarizing slot placed diagonally to the dominant current flow, Fig. 5. The spin linear radiation pattern in Fig. 6 shows that the conditions for circular polarization are fulfilled very well. Two other variations of his circularly polarized antenna are shown in Fig. 7.

4.2. Post-Tuned Patch Antennas for Frequency Agility and Polarization Diversity

Jones et al. presented a paper at the 1977 symposium [14] that described the use of vias in a radial transmission line to tune the operating frequency of an edge-slot antenna mounted on a cylindrical body. After hearing presentations by Kerr about the tuning phenomenon, they recognized that microwave varactors or switching diodes could be used with the via-post technique employed in their edge-slot antennas to produce tunable patch antennas, Fig. 8. As is well known, shorting posts along the centerline of a microstrip patch have no effect on the dominant mode of the patch antenna because the voltage is zero there. However, shorting posts located elsewhere can add inductive reactance that raises the operating frequency of the antenna.

John Kerr's discovery again provided inspiration, and the antenna was modified by removal of metalization, thus lowering the basic operating frequency. Tuning posts can then be employed to adjust the operating frequency to any desired value within a 1.4:1 frequency range that is approximately centered at the operating frequency of the standard patch antenna, Fig. 9. The example in Fig. 9 maintains good impedance match and stable radiation patterns over the tuning range indicated. Unfortunately, the inductive loading causes the antenna to be electrically larger than the untuned version.

By selectively locating posts that affect one polarization of a square patch while being located at voltage nulls of the orthogonal polarization, the effects of Kerr's polarizing slot can be replicated. Overall, although the post-tuned antenna is slightly larger than Kerr's slot-tuned antenna operating at the same frequency, it can produce similar effects, including polarization diversity, Fig. 10. Furthermore, it is easier to implement switching vias than to change the metalization pattern of the patch. Thus, the work of Kerr and of Jones et al.,

stimulated development of an alternative configuration that incorporates the benefits of both.

4.3 Multimode Patch Antennas with Slots and Posts

Considering the cavity model for the microstrip patch antenna [9], it is apparent that the antenna can support different resonant modes at different frequencies. Square and circular patches typically support two orthogonally polarized modes at the frequency of the dominant resonance, but rectangular patches typically support only a single mode with a particular polarization at any specified frequency. By properly selecting the dimensions, post locations and feed point, the post-tuned antenna can support two copolarized modes simultaneously. The combination of these two modes creates an asymmetric beam that may be useful to enhance the gain in a preferred direction, Fig. 11. A feed on the opposite side of the antenna will produce a beam tilted in the opposite direction, and the difference of these two beams could provide a tracking signal as in sequential lobing or monopulse systems. Changing the post configuration allows the same patch also to operate in linear polarization at one or more frequencies.

4.4 Piggyback Patch Antennas

The use of a parasitic patch antenna stacked above a driven antenna is a common means to increase the bandwidth of microstrip antennas. An alternative stacked configuration, sometimes referred to as a piggyback antenna, has been demonstrated [17]. The piggyback antenna is two essentially independent antennas sharing a common aperture. The upper patch covers part of the central region of the larger lower patch, Fig. 12. As observed by Kerr [10], an object attached to the central region of the patch has little impact on its basic operation. Thus, the metalization of the upper patch has little impact on the lower patch. The feed for the upper patch, on the other hand, is connected to the ground plane and to the lower patch forming a tuning post within the lower antenna, which raises the operating frequency as described above. Any combination of half-wavelength and quarter-wavelength antennas can be stacked in the piggyback configuration, and the antennas may be polarized in the same or different directions. Furthermore, additional tuning posts may be included in the antennas or metal may be removed from the patches to alter their characteristics. Kerr's 1977 paper [10] includes a dual-frequency X- and L-band antenna that is coplanar. He removed a portion of the metal from the central region of the L-band patch and then used this vacant region for the X-band patch.

5. "Theory and Experiment on Microstrip Antennas" – Lo et al., 1978

This paper [9] was presented at the Antenna Applications Symposium in 1978, six years after the original Allerton paper by Munson [5] that described microstrip antennas on missiles and flat surfaces. In the intervening years Munson and most other authors had few design guidelines and inadequate theoretical tools to predict element and array performance, so they used transmission line theory for computing patch element size and either a two slot model or a patch current model to estimate radiation patterns. However, it was becoming apparent that much more sophisticated modeling would soon be necessary in order to take advantage of the great versatility of this new antenna. This became even more clear during the 1978 symposium when Kerr [11, 12] presented two papers wherein small changes to basic microstrip patch antennas are incorporated to provide a variable resonant frequency by terminating the patch in an impedance loaded line [11], or by making asymmetric cuts in the patch to produce circular polarization [12]. Although Howell [8] mentioned the similarity between a microstrip patch and a cavity bounded on top and bottom by electric walls and on the sides by magnetic walls, it remained for Y. T. Lo and his student collaborators to develop a theory based upon this idea.

The paper by Lo et al. [9] introduced the cavity method that became the first theoretical solution to include the electromagnetics of the microstrip antenna. The cavity model assumed the patch antenna to have magnetic walls along the edges, and electric walls above and below. The internal fields could then be determined by cavity theory, including probe or other sources. Radiating fields are evaluated via integrals over the current carrying surfaces and aperture fields. This paper and the journal articles that followed it, developed a theoretical basis that was used to explain not only the behavior of the basic patch elements, but also the loading effects of various probes and stubs for frequency tuning and the shape changes that resulted in circularly polarized radiation. Much of this later work is summarized in a book chapter by William Richards [19]. Prof. Lo and his colleagues extended their cavity model theory for microstrip patch antennas to annular sector and circular sector shapes in the 1981 Proceedings [20]. The cavity model is still one of the most widely used theoretical models of the microstrip antenna in existence, as evidenced by its use in major popular texts [2] and reference books [3].

An interesting sidelight to this paper is that although the cavity model was used successfully for many years, the seeds of change were already planted at the same 1978 meeting. James P. (Pat) Montgomery [21] outlined a "full wave" method for an infinite two-dimensional array of microstrip patches. Full wave methods have

since shown the ability to handle thicker dielectrics and shape variations as well as to provide more accurate analysis of mutual coupling, but none of this was to be available until many years after Lo's introduction of the cavity model.

6. Microstrip Antenna Impedance Bandwidth Improvements

One limiting factor in the performance of microstrip patch antennas is the narrow impedance bandwidth. As evidenced even in Munson's first paper [5], this has always been an issue. In a 1983 Symposium paper [22], Dean Paschen showed how filter theory could be used to expand the impedance bandwidth of microstrip antennas up to 35%. Lo and his group attacked the problem of extending the bandwidth of circularly polarized radiation from a patch antenna at the 1984 Symposium [23]. They applied the cavity model theory [9] to a patch with thick substrate and achieved good results in spite of the fact that the theory is only justifiable for antennas on very thin substrates. Bandwidth enhancement through double-tuned patch elements was demonstrated in a 1986 paper by Tanner and Mayes [24]. At the same Symposium, Paschen presented several examples of broadband patch antennas where the matching elements were included in the antenna structure [25]. Gonzalo et al. [26] presented use of photonic crystal structures in microstrip antenna substrates in 1999, showing increased bandwidth as well as a decrease in surface-wave related pattern effects.

7. Microstrip Antenna Feeds

A packaging problem for arrays of large numbers of patch elements was solved by Schaubert and Pozar in two papers given in 1985 [27] and 1986 [28] that employed aperture coupling between the patch elements and the feed network. More recently in 1994, Herscovici et al. [29] developed a new feed network for microstrip that ameliorates parallel-plate modes excited in stripline feed configurations for microstrip antennas. This method solves the problem by using two different dielectric substrates on either side of the stripline center strip in the vicinity of the feed. This material mismatch retards the formation of a strong parallel-plate mode in the stripline, leading to a more efficient coupling of energy to the antenna.

8. Future Directions

As the years of the Symposia Proceedings attest, the number of approaches to implementing microstrip antennas and related structures for a variety of interesting and useful applications continues to grow. Certainly, new feed methods, new kinds of slotted and loaded designs, and new kinds of substrates are

expanding the capabilities of single elements as well as arrays. Ironically, another way that the microstrip antenna is being re-invented is in the third dimension – in ways much like that first described by Deschamps and Sichak in 1953. Recent Symposia papers [e.g., 30, 31] detail developments that lift the radiating element off of the plane using now-practical microelectromechanical fabrication methods, providing dramatic improvements in impedance bandwidth.

9. Conclusions

The Antenna Symposia at Allerton Park have provided a rich and varied resource on cutting-edge antenna techniques and technologies. Deschamps' and Sichak's paper is but one example of many that have provided attendees with "something to chew on." We look forward to many more years of this unique and valuable scientific event.

10. Acknowledgments

11. References

[1] G. Deschamps and W. Sichak, "Microstrip Microwave Antennas," *Proceedings of the Third Symposium on the USAF Antenna Research and Development Program*, October 18-22, 1953.

[2] R. Garg, P. Bhartia, I. Bahl, and A. Ittipiboon, *Microstrip Antenna Design Handbook*. Artech House: Boston. 2001.

[3] D. Pozar and D. H. Schaubert, Eds., *Microstrip Antennas*. IEEE Press: New York. 1995.

[4] E. V. Byron, "A new flush-mounted antenna element for phased array application," in *Proc. Phased-Array Antenna Symp.*, 1970, pp. 187-192.

[5] R. E. Munson, "Microstrip Phased Array Antennas," *Proc. of the Twenty-Second Symposium on the USAF Antenna Research and Development Program*, October 1972.

[6] R. E. Munson, "Conformal Microstrip Antennas and Microstrip Phased Arrays," *IEEE Trans. on Antennas and Propagat.*, vol. 22, pp. 74-78, 1974.

[7] J. Q. Howell, "Microstrip Antennas," in *IEEE AP-S Int. Symp. Digest*, 1972, pp. 177-180.

[8] J. Q. Howell, "Microstrip Antennas," *IEEE Trans. on Antennas and Propagat.*, vol. 23, pp. 90-93, 1974.

[9] Y. T. Lo, D. Solomon and W.F. Richards, "Theory and Experiment on Microstrip Antennas," *Proc. of the 1978 Antenna Applications Symposium*, September 20-22, 1978.

[10] J. L. Kerr, "Other Microstrip Antenna Applications," *Proc. of the 1977 Antenna Applications Symposium*, April 27-29, 1977.

[11] J. L. Kerr, "Terminated Microstrip Antenna," John L. Kerr, *Proc. of the 1978 Antenna Applications Symposium*, September 20-22, 1978.

[12] J. L. Kerr, "Microstrip Polarization Techniques," *Proc. of the 1978 Antenna Applications Symposium*, September 20-22, 1978.

[13] J. W. Mink, "Circular Microstrip Antenna Elements," in *1980 IEEE Int. Antennas Propagat. Symp. Dig.*, 1980, pp. 605 - 608.

[14] H. S. Jones, Jr., D.H. Schaubert and F. Reggia, "A Conformal, Dielectric-Filled Edge-Slot Antenna for Bodies of Revolution," *Proc. of the 1977 Antenna Applications Symposium*, April 27-29, 1977.

[15] D. H. Schaubert, F.G. Farrar, A. Sindoris and S.T Hayes, "Microstrip Antennas with Frequency Agility and Polarization Diversity," *IEEE Trans. Ant. Propagat.*, vol. 29, pp. 118-123, January 1981.

[16] D. H. Schaubert, F.G. Farrar, A.R. Sindoris and S.T Hayes, "Post-Tuned Microstrip Antennas for Frequency-Agile and Polarization-Diverse Applications," *US Army Electronics R&D Command report, HDL-TM-81-8*, March 1981.

[17] H.S. Jones, Jr., F.G. Farrar and D.H. Schaubert, "Dual-Frequency Piggyback Antenna," *US Patent No. 4,162,499*, 24 July 1979.

[18] D.H. Schaubert, "Multilayer and Parasitic Configurations," Chap. 6, *Handbook of Microstrip Antennas*, J.R. James and P.S. Hall, Ed., Peter Peregrinus, 1999, London.

[19] W.F. Richards, "Microstrip Antennas," Chapter 10 in *Antenna Handbook, Theory, Applications and Design*, Y.T. Lo and S.W. Lee, Eds., Van Nostrand Reinhold Company, New York 1988.

[20] J. D. Ou, W. F. Richards, and Y. T. Lo, "An Analysis of Annular, Annular Sector, and Circular Sector Microstrip Antennas," *Proc. of the 1981 Antenna Applications Symposium*, September 23-25, 1981.

[21] J. P. Montgomery, "A Microstrip Reflectarray Antenna Element," *Proc. of the 1978 Antenna Applications Symposium*, September 20-22, 1978.

[22] D. A. Paschen, "Broadband Microstrip Matching Techniques," *Proc. of the 1983 Antenna Applications Symposium*, September 1983.

[23] Y. T. Lo, B. Engst, and R. Q. Lee, "Circularly Polarized Microstrip Antennas," *Proc. of the 1984 Antenna Applications Symposium*, September 1984.

[24]   D. R. Tanner and P. E. Mayes, "Wide-band, Double-Tuned Microstrip Elements," *Proc. of the 1986 Antenna Applications Symposium*, September 1986.

[25]   D. A. Paschen, "Practical Examples of Integral Broadband Matching of Microstrip Antenna Elements," *Proc. of the 1986 Antenna Applications Symposium*, September 1986.

[26]   R. Gonzalo, B. Martinez, P. de Maagt, and M. Sorolla, "Patch Antennas on Photonic Crystal Structures, *Proc. of the 1999 Antenna Applications Symposium*, September 15-17, 1999.

[27]   D. H. Schaubert, R. W. Jackson, and D. M. Pozar, "Antenna Elements for Integrated Phased Arrays," *Proc. of the 1985 Antenna Applications Symposium*, September 1985.

[28]   D. H. Schaubert and D. M. Pozar, " Aperture Coupled Patch Antennas and Arrays," *Proc. of the 1986 Antenna Applications Symposium*, September 1986.

[29]   N. I. Herscovici, N. K. Das, and J. Klugman, "A Microstrip Array Fed by a New Type of Multilayer Feeding Network," *Proc. of the 1994 Antenna Applications Symposium*, September 1994.

[30]   J. T. Bernhard, N.-W. Chen, R. Clark, P. Mayes, E. Michielssen, "A Canted Sector Antenna with Broad Impedance Bandwidths for High Performance Arrays," *Proc. of the 2000 Antenna Applications Symposium*, September 20-22, 2000, pp. 311-322.

[31]   J. T. Bernhard, B. Herting, J. Fladie, D. Chen, and P. Mayes, "Investigation of Wideband Low-Profile Canted Antennas for Broadside Radiation in Aperiodic Arrays," *Proc. of the 2003 Antenna Applications Symposium*, September 17-19, 2003.

Extensive reference lists on other antenna technologies and advances presented in the Symposia can be found in papers by Mayes [1999] and Mailloux [1999].

Figure 1. Kerr's L-band patch antenna with hole for X-band feed horn. From [10].
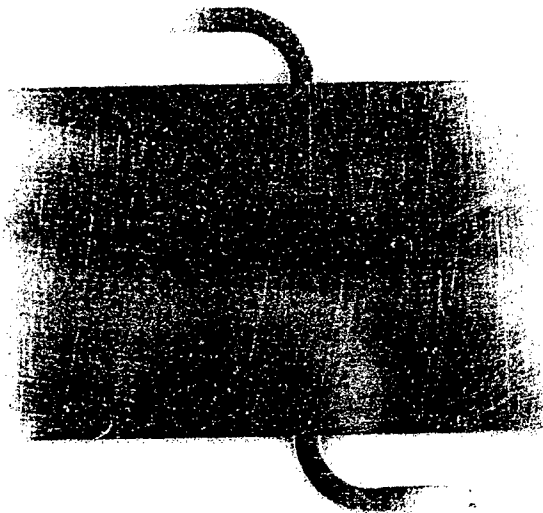
Figure 2. Terminated microstrip antenna demonstrating frequency tuning by reactive loading of the patch. From [11].
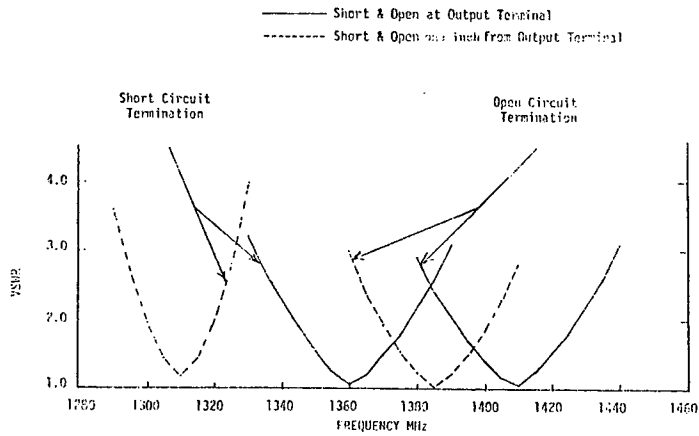
Figure 3. Kerr's results for frequency tuning by open-circuit and short-circuit loads at two locations. From [11].

Figure 4. Corner-fed square patch antenna with horizontal slot to lower vertically polarized resonance slightly, resulting in circularly polarized antenna. From Kerr [12].

201
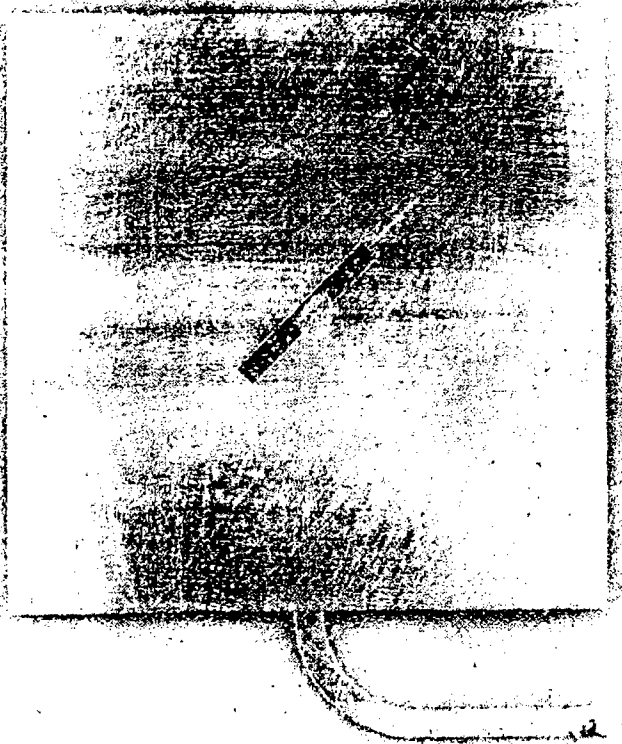
Figure 5. Edge-fed square patch with diagonal slot to create circularly polarized antenna. From [12].
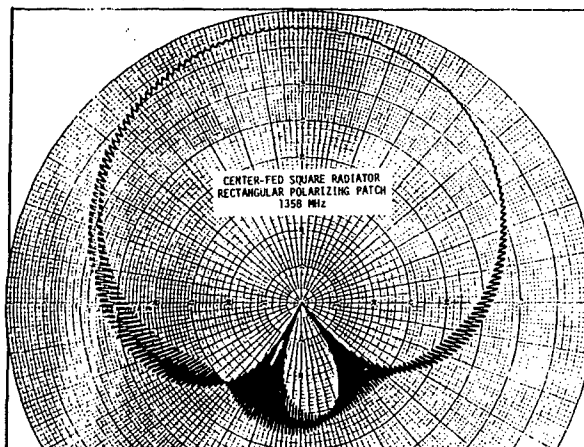
Figure 6. Radiation pattern of antenna in Figure 5. The large back radiation and low axial ratio in horizontal plane suggest that the ground plane was rather small. From [12].
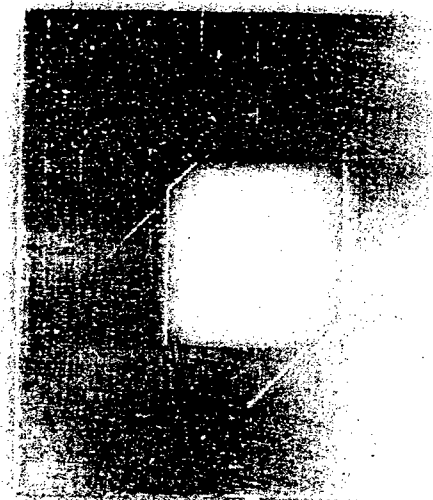
(a)
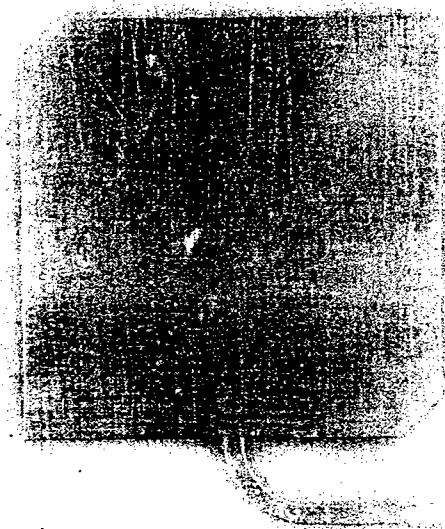
(b)

Figure 7. Two patches produce circular polarization.
(a) Square patch with square central hole that has
opposite corners clipped. (b) Square patch with
opposite corners clipped. From [12].
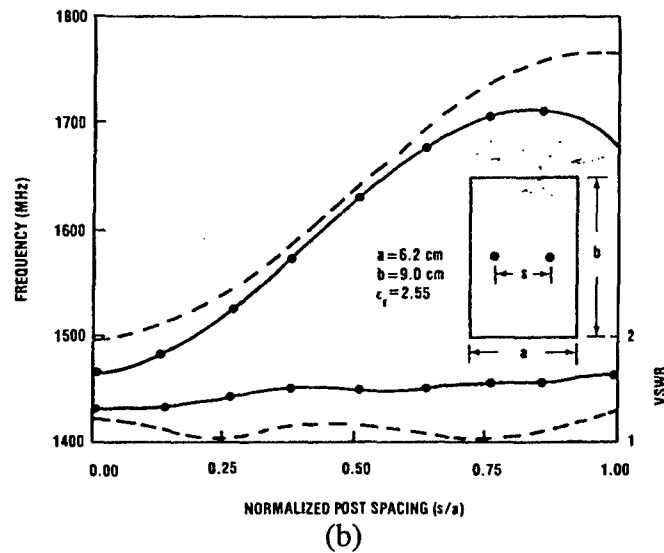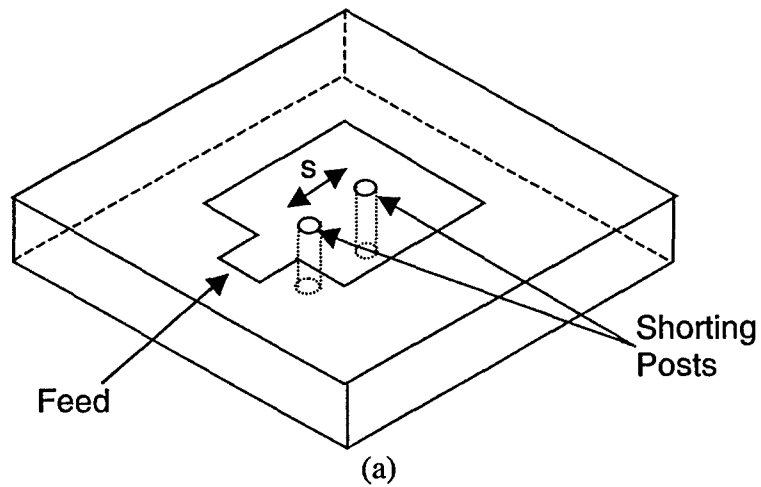
Figure 8. Post-tuned microstrip patch antenna inspired by work in [10], [11] and [14]. (a) Antenna with pair of posts separated by distance *s*. (b) Frequency tuning and VSWR of post-tuned antenna, from [15].

Feed

Conductor
removed

2.5cm x 4.2cm

6.2 cm

9 cm

(a)

(b)
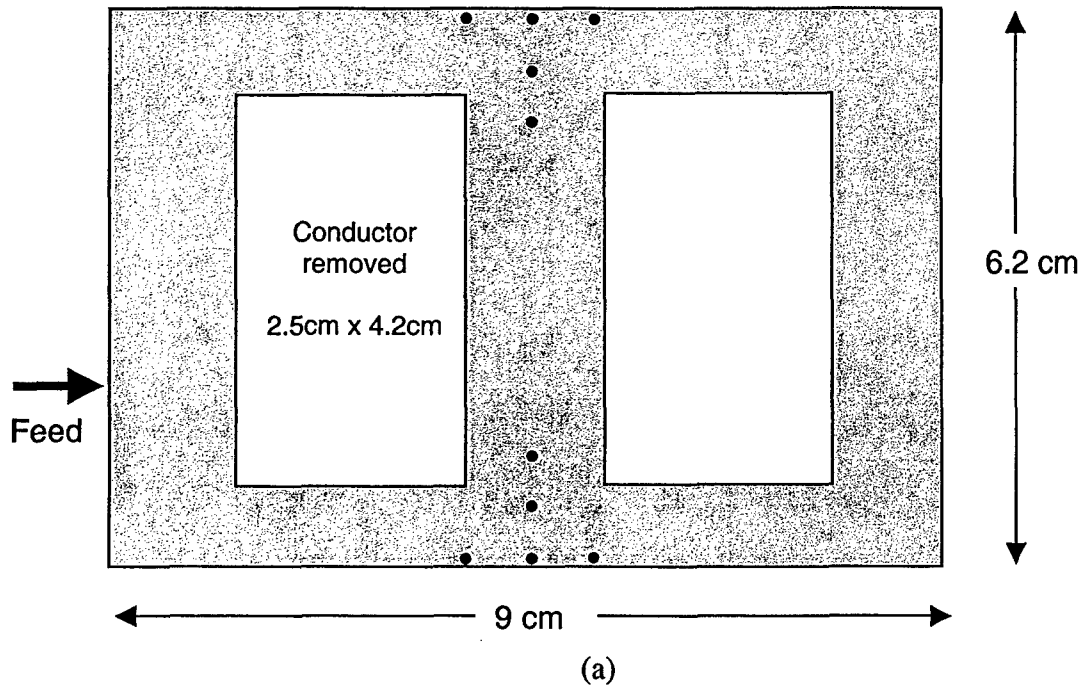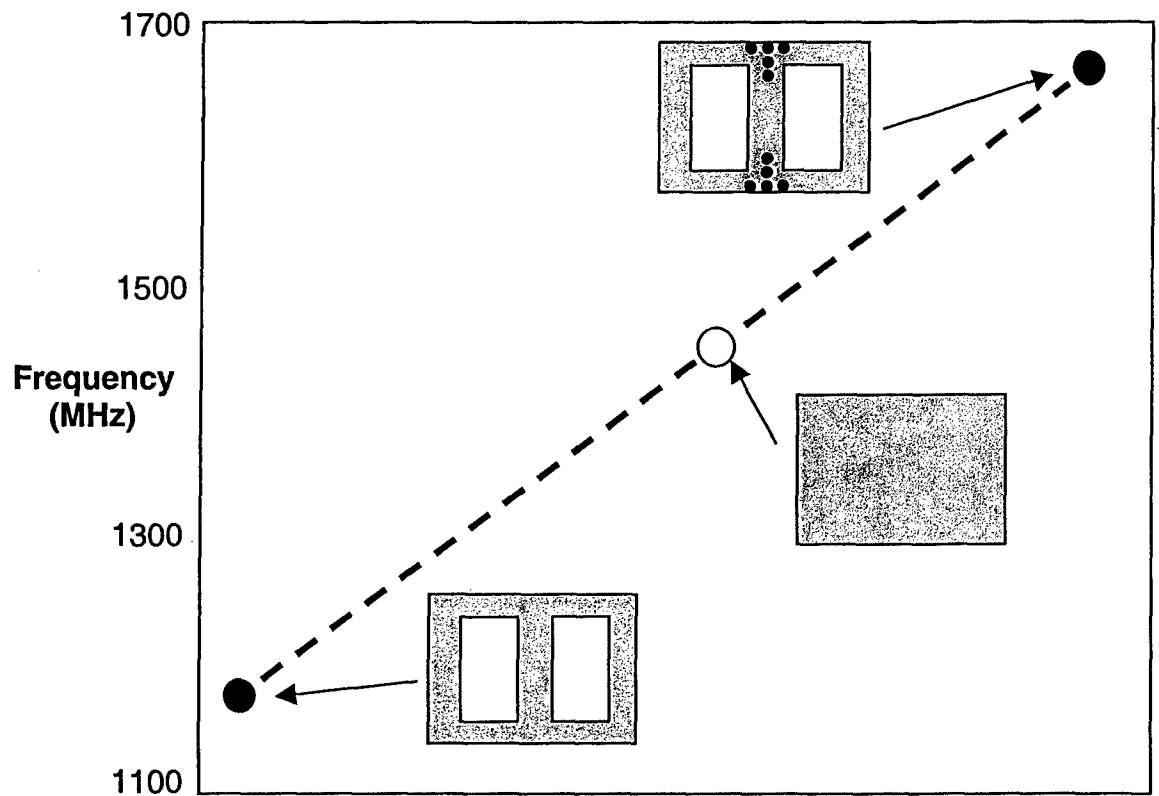
Fgiure 9. (a) Patch antenna with metalization removed to lower basic operating frequency and posts added to then raise it. (b) Typical tuning range of patch antenna. Standard patch antenna of same size operates at 1465 MHz. After [16].
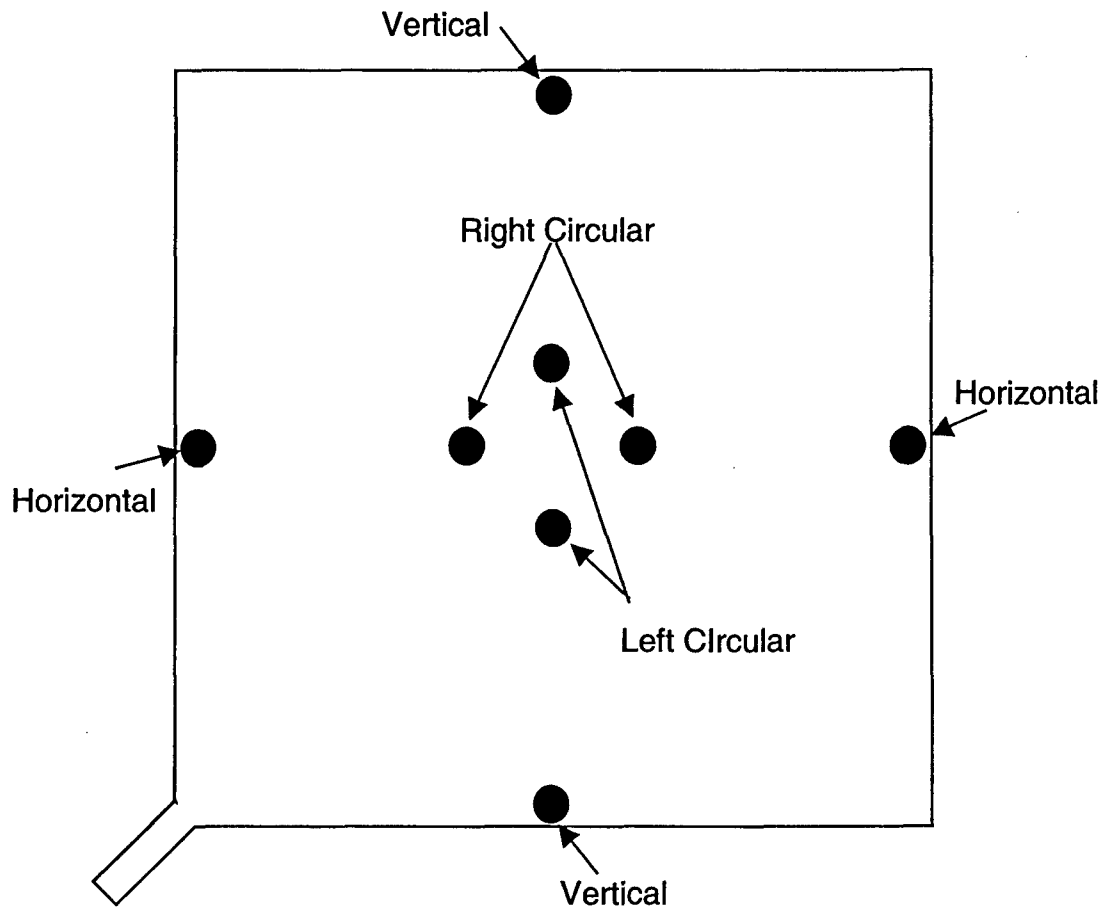
Figure 10. Switchable shorting posts provide polarization diversity of a corner-fed patch antenna. After [15].
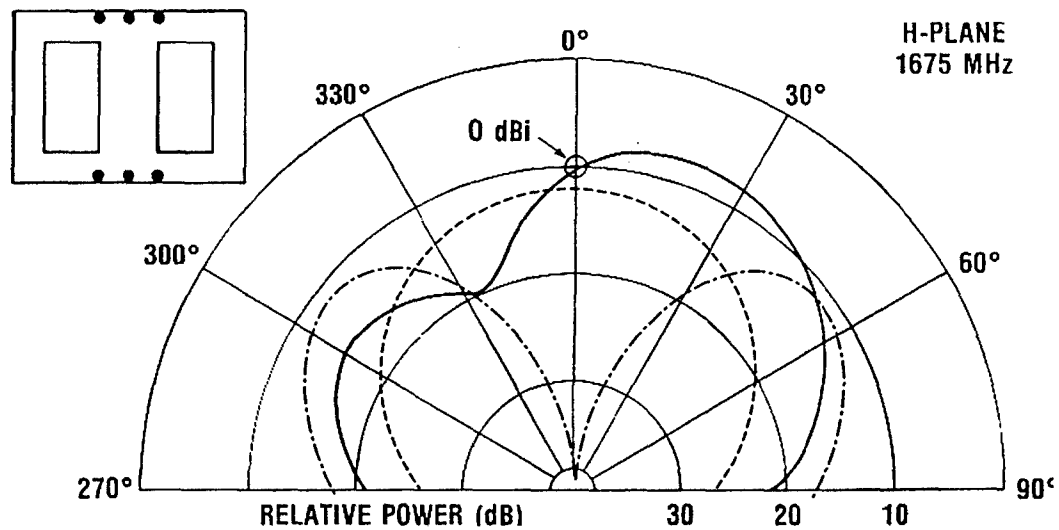
Figure 11. Combining holes in metalization and posts can force two modes of the patch to share a common resonant frequency. The patterns of the individual modes are indicated by the dashed lines sketched onto the plot. The solid curve is the measured radiation pattern of the 6.2-cm x 9-cm antenna at 1675 MHz. From [16].
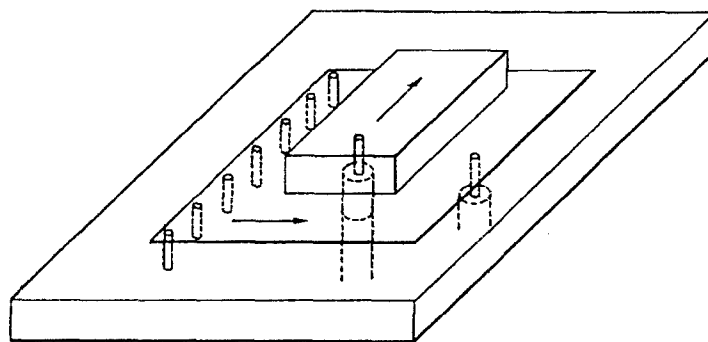
Figure 12. Example of piggyback antennas. The lower antenna is a quarter-wavelength horizontally polarized element and the upper element is a half-wavelength vertically polarized element. From [18].

APPENDIX

G. Deschamps and W. Sichak, "Microstrip Microwave Antennas," *Proceedings of the Third Symposium on the USAF Antenna Research and Development Program*, October 18-22, 1953.

ADB 283180

THE THIRD SYMPOSIUM
ON
THE USAF ANTENNA RESEARCH
AND
DEVELOPMENT PROGRAM

Declassified By

authority of ___ AFAL ltr. ___

20 Jan 1965 ___ from ___ E. M. Turner

Doris M. Richards

ROBERT ALLERTON PARK
(University of Illinois)
Monticello, Illinois
18, 19, 20, 21, 22, October 1953

ESC 04-0289

███████████████

MICROSTRIP MICROWAVE ANTENNA   *and*   W. Sichak

By Georges Deschamps
Federal Telecommunication Laboratories

Contract AF33(038)-13289

INTRODUCTION

The problem was to obtain a high resolution, X-band antenna with shaped vertical-pattern and a horizontal beamwidth of less than one degree. The usual solution of using a long linear array feeding a cylindrical reflector was adopted and it remained to design the linear array, which in the present case was to be 300 wavelength long.

Methods for obtaining such an array are: 1) The pillbox or sectoral lens, 2) The end fed slot array, 3) The linear array where all elements are fed through equal lengths of waveguide. With the second solution the pattern varies with frequency and the design is complicated by mutual effects between slots. The first and third solutions avoid this difficulty and are essentially similar; in (1) the power distribution is done continuously by spreading of the wave and bending by refraction or reflection, in (2) it occurs at the junctions along the feed system.

The third solution with standard waveguides makes a rather bulky system. In the present case since about 300 radiating element spaced one wavelength apart had to be fed, 255 or 511 two-way power dividers would be needed. The recent development at FTL of the microstrip removed this objection and it was decided to investigate a solution based on this transmission medium.

The microstrip is a variant of "wire above ground" transmission line, adapted to microwaves. The conductor can be a strip printed on a dielectric sheet backed by a conducting plane (Fig. 1). In spite of the composite nature of its crossection this waveguide acts substantially as if it was supporting a TEM mode. For instance the dispersion is negligible and it is possible to define a characteristic impedance $1/Cv$ (C = capacity per unit length, v = phase velocity). This impedance is a function of the strip width and distance to the ground plane and accounts well for the properties of the junction between two strips of different characteristics.

The advantages of a feed system using microstrips rather than conventional waveguides would be:

1. Less volume and much less weight

2. Less fabrication cost - possibility of exact photographic reproduction of even critical adjustments

3. Possibility of shaping or stacking

The same advantages would obtain with the dielectric covered microstrip and with the sandwich line[1] (Fig. 1).

In a first model of microstrip feed the line was made of copper foil fastened to polystyrene sheets with polyethylene scotch tape. The antenna worked substantially as expected but had a rather poor pattern. This was attributed to radiation from the junctions and it was decided to make a more systematic study of the elements of the systems:

---

1. R. M. Barrett, "Etched Sheets Serve as Microwave Components," ELECTRONICS, June, 1952.

the line itself, bends, power dividing junctions, transducer from wave-
guide to microstrip and radiating elements. It was also decided to make
a comparison with similar systems constructed with the sandwich line.

Microstrip

The strip width and dielectric thickness were varied and the
wavelength and attenuation constant measured. A relatively low-loss di-
electric was found: a Teflon Fiberglass laminate backed by copper.

A compromise choice of dimensions: width 1/8", thickness 1/8",
was used in the finished antenna. Losses in this case were about 0.6 db
per foot.

Waveguide to Microstrip Transducer

The initial transition must be made between a standard rectan-
gular waveguide and the microstrip. This was achieved by a tapered ridge
connecting the upper side of the waveguide to the strip while the lower
side is soldered to the ground plane (Fig. 2). Insertion loss of less
than 1/4 db was obtained without difficulty.

Bends

Circular bends of various curvature and mitered bends of vari-
ous cuts were tried. Circular bends of appropriate radii appear to give
less radiation loss (1/2 db) and negligible mismatch. The minimum ac-
ceptable radius is a function of strip width.

Short Circuit and Matched Load

For measurement purposes a good reflecting load and an absorb-
ing load are useful. The reflecting load can take the form of a resonant

obstacle, ring or V, placed above the strip (Figure 3). Reflection coefficients of 0.9 were obtained. A matched load producing a standing wave ratio of 1.02 and a loss of more than 30 decibels can be made of a tapered resistive card (400 ohms per square) placed also on top of the strip (Figure 4).

The measurements were made by moving the reflective obstacle in back of the element to be evaluated (junction or line) according to methods which were developed in an early part of this contract.

Power Dividing Junctions

This is the main component of the system. The first configuration (Figure 5a) based on the idea of matching characteristic impedance, showed too much radiation because of abrupt changes (which would not matter in closed waveguides). The most satisfactory solution used a smooth splitting of the upper strip into circular bends of sufficient radius. The tangents at A - A (Figure 5b) must be carefully matched.

Data were taken on symmetrical two-way and three-way power dividers and on two-way assymmetrical power dividers. With the sandwich line the power split was studied as a function of the width of the two conductors, in order to make an array with non uniform distribution.

Radiating Elements

The microstrip can be transformed smoothly into a horn or a parallel plate region by widening progressively the strip (Figure 6).

For the sandwich line the same thing can be done after stopping abruptly the upper plate (Figure 7a). Alternatively the two plates can merge into the floor and ceiling of the horn while a 180-degree phase difference is introduced between the fields above and below the central strip by stopping the dielectric (Figure 7b). This latter transition gave a better E-plane pattern.

Dipole arrangements could also be used (Figure 8). In one of the experimental arrays the radiating elements were small lenses (aperture 8λ).

Arrays and Patterns

A number of experimental arrays have been constructed having relatively small apertures (32 elements). These could be used as building blocks for the larger array. The lines feeding these blocks being relatively long it could be advantageous to use there ordinary waveguides.

The first array was a 32 element microstrip antenna designed with two-way power splitters for uniform illumination. Figure 8 shows the layout before etching of the feed system and Figure 9 a perspective view. The H plane pattern is shown on Figure 10 and the average input impedance of the feed when reflection at the radiating element has been taken out (Figure 11) is shown on Figure 12.

In a second array (Figure 13) four lenses are fed with microstrip. The pattern (Figure 14) is cleaner but scanning would not be possible. The average input impedance is shown on Figure 15.

The third array, Figure 16, was fed with a sandwich line system. Radiation at the junctions ceases to be a problem and the bends can be more sharply curved making the overall system less deep. The strip conductor, however, must be the same distance from the two plates and this seems critical. More care has to be exercised in making the line. The transition to the horn, figure 7b was found to be more satisfactory than 7a.

A fourth array with sandwich line feed was built with a cosine tapered amplitude distribution (end element 12 db below central elements). Junctions with unequal power division as shown in Figure 5c were used.

The patterns in the H and E planes are shown respectively in Figures 17 and 18.

More details can be found in FTL Final Engineering Report, Research on Bombing-Radar Antenna Problems, Contract AF33(038)-13289.

Conclusions:

A choice between microstrip (easier to fabricate) and sandwich line (less radiation) cannot be made yet. More data are still needed on the components, specially the power dividing junctions and the transducers to the radiating elements. It would also be important to find a still better dielectric since the losses in the feed system are a definite limitation to the size of the array (Figure 19).

In spite of this and of the fact that a complete array has not been demonstrated, printed waveguides of the microstrip or sandwich type have obvious advantages over ordinary waveguide and show promising possibilities for the problem considered.
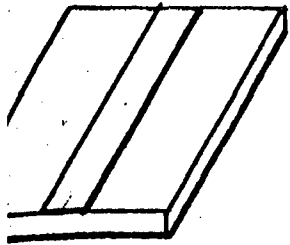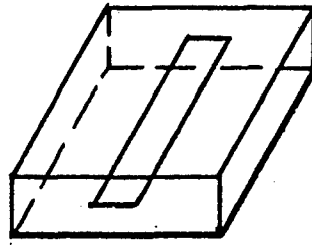
CROSTRIP

DIELECTRIC COVERED
MICROSTRIP
FIG. 1
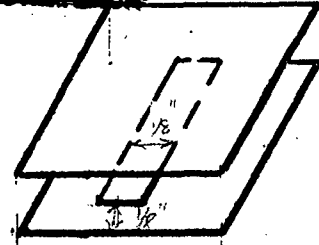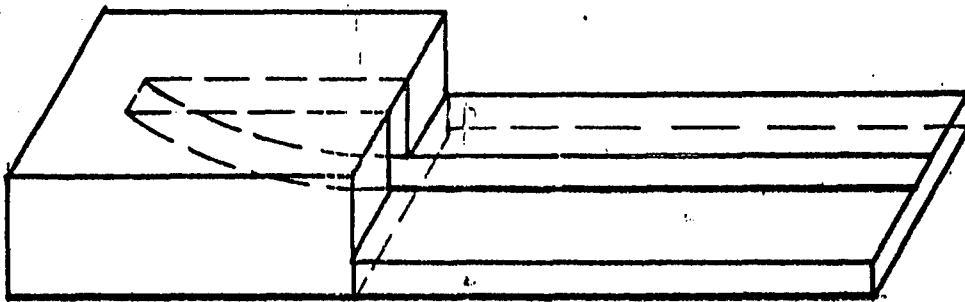
SANDWICH LINE

WAVEGUIDE TO MICROSTRIP TRANSDUCER
FIG. 2
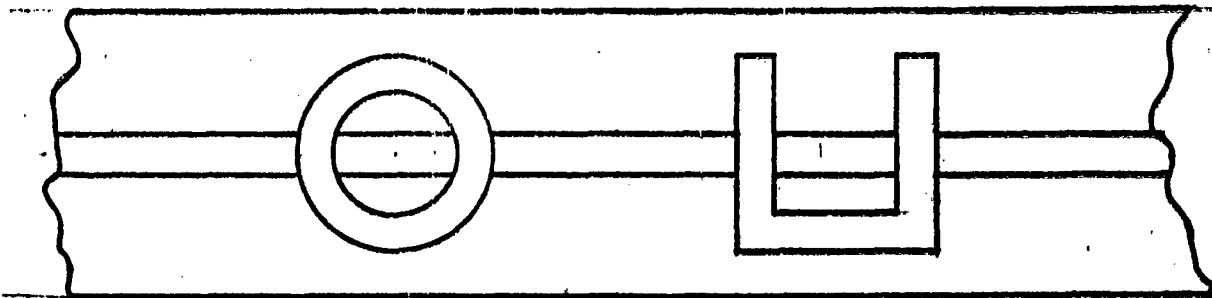
REFLECTIVE OBSTACLES
FIG. 3

Reflection Coeff
.8 to .9

SWR - 1.2 ?
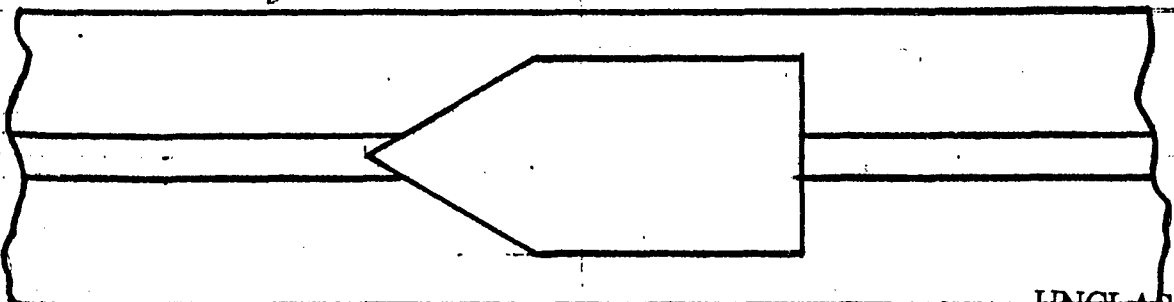
MATCHED LOAD
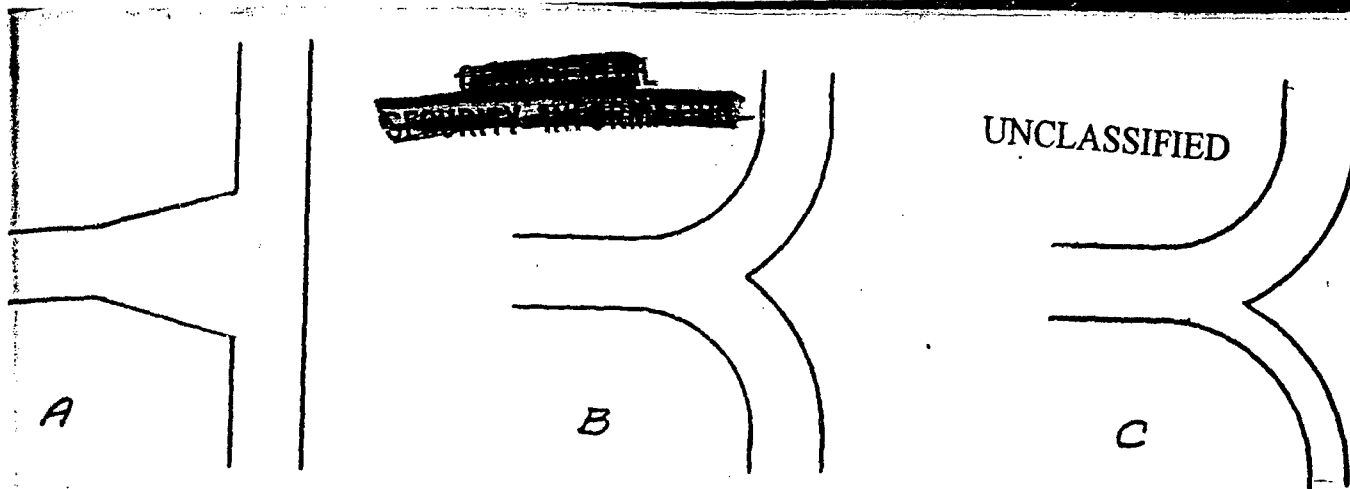
POWER DIVIDING JUNCTIONS
FIG. 5
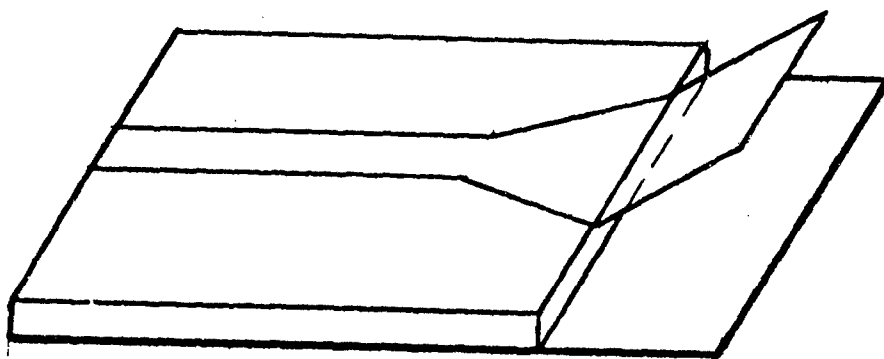
MICROSTRIP TO HORN TRANSITION
FIG. 6
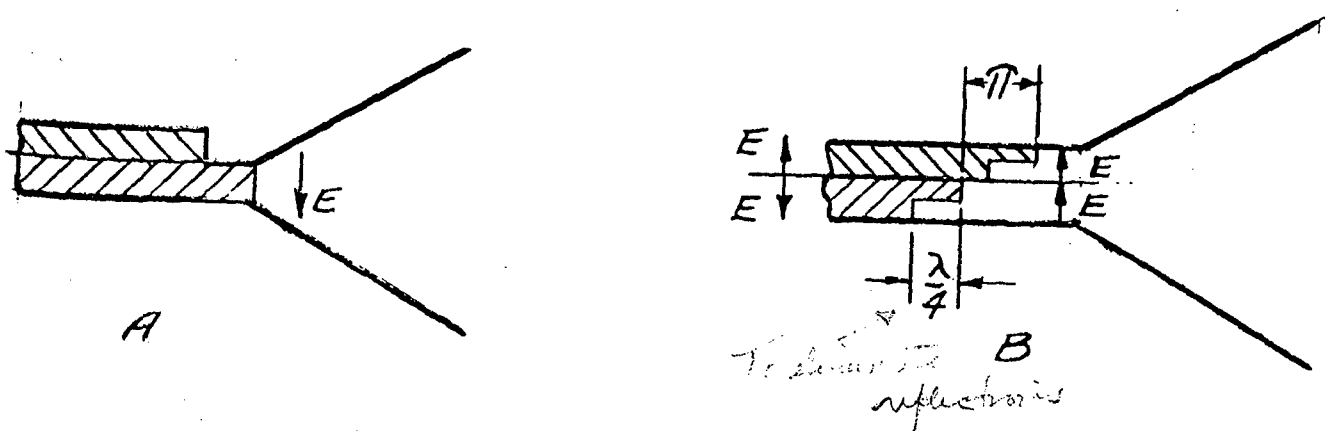
SANDWICH-LINE TO HORN TRANSITIONS
FIG. 7
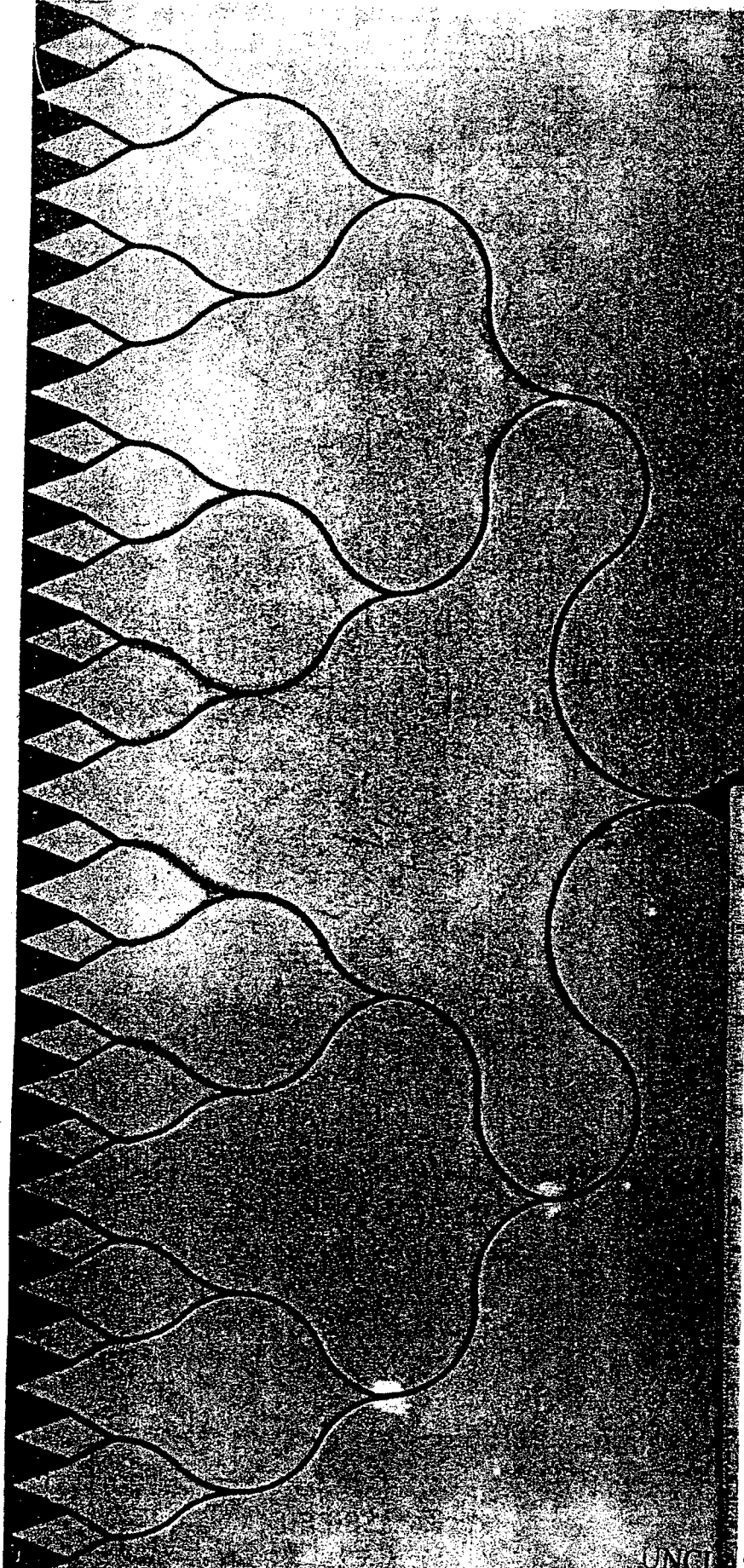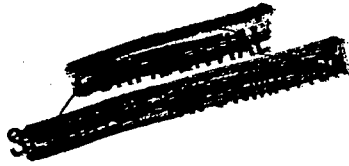
FIGURE 8

19
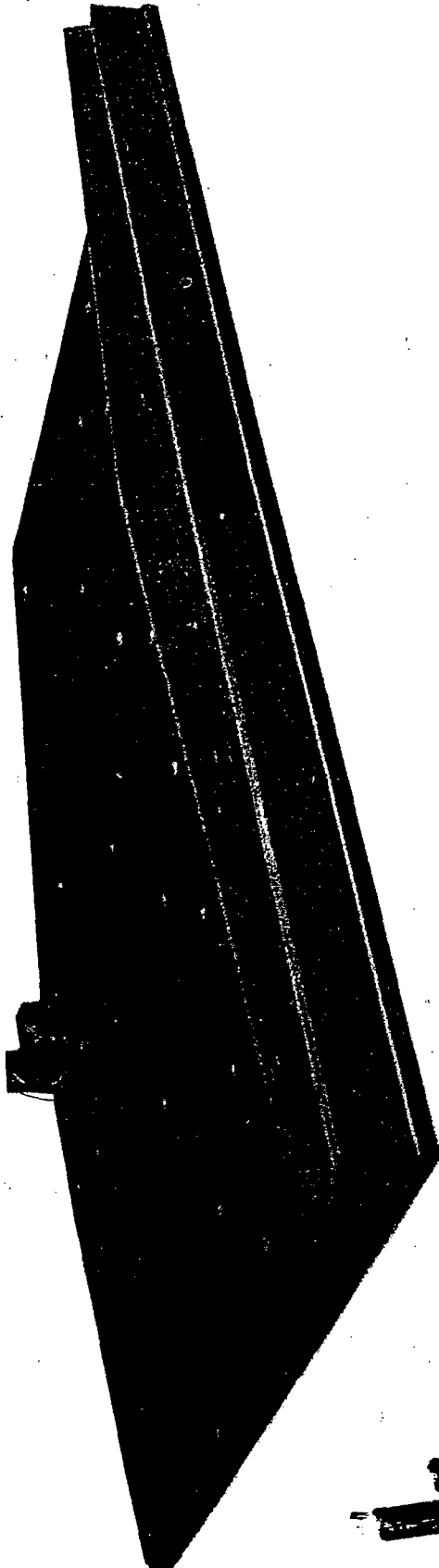
FEDERAL TELECOMMUNICATION LABORATORIES, INC.
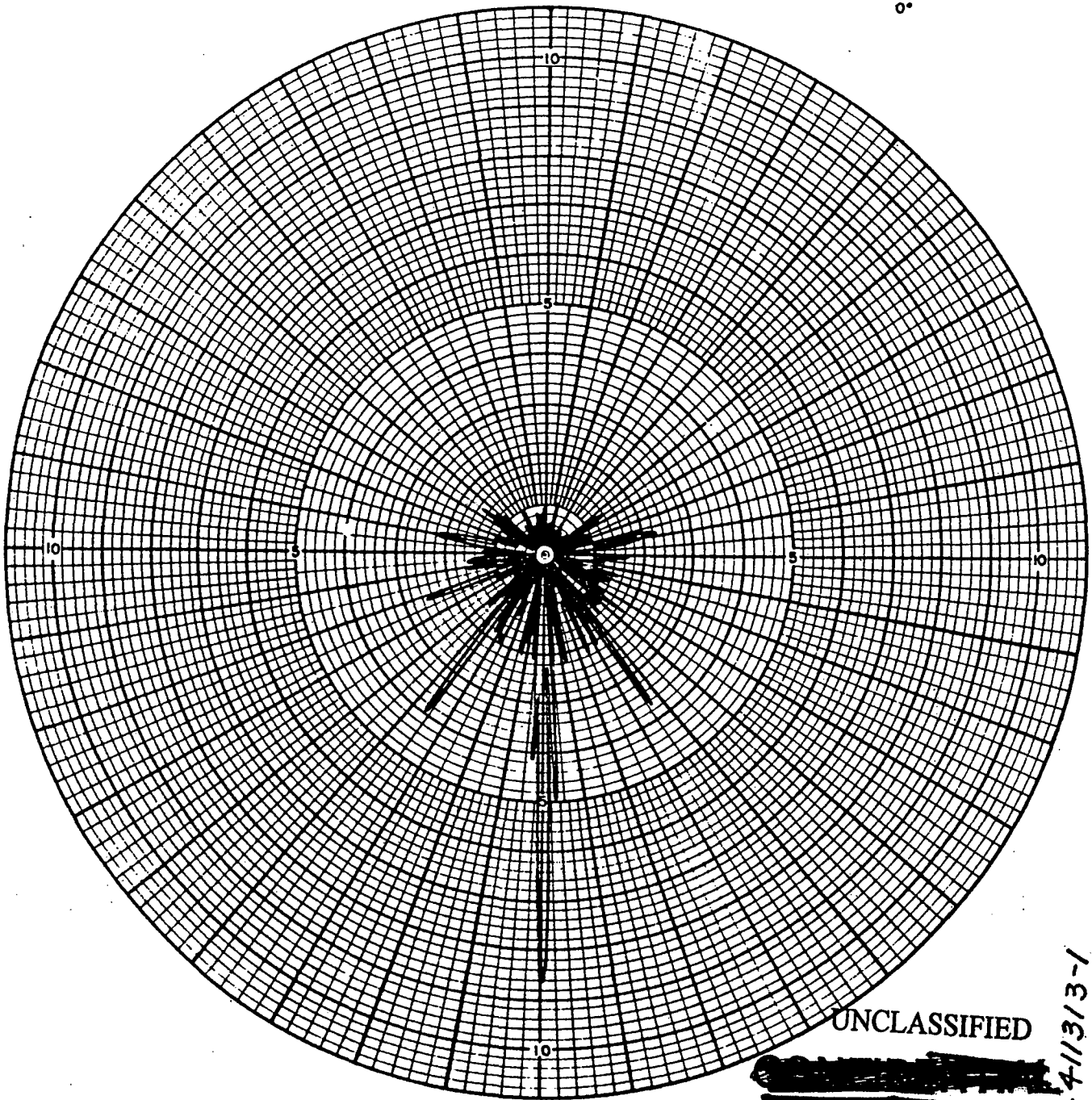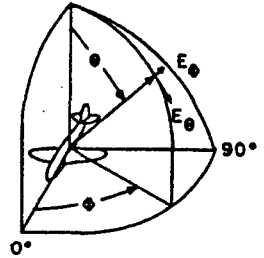
RX-411313-1

DATE: 1-13-53

OBSERVERS: 1 DJL
                2 WE, RM

PLANE TYPE:

SCALE FACTOR: 1:1

MODEL FREQUENCY: 9000 MCS.

FIG. 10

PATTERN: θ. 90° **θ.** VARIABLE

POLARIZATION Eθ ✓   **Eθ**   **OTHER**

CURVE PLOTTED IN: VOLTAGE ✓ **POWER**   **DB**

ANTENNA TYPE: ETCHED MICROSTRIP ARRAY

ANTENNA LOCATION:

DISTANCE FROM ILLUMINATING SOURCE: 60 FT.

11.

MEASURED INPUT VSWR vs FREQUENCY

4 LENS MICROSTRIP ARRAY

$r_1 = \sqrt{r_{MAX} \cdot r_{MIN}}$

$r_2 = \sqrt{\dfrac{V_{MAX}}{V_{MIN}}}$

MEASURED VSWR

r_0

r_0, ANT. VSWR
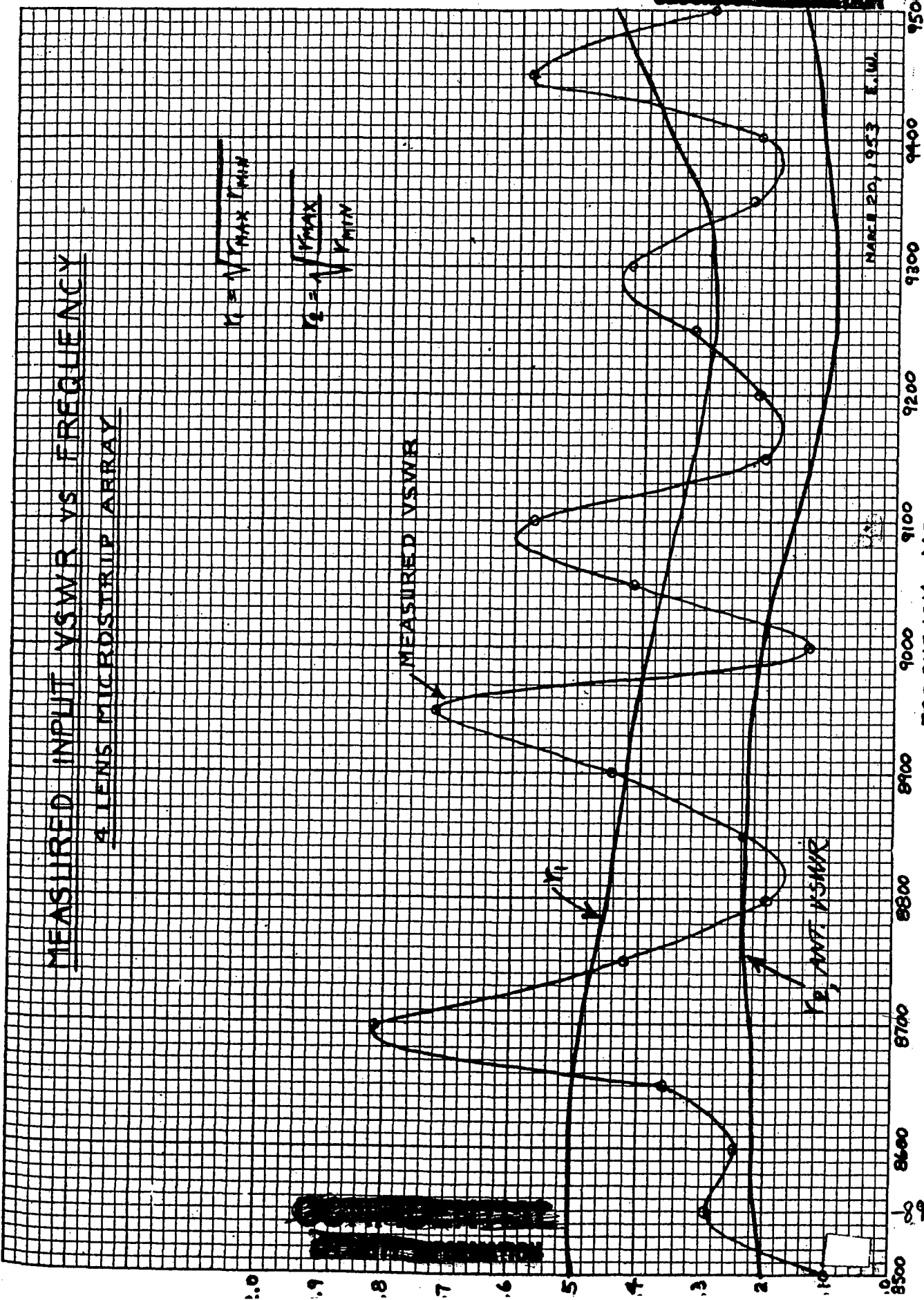
FREQUENCY — MC

FIG. 11

MARCH 20, 953 E.W.

RX-411597-1B

-89-

12

UNCLASSIFIED

AVERAGED INPUT IMPEDANCE VS FREQUENCY
ETCHED MICROSTRIP 32 ELEMENT ARRAY ANTENNA.
MEASURED AT FACE OF FLANGE ON INPUT.

THE EMELOID CO., INC.
HILLSIDE 8. N. J.
JANUARY 1948
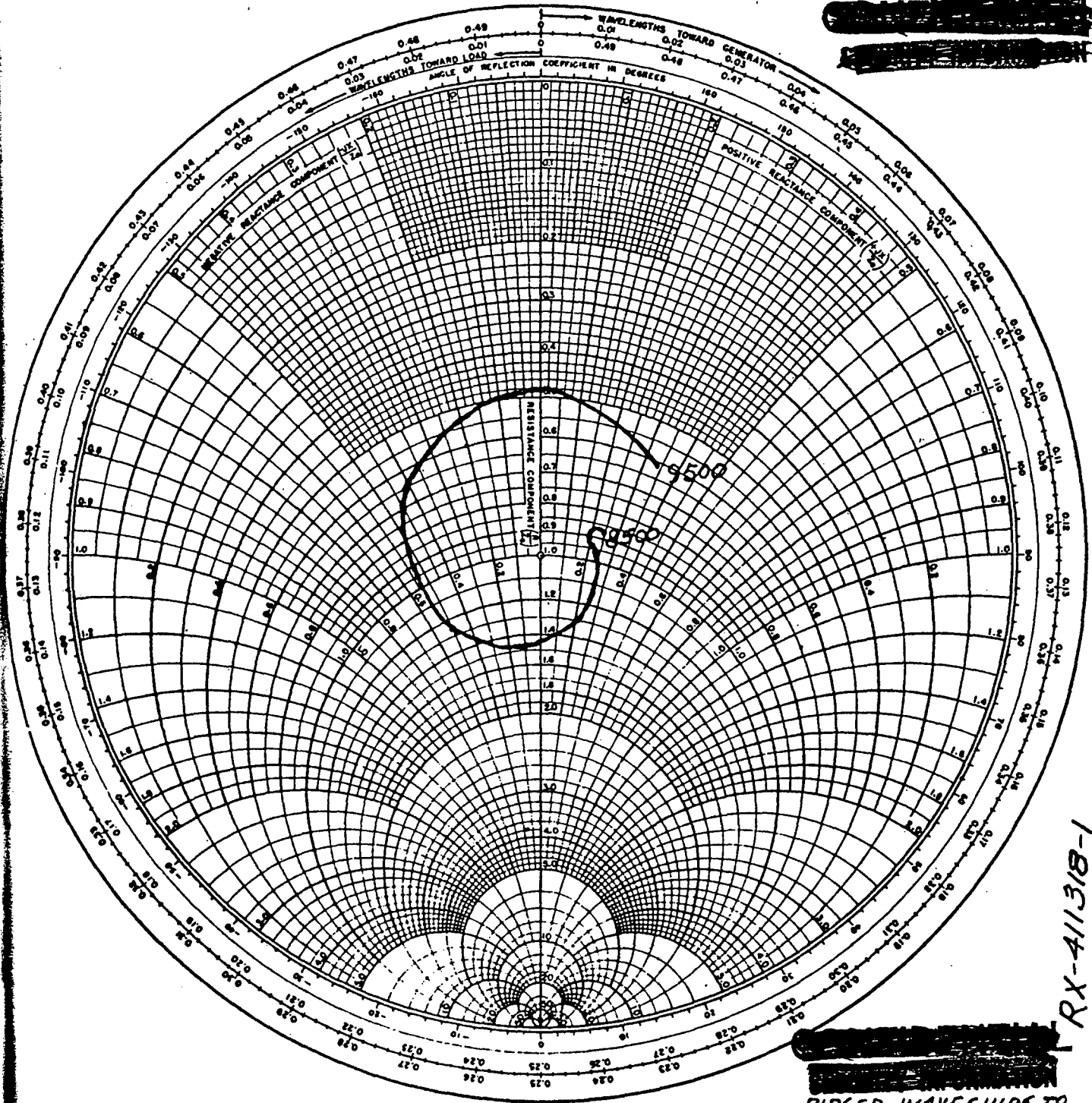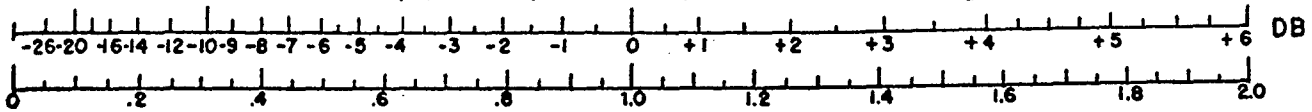
RIDGED WAVEGUIDE TO
MICROSTRIP TRANSDUCER

MICROSTRIP   Printed in U.S.A.
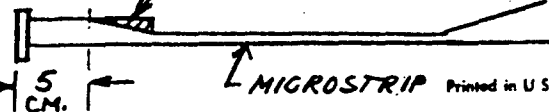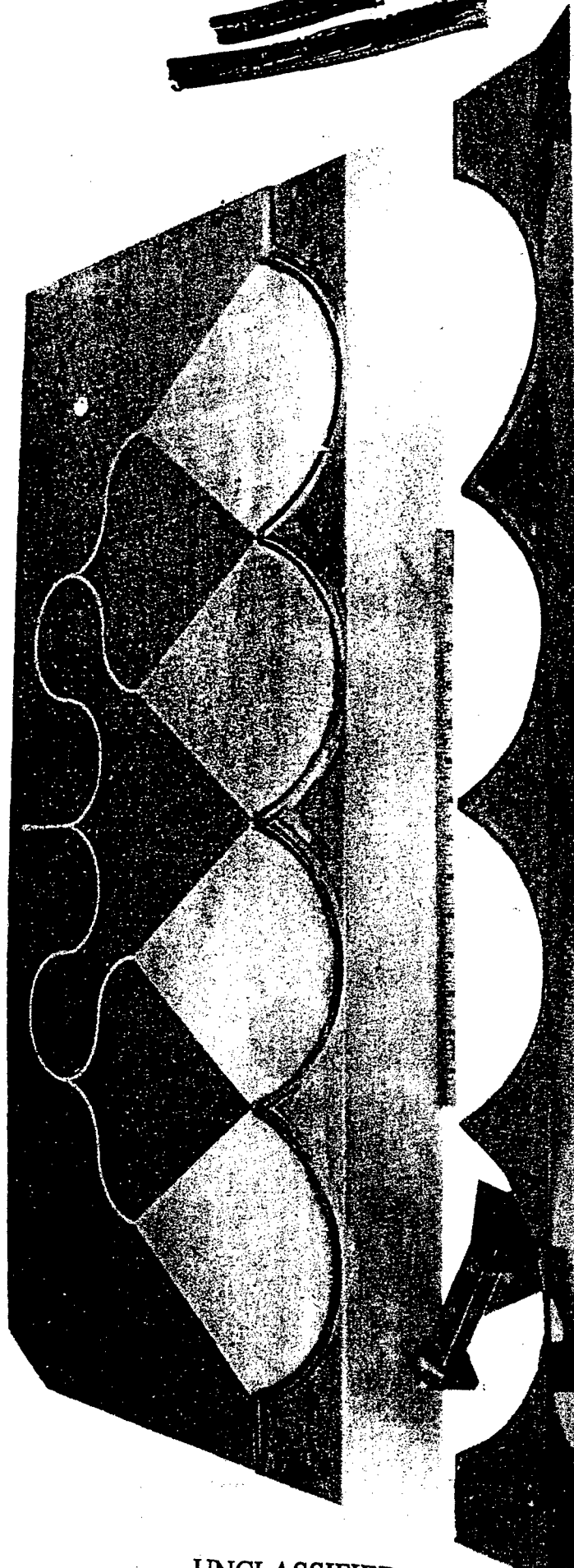
RX-41318-1

1-28-58 DJL

Philip H. Smith "Transmission Line Calculator" Electronics Jan 1939 and Jan 1944

FIG. 12

FIGURE 13

FEDERAL TELECOMMUNICATION LABORATORIES, INC.
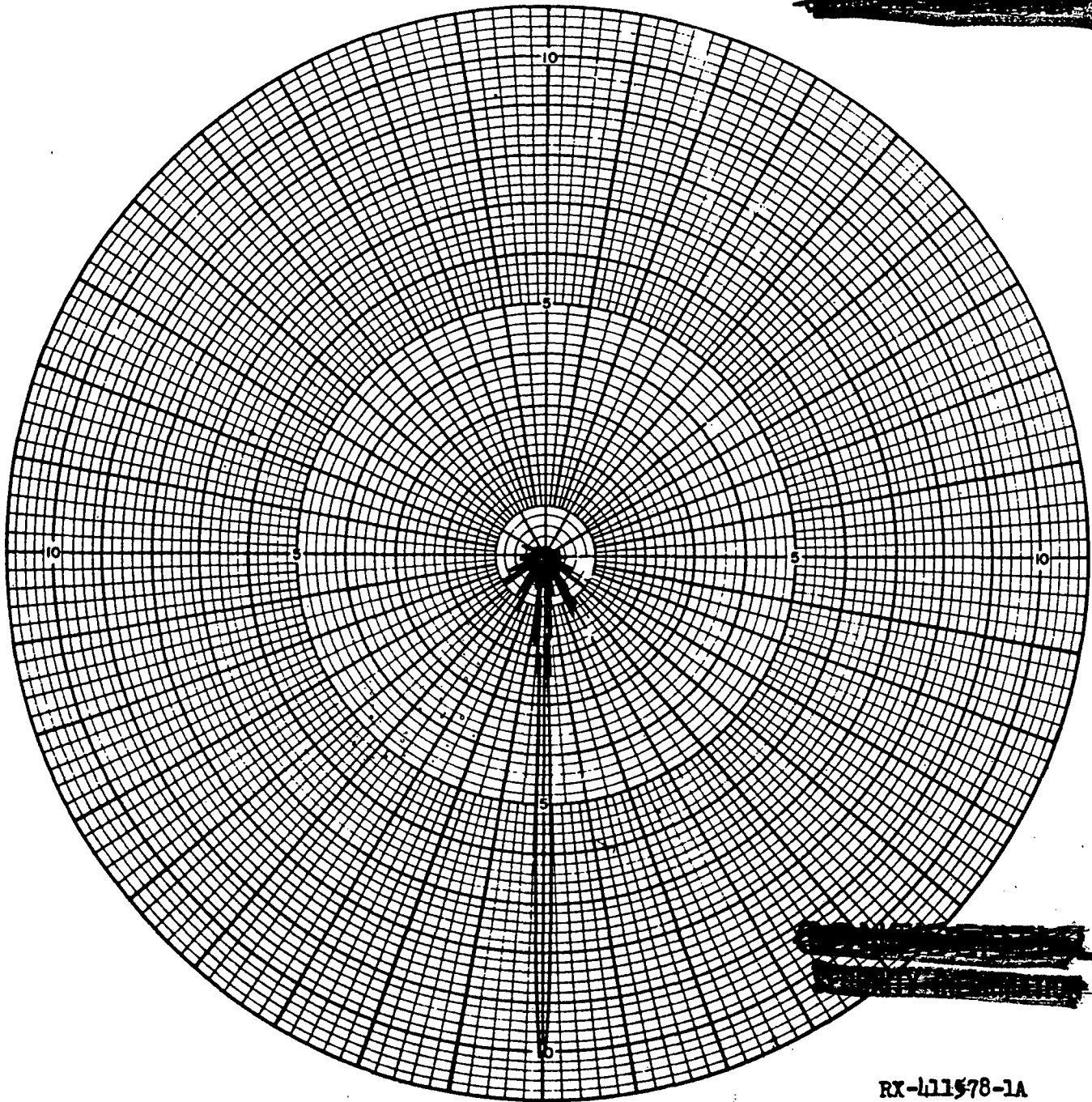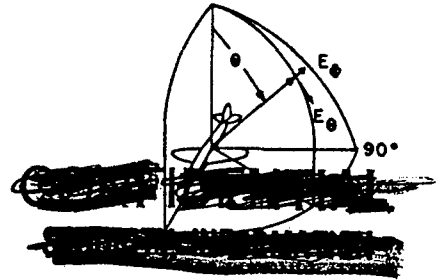
RX-411578-1A

DATE: 3-10-53
OBSERVERS: 1. EW
          2. RM, WE
PLANE TYPE: None
SCALE FACTOR: Full Scale

PATTERN: θ. 90° φ. Variable
POLARIZATION Eθ ⟵ Eφ   OTHER
CURVE PLOTTED IN: VOLTAGE ⟵ POWER   DB
ANTENNA TYPE: 4 lens microstrip array
ANTENNA LOCATION:

16

AVERAGED INPUT IMPEDANCE VS FREQUENCY –

ETCHED MICROSTRIP 4 LENS ARRAY ANTENNA.

MEASURED AT FACE OF FLANGE ON INPUT.
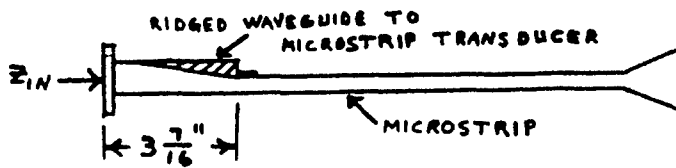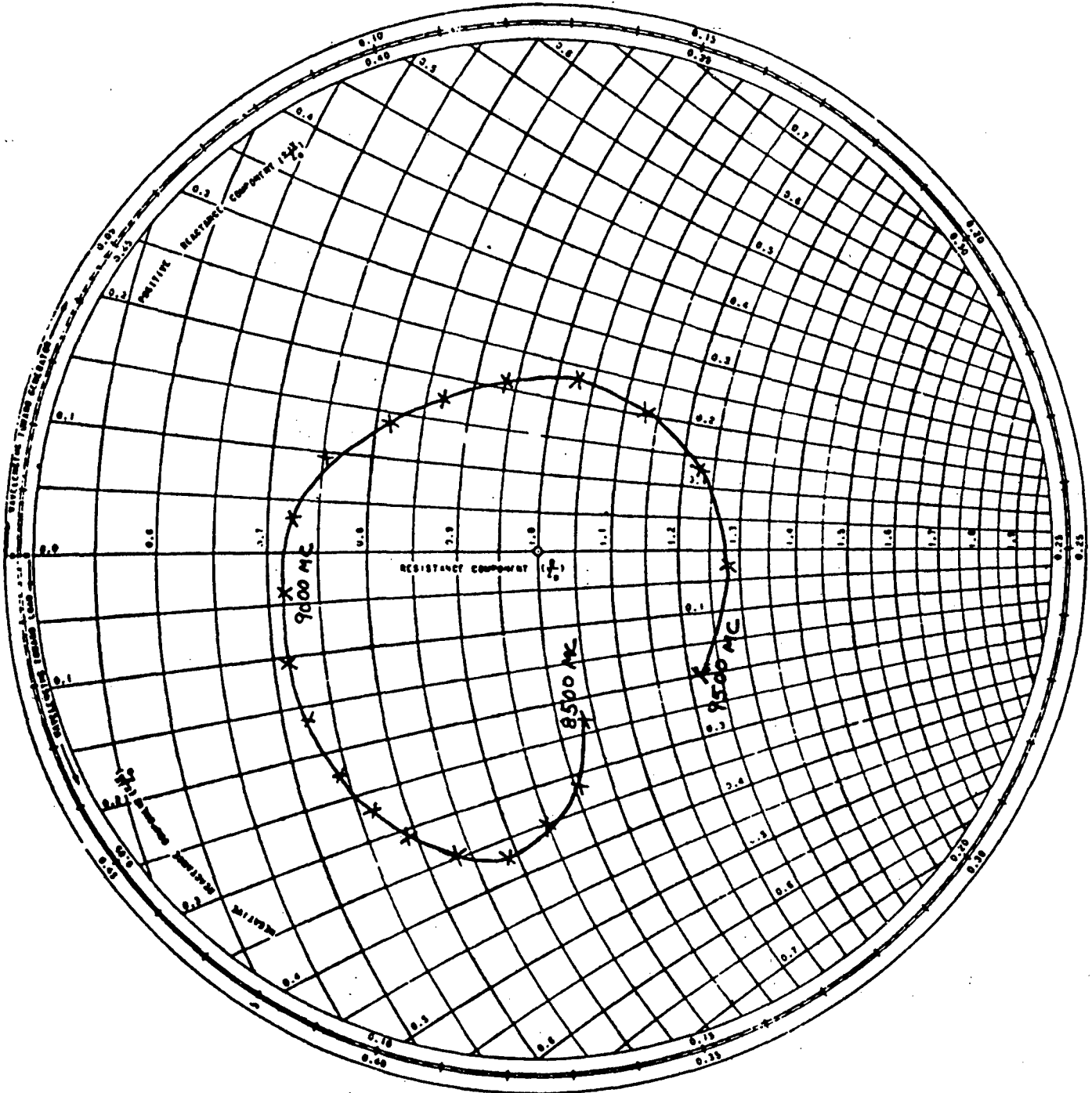
FIG. 15

MARCH 17-1953 F.W.

RX-411595-1A
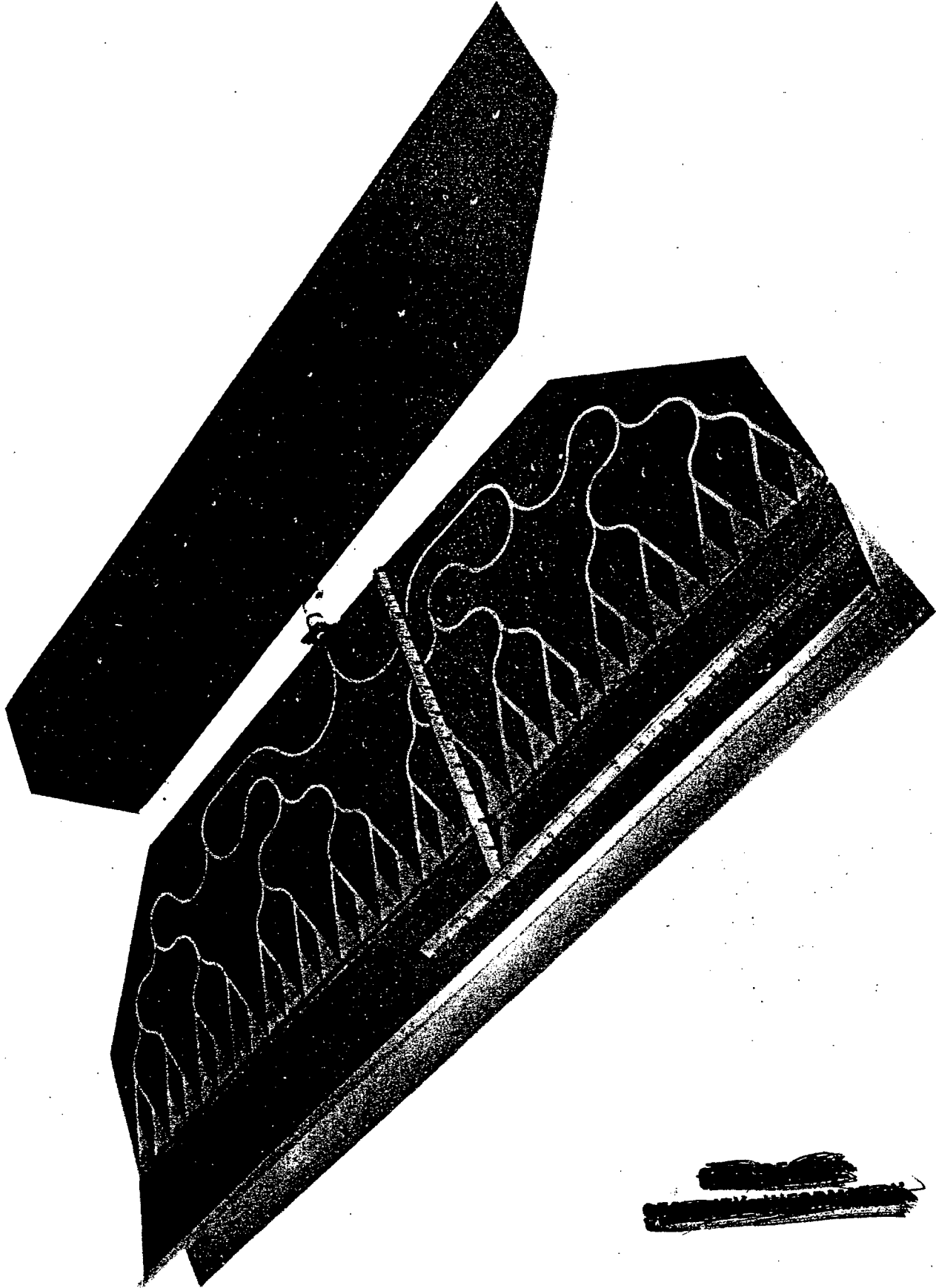
-90-

FIGURE 16

FEDERAL TELECOMMUNICATION LABORATORIES, INC.
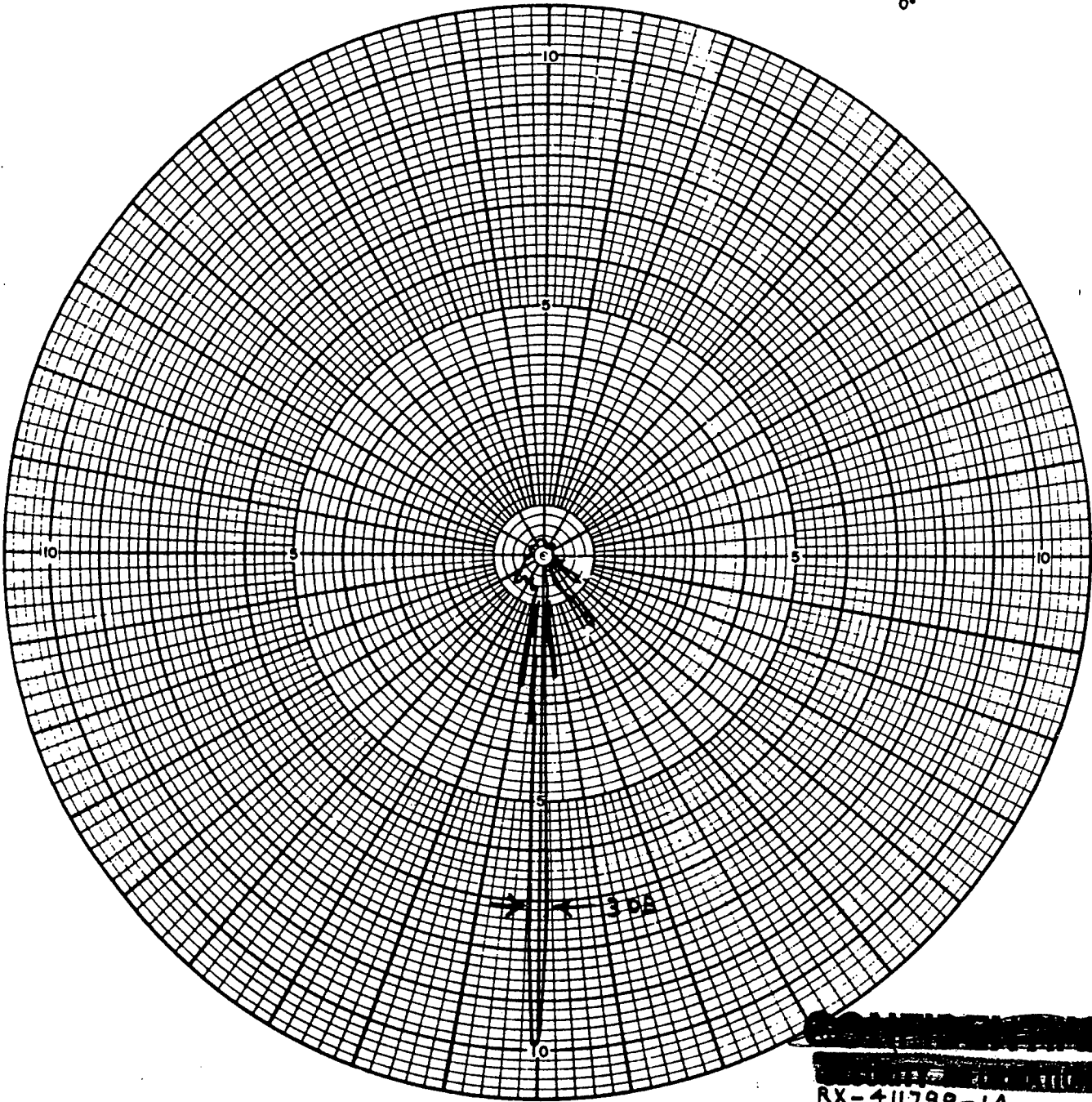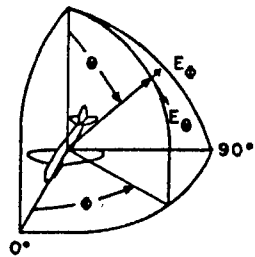
RX-411799-1A

DATE: APRIL 20, 1953

OBSERVERS: I. E.W.

2.

PLANE TYPE:

SCALE FACTOR:

UNCLASSIFIED

PATTERN: θ: 90° ϕ: VARIABLE

POLARIZATION Eϕ ✓   Eθ OTHER

CURVE PLOTTED IN: VOLTAGE   POWER ✓   DB

ANTENNA TYPE: 32 ELEMENT, COSINE POWER DISTRIBUTION, MICROSTRIP SANDWICH, BALANCED FEED

18
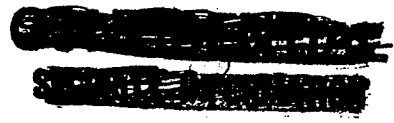
FEDERAL TELECOMMUNICATION LABORATORIES, INC.
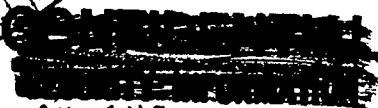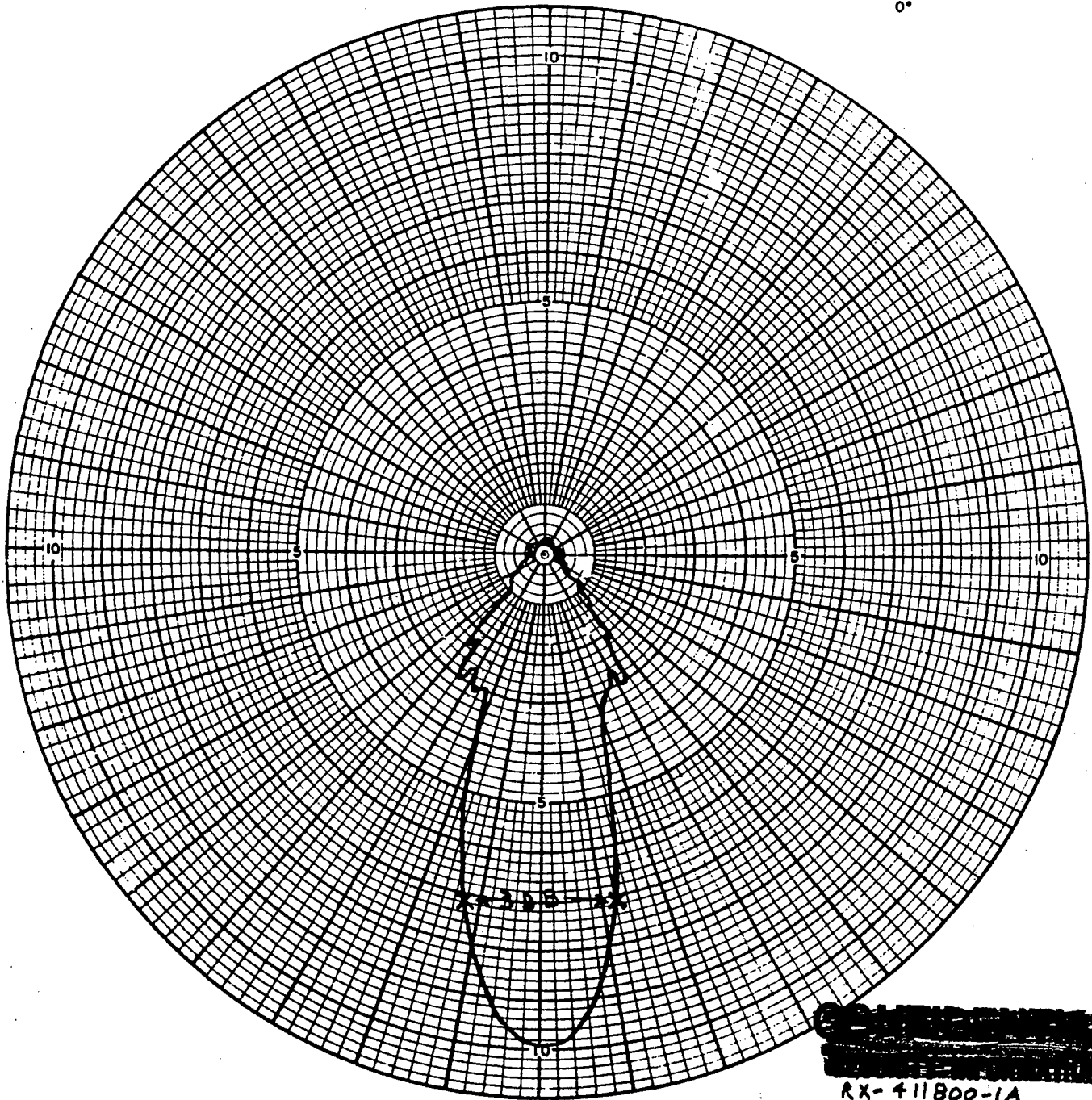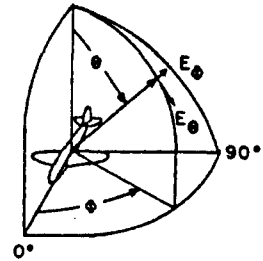
FIG. 18

RX- 411800-1A

DATE: APRIL 20, 1953
OBSERVERS: 1. E.W.
2.
PLANE TYPE:
SCALE FACTOR:

PATTERN: Φ = VARIABLE Φ = 0°
POLARIZATION Eθ ✓ Eφ OTHER
CURVE PLOTTED IN: VOLTAGE POWER ✓ DB
ANTENNA TYPE: 32 ELEMENT, COSINE POWER DISTRIBUTION, MICROSTRIP SANDWICH, BALANCED FEED TO HORN.

29

RELATIVE GAIN VS. LENGTH OF LOSSY FEED LINE
LONG ARRAY

$$GAIN = K \frac{L}{\lambda} e^{-0.23 \alpha L}$$

$\alpha = db/foot$

$L = LENGTH\ OF\ FEED\ OR\ ARRAY\ FEET$

$\lambda = WAVELENGTH$

$K = CONSTANT$

LENGTH L - FEET